
# BATTERY-LESS NEAR FIELD COMMUNICATIONS (NFC) SENSORS FOR INTERNET OF THINGS (IoT) APPLICATIONS

**Martí Boada Navarro**

Martí Boada Navarro

# BATTERY-LESS NEAR FIELD COMMUNICATIONS (NFC) SENSORS FOR INTERNET OF THINGS (IoT) APPLICATIONS

DOCTORAL THESIS

Supervised by Dr. Antonio Lázaro Guillén
and Dr. David Girbau Sala

Department
of Electronic, Electric and Automatic Control Engineering

UNIVERSITAT ROVIRA i VIRGILI

Tarragona

2020

UNIVERSITAT ROVIRA I VIRGILI
BATTERY-LESS NEAR FIELD COMMUNICATIONS (NFC) SENSORS FOR INTERNET OF THINGS (IoT) APPLICATIONS
Martí Boada Navarro

FAIG CONSTAR que aquest treball, titulat “Battery-less Near Field Communications (NFC) Sensors for Internet of Things (IoT) Applications”, que presenta Martí Boada Navarro per a l’obtenció del títol de Doctor, ha estat realitzat sota la meva direcció al Departament DEEEA d’aquesta universitat.

---

HAGO CONSTAR que el presente trabajo, titulado “Battery-less Near Field Communications (NFC) Sensors for Internet of Things (IoT) Applications”, que presenta Martí Boada Navarro para la obtención del título de Doctor, ha sido realizado bajo mi dirección en el Departamento DEEEA de esta universidad.

---

I STATE that the present study, entitled “Battery-less Near Field Communications (NFC) Sensors for Internet of Things (IoT) Applications”, presented by Martí Boada Navarro for the award of the degree of Doctor, has been carried out under my supervision at the Department DEEEA of this university.

---

Tarragona, 29/1/2020

El/s director/s de la tesi doctoral
El/los director/es de la tesis doctoral
Doctoral Thesis Supervisor/s

Antonio Ramón Lázaro Guillén

David Girbau Sala

UNIVERSITAT ROVIRA I VIRGILI
BATTERY-LESS NEAR FIELD COMMUNICATIONS (NFC) SENSORS FOR INTERNET OF THINGS (IoT) APPLICATIONS
Martí Boada Navarro

# List of Publications

## Indexed Journals

[J.1] M. Boada, A. Lazaro, R. Villarino, and D. Girbau, 'Battery-less soil moisture measurement system based on a nfc device with energy harvesting capability', *IEEE Sens. J.*, vol. 18, no. 13, pp. 5541–5549, 2018.

[J.2] M. Boada, A. Lazaro, R. Villarino, and D. Girbau, 'Battery-Less NFC Sensor for pH Monitoring', *IEEE Access*, vol. 7, pp. 33226–33239, 2019.

[J.3] A. Lazaro, M. Boada, R. Villarino, and D. Girbau, 'Color Measurement and Analysis of Fruit with a Battery-Less NFC Sensor', *Sensors*, vol. 19, no. 7, p. 1741, Apr. 2019.

[J.4] A. Lazaro, M. Boada, R. Villarino, and D. Girbau, 'Battery-less Smart Diaper based on NFC Technology', *IEEE Sens. J.*, pp. 1–1, 2019.

[J.5] A. Lazaro, M. Boada, R. Villarino, and D. Girbau, 'Study on the reading of energy-harvested implanted NFC tags using mobile phones', *IEEE Access*, vol. 8, 2019.

## Book chapter

[B.1] A. Lazaro, M. Boada, R. Villarino, and D. Girbau, 'NFC Sensors Based on Energy Harvesting for IoT Applications', in *Wireless Energy Transfer Technology [Working Title]*, IntechOpen, 2019.

## International Conferences

[C.1] M. Boada, A. Lazaro, R. Villarino, E. Gil, and D. Girbau, 'Near-Field Soil Moisture Sensor with Energy Harvesting Capability', in *2018 48th European Microwave Conference, EuMC 2018*, 2018, pp. 235–238.

UNIVERSITAT ROVIRA I VIRGILI
BATTERY-LESS NEAR FIELD COMMUNICATIONS (NFC) SENSORS FOR INTERNET OF THINGS (IoT) APPLICATIONS
Martí Boada Navarro

# Index

# 1. Introduction

## 1.1From barcodes to the internet of things

Streamline industrial processes have been always a priority to reduce time hence reducing costs. Identification of goods is an important factor to consider in almost any process since it is necessary to track and get specific information from the goods, thus, the importance of automatize it. The most common method is to use barcode systems based on a printed label with an identification number which is read by an optical device connected to a computer [1] (see Figure 1.1)


Figure 1.1. Barcode reading.

Barcodes have been applied to several fields such as libraries [2] or medical uses like identification for blood transfusions [3] or medication administration [4] proving that is an easy, fast, and accurate automatic collection method. Linear barcodes are the most common technology related to Automatic Identification Data Capture (AIDC). Usually the reading methods use both, hardware and software implementations, however, there are methods fully implemented with a hardware [5] or software [6] solution. Nonetheless, barcodes only contain information in 1 dimension (1D), thus, containing a limited amount of information. To enlarge the data representation capability, two dimensions (2D) codes have been developed. Within the bunch of 2D barcodes symbologies (e.g. MaxiCode, PDF 417, codablock F, Aztec), there are two that are widespread. One of them is the data matrix (standardised by the ISO/IEC 16022 [7]) and the Quick Response (QR) codes (ISO/IEC 18004/2000 [8]). Data matrix capacity is 2334 alphanumeric characters, or 1556 ASCII characters, and uses between 30% and

60% less space than a QR [9] (See Figure 1.2), however, it does not allow to encode Japanese characters, which is the main reason why QR codes have been more extended worldwide.

(a) (b)

Figure 1.2. "http://google.com encoded" as (a) QR code and (b) data matrix.

The implementation of 2D barcodes in the industry brings some advantages such as the increase data or replace the special-purpose laser scanners with digital cameras, which implies a cost reduction and improves the image processing by using dedicated software and algorithms [10]–[12]. Nowadays the prevailing devices with digital camera embedded are the smartphones. Furthermore, the computational capability of the smartphones allows to install applications to read all kind of barcodes symbologies. Since QR codes are supposed to be widely used by any type of smartphones just taking a photo of the code, the light conditions and possible damages or other alterations of the printed code must be considered [13] as well as security issues [14].

Within AIDC systems, Radiofrequency identification (RFID) [15] arrived to overcome barcode limitations. An RFID system consist of 2 differentiated parts: a reader (also called interrogator) and a tag. The reader generates a signal which is received by the tag, modulated by the tags transponder based on its internal information (e.g. an ID), and sent back to the reader to be interpreted. Table 1.I enumerates some of the differences between barcodes and RFID.

Table 1.I. Comparison barcode and RFID

| Barcode | RFID |
|---|---|
| Line of sight | No need of line of sight |
| Read one by one | Multiple reads simultaneously |
| Fixed content | Updatable content |
| Manual tracking | Can be automatically tracked |

The spread of RFID technology at large-scale began at the firsts years of the 21st century, when three major organizations (Wall-Mart, Tesco, and the US Department of Defense) opted to use such technology streamlining the tracking of stock, sales, and orders [16]. The expansion of RFID came along with the need of analysing it use of commercial applications and the need of regulations [17] as well as methods for security and privacy [18]. RFID have been widespread used for all sort of applications [19] such as object localization [20], [21], cars parking [22], food traceability [23], logistics service [24] or navigation assistance for blind people [25]. The interrogators used to read the tags can be connected to the internet, having the capability of sending the collected data of the identified objects to the cloud in real time, which brings to the so-called internet of things (IoT) [26].

Passive RFID systems reduce the price of the tags to a few cents as well as expand lifetime due the lack of batteries. However, there is still an important drawback: the price of readers besides the fact that each reader works in a specific frequency, thus, they are only useful for certain systems. Nonetheless, nowadays there is a subset of protocols within RFID technology which is growing fast named Near Field Communications (NFC) which is embedded in most of the smartphones sold today due its worldwide implementation as a payment mechanism [27], [28]. The fact of having NFC enabled smartphones brings new opportunities to the usage of RFID applications, since the reader is now on the pocket of millions of end-users and almost always with an internet connection, which turns this technology a suitable option in the IoT paradigm to be used as bridge between the *things* and the *internet* without the need of having all the *things* directly connected to the cloud [29], [30].

## 1.2RFID technology

The first patent of an active RFID transponder able to rewrite the stored data was created by Mario W. Cardullo in 1973 [31], since then, many types of RFID have appeared. RFID systems can be classified by several characteristics such as the operational frequency, the range, the physical coupling method or the need of batteries in the transponder (i.e. passive/active systems). Table 1.II shows the classification of RFID based on the three different standardised operational frequencies bands along with their main characteristics.

Table 1.II. RFID technologies

| | LF | HF | UHF |
|---|---|---|---|
| Coupling mode | Inductive (near-field) | Inductive (near-field) | Electro-magnetic backscattered (far-field) |
| Operating frequency | 125 to 134 kHz | 13.56 MHz | 860 to 960 MHz |
| Regulation | Worldwide harmonized | Worldwide harmonized | Different regulations per country |
| Standards | ISO14223 ISO18000-2 | ISO14443 A/B ISO15693 ISO18092 ISO18000-3 NFC Forum | ISO18000-6 B/C EPC Class 1 Gen 2 |
| Environmental influences | Water no problem, metal low attenuation | Water low attenuation, metal critical | Water critical, metal less critical |
| Applications | Animal tagging | Product identification / Public transport / Payment | Containers ID / Logistics / authentication |

A general overview of a RFID system is shown in Figure 1.3, where the signal sent by the reader and the answer from the tag are represented in both, time and frequency.

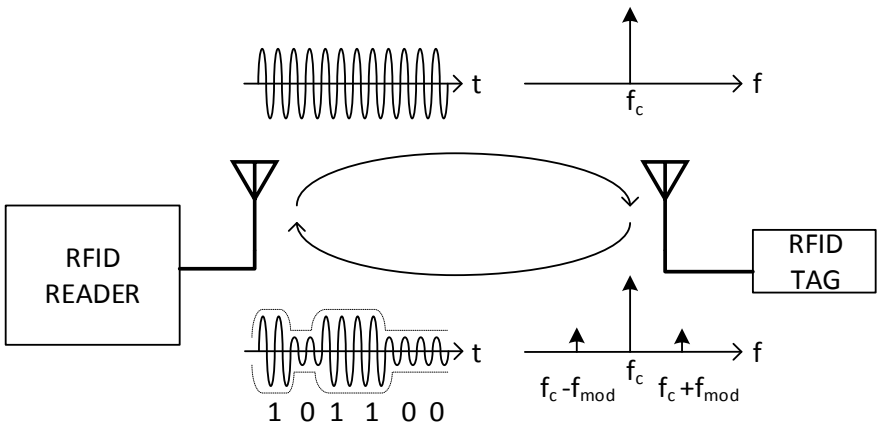


Figure 1.3. RFID System overview.

RFID devices can be divided into two categories: passive and active. Active tags require to be powered by a battery or a connection to a power source whereas passive tags use the energy received by the reader to answer. Active tags have better performance than the passives, reaching longer ranges and allowing larger memory banks, however, the cost, size, and lifetime make them not as interesting as passive tags for the retail trade. Passive systems have a limited range determined by factors such as reader parameters, propagation environment, and tag characteristics. Table 1.III shows different characteristics of passive and active tags.

Table 1.III. RFID active and passive tags comparison.

| | Active | Passive |
|---|---|---|
| Power source | Internal | Harvested from RF field |
| Required signal strength (reader to tag) | Low | High |
| Available signal strength (tag to reader) | High | Low |
| Communication range | Long range | Short range |
| Multi-tag reading | Thousands of tags | Several tags |
| Sensing capability | Continuously. (all data retrieved when reader approaches) | Only when tag is within the reader's range |
| Data storage | Large | Small |
| Cost | High | Low |
| Typical operational frequency | 433 MHz, 2.45 GHz, 5.8 GHz | 128 KHz, 13.56 MHz, 915 MHz, 2.45 GHz |

## 1.3Near Field Communication (NFC)

NFC is a subset of protocols within RFID technology, which operates at 13.56 MHz, mainly aimed for mobile or handheld devices.

There are three possible operating modes for an NFC tag based on the ISO/IEC 18092 [32], ISO/IEC 14443 [33] and ISO/IEC 15693 [34] standards:

- Card emulation: the device acts like a contactless card, the typical use case is for using the device for payments or ticketing. Can be based on ISO/IEC 14443 or 15693.
- Reade/write: the device can read a tag and overwrite the content if the tag allows it. Used for smart posters, get an

URL or getting the sensed data from a tag. Can be based on ISO/IEC 14443 or 15693.

- Peer to Peer (P2P): allows to exchange data between 2 devices. Used to transfer data such as photos or any other data. Based on ISO/IEC 18092.

There is a fourth mode, whose technical specification is still a candidate, waiting for approval:

- Wireless charging (WLC): power transfer from a device to another device such as a smartwatch or fitness tracker. Four power transfer classes are specified: 250, 500, 750 and 1000 mW.

Five type tags are defined by the NFC Forum, each of them with a certain characteristics as shown in Table 1.IV.

Table 1.IV. NFC Forum type tags.

| | Type 1 | Type 2 | Type 3 | Type 4 | Type 5 |
|---|---|---|---|---|---|
| Technology | NFC-A | NFC-A | NFC-F | NFC-A NFC-B | NFC-V |
| Standard | ISO14443 A | ISO14443 A | JIS 6319-4 | ISO14443 A/B | ISO15693 |
| Memory size | Up to 2 kBytes | Up to 2 kBytes | Up to 1 MBytes | Up to 32 Kbytes | Up to 64 kBytes |
| Transmission Speed (kbits/s) | 106 | 106 | 212 /424 | 106 | Up to 26.5 |
| Unit price | Low | Low | High | Medium / High | Low / Medium |
| Range | Proximity | Proximity | Proximity | Proximity | Proximity & vicinity |
| Chip examples | Topaz | Mifare ultralight | Felica | Mifare DESFire | ICODE SLI |
| Use case | Business cards, smart poster | Event tickets, transit tickets | e-money, membership cards | Transit tickets | Packaging, ticketing |

Further information about NFC can be found on Annex 1.

### 1.3.1 State of the art: current NFC applications

As the IoT scenario grows, the number of devices and the ways people interact with devices grows with it. Even though NFC has the shortest range among radiofrequency technologies, it has been widely extended due its security, compatibility, user friendly interface, large amount of applications, and low-cost components. The main reason of the current growing implementation of NFC in almost any smartphone is due its use for contactless payments, making it increasingly indispensable for the end-user, as happens with other wireless technologies such as Wi-Fi or Bluetooth. The different standards of the NFC Forum allows to select between the different standardised technologies to find the most suitable option for each case scenario [35], [36]. Each operation mode has its own range of applications. The main advantages of each mode are:

- Card emulation: replace physical objects. Mobile payments and access control.
- Read/write: requires a low physical effort (*tap-and-go*), increase mobility, adaptable to many scenarios and easy to implement.
- Peer-to-Peer: easy way to exchange data at low rates.

Card emulation mode is mainly used to replace physical objects like credit cards [37], [38], tickets [39] or coupons [39]. Read/write mode is the most extended mode of operation since it encompass a huge variety of uses such as smart posters [40]–[42], healthcare applications [43]–[46], medication dispensing [47]–[49], catering meal service [50], social networking [51], museums interaction [52], attendance supervision[53], enterprise workflow control [54], sales assistance for retailers [55], or control of multimedia players [56]. Peer-to-Peer mode has less applications since it is mainly focused in the exchange of data. However, there are some application studies for its use in cases where other operation modes are more common. For instance for mobile payments, P2P mode adds some characteristics like customizable confirmations and the possibility to avoid the use of a secure element [57]. Another possible application of P2P is to transfer data between medical devices and the nursing station where the patients information is collected [58].

More recent works found on the literature use NFC for sensing applications [59]–[61]. An extensive range of applications exists on the literature, including cold-chain temperature control [62][63], gas sensors [64], [65], soil moisture [66] or tire pressure [67].

Healthcare can clearly benefit from the easy sensing methods that NFC provides. Body pressure and temperature [68]–[71], sweat analysis [72], [73], glucose monitoring [74], [75], ultraviolet radiation [76], pH measure [77], [78] and electrocardiography (ECG) [79] are some of its applications. Implantable devices is a promising challenge and widely studied issue [74], [75], [80]–[84]. The simplicity of the *tap-and-go* philosophy altogether with the widespread of smartphones with connection to internet, makes NFC technology a promising technology for telemedicine. Furthermore, the fact of developing sensing devices without battery, turns NFC to a very interesting technology for implantable devices.

### 1.3.2 NFC Antenna design

Beyond the specific application of the tags, the antenna design becomes an important factor since it has to be incorporated into compact devices (i.e. smartphones), surrounded by metallic parts that degrades its performance.

Antenna performance takes more importance when the inductive link is pretended to transmit energy to power up the tags circuitry. Several works have are devoted to improve the performance of the antenna, most of them using ferrite sheets with high relative permeability to avoid the effect of eddy currents. [85] proposes to add a parasitic loop on the outer side of a conventional loop antenna, and the use of a ferrite-polymer composite sheet, which is less expensive than ferrite sheets. In [86] and [87] an "8" shape antenna as improvement of the Murata ZB antenna [88] is presented to overcome the shielding effect of the metal cover. A 5-turn coil design for tablet pc devices is introduced in [89], taking into account that these devices use to have large touch panels and narrow borders, thus the interest on developing rectangular antennas to fit in the frame space. The proposed antenna size is 41.5×7.5 mm, with ferrite sheets on both sides. Another solution for metal-case devices with a no uniform meandering lines and partial coverage of ferrite is

presented in [90], proposing a six-turn coil with six-sided irregular hexagonal shape.

The mere fact of the huge number of applications, and antenna designs found in the literature reflects the importance and possibilities that this technology can offer to daily activities and its encouraging future.

### 1.3.3 Passive sensing tags

The present work is motivated by the possibilities that NFC brings, to create sensing applications without batteries, thus, avoiding toxic waste while extending devices lifetime. To accomplish that goal, some issues must be deal with. The main constraint is to ensure, beyond the communication, an efficient and dependable energy transfer. Guarantee a reliable power supply is pivotal to develop sensors embedded on passive tags. On the other hand, the fact of avoiding batteries open the doors to applications which otherwise would not be feasible. For instance, when using sensing tags to control food quality, the toxicity of a battery should be dealt with by using expensive coating methods. Likewise happens to implantable devices, which have the same problem with battery toxicity. Furthermore, when developing implantable devices, the size is vitally important. Hence the benefit of evade the use of batteries thus reducing tags dimensions.

A large variety of passive sensing NFC tags can be found on the literature. The simplest ones consist of an ON/OFF sensing. Within this category, different methodologies are observed. For instance, in [91] a tag composed by an SL13A [92] chip to detect presence of urine in a diaper is based on measuring the resistance between two parallel conductors, allowing to detect if the diaper is wet or dry if the conductors are short-circuited by the urine. An ON/OFF temperature indicator for supply chain monitoring system is presented in [62]. It consists of a critical temperature indicator (CTI) based on a solvent melting point. The tag, with a Melexis MLX90129 [93] as an NFC interface, measures the change in resistance of multi-walled carbon nanotubes (MWCNT) connected to a couple of copper wires. Another methodology is used in [94] for a food spoilage sensor. This sensor relays on the detection of the total volatile basic nitrogen (TVBN) by placing Nano-structured polyaniline (PAni) between the

NFC coil terminals, taking advantage of its change on resistance when exposed to TVBN inducing a short-circuit when the TVBN is above a threshold, thus, modifying the antenna impedance and making the tag impossible to read. This approach can lead to a false negative reading, since when the tag cannot be read, the user must interpret that the food is spoiled but it could be that the impossibility to read it comes from another issue. The same issue may occur in [95] where a passive LC resonating sensor tag for detecting wet in diapers is shown. In this case the resonance frequency (12 MHz) is shifted by the presence of urine near the antenna, thus making the non-standardised custom reader used impossible to detect the tag.

Other works use ICs which have NFC interface as well as an embedded sensor. [96] presents a tag consisting of a squared 25×25 mm printed coil on flexible biocompatible plastic substrate, connected to a temperature logger with embedded NFC interface (NHS3100 [97] from NXP). In [71] a tag based on the RF430FRL152H [98] chip from Texas Instruments is presented. The tag is designed on a flexible substrate, with an overall size of 74×50 mm. A serpentine-shaped coil is used as an antenna to provide stretchability and flexibility, since this tag is supposed to be adhered to the skin to measure temperature (which sensor is embedded into the same NFC chip), and the ambient light, captured by a phototransistor. The designed circuit is carved onto a cupper foil, which is laminated on thermal release tape. SL13A [92] chip from AMS also integrates a temperature sensor, and is used in several works [64], [68], [77], [91]. In [68] an array of 65 NFC sensors for pressure and temperature are placed on a bed, for mapping these parameters in specific areas of the body creating a wireless sensors network. A dual-antenna system between the mattress and the body provides the energy and gets the information from the sensors.

In order to extend the functionality and capability of the NFC sensing tags, some works incorporate a microcontroller (MCU). Since the MCU will be energized from the rectification of the RF received signal, it is crucial to use low power chips. In [63] an open source programmable sensing and computationally enhanced platform named NFC-WISP (wireless identification and sensing platform) is presented. This work is based on previous study of a RFID-based

battery-less programmable sensing platform [99], and It consists of a printed circuit board with a 42×53 mm antenna and a software defined NFC tag (ISO/IEC 14443 protocol) on a microcontroller (TI MSP430F5310 [100]). This device incorporates an E-ink screen, and the conversion from RF to DC is done with an external full-wave rectifier. It incorporates a temperature sensor as well as an accelerometer. The NFC-WISP is used as a basis in [69] for temperature sensing of premature new-borns in neonatal incubators in a non-invasive way, placing the tag on the incubators mattress. [64] introduces an NFC tag composed by an SL13A NFC chip and a PIC16LF1703 [101] microcontroller for gasses concentration determination. It contains four chemical sensors with optical response for measuring oxygen, carbon dioxide, ammonia, and relative humidity surrounding a white led to light them. It also uses the embedded temperature sensor of the SL13A. A recent work presents an electronic platform for general-purpose sensing [102]. The system allows voltammetry, potentiometry, amperometry, and electrochemiluminescence (ECL) analysis based on a screen-printed electrode. The design has been applied to glucose, pH, and $H_20_2$ determination. The system uses a PIC16LF1703 microcontroller connected to an AS3955 [103] as an NFC interface.

As mentioned above, NFC passive tags are very interesting for medical applications due the lack of battery and the possibility of developing implantable medical devices (IMD). A miniaturized flexible tag is presented in [104]. Even though it says that can be used for biosensors and electronic implants, and two chips with energy harvesting capability are used (M24LR04E [105] from ST and NTAG216 [106] from NXP), the study focuses on the tag's antenna miniaturization, developing a 7×5 mm tag, but does not implement the sensors. It analyses the effects on the electromagnetic characteristics when the tag is bent. [107] propose a study of planar coils printed on flexible substrate with different number of turns, conductor widths, and other physical parameters for implantable temperature sensors using the SL13A NFC chip. The measurements have been evaluated by implanting the tag into a porcine model being able to communicate with a commercial NFC-enabled smartphone with depths up to 10 mm. The communication between tag and reader is done by using a Texas Instruments evaluation

board which includes a software to measure the received signal strength indicator (RSSI).

Most of the works regarding implantable battery-less devices found in the literature use application-specific integrated circuit (ASIC) which are not standardised and need specific readers to supply the energy and retrieve the data from the tag. An ASIC is, for instance, used in [74], presenting a battery assisted implantable passive amperometric electrochemical glucose sensor with an off chip printable battery which stores the harvested energy allowing a continuous monitoring. In [75] the authors present another glucose implantable sensor based on an ASIC which implements the ISO/IEC 15693. It consists of a LED which light is reflected on a biosensing fluorophore, and a photodiode for detecting the fluorescent reflected emission.

Beyond the use of the 13.56 MHz ISM (industrial, scientific and medical) band, some works use the same principle but with different frequencies. Is the case of [108], where a battery-less implantable neuro-electronic interface suitable for studying deep brain stimulation (DBS) working at 10 MHz is presented. The implant has 8 electrodes which can interact with eight different brain regions bi-directionally. The implant communicates with an external wearable transceiver by 2 coils using LSK (load shift keying) modulation, used for both, data and power transfer, reaching transmission speeds up to 2 Mbps. The coils size used in this work are 20 mm and 30 mm for the implanted and the external, respectively. The external module relays the data to a computer or portable device via Bluetooth.

Table 1.V summarises the passive sensing tags reported on the literature exposed above, listing the NFC chip used, the sensing parameters, the size, and some additional comments for each.

As can be seen, the type of applications where passive sensing tags can be applied is large, and it is expected to keep growing along with the number of smartphones with NFC capability and the number of tags ICs. These factors, altogether with the interest on low-power devices, especially on sensors, envision an expansion of the possibilities provided by NFC passive sensing tags.

Table 1.V. Sensing tags references

| Ref | Chip | Sensor | Size (mm) | Comments |
|---|---|---|---|---|
| [62] | MLX90129 | Temperature | 32×51 | ON/OFF |
| [63] | Software defined in a MCU (MSP430) | Temperature, accelerometer | 85×54 | Open source platform |
| [64] | SL13A | Multigas | 65×40 | Optical |
| [67] | ASIC | Tire pressure | 35×15 | |
| [68] | SL13A | Temperature, pressure | 16×16 | Sensors network |
| [71] | RF430FRL152H | Temperature, phototransistor | 74×50 | Flexible |
| [74] | ASIC | Glucose | | |
| [75] | ASIC | Glucose | 3×15 | Implantable |
| [77] | SL13A | pH | | |
| [94] | - | Nitrogen | | ON/OFF |
| [96] | NHS3100 | Temperature | 25×25 | Flexible |
| [102] | AS3955 | General-purpose | 31×20 | |
| [104] | M24LR04E NTAG216 | Not implemented | 7×5 | Flexible, miniaturized |
| [107] | SL13A | Temperature | | Implantable |
| [108] | ASIC | Brain stimulation | 20×20 | 10 MHz |

## 1.4Scope and objectives of this Doctoral Thesis

This work focusses on the study of NFC battery-less sensors using commercial smartphones as a reader. To that end, the scope of this work is framed within RFID, in the HF band, using NFC Forum standards, in read/write operational mode with passive tags with NFC-V technology and sensing capability.

The purpose of the research is to demonstrate the feasibility of integrating NFC passive sensors within the growing IoT scenario. The main objectives are listed below:

- Study the operation and constrains of WPT applied to NFC in real-case scenarios using commercial smartphones as a reader.

- Study, design and implementation of custom passive tags, and the effects of different antenna topologies, and manufacturing materials as well as compare the performance of different NFC chips and different power requirements.
- Demonstration of NFC capabilities and advantages for passive sensing devices, using both, analog and digital sensors.
- Study of the read range and the energy harvesting range.
- Design of new NFC sensing applications not present in the literature.
- Analyse the effects of the body in implantable NFC tags and evaluate techniques to improve the maximum implantable depth.

## 1.5 Organization of this document

The document is organised as follows:

- Chapter 2 analyse the architecture, constraints, and limitations of wireless power transfer applied to NFC systems. It describes the theory background and the main parameters that influence on the efficiency of the system such as antenna design, environmental effects and coupling conditions.
- Chapter 3 presents a soil moisture sensor embedded in a battery-less tag able to measure the volumetric water content of the soil as well as the relative humidity and temperature.
- Chapter 4 describes the application of a wet detection for diapers designed on flexible substrate, based on the change in capacity between electrodes.
- Chapter 5 proposes a prototype of a colour sensor for determining the pH based on colour determination of pH reactive paper-based colour strips. The repeatability of the proposed device is addressed as well as a comparison to image processing alternatives.
- Chapter 6 studies the possibility of using the same colour sensor presented in the previous chapter to analyse fruit ripeness. An analysis of the different colour components of different colour spaces is presented, along with a machine learning algorithm study, to create a classification matrix used in an Android application to discriminate the ripeness state.

- Chapter 7 examines the feasibility of implanted NFC tags, including the effect of the body and the use of small tag antennas (15x15 mm). An improved resonant coupling system with 3 coils is introduced and analysed, adding a relay coil between the reader and the tag, to increase the read range and power transfer.
- Chapter 8 exposes the conclusions of this work.

## 1.6 Bibliography

[1] R. C. Palmer, *The bar code book : a comprehensive guide to reading, printing, specifying, evaluating and using bar code and other machine-readable symbols*. Trafford, 2007.

[2] G. Singh and M. Sharma, 'Barcode technology and its application in libraries and Information centers', *Int. J. Next Gener. Libr. Technol.*, vol. 1, no. 1, pp. 1–8, 2015.

[3] M. F. Murphy and J. D. . Kay, 'Barcode identification for transfusion safety', *Current Opinion in Hematology*, vol. 11, no. 5. pp. 334–338, Sep-2004.

[4] M. M. B.-A. A. N. Baldominos;, F. A. Bernabeu-Andreu, I. Arribas, F. Navarro, and G. Baldominos, 'Impact of a Barcode Medication Administration System on Patient Safety', *Oncol. Nurs. Forum*, vol. 45, no. 1, pp. E1–E13, 2018.

[5] J. De Maeyer, H. Devos, W. Meeus, P. Verplaetse, and D. Stroobandt, 'Hardware implementation of an EAN-13 bar code decoder', in *Proceedings of the ASP-DAC Asia and South Pacific Design Automation Conference, 2003.*, 2005, no. 2, pp. 583–584.

[6] R. Muniz, L. Junco, and A. Otero, 'A robust software barcode reader using the Hough transform', in *Proceedings 1999 International Conference on Information Intelligence and Systems (Cat. No.PR00446)*, 1999, pp. 313–319.

[7] 'ISO/IEC 16022: Information technology -- International symbology specification -- Data Matrix.' International Organization for Standardization, 2000.

[8] 'ISO/IEC 18004: Information technology - Automatic identification and data capture techniques - Bar code symbology - QR Code', *ISO*

*Standards*. International Organization for Standardization, 2000.

[9] Semacode, 'Choosing the best 2D barcode format for mobile apps', pp. 1–7, 2006.

[10] T. Falas and H. Kashani, 'Two-Dimensional Bar-Code Decoding with Camera-Equipped Mobile Phones', in *Fifth Annual IEEE International Conference on Pervasive Computing and Communications Workshops (PerComW'07)*, 2007, pp. 597–600.

[11] E. Ohbuchi, H. Hanaizumi, and Lim Ah Hock, 'Barcode Readers using the Camera Device in Mobile Phones', in *2004 International Conference on Cyberworlds*, 2004, pp. 260–265.

[12] K.-C. Liao and W.-H. Lee, 'A Novel User Authentication Scheme Based on QR-Code', *J. Networks*, vol. 5, no. 8, pp. 937–941, Aug. 2010.

[13] Yue Liu, Ju Yang, and Mingjun Liu, 'Recognition of QR Code with mobile phones', in *2008 Chinese Control and Decision Conference*, 2008, pp. 203–206.

[14] P. Kieseberg *et al.*, 'QR code security', in *Proceedings of the 8th International Conference on Advances in Mobile Computing and Multimedia - MoMM '10*, 2010, p. 430.

[15] K. Finkenzeller, *RFID Handbook: Fundamentals and Applications in Contactless Smart Cards, Radio Frequency Identification and near-Field Communication*. Wiley, 2010.

[16] R. Want, 'An Introduction to RFID Technology', *IEEE Pervasive Comput.*, vol. 5, no. 1, pp. 25–33, Jan. 2006.

[17] E. P. Kelly and G. S. Erickson, 'RFID tags: Commercial applications v. privacy rights', *Ind. Manag. Data Syst.*, vol. 105, no. 6, pp. 703–713, 2005.

[18] A. Juels, 'RFID security and privacy: a research survey', *IEEE J. Sel. Areas Commun.*, vol. 24, no. 2, pp. 381–394, Feb. 2006.

[19] R. Weinstein, 'RFID: a technical overview and its application to the enterprise', *IT Prof.*, vol. 7, no. 3, pp. 27–33, May 2005.

[20] D. Hahnel, W. Burgard, D. Fox, K. Fishkin, and M. Philipose,

'Mapping and localization with RFID technology', in *IEEE International Conference on Robotics and Automation, 2004. Proceedings. ICRA '04. 2004*, 2004, vol. 2004, no. 1, pp. 1015-1020 Vol.1.

[21] L. M. Ni, Yunhao Liu, Yiu Cho Lau, and A. P. Patil, 'LANDMARC: indoor location sensing using active RFID', in *Proceedings of the First IEEE International Conference on Pervasive Computing and Communications, 2003. (PerCom 2003).*, 2014, vol. 23, no. 4, pp. 407–415.

[22] Z. Pala and N. Inanç, 'Smart parking applications using RFID technology', *2007 1st Annu. RFID Eurasia*, 2007.

[23] E. Abad *et al.*, 'RFID smart tag for traceability and cold chain monitoring of foods: Demonstration in an intercontinental fresh fish logistic chain', *J. Food Eng.*, vol. 93, no. 4, pp. 394–399, 2009.

[24] H. K. H. Chow, K. L. Choy, W. B. Lee, and K. C. Lau, 'Design of a RFID case-based resource management system for warehouse operaChow, H. K. H., Choy, K. L., Lee, W. B., & Lau, K. C. (2006). Design of a RFID case-based resource management system for warehouse operations. Expert Systems with Applications, 30(4', *Expert Syst. Appl.*, vol. 30, no. 4, pp. 561–576, 2006.

[25] S. Chumkamon, P. Tuvaphanthaphiphat, and P. Keeratiwintakorn, 'A blind navigation system using RFID for indoor environments', *5th Int. Conf. Electr. Eng. Comput. Telecommun. Inf. Technol. ECTI-CON 2008*, vol. 2, pp. 765–768, 2008.

[26] X. Jia, Q. Feng, T. Fan, and Q. Lei, 'RFID technology and its applications in Internet of Things (IoT)', in *2012 2nd International Conference on Consumer Electronics, Communications and Networks (CECNet)*, 2012, pp. 1282–1285.

[27] I. Ramos-de-Luna, F. Montoro-Ríos, and F. Liébana-Cabanillas, 'Determinants of the intention to use NFC technology as a payment system: an acceptance model approach', *Inf. Syst. E-bus. Manag.*, vol. 14, no. 2, pp. 293–314, 2015.

[28] D. Pal, V. Vanijja, and B. Papasratorn, 'An Empirical Analysis towards the Adoption of NFC Mobile Payment System by the End

User', *Procedia Comput. Sci.*, vol. 69, pp. 13–25, 2015.

[29] S. H. Shah and I. Yaqoob, 'A survey: Internet of Things (IOT) technologies, applications and challenges', *2016 4th IEEE Int. Conf. Smart Energy Grid Eng. SEGE 2016*, vol. i, pp. 381–385, 2016.

[30] G. Cerruela García, I. Luque Ruiz, and M. Gómez-Nieto, 'State of the art, trends and future of bluetooth low energy, near field communication and visible light communication in the development of smart cities', *Sensors (Switzerland)*, vol. 16, no. 11, 2016.

[31] M. W. Cardullo, 'US3713148A - Transponder apparatus and system', US3713148A.

[32] 'ISO/IEC 18092: Information technology — Telecommunications and information exchange between systems — Near Field Communication — Interface and Protocol (NFCIP-1)'. International Organization for Standardization, 2013.

[33] 'ISO/IEC 14443: Identification cards – Contactless integrated circuit cards – Proximity cards'. International Organization for Standardization, 2018.

[34] 'ISO/IEC 15693: Identification cards — Contactless integrated circuit cards — Vicinity cards'. International Organization for Standardization, 2010.

[35] V. Coskun, B. Ozdenizci, and K. Ok, 'The Survey on Near Field Communication', *Sensors*, vol. 15, no. 6, pp. 13348–13405, Jun. 2015.

[36] K. Ok, M. Aydin, V. Coskun, and B. Ozdenizci, 'Exploring underlying values of NFC applications', *Proc. Int. Conf. Manag. Technol. Appl.*, vol. 12, pp. 290–294, 2010.

[37] M. Pasquet, J. Reynaud, and C. Rosenberger, 'Secure payment with NFC mobile phone in the SmartTouch project', in *2008 International Symposium on Collaborative Technologies and Systems*, 2008, pp. 121–126.

[38] P. Pourghomi, M. Qasim, and G. Ghinea, 'A Proposed NFC Payment Application', *Int. J. Adv. Comput. Sci. Appl.*, vol. 4, no. 8, pp. 173–181, 2013.

[39] S. L. Ghìron, S. Sposato, C. M. Medaglia, and A. Moroni, 'NFC ticketing: A prototype and usability test of an NFC-based virtual ticketing application', *Proc. - 2009 1st Int. Work. Near F. Commun. NFC 2009*, pp. 45–50, 2009.

[40] I. L. Ruiz and M. Á. Gómez-Nieto, 'University smart poster: Study of NFC technology applications for university ambient', *Adv. Soft Comput.*, vol. 51, pp. 112–116, 2009.

[41] J. Wu, L. Qi, R. S. S. Kumar, N. Kumar, and P. Tague, 'S-SPAN: Secure smart posters in android using NFC', *2012 IEEE Int. Symp. a World Wireless, Mob. Multimed. Networks, WoWMoM 2012 - Digit. Proc.*, pp. 1–3, 2012.

[42] K. Boes, L. Borde, and R. Egger, 'The Acceptance of NFC Smart Posters in Tourism', in *Information and Communication Technologies in Tourism*, Springer International Publishing, 2015.

[43] D. Sethia, D. Gupta, T. Mittal, U. Arora, and H. Saran, 'NFC based secure mobile healthcare system', *2014 6th Int. Conf. Commun. Syst. Networks, COMSNETS 2014*, 2014.

[44] J. Fontecha, R. Hervás, J. Bravo, and V. Villarreal, 'An NFC approach for nursing care training', *Proc. - 3rd Int. Work. Near F. Commun. NFC 2011*, pp. 38–43, 2011.

[45] J. P. Puma, M. Huerta, R. Alvizu, and R. Clotet, 'Mobile identification: NFC in the healthcare sector', *Proc. 6th Andean Reg. Int. Conf. Andescon 2012*, pp. 39–42, 2012.

[46] H. Köstinger, M. Gobber, T. Grechenig, B. Tappeiner, and W. Schramm, 'Developing a NFC based patient identification and ward round system for mobile devices using the android platform', *IEEE EMBS Spec. Top. Conf. Point-of-Care Healthc. Technol. Synerg. Towar. Better Glob. Heal. PHT 2013*, pp. 176–179, 2013.

[47] J. Morak, M. Schwarz, D. Hayn, and G. Schreier, 'Feasibility of mHealth and Near Field Communication technology based medication adherence monitoring', *Proc. Annu. Int. Conf. IEEE Eng. Med. Biol. Soc. EMBS*, pp. 272–275, 2012.

[48] A. Lahtela, M. Hassinen, and V. Jylhä, 'RFID and NFC in healthcare: Safety of hospitals medication care', *Proc. 2nd Int.*

*Conf. Pervasive Comput. Technol. Healthc. 2008, PervasiveHealth*, pp. 241–244, 2008.

[49] M. Alabdulhafith, R. V. Sampangi, and S. Sampalli, 'NFC-enabled smartphone application for drug interaction and drug allergy detection', *2013 5th Int. Work. Near F. Commun. NFC 2013*, pp. 1–6, 2013.

[50] E. Siira and J. Haikio, 'Experiences from Near-Field Communication (NFC) in a Meal Service System', in *2007 1st Annual RFID Eurasia*, 2007, pp. 1–6.

[51] A. Fressancourt, C. Hérault, and E. Ptak, 'NFCSocial: Social networking in mobility through IMS and NFC', *Proc. - 2009 1st Int. Work. Near F. Commun. NFC 2009*, pp. 24–29, 2009.

[52] M. Blöckner, S. Danti, J. Forrai, G. Broll, and A. De Luca, 'Please touch the exhibits! using NFC-based interaction for exploring a museum', in *Proceedings of the 11th International Conference on Human-Computer Interaction with Mobile Devices and Services - MobileHCI '09*, 2009, vol. 1, p. 1.

[53] M. Ervasti, M. Isomursu, and M. Kinnula, 'Experiences from NFC supported school attendance supervision for children', *3rd Int. Conf. Mob. Ubiquitous Comput. Syst. Serv. Technol. UBICOMM 2009*, pp. 22–30, 2009.

[54] J. Müller, V. Borovskiy, O. Panchenko, A. Bog, and A. Zeier, 'NFC at the workplace - Simplify enterprise work flows with NFC', *IE EM 2009 - Proc. 2009 IEEE 16th Int. Conf. Ind. Eng. Eng. Manag.*, pp. 1539–1542, 2009.

[55] S. Karpischek, F. Michahelles, F. Resatsch, and E. Fleisch, 'Mobile sales assistant: An NFC-based product information system for retailers', *Proc. - 2009 1st Int. Work. Near F. Commun. NFC 2009*, pp. 20–23, 2009.

[56] I. Sánchez, M. Cortés, and J. Riekki, 'Controlling multimedia players using NFC enabled mobile phones', *Proc. - MUM 2007 6th Int. Conf. Mob. Ubiquitous Multimed.*, vol. 284, pp. 118–124, 2007.

[57] L. Mainetti, L. Patrono, and R. Vergallo, 'IDA-Pay: A secure and efficient micro-payment system based on Peer-to-Peer NFC

technology for Android mobile devices', *J. Commun. Softw. Syst.*, vol. 8, no. 4, pp. 117–125, 2012.

[58] C. H. Huang and S. L. Chang, 'Study on the feasibility of NFC P2P communication for nursing care daily work', *J. Comput.*, vol. 24, no. 2, pp. 33–45, 2013.

[59] A. Lazaro, R. Villarino, D. Girbau, A. Lazaro, R. Villarino, and D. Girbau, 'A survey of NFC sensors based on energy harvesting for IoT applications', *Sensors (Switzerland)*, vol. 18, no. 11, p. 3746, Nov. 2018.

[60] Z. Cao *et al.*, 'Near-Field Communication Sensors', *Sensors*, vol. 19, no. 18, p. 3947, Sep. 2019.

[61] L. Cui, Z. Zhang, N. Gao, Z. Meng, and Z. Li, 'Radio Frequency Identification and Sensing Techniques and Their Applications—A Review of the State-of-the-Art', *Sensors*, vol. 19, no. 18, p. 4012, Sep. 2019.

[62] G. S. Lorite *et al.*, 'Novel, smart and RFID assisted critical temperature indicator for supply chain monitoring', *J. Food Eng.*, vol. 193, pp. 20–28, Jan. 2017.

[63] Y. Zhao, J. R. Smith, and A. Sample, 'NFC-WISP: A sensing and computationally enhanced near-field RFID platform', *2015 IEEE Int. Conf. RFID, RFID 2015*, pp. 174–181, 2015.

[64] P. Escobedo *et al.*, 'Flexible Passive near Field Communication Tag for Multigas Sensing', *Anal. Chem.*, 2017.

[65] J. M. Azzarelli, K. A. Mirica, J. B. Ravnsbæk, and T. M. Swager, 'Wireless gas detection with a smartphone via rf communication', *Proc. Natl. Acad. Sci.*, 2014.

[66] M. Boada, A. Lazaro, R. Villarino, and D. Girbau, 'Battery-less soil moisture measurement system based on a nfc device with energy harvesting capability', *IEEE Sens. J.*, vol. 18, no. 13, pp. 5541–5549, 2018.

[67] C. Kollegger *et al.*, 'A system-on-chip NFC bicycle tire pressure measurement system', in *2017 IEEE 60th International Midwest Symposium on Circuits and Systems (MWSCAS)*, 2017, pp. 60–63.

[68] S. Han *et al.*, 'Battery-free, wireless sensors for full-body pressure and temperature mapping', *Sci. Transl. Med.*, vol. 10, no. 435, 2018.

[69] J. I. De Oliveira Filho and M. E. Do Prado Villarroel Zurita, 'Development of NFC TAG for temperature sensing of premature newborns in neonatal incubators', in *INSCIT 2017 - 2nd International Symposium on Instrumentation Systems, Circuits and Transducers: Chip on the Sands, Proceedings*, 2017, pp. 1–4.

[70] J. M. Vicente, E. Avila-Navarro, C. G. Juan, N. Garcia, and J. M. Sabater-Navarro, 'Design of a wearable bio-patch for monitoring patient's temperature', in *2016 38th Annual International Conference of the IEEE Engineering in Medicine and Biology Society (EMBC)*, 2016, pp. 4792–4795.

[71] H. Jeong *et al.*, 'NFC-enabled, tattoo-like stretchable biosensor manufactured by "cut-and-paste" method', *Proc. Annu. Int. Conf. IEEE Eng. Med. Biol. Soc. EMBS*, pp. 4094–4097, 2017.

[72] A. Koh *et al.*, 'A soft, wearable microfluidic device for the capture, storage, and colorimetric sensing of sweat', *Sci. Transl. Med.*, vol. 8, no. 366, pp. 1–14, 2016.

[73] D. P. Rose *et al.*, 'System-level design of an RFID sweat electrolyte sensor patch', *2014 36th Annu. Int. Conf. IEEE Eng. Med. Biol. Soc. EMBC 2014*, pp. 4038–4041, Aug. 2014.

[74] N. Anabtawi, S. Freeman, and R. Ferzli, 'A fully implantable, NFC enabled, continuous interstitial glucose monitor', in *Physiology & behavior*, 2016, vol. 176, pp. 612–615.

[75] A. De Hennis, S. Getzlaff, D. Grice, and M. Mailand, 'An NFC-enabled CMOS IC for a wireless fully implantable glucose sensor', *IEEE J. Biomed. Heal. Informatics*, vol. 20, no. 1, pp. 18–28, Jan. 2016.

[76] Y. Shi *et al.*, 'Soft, stretchable, epidermal sensor with integrated electronics and photochemistry for measuring personal UV exposures', *PLoS One*, vol. 13, no. 1, pp. 1–15, 2018.

[77] R. Rahimi, U. Brener, M. Ochoa, and B. Ziaie, 'Flexible and transparent pH monitoring system with NFC communication for wound monitoring applications', in *Proceedings of the IEEE*

*International Conference on Micro Electro Mechanical Systems (MEMS)*, 2017.

[78] M. Douthwaite and P. Georgiou, 'Live demonstration: An NFC based batteryless CMOS ISFET array for real-time pH measurements of bio-fluids', in *2017 IEEE SENSORS*, 2017, pp. 1–1.

[79] C. C. Wu *et al.*, 'A pliable and batteryless real-time ECG monitoring system-in-a-patch', *2015 Int. Symp. VLSI Des. Autom. Test, VLSI-DAT 2015*, pp. 4–7, 2015.

[80] V. K. Samineni *et al.*, 'Fully implantable, battery-free wireless optoelectronic devices for spinal optogenetics', *Pain*, vol. 158, no. 11, pp. 2108–2116, 2017.

[81] M. A. Hannan, S. Mutashar, S. A. Samad, and A. Hussain, 'Energy harvesting for the implantable biomedical devices: Issues and challenges', *Biomed. Eng. Online*, vol. 13, no. 1, pp. 1–23, 2014.

[82] K. Bazaka and M. V. Jacob, *Implantable devices: Issues and challenges*, vol. 2, no. 1. 2012.

[83] S. Tankiewicz, J. Schaefer, and A. Dehennis, 'A co-planar, near field communication telemetry link for a fully-implantable glucose sensor using high permeability ferrites', *Proc. IEEE Sensors*, 2013.

[84] R. Altawy and A. M. Youssef, 'Security Tradeoffs in Cyber Physical Systems: A Case Study Survey on Implantable Medical Devices', *IEEE Access*, vol. 4, pp. 959–979, 2016.

[85] B. Lee, B. Kim, and S. Yang, 'Enhanced loop structure of NFC antenna for mobile handset applications', *Int. J. Antennas Propag.*, vol. 2014, 2014.

[86] H. Chen and A. Zhao, 'NFC antenna for portable device with metal back cover', *2016 IEEE Antennas Propag. Soc. Int. Symp. APSURSI 2016 - Proc.*, pp. 1471–1472, 2016.

[87] A. Zhao and H. Chen, 'Small size NFC antenna with high performance', *2016 IEEE Antennas Propag. Soc. Int. Symp. APSURSI 2016 - Proc.*, vol. 3, pp. 1469–1470, 2016.

[88] 'WO2013115147A1 - Antenna apparatus and communication

terminal apparatus - Google Patents'. [Online]. Available: https://patents.google.com/patent/WO2013115147A1/en. [Accessed: 14-Jan-2020].

[89] M. A. Chung and C. F. Yang, 'Miniaturized NFC Antenna Design for a Tablet PC With a Narrow Border and Metal Back-Cover', *IEEE Antennas Wirel. Propag. Lett.*, vol. 15, pp. 1470–1474, 2016.

[90] J. Q. Zhu, Y. L. Ban, C. Y. D. Sim, and G. Wu, 'NFC antenna with nonuniform meandering line and partial coverage ferrite sheet for metal cover smartphone applications', *IEEE Trans. Antennas Propag.*, vol. 65, no. 6, pp. 2827–2835, Jun. 2017.

[91] J. Sidén *et al.*, 'Home care with NFC sensors and a smart phone', no. October, pp. 1–5, 2012.

[92] AMS, 'SL13A - Smart Sensory Tag Chip For Unique'. 2014.

[93] MELEXIS, 'MLX90129 - 13.56MHz sensor tag / datalogger'. 2012.

[94] Z. Ma *et al.*, 'Highly Sensitive, Printable Nanostructured Conductive Polymer Wireless Sensor for Food Spoilage Detection', *Nano Lett.*, vol. 18, no. 7, pp. 4570–4575, 2018.

[95] L. Yambem, M. K. Yapici, and J. Zou, 'A new wireless sensor system for smart diapers', *IEEE Sens. J.*, vol. 8, no. 3, pp. 238–239, 2008.

[96] Y. Kifle, J. Wikner, J. Zotterman, L. Ryden, and S. Farnebo, 'NFC Powered Implantable Temperature Sensor', in *2019 41st Annual International Conference of the IEEE Engineering in Medicine and Biology Society (EMBC)*, 2019, pp. 4359–4362.

[97] NXP Semiconductors, 'NHS3100 - Temperature logger with embedded NFC interface'. 2018.

[98] Texas Instruments, 'RF430FRL15xH NFC ISO 15693 Sensor Transponder'. 2014.

[99] A. P. Sample, D. J. Yeager, P. S. Powledge, A. V. Mamishev, and J. R. Smith, 'Design of an RFID-Based Battery-Free Programmable Sensing Platform', *IEEE Trans. Instrum. Meas.*, vol. 57, no. 11, pp. 2608–2615, Nov. 2008.

[100] Texas Instruments, 'MSP430F5310 , MSP430F530x Mixed-Signal

Microcontrollers'. 2018.

[101] Microchip, 'PIC16(L)F1703/7 - 14/20-Pin 8-Bit Advanced Analog Flash Microcontroller'. 2015.

[102] P. Escobedo *et al.*, 'General-purpose passive wireless point–of–care platform based on smartphone', *Biosens. Bioelectron.*, vol. 141, no. March, p. 111360, 2019.

[103] AMS, 'AS3955 - NFC Forum Compliant Dynamic Tag'. 2017.

[104] J. Kim *et al.*, 'Miniaturized Flexible Electronic Systems with Wireless Power and Near-Field Communication Capabilities', *Adv. Funct. Mater.*, vol. 25, no. 30, pp. 4761–4767, 2015.

[105] ST Microelectronics, 'M24LRxxx - Dynamic NFC/RFID tag IC'. 2017.

[106] NXP Semiconductors, 'NTAG213/215/216 NFC Forum Type 2 Tag compliant IC with 144/504/888 bytes user memory', vol. Rev. 3.2, no. June. p. 60, 2015.

[107] J. J. Wikner, J. Zötterman, A. Jalili, and S. Farnebo, 'Aiming for the cloud - A study of implanted battery-free temperature sensors using NFC', *2016 Int. Symp. Integr. Circuits, ISIC 2016*, pp. 1–4, 2017.

[108] Y. P. Lin *et al.*, 'A Battery-Less, Implantable Neuro-Electronic Interface for Studying the Mechanisms of Deep Brain Stimulation in Rat Models', *IEEE Trans. Biomed. Circuits Syst.*, vol. 10, no. 1, pp. 98–112, 2016.

# 2. Wireless Power Transfer applied to NFC

## 2.1 Introduction

Our knowledge of physics determines 4 different fundamental forces, two of them produce forces at subatomic distance and govern nuclear interactions, the other two, gravity and electromagnetism, produce long-range effects. Each of them can be described mathematically as a field. Michael Faraday was the first to describe one of these forces as a field in 1831: the electromagnetism. He studied the magnetic field generated around a conductor carrying current. Few years later, in 1860s, James Clerk Maxwell develop and unified the theory of electromagnetism, summarizing it in four equations that now bear his name. However, it was Heinrich Hertz who, in 1887, proved the existence of the electromagnetic waves predicted by Maxwell's equations, inventing the dipole oscillator and the resonator [1]. The evidence of radiowaves was the beginning of wireless power transfer (WPT), and Nikola Tesla was one of the most implicated researchers about it. He invented radio frequency resonant transformers (Tesla coils) by inductive and capacitive coupling trying to develop a wireless lighting system. In 1921 he stated:

*"Power can be, and at no distant date will be, transmitted without wires, for all commercial uses, such as the lighting of homes and the driving of aeroplanes. I have discovered the essential principles, and it only remains to develop them commercially." [2]*

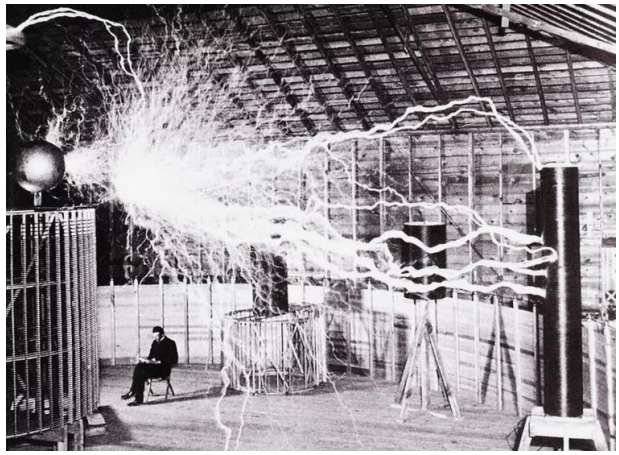

Figure 2.1. Nikola Tesla in his laboratory in 1899.

Despite the efforts and dedication that Tesla put on wireless power transfer, it never accomplished a commercial use due the dispersion of wireless power, which depends on the frequency of the operation and size of the transmitting antenna. Later, in the 1960s, after the ability acquired during World War II of working at microwave frequencies where the energy could be focused into a narrow beam, a new era of WPT [3], [4] began.

Nowadays, three different methods for WPT using electromagnetic fields are employed: inductive coupling, resonant coupling and far field [5] (see Table 2.I). These three technologies are similar, all of them follow Maxwell's equations. However, each of them implies its own characteristics and design constrains.

Table 2.I. Characteristics of different WPT methods.

| | Inductive coupling | Resonant coupling | Far field |
|---|---|---|---|
| Field | Magnetic field | Resonance (magnetic, electric, EM) | EM |
| Method | Coil | Resonator | Antenna |
| Distance | Short | Medium | Short to long |
| Efficiency | Low to high | High | High |
| Power | High | High | Low to high |
| Uses | Felica cards, Qi standard (Mobile phones charging) | NFC, eZone (mobile phones charging) | Far-field RFID |

Inductive coupling (Figure 2.2(a)) is based on Ampère's circuital law and Faraday's law of induction. The first describes the magnetic field generated by an electrical current passing through a loop (coil) and vice versa, the second predicts the interaction between a time-varying magnetic field and an induced electromotive force. The efficiency of the transmitted power depends on the coupling coefficient, which depends on the distance between transmitter and receiver. It is used for short-range applications, usually working with frequencies of a few megahertz. This method was the first WPT technology applied in real applications [6]–[8].

Resonant coupling (Figure 2.2(b)) have been widely applied to microwave band-pass filters (BPF) [9], [10], however, it was not until 2007 when researchers from the Massachusetts Institute of Technology demonstrate its use for WPT achieving up to 40% efficiency over more than 2 meters [11], [12]. A resonator is composed by a coil ($L$) and a capacitor ($C$), and the transmitted power is mainly magnetic. It is currently used for smartphones and other mobile devices.

Unlike inductive and resonant coupling, WPT via radiowaves (Figure 2.2(c)) uses the radiated electromagnetic. Thus, uses antennas rather than coils. It is mainly used in far-field RFID systems [13]. It achieves lower power transfer but a much longer range.

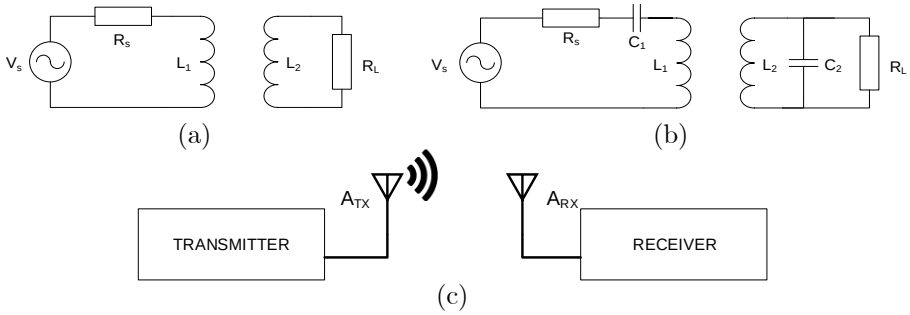


Figure 2.2. Methods of WPT. (a) Inductive coupling, (b) resonant coupling, (c) far field.

Resonant coupling, which is the technique used in NFC systems, relies on the principle that resonant objects exchange energy efficiently. To accomplish the power transfer, the source resonator generates an oscillating magnetic field, commonly working at MHz range, which is received by another resonator located few centimetres away. WPT using resonant coupling can be classified by different parameters [14], shown in Table 2.II.

There are two possible approaches to analyse resonant coupling. The first is by coupled-mode theory (CMT) [15]. On the other hand, since resonators are based on RLC circuits (see Figure 2.2(b)), the circuit theory can be applied as well, which is more straightforward, and it's the method used in this work.

Table 2.II. Coupled resonant WPT systems classification.

| Classifications | Types | Description | comments |
|---|---|---|---|
| Field used in coupling | Magnetic-coupled | Affected by surrounding permeability | Not affected by the body (medical applications) |
| | Electric-coupled | Affected by surrounding permittivity | |
| Power feeding | Direct fed | Power source and load directly connected to the resonant structure | |
| | Indirect fed | Feeding loop | Impedance matching by adjusting the spacing between the resonant structure and the loop |
| Resonant scheme | Self-resonant | Inductance and capacitance realized by identical structure | |
| | External resonant | Different structures | Usually loop structure used for inductance and a capacitor is added |

## 2.2 Theory background

The underlying physical principles of electromagnetism are needed to understand NFC technology and WPT. Inductive coupling consists of a primary coil generating a sinusoidal varying magnetic field, which induces a voltage on the terminals of a secondary coil, thus transferring power to a load. This effect is produced by the fact that a flow of current generates a magnetic field, the magnitude of this field is described as the magnetic field strength, and represented by *H*. The Biot-Savart law allows for calculating the *H* field strength and direction from any geometry and current, for any point in space (Figure 2.3). Its integral form is given by (2.1):

$$\vec{H} = \frac{I}{4\pi} \oint_S \frac{d\vec{s} \times \vec{r}}{|r|^3} \tag{2.1}$$

where $I$ is the current, $d\vec{s}$ is a vector along the path $S$, and $r$ is the point in which the field is being computed.

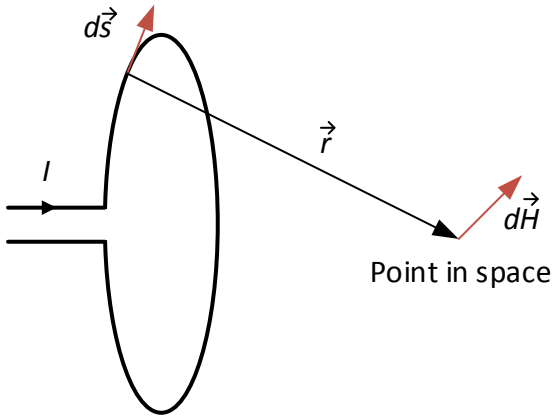


Figure 2.3. Representation of Biot-Savart law to measure $H$ field strength in any point of the space.

For practical applications the previous integral is not appropriated, as closed analytical solutions only exist for special cases. The $H$ field on the centre axis of a cylindrical coil is given by [16]:

$$H = \frac{INr^2}{2\sqrt{(r^2 + x^2)^3}} \tag{2.2}$$

where $N$ is the number of turns, $r$ is the radius of the loop and $x$ is the distance from the centre of the coil. Furthermore, when the loop has rectangular shape, with side lengths $a$ and $b$, the strength of the magnetic field at distance $x$ is [16]:

$$H = \frac{INab}{4\pi\sqrt{\left(\frac{a}{2}\right)^2 + \left(\frac{b}{2}\right)^2 + x^2}} \cdot \left( \frac{1}{\left(\frac{a}{2}\right)^2 + x^2} + \frac{1}{\left(\frac{b}{2}\right)^2 + x^2} \right) \tag{2.3}$$

The Biot-Savart law accomplish accurate results for near field region, and it is used to obtain the homogeneity of the emitted $H$ field and the optimum antenna radius.

The amount of magnetic field that passes through a given surface ($\Phi$) can be measured by

$$\Phi = BA \tag{2.4}$$

where $B$ represents de magnetic flux density, and $A$ the area of the given surface. The relationship between the flux density ($B$) and the field strength ($H$) is given by:

$$B = \mu_0 \mu_r H = \mu H \tag{2.5}$$

being $\mu_0$ the permeability of vacuum, and $\mu_r$ the relative permeability ($\mu$ is the product of $\mu_0$ and $\mu_r$). When using coils of $N$ loops, the total magnetic flux ($\psi$) is the sum of the flux ($\Phi$):

$$\psi = \sum \Phi_N = N\Phi = N\mu HA \tag{2.6}$$

The relationship between the magnetic flux and the current is the inductance ($L$), and can be expressed as:

$$L = \frac{\psi}{I} = \frac{N\Phi}{I} = \frac{N\mu HA}{I} \tag{2.7}$$

The physical principle of NFC for communication relies on the mutual inductance between two coils ($M_{21}$). Mutual inductance defines the effect of the magnetic field generated on the first coil with area $A_1$ over a second coil, located near the first, with area $A_2$:

$$M_{21} = \frac{\psi_{21}(I_1)}{I_1} = \oint_{A_2}^{\infty} \frac{B_2(I_1)}{I_1} dA_2 \tag{2.8}$$

where the sub-indexes *1* and *2* refer to the first and second coil respectively, and $\psi_{21}$ is the coupling flux which passes through both coils. Combining Ampere's law and the Biot-Savart law, thus applying the reciprocity theorem, we can state that:

$$M = M_{21} = M_{12} \tag{2.9}$$

The mutual inductance is directly related to the coil inductance by:

$$M = k\sqrt{L_1 L_2} \tag{2.10}$$

where $k$ is coupling coefficient.

Figure 2.4 depicts the mutual inductance ($M$) between two coils.

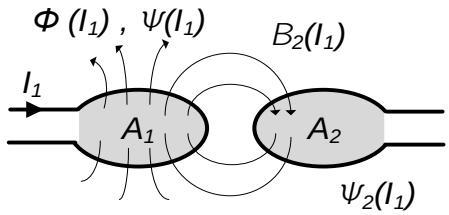


Figure 2.4. Representation of mutual inductance (M) between coils.

This chapter analyses WPT within the NFC scenario using a smartphone as transmitter. Thus, beyond the basic background of WPT, it exposes certain specific constrains such as the resonator design, NFC IC characterization, potential environmental effects, and chips comparison.

## 2.3 NFC system

This section describes the reader and the tag and introduces the system model used in this work.

### 2.3.1 Reader model

Figure 2.5 shows the schema of the transmitter with the matching network and the EMI filter. The reader consists of a voltage source ($V_{out}$) which is connected to an EMI filter through a resistance ($R_{out}$). The EMI filter is a low-pass filter reducing the second and higher harmonics and performs an impedance transformation. This filter is composed by two resistors ($R_0$), two inductors ($L_0$), and two capacitors ($C_0$). Two capacitors ($C_s$) are used as matching network to match the impedance between the EMI filter and the antenna. Two resistors ($R_x$) and a capacitor ($C_{in}$) compose the receiver circuit to adjust the received power levels, avoiding its saturation. The antenna is modelled as an inductance ($L_1$) in series with a resistance ($R_a$) and a capacitance ($C_a$). Two resistors ($R_Q$) may be added between the antenna and the matching network to reduce the quality factor ($Q$) to accomplish with the standards requirements. The reader can be modelled using a Thevenin equivalent circuit with a voltage source and an output impedance ($R_s$). A series capacitance ($C_1$) is added to make the circuit resonant ($f_r$) at the operating frequency ($f_0$). The parasitic capacitance of the reader antenna ($C_p$) has been considered in the matching network. An equivalent model can be used for the reader antenna, which is modelled as an

inductance ($L_1$) and its losses ($R_1$, including $R_Q$) in series with the inductance. The reader includes a matching network, so therefore, assuming a perfect match at the resonance frequency, $R_s$=$R_1$. The parasitic capacitance of the reader antenna has been considered in the matching network and is included in the equivalent Thevenin model.

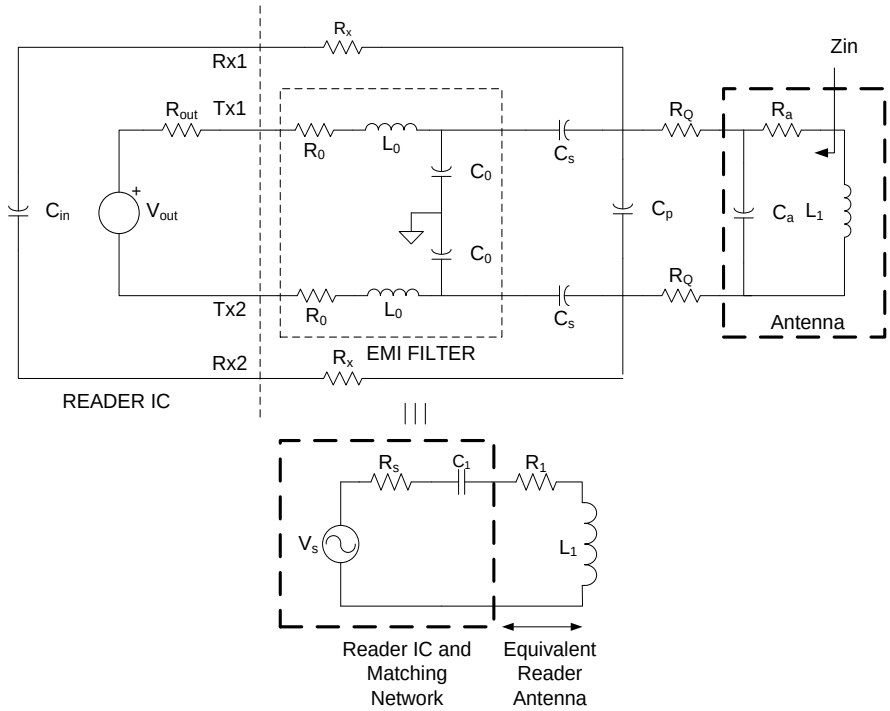


Figure 2.5. Model of the reader, including the matching network (top) and the simplified model (bottom).

It is known that in some applications the reader communicates correctly with a smart card at a large distance but not at short distances, independently of the (good) demodulation quality of the backscattered signal [17], [18]. This phenomenon is known as the loading effect, resulting in a lack of transmitted power due to the strong influence of the tag's load on the reader [17], [18].

The final consideration is that when using a smartphone as an NFC reader, unlike with other WPT systems, the transmitted power and reader antenna topology depend on the mobile model. Typical transceiver IC for NFC in commercial smartphones can achieve

transmitted powers of between 20 and 23 dBm (e.g. NXP PN7120 [19]or TI TRF7970A [20] IC transceivers).

### 2.3.2 Tag model

Figure 2.6 describes the main block of an NFC tag IC. There are two main blocks connected to the antenna [23]. The first is the wireless power transfer unit in charge of the energy harvesting to power up the IC, while the second is the communication unit that demodulates the data and generates the clock for the transmission of information back to the reader. In this work we focus on the WPT unit. This is composed of an RF limiter, a rectifier, a shunt regulator and a load modulator, which can be modelled as a shunt capacitance with the antenna.

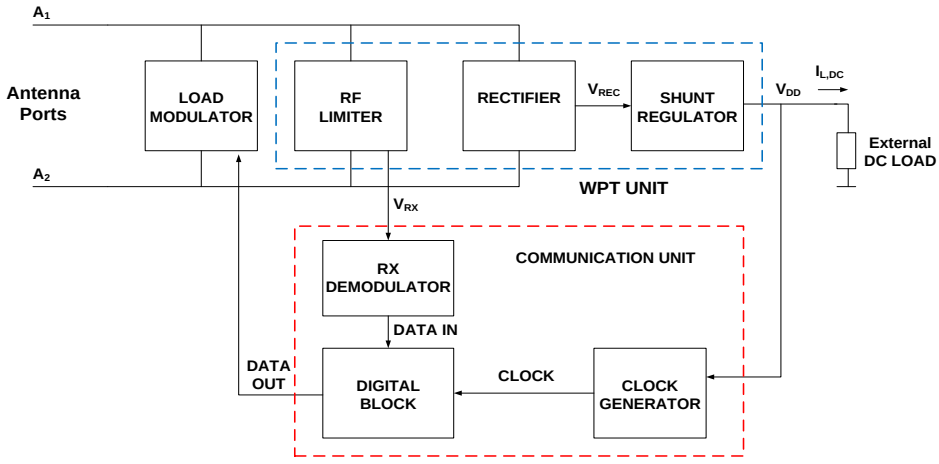


Figure 2.6. Block diagram of the NFC tag IC.

Due to its proximity to the reader, the coupled AC signal at the antenna can be large, which might lead to the destruction of the MOS transistor. Therefore, an RF limiter is needed to prevent damage to the internal circuit from any undesired high-input signal. After this limiting step, the AC signal is translated into a DC signal by means of a full-wave rectifier. The rectified DC voltage is regulated in order to obtain a stable voltage for the communication unit operation.

For modelling the limiter, the circuit described in [23] and shown in Figure 2.7 is considered. This limiter is based on two large-area NMOS shunt transistors that are activated when the input power is

enough to produce a current through the diodes larger than the threshold voltage needed to activate the transistors. The limiter is also used to implement an envelope detector using the diodes and the $R_C$ filter ($R_1$ and $C_1$) for ASK demodulation. The demodulated data are used as the input of a slicer circuit for data demodulation.

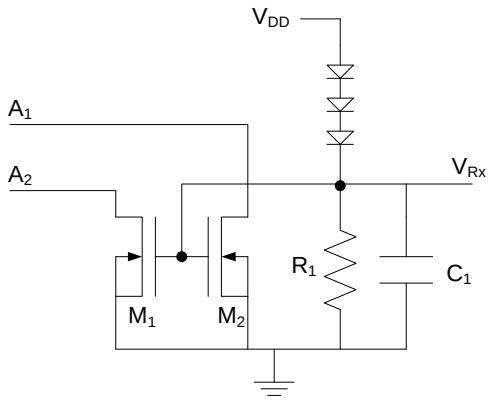


Figure 2.7. RF limiter model inside the NFC IC.

A high efficiency rectifier is required for the RF-to-DC conversion. This is often based on a full-wave bridge rectifier in which the diode pairs turn on during each cycle of the AC signal. However, efficiency is limited for the threshold voltage of the diodes. Schottky diodes can be used in this topology to reduce these voltage drops, but these devices are not compatible with conventional CMOS technology. Several CMOS-based rectifiers have been proposed in the literature. The most frequently used are the NMOS bridge and the CMOS gate cross-coupled (or cross-connected) rectifier [24] (Figure 2.8)

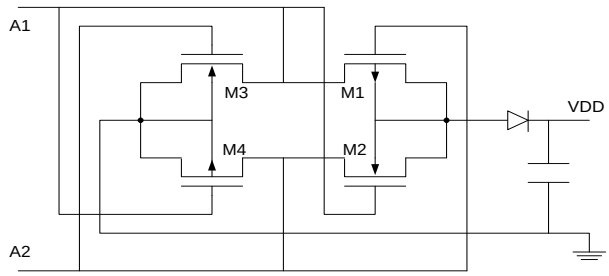


Figure 2.8. Model of the full-wave rectifier based on CMOS gate cross-coupled rectifier.

A shunt regulator can be used to model the regulator in the simulation (for example based on a zener diode). Although lateral zener diodes can be implemented in standard CMOS processes [25], the shunt regulator is often implemented with transistors. Nevertheless, all the topologies are based on the same principle that consists of reducing the shunt resistance of a bypass transistor when the input voltage is higher than the desired output voltage. Figure 2.9 shows the shunt regulator used in [17], [26], [27]. In this circuit, the shunt impedance to reduce the voltage is controlled comparing a band gap-based reference voltage and the output voltage.

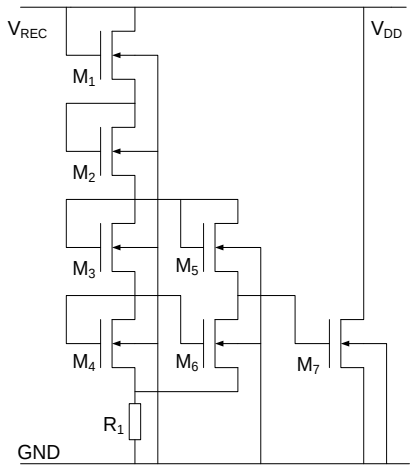


Figure 2.9. Shunt regulator circuit model.

The load modulator (Figure 2.10) is formed by two NMOS transistors that act as switches, each of them connecting one capacitor from the RF input to ground [28], [29]. In order to transmit information to the reader, the transistors are switched on and off by the data signal connected to the gate, resulting in a change of load impedance at the antenna as a function of the data.

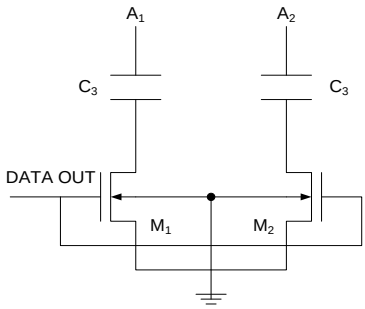


Figure 2.10. Load modulator model formed by two NMOS transistors.

In this work the tag is modelled as a resistance ($R_{IC}$) in parallel with a capacitor ($C_{IC}$). A tuning capacitance $C_{tun}$ is added to make the circuit resonant at the operating frequency. This model for the tag is shown in Figure 2.11.

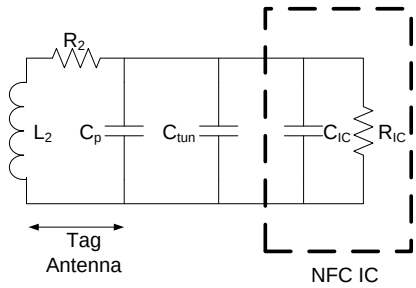


Figure 2.11. Simplified model of the tag including the tag antenna, tuning capacitor and NFC IC.

An important point to consider is that the chip impedance presents a nonlinear behaviour, thus, the impedance at the operational frequency changes depending on the received power. However, it is not easy to measure the nonlinearity. The impedance of the laboratory equipment is usually 50 $\mathbf{\Omega}$, and the transponder chip is expected to have a high impedance (in order of k$\mathbf{\Omega}$). The other problem is the high power level required comparable to the real power levels generated by the reader. In [21], a high-power method for impedance characterization of HF RFID chips is proposed, by using the shunt or series method, measuring the transmission coefficients ($S_{21}$) using a series setup. This method improves the accuracy obtained by the reflected method (measuring $S_{11}$) [22], since this is prone to error when measuring high impedance chips. As

shown in [21], HF RFID transponders behave in a strong nonlinear way when the received power increases.

### 2.3.3 NFC system model

Figure 2.12 brings together the reader and tag models introduced above, showing the simplified model of the wireless power transfer between the reader and the tag used in this work. The reader, composed by the IC model altogether with the matching network and its antenna is related to the tag, which is modelled as an antenna, a tuning capacitor and the IC model, through the coupling coefficient ($k$) that is explained later in this chapter.

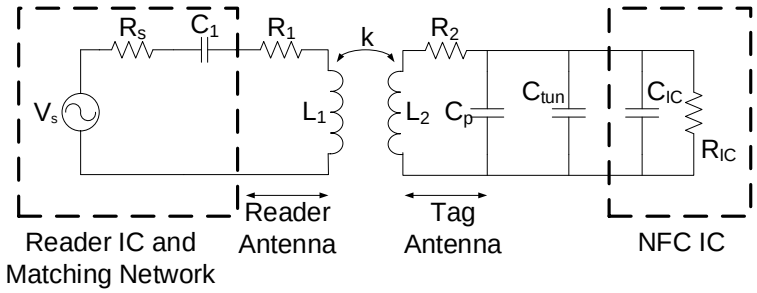


Figure 2.12 Wireless power transfer model between the reader and the tag.

## 2.4 NFC constraints

Even though NFC allows to transmit energy wirelessly from a source (reader) to power-up a receiver (tag), its main purpose is the data transfer. Furthermore, with the incorporation of this technology in most of the smartphones manufactured today, the methods to apply it encompass a huge variety of solutions, with different antenna sizes and materials, as well as different emission power levels and electrical characteristics. Unlike other specific WPT systems, developing NFC devices must consider all the previous mentioned constrains, thus allowing an efficient power transfer while ensuring a correct data transfer, independently of the reader used.

### 2.4.1 Antenna design

As any wireless communication system, NFC needs an antenna to communicate the transmitter and receiver. In addition, for the purpose of passive tags, it is crucial to ensure the maximum power

transfer through the antennas. This section describes the main parameters to consider for the design of the antennas.

#### 2.4.1.1 Resonance frequency ($f_r$), operational frequency ($f_0$) and antenna tuning

In this work the nominal operational frequency (13.56 MHz) is denoted as $f_0$. The resonance frequency ($f_r$) of the antenna is the frequency where the inductive and capacitive reactances of the antenna cancel each other out, thus behaving as purely resistive. Notice that, in some cases, the angular frequency is referenced using the symbol $\omega$ ($\omega = 2\pi f$). In order to optimise the power and data transfer, it is critical to adjust the resonance frequency ($f_r$) of the antenna to the operational frequency ($f_0$) of the system, this process can be done by tuning the antenna. However, it may be needed to adjust a smoothly higher frequency when considering the frequency shift produced by environmental conditions, such as the tag material or the presence of metallic object like the metallic reader enclosure when working in very short range. The presence of metal near the coil produce an eddy currents in opposite direction of the generated field, absorbing part of the power. This metal introduces a capacitance to the antenna impedance and reduces its inductance which makes the energy to be reflected to the antenna terminals since it does not match to the input impedance ($Z_0$). The reduction of the antenna inductance ($L_a$) and modification of the parasitic capacitance ($C_p$), modifies the resonance frequency of the antenna since it is determined by:

$$f_r \approx \frac{1}{2\pi\sqrt{L_a\left(C_{IC} + C_p + C_{tun}\right)}} \tag{2.11}$$

where $L_a$ is the tag's antenna inductance, $C_{IC}$ is the internal IC capacitance, $C_p$ is the layout parasitic capacitance (which includes the antenna capacitance and the parasitic capacitance due to the interconnections), and $C_{tun}$ is the capacitor used to adjust the resonance frequency ($f_r$) to the operation frequency $f_0$ (13.56 MHz). The resonance frequency can be verified by measuring the $S_{11}$ parameter connecting another loop antenna to a vector network analyser close to the tag.

As mentioned before, the operational frequency of NFC is $f_0 = 13.56$ MHz, which leads to a wavelength of about 22 meters ($\lambda = C/f_0$, where $C \approx 3 \cdot 10^8\ m/s$). This leads to a half-wave dipole antenna of 11 meters which is not suitable for a handheld or a smartcard. The antenna used is much smaller, therefore, the radiation efficiency is very small, and the typical parameters measured in antennas such as the gain or the radiation pattern are not relevant. An NFC antenna is basically an inductor, as shown on Figure 2.13, and its performance depends mostly on the area ($A$) and the number of turns ($N$). As a rule, as bigger is the area, and as much turns it has, the better is its performance. The parasitic capacitance ($C_p$) and resistance ($R_p$) must be considered. The inductance ($L_a$) is mainly defined by the number of turns of the loop, the resistance ($R_a$) by the diameter and total length of the loops, and the capacitance ($C_p$) by the separation between the antenna loops and the number of turns.

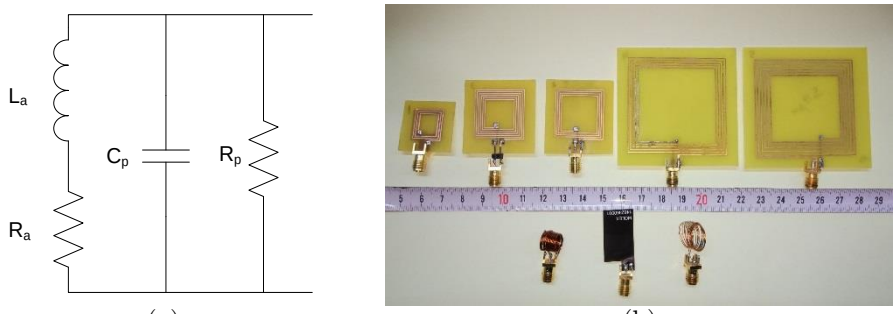


(a) (b)

Figure 2.13. (a) Antenna circuit model for a loop antenna, (b) antennas with different sizes and number of turns.

The theoretical inductance for a rectangular wire coil can be calculated from [30]:

$$L_a = N^2 \frac{\mu}{\pi}\left[-2(w+h) + 2\sqrt{h^2+w^2} - h\ln\left(\frac{h+\sqrt{h^2+w^2}}{w}\right) - w\ln\left(\frac{w+\sqrt{h^2+w^2}}{h}\right) + h\ln\left(\frac{2h}{a}\right) + w\ln\left(\frac{2w}{a}\right)\right] \quad (2.12)$$

where $N$ is the number of turns, $w$ and $h$ the average width and height of the coil, and $a$ is the PCB width. The inductance can be measured from the Z parameters as: $L_a = Im(Z)/\mu_0$.

The easiest way to precisely calculate $L_a$ and $R_a$ is connecting the antenna coil to a VNA and measure the impedance of the antenna ($Z_{11}$) at the operational frequency ($f_0$), knowing that [31]:

$$Z_{11} = R_a + j2\pi f_0 L_a \tag{2.13}$$

The values of resistance and inductance are usually given by the VNA, however, the capacitance is not measured, but can be estimated using the equation [32]:

$$C_p = \frac{1}{(2\pi f_r)^2 L_a} \tag{2.14}$$

The series equivalent total resistance of the antenna ($R_T$) at the operational frequency ($f_0$), which combines the antenna and parasitic resistance ($R_a$ and $R_p$ respectively), can be calculated by first measuring the equivalent resistance at the self-resonance frequency ($R_{p(fr)}$) with the VNA, and using its value to measure the parallel equivalent at $f_0$ ($R_{p(f0)}$):

$$R_{p(f_0)} = \frac{R_{p(f_r)}}{\sqrt{\frac{f_0}{f_r}}} \tag{2.15}$$

and then calculate $R_T$ using:

$$R_T = R_a + \frac{(2\pi f_0 L_a)}{R_{p(f_0)}} \tag{2.16}$$

The parasitic resistance ($R_p$) can be calculated using the equation [32]:

$$R_p = \frac{(2\pi f_0 L_a)^2}{R_a + 2R_q} \tag{2.17}$$

where $R_q$ is the damping resistor used to adjust the quality factor (defined in equation (2.28))

#### 2.4.1.2 Antenna factor ($AF$)

The magnetic antenna factor ($AF$) at a determined frequency ($f$) is defined as the ratio between the incident magnetic field ($H$) to the output voltage at the load ($V_o$) [33]:

$$AF(f) = H(f)/V_o(f) \tag{2.18}$$

The AF of the coil antenna is used to measure the average magnetic field in the tag. In order to obtain the AF of the antenna, the circuit of Figure 2.14 can be used.

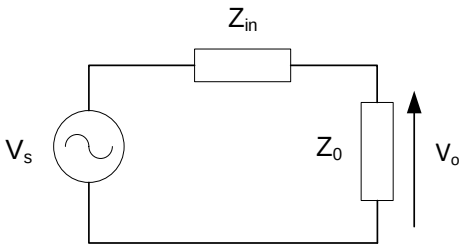


Figure 2.14. Equivalent circuit of the antenna.

Taking into account Faraday's law: $V_s = -j\omega_0 \pi a^2 \mu_0 H$, where $a$ is the radius of the antenna, and knowing that $V_0 = (Z_0/(Z_{in} + Z_0))V_s$, being $Z_{in}$ the antenna impedance and $Z_0$ the reference impedance (50Ω), the $AF$ can be obtained from the measured antenna impedance as [33]:

$$AF = \frac{Z_0 + Z_{in}}{j2\pi f \mu_0 Z_0 A \cdot N} \tag{2.19}$$

where $A$ is the loop area and $N$ is the number of turns of the loop, thus, these two parameters ($A$ and $N$) must be considered when designing the antenna.

### 2.4.2 Coupling coefficient ($k$)

The coupling coefficient of a pair of coils ($C_1$, $C_2$) is a measure of the magnetic field transferred between them and therefore it is a fundamental parameter in NFC. It depends on the shape of the antennas, distance and alignment between antennas, and the materials. The coupling coefficient can be calculated from the $Z$

parameters from electromagnetic simulations or $S$ parameters measurements performed with VNA [34]:

$$k = \frac{M}{\sqrt{L_1 L_2}} = \frac{\sqrt{Im(Z_{12}) \cdot Im(Z_{21})}}{\sqrt{Im(Z_{11}) \cdot Im(Z_{22})}} \tag{2.20}$$

It is known that the maximum coupling coefficient between two coils is obtained when the radius of the coils are identical [35], [36]. However, NFC antennas are embedded in a large variety of devices, and each of them uses a different antenna configuration. This factor must be considered when designing NFC tags.

### 2.4.3 Quality factor ($Q$)

The quality factor ($Q$) of a resonator determines its bandwidth and depends on the inductance ($L$) and resistance ($R$). It can also be computed from the $Z$ parameters.

$$Q = \frac{\omega L}{R} = \frac{Im(Z)}{Re(Z)} \tag{2.21}$$

The relationship between the quality factor at the resonance frequency ($f_r$) and the bandwidth can be described as:

$$BW = \frac{f_r}{Q} \tag{2.22}$$

A high value of $Q$ in the transmitter (reader) is translated into a narrow band, as can be seen in Figure 2.15, which benefits the power transfer. To ensure that the sidebands produced by the backscattering modulation that contains the information are received correctly by the reader, the standards determine a maximum $Q$ factor.

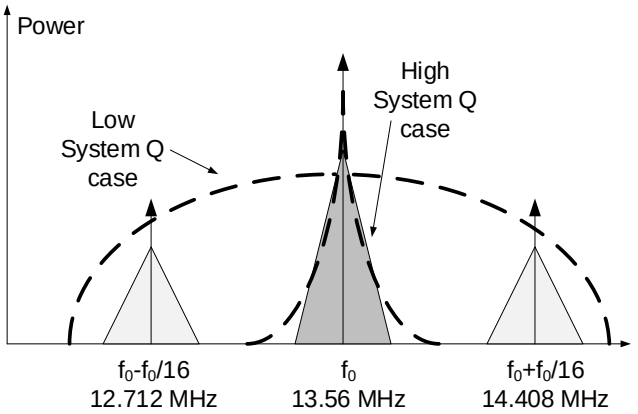


Figure 2.15. Frequency spectrum of NFC system with the carrier frequency ($f_0$) and the sidebands

The maximal $Q$ of a transmitter depends on the subcarrier frequency and the type of coding used. In the worst-case scenario (ISO/IEC 14443A), the maximal value of $Q$ is $f_0/(2\ x\ bit\ rate)$, which, at 106 kbps, leads to a maximum $Q$ of 64. ISO/IEC 15693 allows higher values of $Q$, and its maximum value comes from the pause on the carrier frequency ($T_p$, depicted in Figure 2.16) such as $Q_{max} = f_0 \times T_p$, being $T_p = 9.44\,\mu s$, thus, $Q_{max} = 128$. It is important to mention that the quality factor of printed antennas use to have higher $Q$ than the required by the standards, therefore, a series resistor is added in order to reduce it (included in $R_1$ in the Figure 2.12 which models the antenna resistance and this series resistance).

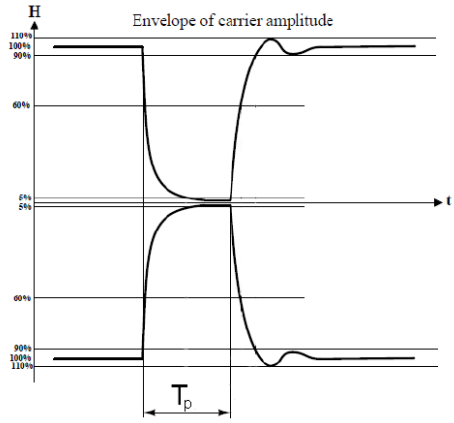


Figure 2.16. ASK with 100% modulation envelope amplitude. $T_p$ is the protocol pause time, which determines the maximum $Q$.

Three different $Q$'s can be defined for each side (reader and tag): the antenna quality factor ($Q_i$), the quality factor of the load (i.e. the NFC chip, $Q_L$) and the total quality factor of the whole transponder ($Q_{iL}$). The unload quality factor of the coil $i$ (being $i$=1 for the reader, and $i$=2 for the tag) is obtained from the inductance and resistance at the angular resonance frequency ($\omega_0$) with (2.12). The total quality factor ($Q_{iL}$) is computed from:

$$Q_{iL} = \frac{Q_i Q_L}{Q_i + Q_L} \tag{2.23}$$

where the external quality factor ($Q_L$):

$$Q_L = \frac{R_{IC}}{\omega_0 L_i} \tag{2.24}$$

where $i = 1,2$, and corresponds to the component values in Figure 2.12.

Analogously to the case of the transmitter, the total quality factor of the tag ($Q_{2L}$) is limited to avoid degradation of the modulation of the subcarrier. Therefore the maximum value of $Q_{2L}$ is approximately $Q_{2L,max}=8\pi\approx25$ [37]. A higher quality factor would increase the time constants for the transition and decrease the load modulation. This limitation is not present in WPT systems devoted to wireless charging. The total quality factor of the tag ($Q_{2L}$) is given by the hyperbolic average of the quality factor of the tag antenna ($Q_2$) and the quality factor associated with the IC impedance ($Q_L$). Thus, the quality factors of the tag are defined by:

$$Q_2 = \frac{\omega_0 L_2}{R_2} \tag{2.25}$$

$$Q_L = \frac{R_{IC}}{\omega_0 L_2} \tag{2.26}$$

$$Q_{2L} = \frac{Q_2 Q_L}{Q_2 + Q_L} \tag{2.27}$$

As mentioned above, the $Q$ factor of an antenna depends on its inductance and series impedance, and, since standards determine a maximal value of $Q$, it is common to add two dumping resistor ($R_Q$)

at each side of the antenna to reduce the quality factor. The value of such resistor can be calculated to reach the desired value ($Q_{des}$) with the following equation [32]:

$$R_Q = 0.5\left(\frac{\omega_0 L_a}{Q_{des}} - R_a\right) \tag{2.28}$$

The maximum quality factor to ensure the bandwidth required for the backscattering communication ($Q_{2L}$) is given by:

$$R_{IC} < \omega_0 L_2 Q_{2L,maz} \tag{2.29}$$

### 2.4.4 Efficiency ($\eta$)

In WPT the efficiency, defined as the ratio between the power on the load and the emitted power, is crucial. The efficiency depends on the coupling coefficient ($k$) between the coils, and the quality factor ($Q$) of each element, following the formula:

$$\eta = \frac{P_L}{P_{in}} = \frac{k_{12}^2 Q_1 Q_{2L}}{1 + k_{12}^2 Q_1 Q_{2L}} \cdot \frac{Q_{2L}}{Q_L} \tag{2.30}$$

where $P_L$ is the power on the load, $P_{in}$ in the emitted power, $k_{12}$ is the coupling coefficient between coils 1 and 2, and $Q_1$, $Q_L$ and $Q_{2L}$ are the quality factors of the reader antenna, the tag NFC IC, and the whole tag, respectively. It is important to notice that magnetic coupling efficiency is very sensitive to primary-secondary coils alignment and distance, since magnetic field decays as $1/r^3$, being $r$ de distance between coils.

### 2.4.5 Average magnetic field ($H_{AV}$)

The average magnetic field ($H_{AV}$) is obtained from the Root-Mean-Square voltage ($V_{RMS}$) calculated from the measured power (using a spectrum analyser) at the carrier frequency from the antenna terminals. This parameter, as the name suggest, determines the magnetic field received by the antenna, and is given by the voltage generated on the coil terminals and the antenna factor, thus, depends on the electrical and geometrical parameters of the antenna. It can be obtained as:

$$H_{av}(A_{RMS}/m) = V_{RMS} \cdot |AF| \tag{2.31}$$

### 2.4.6 Environmental effects

At is it widely studied [38], the magnetic and electric fields with a ground plane directly beneath are hugely degraded. The presence of metal close to the antenna produces an eddy currents which create a magnetic field in opposite direction, absorbing power and detuning the antenna due a decrease of its inductance and quality factor. Considering that the most common readers used in NFC are smartphones, which use to have a metallic enclosure, or, in some cases, place the antenna over the battery surface, this problem must be addressed. The most common way to deal with this undesired effect is to put a sheet of a high permeability material between the antenna and the ground plane thus creating a shield. The most frequent used material for that end is the ferrite, which can help to isolate the antenna, however, it does not eliminate the total effect of the metal surface since only a part of the magnetic flux will be conducted through the thin foil of ferrite, as depicted in Figure 2.17.

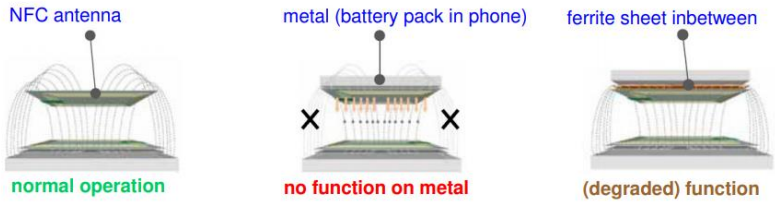


Figure 2.17. Presence of metal close to the antenna. (a) Normal operation, (b) field affected by metal, and (c) use of ferrite sheet.

#### 2.4.6.1 Body effects

When designing tags for medical applications where the tag is on the skin it is important to note that the inductance ($L_a$) is not affected by the dielectric material and is therefore unaltered when the antenna is implanted in the body. However, implantable devices must use a coating layer to isolate the electronics from the body. This is commonly done by using silicon rubber due to its high chemical inertness and durability. The capacitances introduced by the coating layer is modelled with $C_s$ in Figure 2.18.

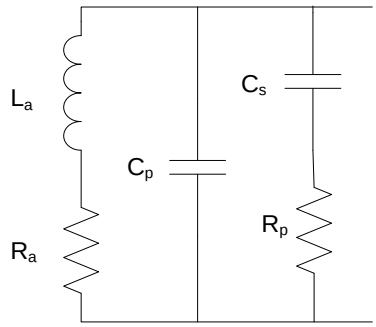


Figure 2.18. Circuital antenna model for a loop antenna for implanted loop antenna, adding a parasitic resistance $R_p$.

The series antenna resistance ($R_a$) is frequency-dependent, mainly due to the skin effect. The conductivities of biological tissues are much lower than those of the metal used for the coil strips, so the eddy-current generation in the tissue is insignificant. The effects of the presence of biological matter and the feasibility of implantable NFC tags is deeply studied in chapter 7 of this thesis.

## 2.5 Simulations and measurements

This section presents how the concepts and theory exposed above are developed during this thesis, using simulation tools and measurement equipment. Practical methods to measure the magnetic field, the coupling coefficient, the difference between antennas topologies and materials, differences when using different readers, and different NFC ICs on the tag and its aftereffect on the energy harvesting capability, as well as the setups used are shown with the purpose of giving a general overview of the processes used for analysing the performance and viability of the tags presented in the next chapters.

Most of the measurements presented in this thesis have been done using a smartphone model Xiaomi Mi Note 2 as a reader. The NFC antenna of this model is placed on a metallic cover that protects the circuitry of the phone, surrounding the camera. The antenna, with 5 loops, is shown in Figure 2.19. This antenna is shielded by a high permeability material sheet (ferrite sheet).

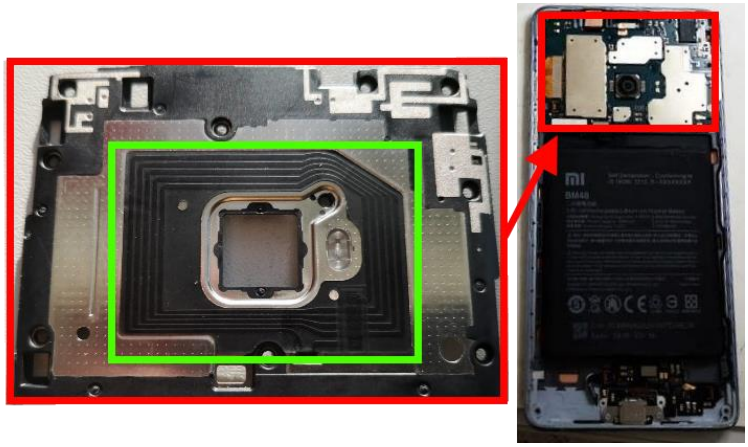

Figure 2.19. Xiaomi Mi Note 2 back side (right), and the NFC antenna (green square).

### 2.5.1 Magnetic field ($H_{av}$)

An automatized setup to measure the magnetic field received at the antenna is shown in Figure 2.20. It is composed by the reader (commercial smartphone, placed on a moving part controlled by a stepper motor, Nema 24), the antenna under test (Coil 1 of Table 2.III), which is connected to the Vector Network Analyser (VNA, Agilent E5062A) or to the Spectrum Analyser (SA, Rhode & Schwarz FSP) by means of the switch MSP2T-18 from Mini-circuits, which is governed by a voltage supply (Agilent E3631A). The SA, the VNA and the power supply are connected to a computer through the General-Purpose Instrumentation Bus (GPIB), and the stepper motor through a Universal Serial Bus (USB). The procedure to control the instruments is programmed using a Matlab script, first selecting the appropriate voltage on the power supply to select the switch output, choosing the VNA to measure the $S_{11}$ parameter, and then the SA to measure the power received at the operation frequency ($f_0$, 13.56 MHz). Once the readings from the VNA and the SA are done, the stepper motor moves the reader 1 mm, and the process is repeated.

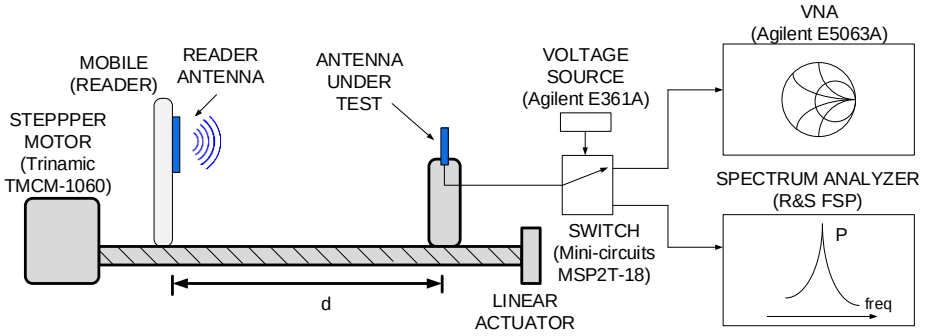


(a)

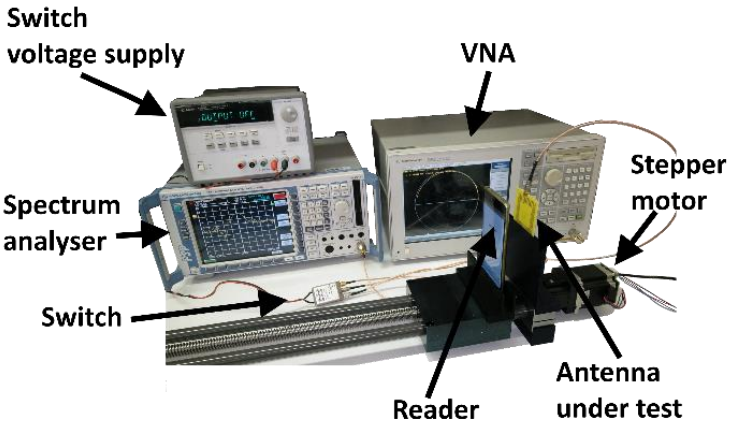


(b)

Figure 2.20. Setup to measure the magnetic field, schema (a), and photography (b), composed by reader, antenna under test, spectrum analyser, VNA, SPDT switch and voltage supply.

The performance of the antennas is analysed by measuring the reflection coefficient ($S_{11}$) at each distance ($d$), which is used to calculate the antenna factor ($AF$) that will be multiplied by the power received ($V_{RMS}$) (Figure 2.21(a)) to measure the received magnetic field ($H_{av}$) (Figure 2.21(b)). From the $S$ parameters it is possible to calculate the $Z$ parameters which are used to calculate the inductance ($L_2$) (Figure 2.21(c)), and quality factor ($Q_2$) (Figure 2.21(d)) for different distances. Figure 2.21 depicts the plots of these parameters for a 50×50 mm 6 loops coil, using a Xiaomi Mi Note 2 as a reader. It can be observed that the inductance and the quality factor decrease due the proximity of the metallic mobile which

produces an induced currents (image current in the metal). This effect will be studied with more detail in section 2.5.3.

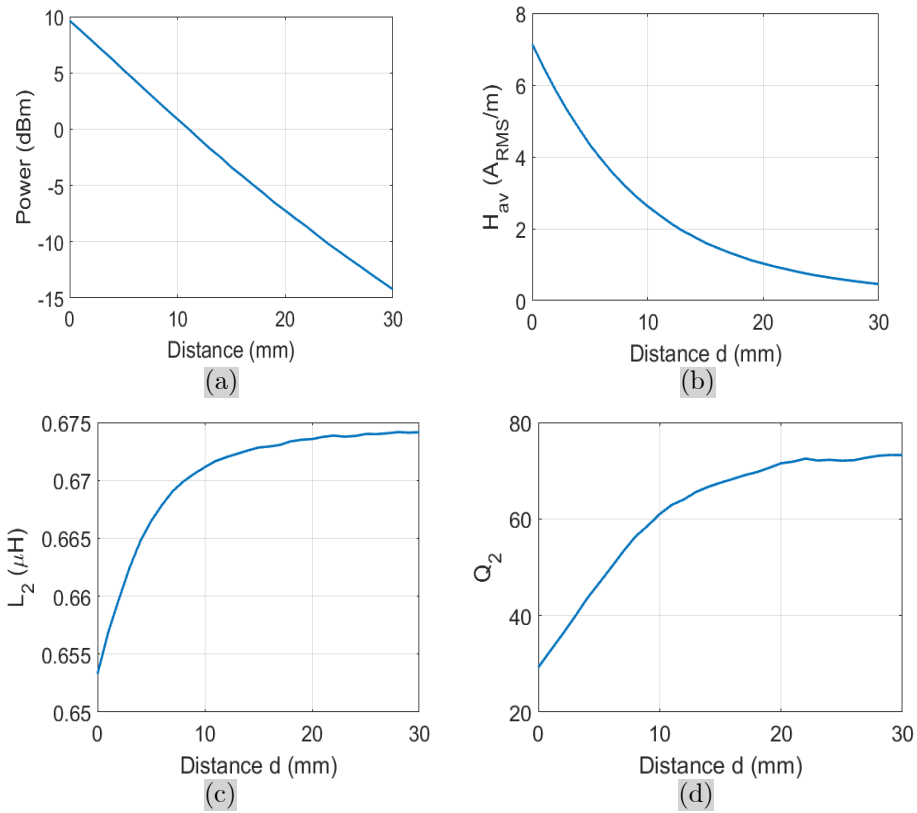


Figure 2.21. Magnetic field measurements of Coil 1 as a function of distance using Xiaomi Mi Note 2 as a reader. (a) Power received, (b) Magnetic field received ($H_{av}$), (c) inductance ($L_2$), and (d) quality factor ($Q_2$).

### 2.5.2 Coupling coefficient ($k$)

In order to evaluate the behaviour of the coupling coefficient ($k$) between antennas, several coil configurations have been tested. The measurements have been performed with three different coils, each tested on two different substrate materials: FR4 and Ultralam [39] (see Figure 2.22).

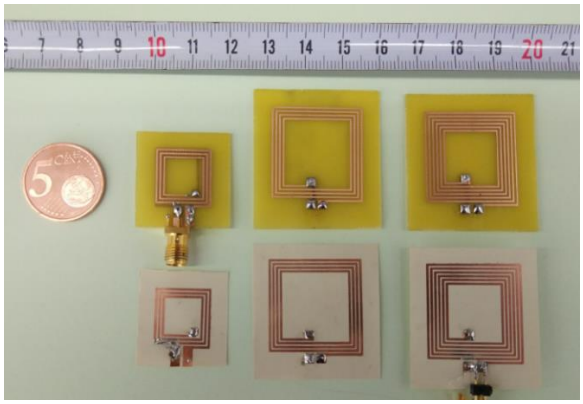

Figure 2.22. Tested coils for the coupling coefficient. (a) Left coil 1, centre coil 2, and right coil 3. The three at the top are printed on FR4 substrate and the three on the bottom in Ultralam. (b) NFC antenna of the Xiaomi Mi Note 2 used as a reader.

The parameters of each coil are shown in Table 2.III. Beyond the calculation of the coupling coefficient, Table 2.III can be used to compare the influence of the substrate and to compare the same coils in FR4 substrate against a flexible substrate (i.e. Ultralam)

Table 2.III. Coil parameters. Three different configurations, in two different substrates, FR4 and Ultralam (UL)

| | Coil 1 | | Coil 2 | | Coil 3 | |
|---|---|---|---|---|---|---|
| | FR4 | UL | FR4 | UL | FR4 | UL |
| Size (mm) | 15x15 | | 25x25 | | 25x25 | |
| Turns ($N$) | 6 | | 4 | | 6 | |
| Printed sides | 2 | | 1 | | 1 | |
| Trace width (mm) | 0.7 | | 0.7 | | 0.7 | |
| Spacing between traces (mm) | 1 | | 1 | | 1 | |
| Inductance ($L_2$, nH) | 683 | 757 | 724 | 697 | 1182 | 1154 |
| Self-resonance frequency ($f_r$, MHz) | 106.33 | 66.57 | 115.83 | 130.29 | 96.69 | 104.31 |
| Quality factor at 13.56 MHz ($Q_2$) | 58.88 | 41.16 | 66.57 | 51.86 | 75.92 | 56.55 |
| Antenna Factor at 13.56 MHz ($AF$) | 0.96 | 1.03 | 5.98 | 5.86 | 5.63 | 5.53 |

Coil 1 in FR4 has been used as a reference coil, measuring the coupling coefficient ($k$) between this coil and the others. The results, shown in Figure 2.23, demonstrate that the best coupling is found when the two coils are identical (blue continuous line). When using the same configuration but with different substrate (blue dashed line) a degradation on $k$ is observed. However, when the two coils have different parameters (coil 2 and 3, red and orange lines respectively), the difference between substrates (continuous line for FR4 and dashed line for Ultralam) is almost imperceptible.

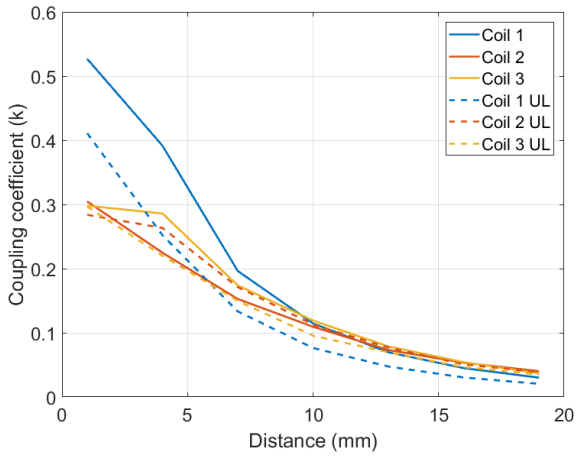


Figure 2.23. Coupling coefficient between coil 1 and six different coils.

### 2.5.3 Presence of metal near the antenna

As explained in section 2.4.6, the presence of metal near the antenna produces undesirable effects. Figure 2.24 compares the measured inductance ($L_2$) and quality factor ($Q_2$) at 13.56 MHz as a function of the distance to a metal plane that simulates the effect of metallic parts of the mobile phone case. The antenna used for this test is a 50×50 mm with 6 loops, trace width of 0.7 mm, and space between traces of 1 mm. It is important to highlight that the inductance decreases when the loop antenna is close to metal, due to the induced image currents with opposite directions that reduce the magnetic flux. For distances greater than 15 mm the inductance is nearly flat with an average value around 2.8 µH. Therefore, the resonance frequency of the tag can be tuned adding a tuning capacitor in parallel with the antenna. Depending of the value chosen, the tag can be designed to improve its operation for ultra-short, short or

long ranges. Usually the selected distance is greater than 15 mm, because the coupling coefficient is lower than in the other cases and, therefore, the power received by the tag can be expected to be higher as it is close to the mobile.

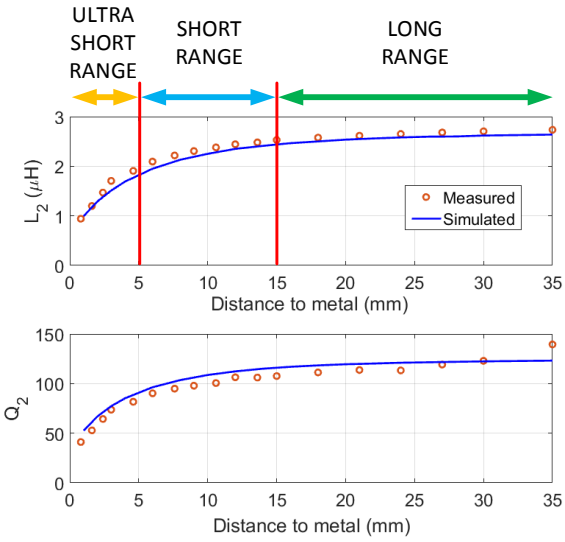


Figure 2.24. Measured (o) and simulated (solid line) inductance ($L_a$) (a) and quality factor ($Q_2$) (b) of the loop antenna used in the prototype as a function of the distance to a metal plate.

This effect at very short distances is compensated by the higher power received. The detuning caused by the presence of metal is shown in Figure 2.25.

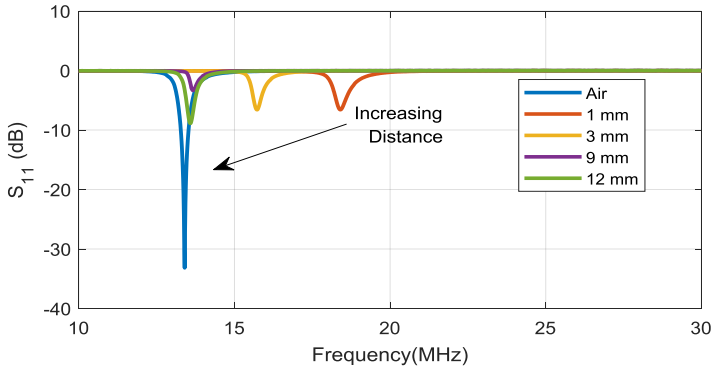


Figure 2.25. Measured $S_{11}$ of the test antenna as a function of the frequency for different distances between the tag and the mobile.

In addition, when the tag is close to the mobile, the bandwidth of the system increases because the tag quality factor decreases. This is caused by the antenna quality factor reduction and by the decrease of the IC load resistance (due to higher power received by the tag). It is important to notice that, due to power limitation of standard VNA (often 20 dBm), the excitation field measured with the lab equipment is smaller than in a real reader. Therefore, the IC impedance (especially the equivalent resistance) is higher than in a real situation. The chip resistance decreases typically from $R_{IC}$=5 kΩ to 1 kΩ under high power excitation when the tag is very close to the reader [21]. Therefore, the quality factor of the tag decreases, and the tag bandwidth ($BW$) increases. Figure 2.26 shows the quality factor and $BW$ as a function of the tag to mobile distance showing that the $BW$ is higher than the required in ISO/IEC 15693 (968 kHz) and the shape distortion is due to the reader more than the tag.

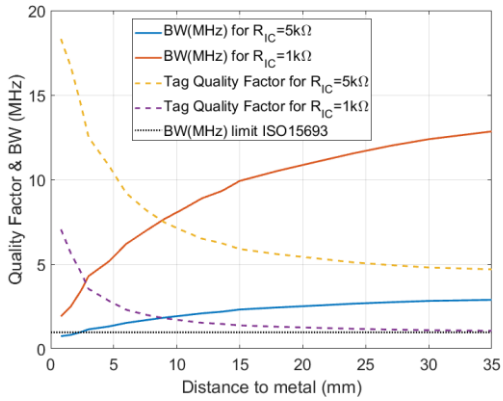


Figure 2.26. Tag quality factor and bandwidth as a function of the distance to metal depending on chip resistance $R_{IC}$. The limit $BW$ for ISO 15693 is shown.

### 2.5.4 Energy harvesting

The average magnetic field ($H_{av}$) received at the NFC tag must be above a threshold value ($H_{min}$) for a correct RF to DC conversion. $H_{min}$ as a function of tag resonance frequency is obtained from [37]:

$$H_{min} \approx \frac{\sqrt{\left[1-\left(\frac{f_{op}}{f_r}\right)^2\right]^2+\frac{1}{Q_{2L}^2}}}{2\pi f_{op}\mu_0 AN}\cdot U_{min} \tag{2.32}$$

where $U_{min}$ is the minimum voltage required for the tag operation, which depends on the chip IC design and the used technology. It is important to mention that the $H_{min}$ changes depending on the chip, since each IC has different $U_{min}$ and chip resistance impedance, $R_{IC}$. It also depends on the coil size ($A$) and number of turns ($N$). Considering that the tag is tuned ($f_r$=$f_0$), and that $Q_L \ll Q_2$, it can be considered that $Q_{2l} \approx Q_L = R_{IC}/\omega_0 L_a$. Thus, under this approximations $H_{min}$ can be estimated as:

$$H_{min} \approx \frac{1}{\omega_0 \mu_0 A \cdot N} \cdot \frac{U_{min}}{R_{IC}} \cdot \omega_0 L_a = \frac{I_{min}}{\omega_0 \mu_0} \cdot \left(\frac{L_a}{A \cdot N}\right) \qquad (2.33)$$

Hence, the minimum magnetic field to activate the energy harvesting depends on the minimum threshold current of each chip ($I_{min}$), and the antenna parameters ($L_a$, $A$, and $N$).

The average magnetic field ($H_{av}$) depends on the transmitted power by the reader and the coupling between the loop antennas. Therefore, it depends on the smartphone and its distance to the tag. On the other hand, $H_{min}$ can be considered a figure of merit of the tag because depends only on the tag parameters (IC and antenna). Therefore, it can be employed to evaluate the tag performance independently of the reader used to generate the field. Figure 2.27 shows the calculated $H_{min}$ considering $Q_{2L}$=70, $L_2$=0.7 µH, A=15×15 mm, $N$=6, and $U_{min}$=4.8V, for two different values of $R_{IC}$ (450 Ω and 525 Ω) [21].

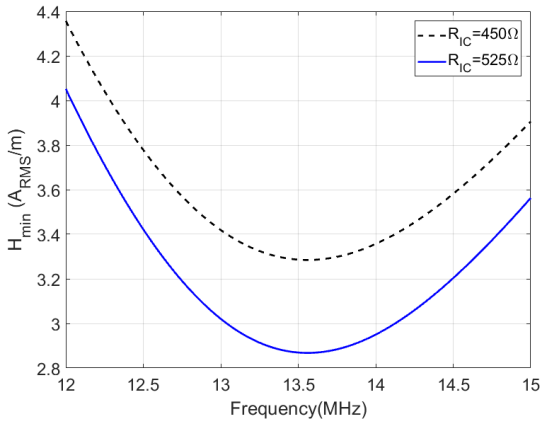


Figure 2.27. Calculated minimum magnetic field $H_{min}$($A_{RMS}$/m) as a function of the frequency.

Figure 2.28 shows the $H_{av}$ as a function of the distance for two mobiles. The measurements have been done with a tag on FR4 substrate, with an antenna with 6 loops of 50×50 mm (the same used in previous section 2.5.3) connected to a MR24LR NFC IC and this connected through $I^2C$ bus to an ATtiny85 microcontroller as a load. For the current consumption of the tag, a read range of between 1 cm and 1.75 cm is obtained, depending on which smartphone is used as reader. This distance corresponds to a measured minimum magnetic field ($H_{min}$) equal to 1.1 $A_{RMS}/m$ (black dashed line on Figure 2.28). At the threshold distance, the measured power performed with the spectrum analyser (that corresponds to the tag loaded with $R_L$=50 Ω) is approximately 3 dBm. It can be seen that once the magnetic field goes below the threshold, voltage output falls to zero [40]. The mobile 1 transmits higher power than the older model (mobile 2) and consequently the read range is noticeable higher.

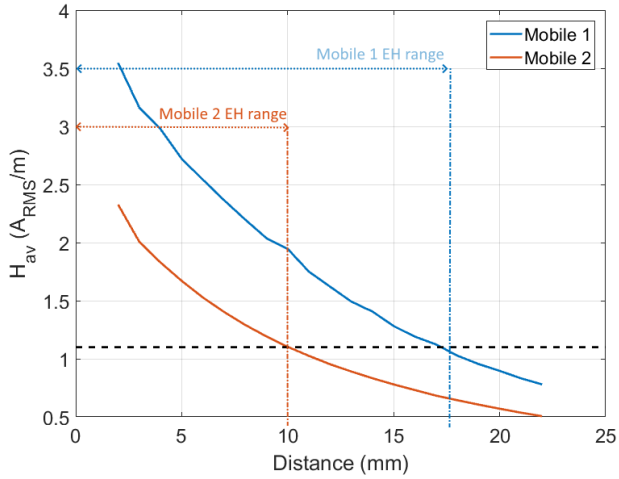


Figure 2.28. Measured average magnetic field as a function of the tag-to-reader distance for two mobile models.

Another factor to be considered is the stability of the rectified voltage generated from the harvested energy. In order to assure the correct communication within the tag, Figure 2.29(a) shows the energy harvested when it is illuminated with a smartphone, and Figure 2.29(b) shows the data communication between the microcontroller, the tag and the sensors using the $I^2C$ protocol. The result shows the viability of using digital communication while being powered up by the reader.

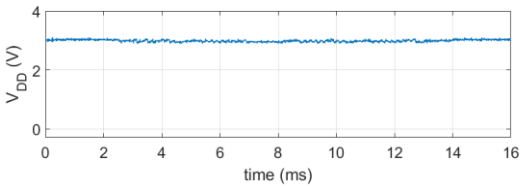


(a)

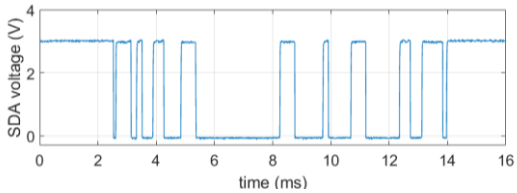


(b)

Figure 2.29. Measurement of the energy harvesting output ($V_{DD}$) (a) and the data of SDA line from the I²C bus (b) when the tag is powered by the NFC reader.

### 2.5.5 Backscattering measurement

When a tag is powered up by receiving a magnetic field generated by the reader ($H_{av}$), it modulates the amplitude of the carrier frequency ($f_c$) with the information contained in the NFC IC memory. This modulation produces two mirror-images sidebands which contain the information. Thus, the retrieved data of the tag depends on these sidebands signals. Even though the correct reception of the information can be checked on the reader after reading the information, it is interesting to analyse the power of those sidebands as they are the signals which must be demodulated by the reader to retrieve the information. In order to measure it without affecting the communication, a test coil connected to a spectrum analyser is located rear the tag at 10 mm (Figure 2.30). Since the tag is emitting in both perpendicular directions symmetrically (forwards and backwards), the test antenna receives a signal very similar to the signal received by the reader.

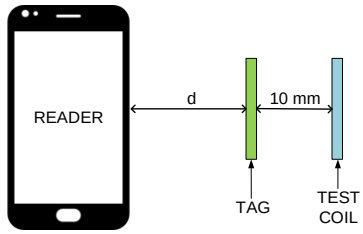


Figure 2.30. Setup for backscattering measurement.

Figure 2.31 shows the measured spectrum when the distance between reader and tag ($d$) is 10 mm. The centre frequency can be observed at 13.56 MHz as well as the sidebands, with an offset of ± 424 kHz from the 13.56 MHz carrier (tags based on ISO/IEC 15693 standard where $f_{sidebands} = f_c \pm f_c/32$). The setup used for this test integrates a Xioami Mi Note 2 as reader, and a tag based on an M24LR04 NFC IC, with an antenna of 15x15 mm (Coil 1 of Table 2.III).

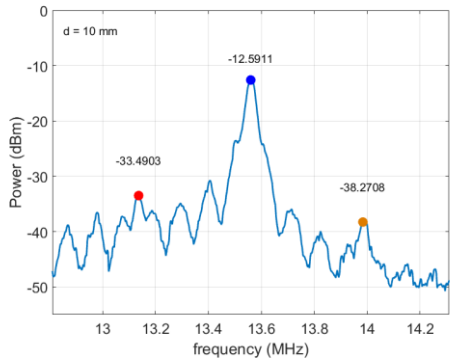


Figure 2.31. Spectrum of the signal generated by the tag, at 10 mm separation between reader and tag.

The measure of the power of the carrier, the lower and the upper bands (blue, red and orange points, respectively, in Figure 2.31) for different distances are shown in Figure 2.32. It can be observed that the sidebands have different levels of power, which is due a resonant frequency ($f_r$) being not centred exactly at 13.56 MHz, but at a lower frequency. Furthermore, at very short distances, the sidebands are hugely degraded due the reduction of the chip resistance under high power excitation. The sidebands power for the presented setup is under the noise floor for distances higher than 25 mm.

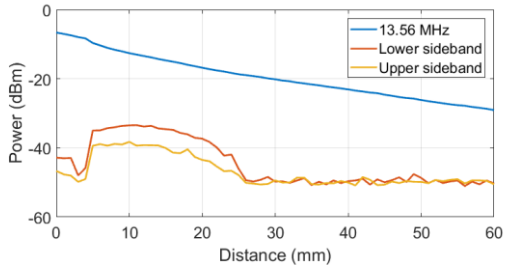


Figure 2.32. Measured power of the carrier frequency (blue) and the sidebands (red and orange) as a function of the distance.

### 2.5.6 NFC ICs comparison

This section pretends to analyse viable options to develop applications in a real-life scenario, hence the importance of analyse the current NFC chips on the market. Several NFC ICs for tags are present on the market. Table 2.IV shows a comparison of some of the NFC ICs with energy harvesting capability, with their maximum current sink and the typical voltage provided after the AC-DC rectifier.

Table 2.IV. NFC ICs with energy harvesting comparison [36].

| Manufacturer | IC model | EH max. current (mA) | Typical Voltage (V) | Standard (ISO/IEC) |
|---|---|---|---|---|
| ST Microelectronics | M24LR-E-R [41] | 6 | 3 | 15693 |
| | ST25DV-12C [42] | 6 | 3 | 15693 |
| NXP | NT3H1101 [43] | 5 | 2 | 14443A |
| | NT3H1201 [43] | 5 | 2 | 14443A |
| EM Microelectronics | NF4 [44] | 5 | 3.6 | 14443A |
| Giantec Semiconductor | GT23SC6699 [45] | NA | 3.2 | 14443A |
| Silicon Craft | SIC4310 [46] | 10 | 3.3 | 14443A |
| | SIC4340 [47] | 10 | 3.3 | 14443A |
| | SIC4341 [48] | 10 | 3.3 | 14443A |
| AMS AG | AS3953 [49] | 5 | 2 | 14443A |
| | SL13 [50] | 4 | 3.4 | 15693 |
| Melexis | MLX90129 [51] | 5 | 3 | 15693 |
| Texas Instruments | RF430FRL152H [52] | NA | 3 | 15693 |

In order to choose the most suitable NFC chips for the tags designed in this thesis, 3 different models of NFC IC transponders with energy harvesting (EH) capability have been analysed: 2 chips from ST microelectronics (ST25DV04k [41] and M24LR04E [41], both based on NFC Forum type tag 5, NFC-V, ISO/IEC 15693) and other from NXP semiconductors (NT3H1101 [43], Type tag 2, NFC-A, ISO/IEC 14443A). From now on, in this Thesis, these chips are referenced as ST25, M24, and NT3H on this thesis. In order to compare the 3 ICs, the have been integrated in the same tag (see Figure 2.33). The used design has a 50 mm × 50 mm square loop antenna printed on a FR4 PCB with a thickness of 0.8 mm and metallization thickness of 34 µm. In total there are six loops, with a width of 0.7 mm each one,

with 1 mm gap. In all the cases the NFC IC is connected through $I^2C$ bus to a ATtiny85 microcontroller [53] programmed with the same code consisting in a counting loop with the purpose of having the same exact load.

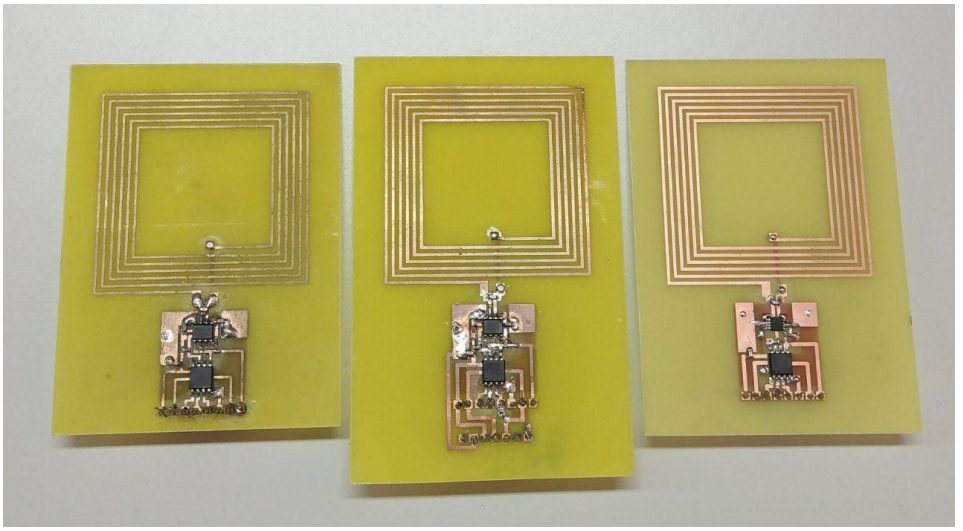

Figure 2.33. Same tag with 3 different chips. M24 (left), ST25 (centre) and NT3H (right)

To measure the performance of each chip, the RMS voltage at the antenna terminals ($V_{ant}$), and the rectified voltage from the RF signal ($V_{DD}$) have been measured respect to the distance between reader and tag with an oscilloscope using a low capacitance probe. Figure 2.34 shows these two parameters for each of the ICs. Measurements have been carried out with two different smartphones, a Xiaomi Mi Note 2 (Figure 2.34(a)) and a BQ Aquarius V (Figure 2.34). Since each manufacturer uses different antenna parameters and different ICs as a transceiver, the power emitted by the reader, the coupling between reader and tag, and the magnetic field received change between them. Hence the importance of measuring the parameters using different smartphones as interrogator.

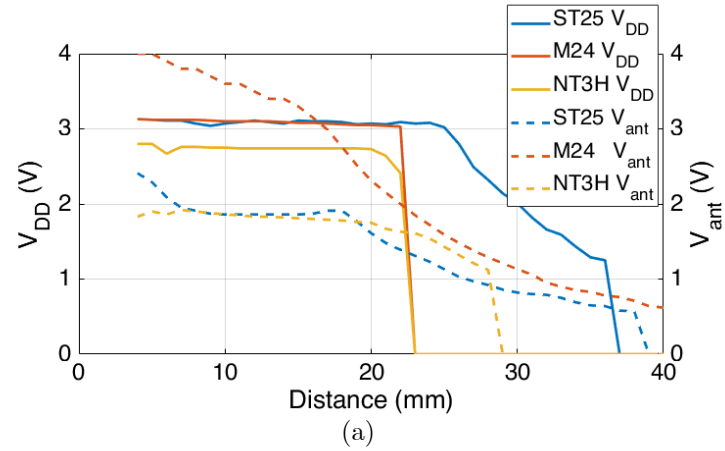


(a)

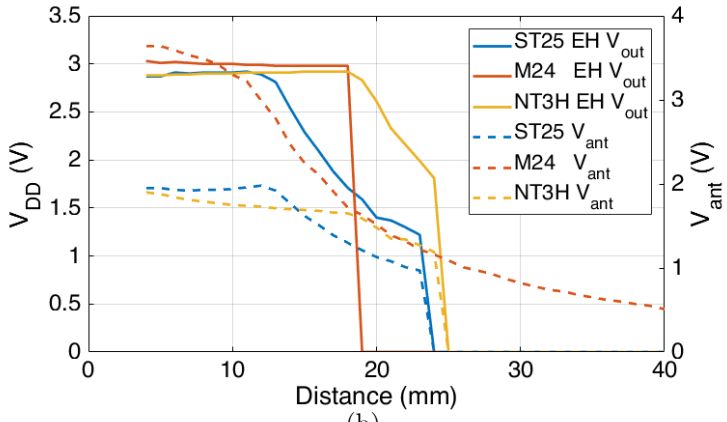


(b)

Figure 2.34. Rectified energy harvesting output of the chip ($V_{DD}$, continuous line) and voltage at the antenna terminals ($V_{ant}$, dashed line) for different distances. Measured with two different smartphones: (a) Xiaomi mi Note 2 and (b) BQ Aquarius V.

As can be seen from de $V_{DD}$ (continuous line),the ST25 has a longer range, however, after a certain point (25 mm in (a), 13 mm in (b)), the output voltage degrades progressively, whereas in the case of the other two chips an ON-OFF behaviour is observed, going from about 3 V when active to 0 V abruptly. This fact may be a benefit depending on the application. For instance, some types of sensors require a certain voltage to work properly, and a smooth decrease of the $V_{DD}$ (observed in the case of the ST25 on Figure 2.34) may produce a malfunction yielding on an erroneous reading. A steeply decrease to zero of the voltage at the antenna terminals ($V_{ant}$, discontinuous line) is observed, using both readers, with the ST25

and the NT3H. This fact happens due a battery-saver operational mode of the NFC readers, which consists on sending periodical short pulses to detect a tag. If the reader cannot demodulate the answer from the backscattering sidebands of such pulse, the reader stops transmitting, since that means that it does not detect any tag. This discovering pulse is generated each few seconds in order to detect a new tag nearby, and, if detects one, maintains the pulse at the operational frequency, which generates the voltage at the antenna terminals. Figure 2.35 depicts the signals generated by the reader to detect a tag. On the top it is shown how, when no tag is presented, the reader emits every 2 seconds approximately a signal modulated with the different discovery requests of each supported standard. As example, the bottom graphics of Figure 2.35 show the request modulation for NFC-B (ISO/IEC 14443B, bottom-left, using 10% ASK modulation), and for NFC-V (ISO/IEC 15693, bottom-right, using 100% ASK modulation). In the case presented in Figure 2.35 the reader has full NFC capability, therefore, the request messages for NFC-A (ISO/IEC 14443A) and NFC-F (JIS X6319) are present as well within the discovery messages (middle-left image on Figure 2.35). This bunch of requests last for about 50 ms, which include the polling requests of a few milliseconds each, followed by a period of unmodulated carrier to send the energy to the tag while waiting for an answer. Between each try of polling a new tag, the reader generates short signals of the carrier frequency without modulation, shown in the middle-right image in Figure 2.35, of around 125 µs. These signals are required by the standards, and its purpose is to ensure that a listening device (i.e. tag) will be correctly reset by a polling device (i.e. reader) which is emitting worst case residual carrier level.

When the reader does not detect the presence of the tag, keeps sending this bursts of requests, which generates a sporadic voltage at the antenna terminals ($V_{ant}$), but if the answer to the request is not detected by the reader, it will not start sending a constant signal, which would be rectified by the NFC IC to power up the tag. Hence, when the voltage at the antenna terminals ($V_{ant}$) keeps a value higher than zero, the reader is detecting the tag, even though when the magnetic field strength is below the minimum threshold to activate the rectified voltage output of the NFC IC.

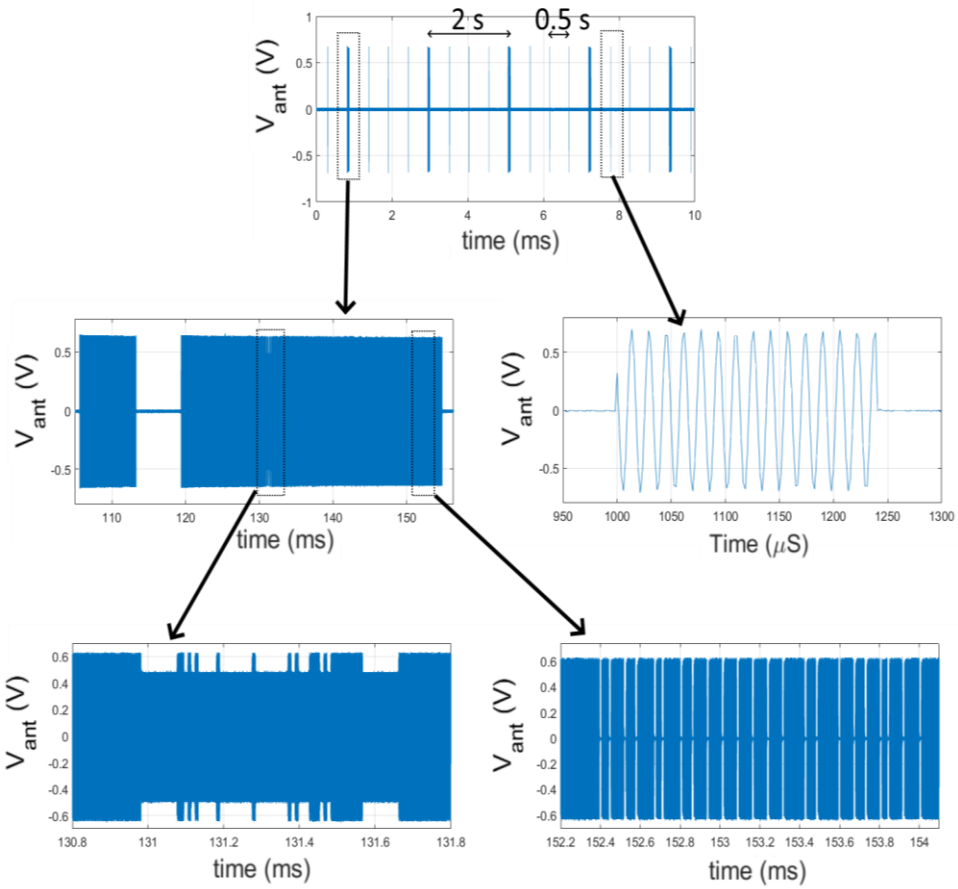


Figure 2.35. Discovery signals sent by the reader when no tag is present.

### 2.5.6.1 Effects of the loads

In order to compare the effect of having different loads connected to the rectified voltage generated by the NFC chip ($V_{DD}$), the tags shown in Figure 2.33 have been modified, removing the MCU and connecting discrete resistances instead. Figure 2.36 shows the measurements obtained for the M24 (Figure 2.36(a)), the ST25 (Figure 2.36(b)), and the NT3H (Figure 2.36(c)). The reader used for these measurements is a Xiaomi Mi Note 2.

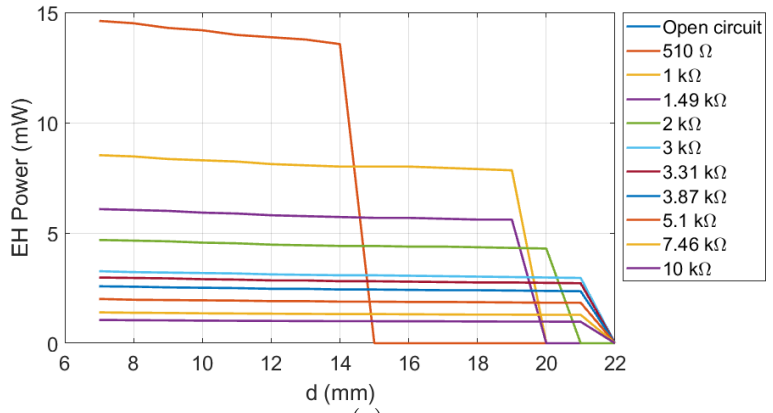


(a)

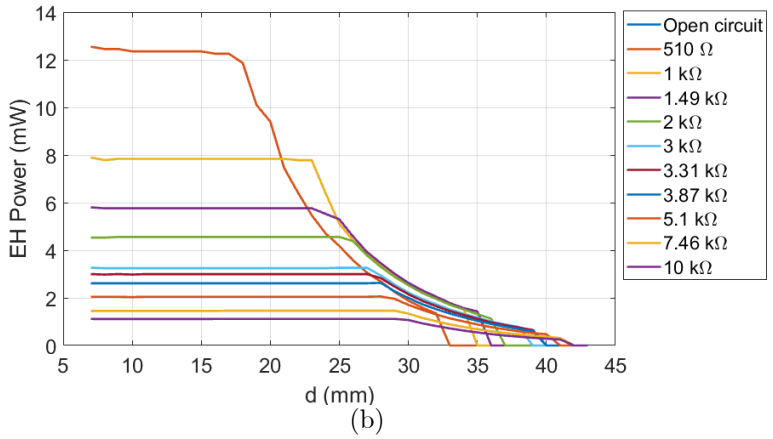


(b)

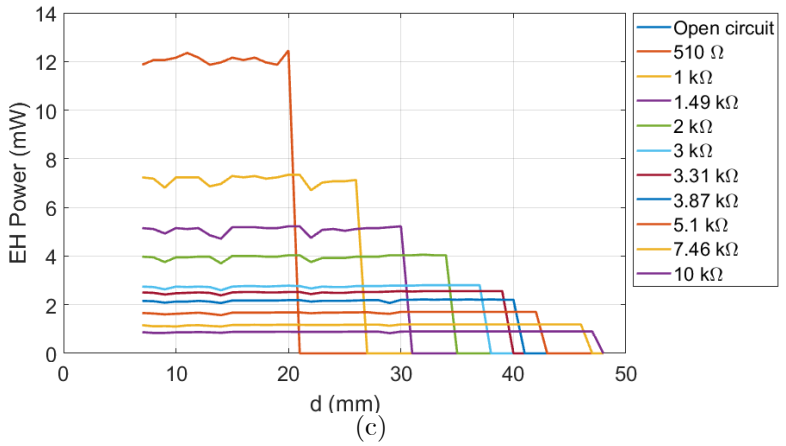


(c)

Figure 2.36. Energy harvesting power for different loads, with different NFC ICs. (a) M24, (b) ST25, and (c) NT3H. All the tags have a 50×50 mm antenna, and a Xiaomi Mi Note 2 used as a reader.

Figure 2.36 shows the dependence of the maximum distance at which the NFC ICs can provide constant power on the load connected. The lower the load, the lower is the maximum distance and the supplied power. Considering the lowest load on this setup (510 Ω), the M24 can provide around 14 mW for distances up to 14 mm, the ST25 12 mW up to 18 mm, and the NT3H 12 mW up to 20 mm. On the other hand, when connecting a 10 kΩ load, the M24 gives 1 mW up to 21 mm, the ST25 1.07 mW up to 30 mm, and the NT3H 0.9 mW up to 47 mm. Figure 2.37 shows the supplied power depending on the load connected, for a distance of 14 mm between reader and tag. It can be observed how the power decreases abruptly for loads between 0.5 kΩ and 2 kΩ, going from around 12 mW at 500 Ω, to 4 mW at 2 kΩ.

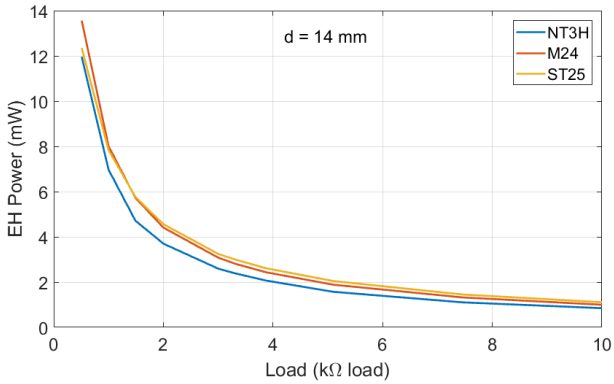


Figure 2.37. Power at the rectified output for the M24, the ST25 and the NT3H chips depending on the connected load at 14 mm between reader and tag.

As can be seen, the power supplied by the chips is almost constant until certain point where it drops to zero. The maximum distance at which the chips can supply certain current is shown in Figure 2.38. It can be seen how the NT3H has longer range for supplying the same current than the other two chips, and it's the most distant-dependent since from 5 mA to 0.3 mA it has 27 cm of difference (from 20 to 47 cm), whereas the ST25 has 12 mm difference (from 17 to 29 mm), and the M24 7 mm (from 14 to 21 mm).

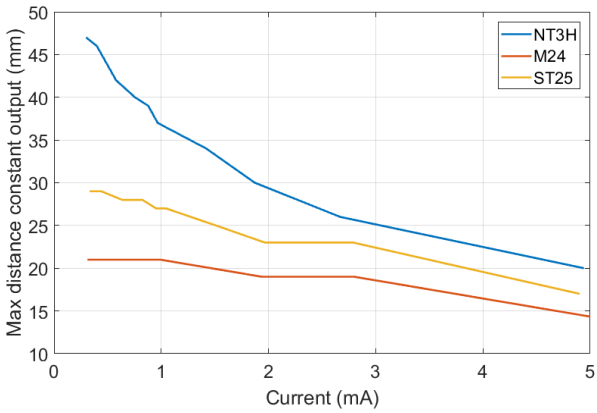


Figure 2.38. Maximum distance at which the NFC ICs can supply constant current for different loads for the NT3H (blue), the M24 (red), and the ST25 (yellow).

### 2.5.7 Antenna dimension

As mentioned previously, NFC has a wide range of possible applications. In some of those applications, the size of the tag does not matter, but in others the size is essential (e.g. implantable tags). Hence the importance of evaluating the differences between using a large or small antenna. For this study two antennas are compared. The first is a 50×50 mm coil (Figure 2.39(a)), and the second is a 15×15 mm coil (Figure 2.39(b)), both with 6 turns.

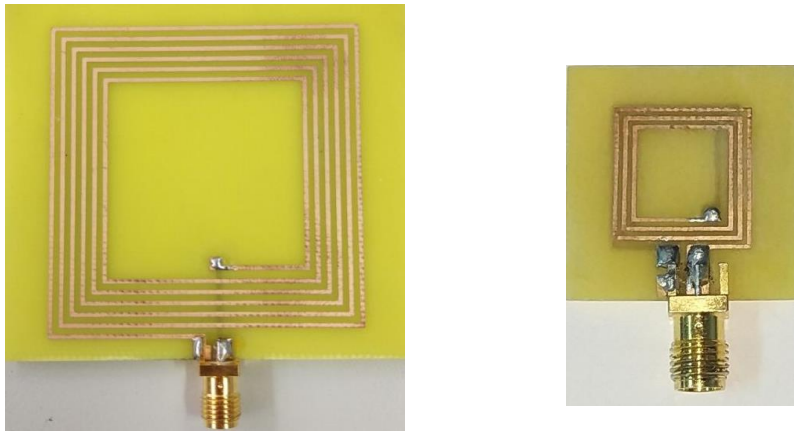

(a) (b)

Figure 2.39. (a) Coil 50×50 mm, 6 loops printed in one side and (b) coil 15×15 mm 6 loops, double-sided.

Figure 2.40 plots the power and the average magnetic field received at these antennas using a Xiaomi Mi Note 2 as an interrogator. The power is slightly higher in the case of the larger antenna because its size is closer to the reader antenna size, situation that optimises the received power. On the other hand, the average magnetic field is higher for the smallest one, since, as explained in section 2.4.5, the received magnetic field ($H_{AV}$) depends on the antenna factor ($AF$), and the $AF$ (defined in equation (2.19)) increases when the area of the antenna ($A$) decreases.

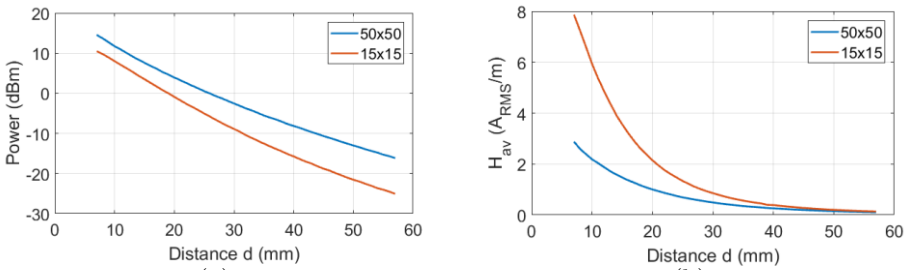


(a) (b)

Figure 2.40. Comparison of (a) power and (b) magnetic field received by a 50×50 mm coil (blue line) and a 15×15 mm coil (red line).

To compare the effects of the antenna size for the three NFC ICs analysed in the previous section, the same three tags have been built with the smaller antenna (see Figure 2.41).

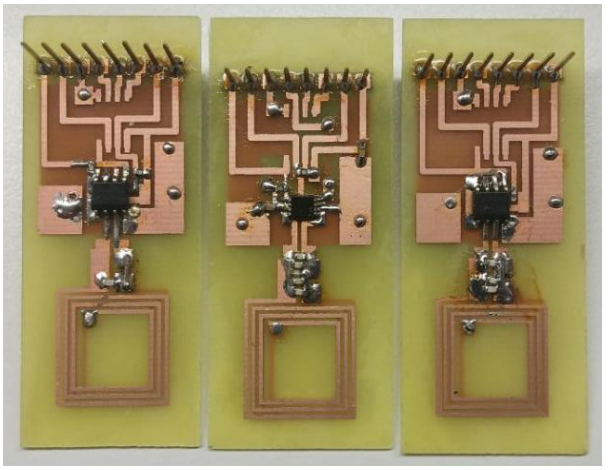

Figure 2.41. Same tag with 3 different chips. M24 (left), NT3H (centre) and ST25 (right) with a 15×15 mm antenna.

Each tag consists of the antenna connected to the NFC chip, with a 3 kΩ resistor as a load, which leads to 1 mA, approximately. Figure 2.42 displays the measured voltage at the load for each tag, using a Xioami Mi Note 2 as a reader. The results show how the M24 (red) and the ST25 (orange) have almost the same behaviour with the two antennas, however, the NT3H reduces its range 1 cm (from 38 mm to 28 mm) when using the smaller antenna.

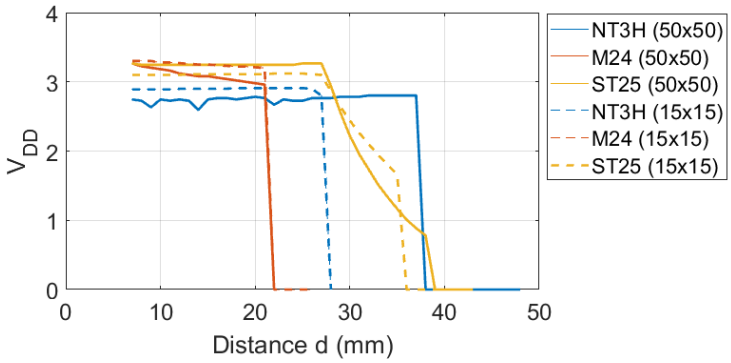


Figure 2.42. Measured voltage ($V_{DD}$) for three different chips (NT3H blue, M24 red, and ST25 orange), with a 50×50 antenna (continuous line) and a 15×15 mm antenna (dashed line), with a 3 kΩ load.

The maximum distance at which the energy harvesting is activated is obtained from the measurements shown in Figure 2.42. With those distances, and using the measurements shown in Figure 2.40(b), and taking into account the calculations explained in section 2.5.4, the $H_{min}$ for each case can be estimated. The relationship between the $H_{min}$ of two antennas can be deduced from equation (2.33) by:

$$\frac{H_{min}{}'}{H_{min}} = \frac{(L_2{}'/A'N')}{(L_2/AN)} \tag{2.34}$$

where $H_{min}$ and $H_{min}$‘ represent the magnetic field threshold to activate the energy harvesting output of the compared antennas. Using the values of each antenna, summarised in Table 2.V, the expected ratio between the $H_{min}$ of these two antennas is around 2.7. However, this is a theoretical value, and the real measurements give ratios of 2.1 for the M24, 1.8 for the ST25 and 3.7 for the NT3H. This difference between the theoretical and measured values may be caused for several reasons. The miss-alignment between coils during

the experimental measurements could lead to a mismatch between the $H_{av}$ measured with the test coil and the $H_{av}$ received by the tag. Even though $f_r$ has been carefully adjusted using the VNA, a possible factor that could induce this difference between the theoretical and the measured value is the antenna tuning, since equation (2.34) assumes that the resonance frequency ($f_r$) is equal to the operational frequency ($f_0$).

Table 2.V. Coils comparison with three different chips

| | Coil 50×50 | | | Coil 15×15 | | |
|---|---|---|---|---|---|---|
| | M24 | ST25 | NT3H | M24 | ST25 | NT3H |
| Area ($A$, mm$^2$) | 50 | | | 15 | | |
| Turns ($N$) | 6 | | | 6 | | |
| Inductance ($L$, µH) | 2.74 | | | 0.683 | | |
| Minimum magnetic field ($Hmin$, $A_{RMS}$/m) | 0.93 | 0.6 | 0.31 | 1.94 | 1.1 | 1.22 |

## 2.6 Conclusions

This chapter has presented the parameters to consider when designing NFC devices with energy harvesting capability. The main concerns regarding both, communication and power transfer have been addressed. While most of the WPT systems focus on the efficiency, NFC must ensure also the data transfer. On the other hand, since this technology is implemented in a huge variety of devices, general solutions should be studied and applied. Besides the fact that the size and number of turns of the antenna coils are basic parameters to increase the coupling, efficiency and the average magnetic field received, the use of small devices require the implementation of small antennas, thus, the importance of studying the performance of such small antennas. Three different NFC ICs have been analysed, with different antenna sizes and the effect of having different loads has been presented, studying the relationship between the supplied power and the maximum distance at which the chips are still able to provide a rectified voltage.

The environmental effects are another issue considered in this chapter. The main problem found is due the presence of metal near the antenna. Its effects have been demonstrated and a solution using high permeability materials like ferrite exposed. The placement of tags close to the body has been introduced as well. NFC is a

promising technology for implantable and other medical sensors, since thanks to the energy harvesting capability, batteries can be avoided, thus removing the principal toxic element of electronic circuits.

## 2.7 Bibliography

[1] J. Z. Buchwald, *The Creation of Scientific Effects: Heinrich Hertz and Electric Waves*. University of Chicago Press, 1994.

[2] "Making Your Imagination Work for You | Tesla Universe." [Online]. Available: https://teslauniverse.com/nikola-tesla/articles/making-your-imagination-work-you. [Accessed: 08-Nov-2019].

[3] W. C. Brown, "The History of Power Transmission by Radio Waves," *IEEE Trans. Microw. Theory Tech.*, vol. 32, no. 9, pp. 1230–1242, Sep. 1984.

[4] W. C. Brown, "The history of wireless power transmission," *Sol. Energy*, vol. 56, no. 1, pp. 3–21, 1996.

[5] N. Shinohara, "The wireless power transmission: Inductive coupling, radio wave, and resonance coupling," *Wiley Interdiscip. Rev. Energy Environ.*, vol. 1, no. 3, pp. 337–346, 2012.

[6] F. C. Flack, E. D. James, and D. M. Schlapp, "Mutual inductance of air-cored coils: Effect on design of radio-frequency coupled implants," *Med. Biol. Eng.*, vol. 9, no. 2, pp. 79–85, 1971.

[7] T. Akin, K. Najafi, and R. M. Bradley, "A wireless implantable multichannel digital neural recording system for a micromachined sieve electrode," *IEEE J. Solid-State Circuits*, vol. 33, no. 1, pp. 109–118, 1998.

[8] L. Peng, O. Breinbjerg, and N. A. Mortensen, "Wireless energy transfer through non-resonant magnetic coupling," *J. Electromagn. Waves Appl.*, vol. 24, no. 11–12, pp. 1587–1598,

2010.

[9] S. B. Cohn, "Parallel-Coupled Transmission-Line-Resonator Filters," *IEEE Trans. Microw. Theory Tech.*, vol. 6, no. 2, pp. 223–231, Apr. 1958.

[10] J. García-García *et al.*, "Spurious passband suppression in microstrip coupled line band pass filters by means of split ring resonators," *IEEE Microw. Wirel. Components Lett.*, vol. 14, no. 9, pp. 416–418, 2004.

[11] A. Kurs, A. Karalis, R. Moffatt, J. D. Joannopoulos, P. Fisher, and M. Soljacic, "Wireless power transfer via strongly coupled magnetic resonances," *Sicnece*, vol. 317, no. 5834, p. 83(4), 2007.

[12] X. Wei, Z. Wang, and H. Dai, "A critical review of wireless power transfer via strongly coupled magnetic resonances," *Energies*, vol. 7, no. 7, pp. 4316–4341, 2014.

[13] N. Shinohara, *Wireless Power Transfer via Radiowave*. Wiley-ISTE, 2014.

[14] K. Y. Kim, *Wireless Power Transfer - Principles and Engineering Explorations*. 2012.

[15] R. E. Hamam, A. Karalis, J. D. Joannopoulos, and M. Soljačić, "Coupled-mode theory for general free-space resonant scattering of waves," *Phys. Rev. A - At. Mol. Opt. Phys.*, vol. 75, no. 5, pp. 1–5, 2007.

[16] Dominique Paret, *Antenna Designs for NFC Devices*. 2016.

[17] Bing Jiang, J. R. Smith, M. Philipose, S. Roy, K. Sundara-Rajan, and A. V. Mamishev, "Energy Scavenging for Inductively Coupled Passive RFID Systems," *2005 IEEE Instrumentationand Meas. Technol. Conf. Proc.*, vol. 2, no. May, pp. 984–989, 2005.

[18] C. Marechal and D. Paret, "The loading effect of proximity

contactless smart card. Incidences of impedance of the shunt regulator," *2008 Int. Conf. Wirel. Commun. Netw. Mob. Comput. WiCOM 2008*, pp. 8–11, 2008.

[19] NXP Semiconductors, "PN7120 - NFC controller with integrated firmware, supporting all NFC Forum modes," *Datasheet*, 2018.

[20] Texas Instruments, "TRF7970A Multiprotocol Fully Integrated 13 . 56-MHz RFID and Near Field Communication ( NFC ) Transceiver IC," *Datasheet*. 2014.

[21] N. Gvozdenovic, L. W. Mayer, and C. F. Mecklenbrauker, "Measurement of harmonic distortions and impedance of HF RFID chips," in *8th European Conference on Antennas and Propagation, EuCAP 2014*, 2014, pp. 2940–2944.

[22] M. Gebhart, J. Bruckbauer, and M. Gossar, "Chip impedance characterization for contactless proximity personal cards," in *2010 7th International Symposium on Communication Systems, Networks and Digital Signal Processing, CSNDSP 2010*, 2010, pp. 826–830.

[23] C. H. Lu, J. A. Li, and T. H. Lin, "A 13.56-MHz passive NFC tag IC in 0.18-μm CMOS process for biomedical applications," *2016 Int. Symp. VLSI Des. Autom. Test, VLSI-DAT 2016*, pp. 7–10, 2016.

[24] B. Jamali, D. C. Ranasinghe, and P. H. Cole, "Analysis of UHF RFID CMOS rectifier structures and input impedance characteristics," *Microelectron. Des. Technol. Packag. II*, vol. 6035, no. January 2006, p. 60350D, 2005.

[25] J. Teichmann, K. Burger, W. Hasche, J. Herrfurth, and G. Täschner, "One time programming (OTP) with Zener diodes in CMOS processes," in *European Solid-State Device Research Conference*, 2003, pp. 433–436.

[26] Z. Zhu, "RFID analog front end design tutorial," *Auto-ID lab*

*Univ. Adelaide*, pp. 3–34, 2004.

[27] J. Hu, S. Wu, K. Lin, and H. Tan, "Low-power energy supply circuit for passive RFID transponder," *2009 IEEE Int. Conf. RFID, RFID 2009*, no. 2008, pp. 1–6, 2009.

[28] F. Alcalde, O. Alpago, and J. Lipovetsky, "CMOS design of an RFID interface compatible with ISO/IEC-14443 type a protocol," *Proc. 2014 Argentine Sch. Micro-Nanoelectronics, Technol. Appl. EAMTA 2014*, pp. 41–47, 2014.

[29] H. Jianguo, T. Hongzhou, and X. Yongjian, "A novel design of low power RFID tag interface circuit," *IET Conf. Publ.*, no. 533 CP, pp. 478–481, 2007.

[30] R. Jacobi and E. LaCost, "Antenna Design Guide for the TRF79xxA Application Report," 2017.

[31] NXP Semiconductors, "PN5180 Antenna design guide," no. June. 2018.

[32] NXP Semiconductors, "PN7150 Antenna Design and Matching Guide," no. July, 2019.

[33] M. Ishii and K. Komiyama, "A Measurement Method for the Antenna Factor of Small Loop Antenna by Measuring the Input Impedance," in *2004 Conference on Precision Electromagnetic Measurements*, 2004, pp. 80–81.

[34] M. Zargham and P. G. Gulak, "Maximum Achievable Efficiency in Near-Field Coupled Power-Transfer Systems," *IEEE Trans. Biomed. Circuits Syst.*, vol. 6, no. 3, pp. 228–245, Jun. 2012.

[35] C. M. Zierhofer and E. S. Hochmair, "Geometric approach for coupling enhancement of magnetically coupled coils," *IEEE Trans. Biomed. Eng.*, vol. 43, no. 7, pp. 708–714, 1996.

[36] A. Lazaro, R. Villarino, and D. Girbau, "A survey of NFC sensors based on energy harvesting for IoT applications,"

*Sensors (Switzerland)*, vol. 18, no. 11, p. 3746, Nov. 2018.

[37] M. Gebhart, "Analytical considerations for an ISO / IEC14443 compliant SmartCard transponder," *Proc. 11th Int. Conf. Telecommun.*, pp. 9–16.

[38] S. Y. Huang, "The effects of ground planes in modern electromagnetic applications," Nanyang Technological University, 2010.

[39] R. C. ULTRALAM® 3000 Liquid Crystalline Polymer Circuit Material Double-Clad Laminates, "Ultralam datasheet.pdf." .

[40] M. Boada, A. Lazaro, R. Villarino, E. Gil, and D. Girbau, "Near-Field Soil Moisture Sensor with Energy Harvesting Capability," in *2018 48th European Microwave Conference, EuMC 2018*, 2018, pp. 235–238.

[41] ST Microelectronics, "M24LRxxx - Dynamic NFC/RFID tag IC." 2017.

[42] ST, "ST25DVxxx," no. October. 2017.

[43] NXP Semiconductors, "NT3H1101/NT3H1201 - NTAG I2C." 2015.

[44] EM Microelectronics, "NF4 - NFC Forum Type 4 Dual Interface." 2014.

[45] Giantec Semiconductor, "GT23SC6699-1/2 NFC Type 2." 2011.

[46] Silicon Craft, "SIC4310 RFIC/NFC Tag IC with UART interface." 2014.

[47] Silicon Craft, "SIC4340." [Online]. Available: http://www.sic.co.th/product.php?product=158&category=6&name=SIC4340. [Accessed: 28-Nov-2019].

[48] Silicon Craft, "SIC4341." [Online]. Available: http://www.sic.co.th/product.php?product=159&category=6

&name=SIC4341. [Accessed: 28-Nov-2019].

[49] AMS, "AS3953 - 14443 High Speed Passive Tag Interface." 2013.

[50] AMS, "SL13A - Smart Sensory Tag Chip For Unique." 2014.

[51] MELEXIS, "MLX90129 - 13.56MHz sensor tag / datalogger." 2012.

[52] Texas Instruments, "RF430FRL15xH NFC ISO 15693 Sensor Transponder." 2014.

[53] Atmel, "ATTiny - MCU ARM 8 bit AVR RISC ATTiny85 ATTiny45 ATTiny25," 2014.

# 3. Soil Moisture Sensor

## 3.1 Motivation

Soil moisture measurement is a key aid for irrigation water management. Regulating irrigation is crucial to satisfy the water requirement of crops without wasting water, to treat the soil correctly, and to control the plant nutrients in order to save energy. Most sophisticated systems are automated using climate-based electronic controllers whereas the simplest ones repeat a set of scheduled tasks as function of time. Low-cost monitoring systems are demanded for personal use at home or to monitor a crop, as for example in a greenhouse or plants shop. In these cases, irrigation is often manual or semiautomatic and the conditions are usually specific for each crop. Therefore, the control of the soil moisture must be considered for an appropriated plant care. There are several soil moisture measurement techniques [1] but most of them are not suitable for amateur or low-cost applications. Most typical portable low-cost meters use a sensor connected to the analog-to-digital converter (ADC) of a microcontroller, which translates a physical value to the corresponding magnitude. The result is often shown in a display or acquired by an external data logger. In all the cases these methods use a battery to supply energy to the electronic components.

Several wireless soil moisture sensors can be found on the literature [2], [3]. However, those sensors require an expensive reader (in the case of RFID systems), or batteries and expensive chips in the case of Bluetooth. NFC has as an advantage in its price (less than 1 euro per NFC IC), and the possibility to use any conventional smartphone as reader, which can upload the sensed data to the cloud. The limitation is in the readout range (few centimetres), a characteristic that defines a frame of applications and usages where NFC is very attractive and define the areas where this technology is restricted.

This chapter proposes a soil moisture sensor embedded in a passive NFC-based tag, which powers up the electronics harvesting the energy provided by the reader. The data obtained can be stored into an Internet of Things (IoT) database to be used to program the irrigation schedule and to keep track of the soil conditions. On the other hand, no additional cost for the reader is required since it is a

commercial. The tag also integrates ambient temperature and humidity sensors to complement the information of the environment since these parameters may affect the irrigation schedule. The tags can be installed in several points for individual monitoring thanks to its low cost. In addition to the sensed data, an identification tag number is written into the NFC chip which can be related to information about the plant (name, origin, brief description, specific cares) which can be retrieved by the reader and displayed in a custom app.

This chapter is organized as follows, Section 3.2 provides a review of available soil measurement systems in the literature and the justification of the selection of a capacitive soil measurement for the proposed application. Section 3.3 describes the proposed system, including the part of the tag and the part of the reader. Section 3.4 presents a calibration method and measurements. Finally, section 3.5 summarise the conclusions of the chapter.

## 3.2 Soil moisture measurement techniques

The soil moisture content is often expressed as the Volumetric Water Content (VWC), defined as the volume of water over the total volume, as it is shown in the example of Figure 3.1.

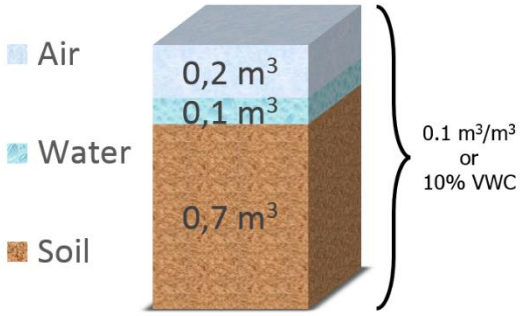


Figure 3.1. Representation of 1 m3 separated into constituent parts where 70% of the total volume is the soil, 10% is water and 20% is air.

Within the bunch of existing techniques to measure soil moisture content there are direct and indirect methods. The most known

direct method is the thermo-gravimetric [1], which is usually used as a standard reference. However, it requires at least one day to get the result and it cannot be performed *in situ*. This method is therefore used for calibration of other sensors in laboratories. On the other hand, there are several indirect techniques [4]. The most common ones are listed below.

Neutron Moisture Meters (NMM) have a large action radius and are insensitive to temperature and salinity. However, it is an expensive method which requires a certification for radiation [5]. Therefore, it can be used on research, but it is not suitable for personal use.

Thermal sensors take advantage of the difference of heat conductance between soil and water. They measure the change on temperature of the surround soil after applying a heat pulse [6]. This type of sensors is inexpensive and easy to use but they are very dependent on the soil temperature, they present a long integration time and they are fragile since the distance between the heater and the thermocouple must be kept.

Electrical resistance blocks or gypsum blocks [7] are made with gypsum around a pair of stainless-steel wires. Most of the probes are based on the measurement of their electrical resistance. Portable probes are available and can be placed in the soil to give the water proportion reading. The main limitation of this approach is the calibration of the probe due to the potential corrosion of the wires with the accumulation of mineral salts.

Besides the above techniques, there are other methods which make use of the dielectric property of the soil to measure its moisture content. These methods are based on the huge difference of the dielectric constant of dry soil (between 3 and 7), and pure water (about 80). Within these dielectric techniques, Time Domain Reflectometry (TDR) is one of the most common [8][9]. It consists of sending electromagnetic pulses along two wave guides of a well-known length and measuring the time delay between the incident and reflected waves. The time delay changes according to the dielectric constant of the soil where they are sunk. However, TDR systems are expensive for domestic applications or when several measuring points need to be monitored, which requires multiplexers to share the readout unit [10].

Still within the dielectric techniques, there are the Frequency Domain Reflectometry (FDR) [10] and capacitive techniques [11], both based on the same working principle. In the case of FDR, the dielectric constant of the soil is determined by applying an oscillating charge to the circuit and measuring its resonant frequency to detect variations on the soil's capacitance [12][13]. The main drawback of this technique is that measuring the resonant frequency requires expensive impedance meters. On the other hand, capacitive methods measure directly the capacitance, usually from the charge time of the capacitor. Since these types of sensors are AC excited and the probe can be covered by a protective layer [14], they are not affected by corrosion. Nonetheless, capacitive measurements often require additional signal conditioning for the measurement with a microcontroller, whereas resistive sensors do not.

Despite the foregoing, a capacitive sensor is the one which better fits with the NFC scenario because printed capacitive sensors for soil measurements are compatible with standard PCB technology used for the design of the coil and integrate the electronics of the NFC sensor. In addition, it is not affected by corrosion issues. A critical point for using this kind of sensor is finding a precise capacitance measurement method compatible with the power available from the RF harvesting.

## 3.3 System description

### 3.3.1 System overview

Figure 3.2 depicts the system proposed in this work. It is composed by an NFC antenna which is connected to the NFC/RFID IC M24LR04E-R [15] (M24), from ST Microelectronics, responsible of receiving and sending NFC Data Exchange Format (NDEF) messages. This device presents the specifications required for this work such as $I^2C$ interface, energy harvesting with 4 configurable currents, and ISO 15693 compatibility. When a magnetic field from a reader is received by the antenna, the NFC IC wakes up automatically. If the energy harvesting mode is activated and the strength of the magnetic field is enough (higher than a threshold that depends on the energy harvesting configuration of the chip) the M24 gets the excess of energy received from the RF field to feed all the

components of the system. This chip is capable to provide currents up to 6 mA in the highest current sink mode.

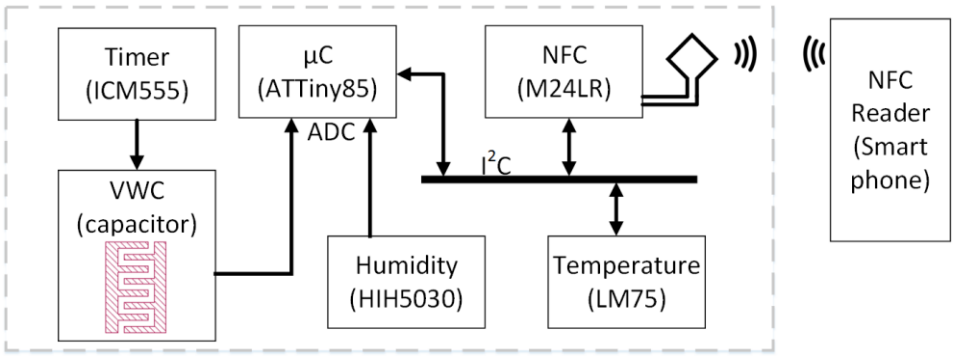


Figure 3.2. System overview.

The antenna is a square loop of 50 mm × 50 mm printed on FR4 PCB. There is a total of 6 loops whose width is 0.6 mm. It is designed with Keysight Momentum electromagnetic simulator. The measured inductance is 3.2 µH in agreement with the simulations. A tuning capacitance of 15 pF is added to the internal capacitance of the IC (27.5 pF) to adjust the resonance at 13.56 MHz.

A low-power Atmel 8-bit AVR ATtiny85 microcontroller [16] has been selected to be integrated in the prototype. It can be configured at different clock speeds and can work down to 1.8V, reducing the clock frequency. Due to the power limitations presented by this system, it has been configured to work at 1 MHz, being its consumption around 300 µA at 3.3V. In addition, it can be programmed with Arduino IDE, which is very popular in open-hardware implementations. This microcontroller has an I²C interface and 2 analog inputs. In order to provide more information to the user, the system also includes a humidity sensor, which is connected to an analog input of the microcontroller, and a temperature sensor, which is used to adjust the moisture sensor curve. The temperature sensor is a low-cost I²C sensor LM75A [17], which consumes less than 280 µA in active mode and 4 µA in sleep mode (at 3V). It is an industry-standard digital temperature sensor with an integrated sigma-delta 9-bit resolution ADC, enough for the proposed application. The temperature accuracy is about 1 ºC from -25ºC to 100ºC. The HIH-5030 [18] is a low-voltage humidity sensor that

operates down to 2.7 V, with a typical current consumption of only 200 µA. This humidity sensor presents a linear output voltage related to the relative humidity. However, an improved readout can be used if the temperature is known.

The technique used for the measurement of soil water content, as it is described below, uses an ICM555 timer oscillator, which is a low-voltage and low-power version of the popular 555 timer, which consumes typical currents of 60 µA at 3V and yields a stable frequency output.

Table 3.I summarizes the current consumption of the different electronic modules integrated in the tag. The energy harvesting needed is in the order of 1.2 mA at 3 V to power the overall system.

Table 3.I. Current consumption

| Element | Consumption (µA) |
|---|---|
| NFC (*M24*) | 400 |
| µC *(ATtiny85)* | 300 |
| Humidity *(HIH5030)* | 200 |
| Temperature *(LM75)* | 280 |
| Timer (*ICM555*) | 60 |

### 3.3.2 Volumetric water content measurement

Following the discussion of section 3.2, there are several methods to measure the Volumetric Water Content of the soil. The approach presented in this work is based on an interdigital capacitor which is sunk in the soil. The dielectric permittivity of the soil depends largely on the changes of the water volume content. Keeping the strip-lines of the interdigital capacitor in contact with the soil allows to measure the dielectric permittivity changes, and then retrieve the soil's VWC.

#### 3.3.2.1 Capacitor

The capacitive sensor is implemented using an interdigital capacitor (IDC) without ground plane (see Figure 3.3). Although various technologies can be used to realize these type of sensors, printed circuit board technology is particularly advantageous. The prototype of capacitive sensor has been fabricated using standard Fiber-Glass substrate (FR4) with 34 µm of copper metallization. An insulator layer is added to prevent that electrodes can be shorted in presence

of water. Solder mask coating or a thin protection layer of plastic (this latter in the prototypes) can be used as insulator. Fig. 3 shows the shape of an interdigital capacitor indicating the different parameters that influence on its capacitance, which depends on length $L$, gap distance between two conductors $g$, finger width $s$, as well as the number of fingers $N$.

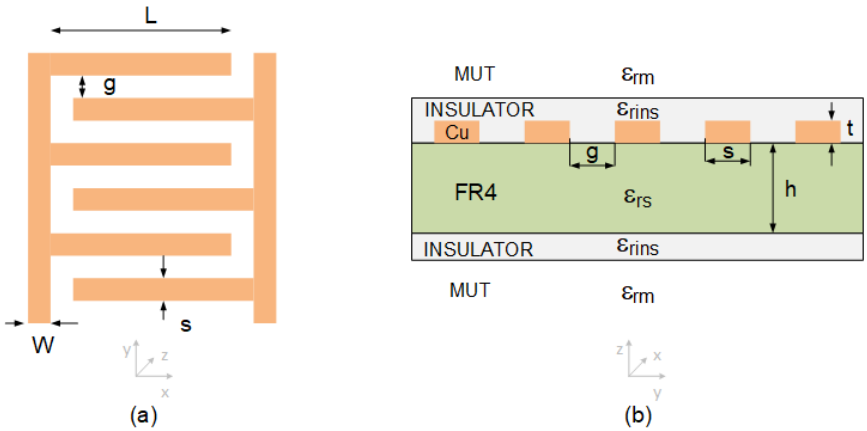


Figure 3.3. (a) Top view of an interdigital capacitor. (b) Cross section view of the interdigital capacitor.

Closed-form expressions for multilayer interdigital capacitors have been proposed in the literature [19]. The capacitance can be expressed as the sum of three contributions:

$$C = C_3 + C_n + C_{end} \tag{3.1}$$

Where $C_3$, $C_n$, and $C_{end}$ represent the three-finger capacitance, the capacitance of the periodical (N-3) structure, and a correction term for the fringing fields of the ends of the strips, respectively. These capacitances are proportional to the effective permittivity and the geometrical factors $a_3$, $a_n$ and $a_{end}$, that are function of the elliptic integrals of the fist kind $K(k)$ resulting of the conforming mapping method [20]:

$$C_3 = \varepsilon_{re3} a_3 L \tag{3.2}$$

$$C_n = \varepsilon_{rn} a_n (N-3) L \tag{3.3}$$

$$C_{end} = \varepsilon_{re,end} a_{end} \tag{3.4}$$

The effective relative permittivity ($\varepsilon_{re,i}$ with i=3, n, end) can be calculated from the filling factor ($q_i$) that is the percentage of fields in each material for each case:

$$\varepsilon_{rei} = \varepsilon_{rm} + q_{1i}\frac{\varepsilon_{rins} - \varepsilon_{rm}}{2} + q_{2i}\frac{\varepsilon_{rS} - \varepsilon_{rins}}{2} + q_{3i}\frac{\varepsilon_{rins} - \varepsilon_{rm}}{2} \tag{3.5}$$

Where $\varepsilon_{rm}$ and $\varepsilon_{rs}$ are the relative permittivity of the medium when the IDC is immersed and of the PCB substrate, respectively. Whereas $\varepsilon_{rins}$ is the permittivity of the insulator layer.

For long fingers (L>>s) the correction for fringing fields at the ends of the fingers can be neglected [19]. Therefore, the capacitance $C$ is mainly proportional to the length and the number of fingers (N). Replacing (3.2-3.4) into (3.1) the linear expression (3.6) for the capacity $C$ as a function of the medium permittivity expression for the IDC capacitance can be found.

$$C = A + B\varepsilon_{rm} \tag{3.6}$$

Where $B$ depends on the geometry, and $A$ depends on the dielectric permittivity of the PCB substrate and insulator. The values $A$ or $B$ can be obtained using closed-form formulas [19] or by simulation using a full-wave simulator.

The electromagnetic simulator Keysight-Momentum is used for the IDC design and evaluation. In order to obtain a value of capacitance easily readable compatible with the minimum gap and trace width achievable with the available PCB fabrication technology. An IDC with N=40, L=30 mm, W=0.8 mm, s=0.8 mm, g=0.5 mm, h=0.8 mm, t=34 µm, $\varepsilon_{rs}$=4.7 has been designed. Two prototypes with two insulator materials and thickness have been manufactured. The first prototype uses an insulator (type 1) that consist of a coating of adhesive plastic ($\varepsilon_{rins}$=2) and with a thickness of 100 µm. In the second prototype, the insulator (type 2) is an acrylic coating spray ($\varepsilon_{rins}$=2.7) with a thickness of about 15 µm.

Figure 3.4 shows a simulation of the IDC capacitance as a function of the relative permittivity of the immersed material under test (MUT). The thickness of MUT is assumed infinite. A linear

dependence is observed when an ideal IDC without insulator layer is analysed. However, the insulator layer introduces a reduction on the sensitivity of the IDC as a function of the permittivity for values of relative dielectric permittivity higher than 10. In addition, the sensitivity (slope as a function of relative permittivity) is not constant as predicted by the closed-form expressions derived from the partial capacitance method [19]. The smaller capacitance values obtained compared with the case without insulator are explained because the effective permittivity of the insulator layer and MUT is smaller than $\varepsilon_{rm}$. The relation between the effective permittivity and the permittivities of the insulator layer and MUT is not linear like in multilayer microstrip lines [20].

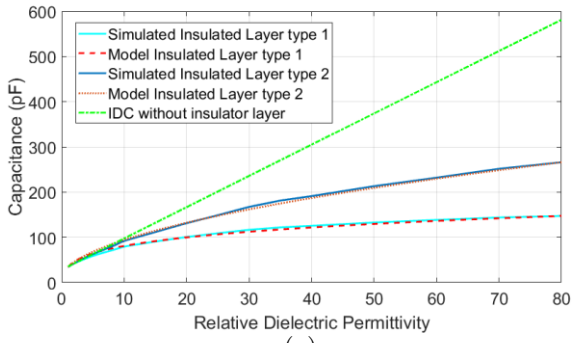


(a)

(b)

Figure 3.4. (a) Simulated and modelled capacitance as a function of the relative dielectric permittivity. Insulator layer type 1 is an adhesive plastic, and type 2 is acrylic coating spray. (b) A photograph of the manufactured IDC.

Figure 3.5 shows a cross-section view of the IDC sensor with the equivalent circuit for low permittivity of the MUT (Figure 3.5 (a)) and for high permittivities (Figure 3.5 (b)). In the first equivalent circuit, the capacitance due to the insulator layer ($C_{INS}$) is in parallel with the capacitance due to the MUT ($C_{MUT}$), whereas in the second, $C_{INS}$ is in series with $C_{MUT}$. The first equivalent circuit is used in the derivation of closed formulas from [19]. In the second circuit, when analysing the fringing electric field path from one electrode to another electrode, it makes more sense that both the capacitance of the insulation layer $C_{INS}$ and the capacitance of MUT $C_{MUT}$ must be connected in series for high dielectric constant values of the MUT [21]. Therefore, it is expected that the effective permittivity and capacitance will be smaller in the second equivalent circuit.

Simulated values of C on Fig. 4 agree with the measured capacitance when the IDC is on air (being air the insulator layer, with $\varepsilon_{rm}$ =1), 23 pF. C also agrees when the IDC is immersed in water ($\varepsilon_{rm}$≈80), C=140 pF, for the first prototype (insulator type 1) and 270 pF for the insulator type 2. In order to interpolate the values of capacitance, a compact expression is proposed:

$$C = C_1 + (C_2 - C_1)\frac{(\epsilon_{rm})^{\gamma} - (\epsilon_{rm1})^{\gamma}}{(\epsilon_{rm2})^{\gamma} - (\epsilon_{rm1})^{\gamma}} \tag{3.7}$$

Where $C_1$ and $C_2$ are the capacitance for two known permittivities, $\varepsilon_{rm1}$=1 (air case) and $\varepsilon_{rm2}$=80 (water case), respectively. The exponent $\gamma$ is a fitting parameter. A value of $\gamma$=0.21 is obtained for the IDC of Figure 3.4.

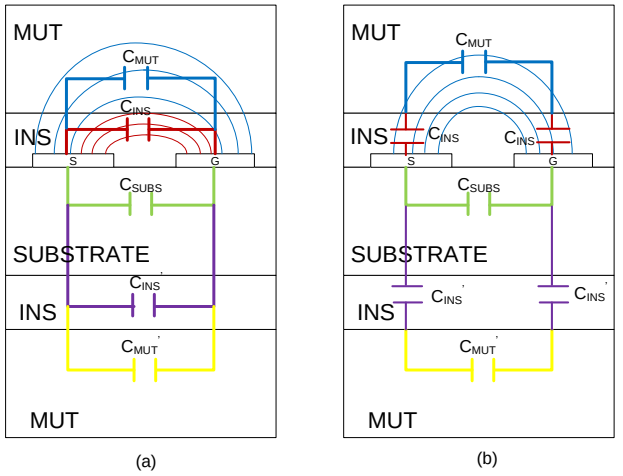


Figure 3.5. (a) Cross-section view of IDC sensor with its superimposed equivalent circuit. For low permittivity of MUT used in partial capacitance technique [19] and (b) proposed equivalent circuit for high permittivity of MUT [21].

### 3.3.2.2 Capacitance measurement

The reduction of clock frequency of the microcontroller to reduce its power consumption introduces some restrictions. In order to decrease the number of components of the tag and reduce, consequently, its cost, the microcontroller clock frequency is fixed using its own internal oscillator. Thus, the precision on capacitance measurement

based on the discharge time of the capacitor is not enough for small capacitances, since when it is in the order of pF, large time constants must be considered. Taking into account that when near field communication is used the power is only available when the reader is close to the tag, a fast measurement method must be applied. A similar problem arises when an oscillator whose frequency depends on the capacitance is used. In this method, the microcontroller works as a frequency counter and the precision depends on the maximum clock frequency. The methodology used in this work to measure the capacitance is shown in Figure 3.6. A custom frequency-to-voltage converter has been designed because the available commercial IC converters require higher currents than the ones available in this system. A low-power timer is used to generate an AC signal, which is filtered by a low-pass filter (RC filter), whose cut off frequency depends on the capacitance under test. The AC amplitude at the output of the filter is measured using a half-wave rectifier used as detector. The DC voltage filtered at the output of the detector is measured with the internal analog-to-digital converter of the microcontroller. Although the output voltage depends on the power supply ($V_{DD}$), thanks to the fact that the microcontroller uses that voltage as a reference, this problem is avoided.

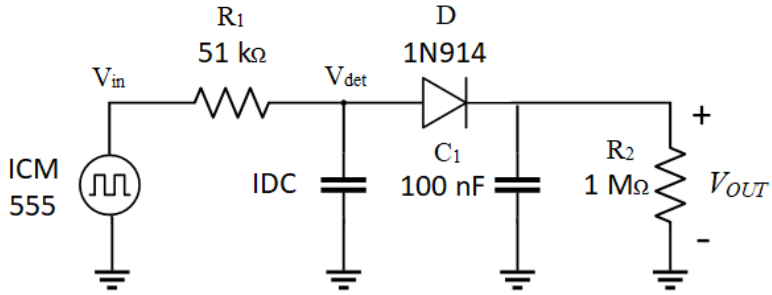


Figure 3.6. Circuit to obtain a voltage proportional the interdigital capacitor (IDC) value.

The proposed solution consists of feeding the circuit with a square wave of 380 kHz into a low-pass filter consisting of a resistor of 10 k**Ω** ($R_1$) and the interdigital capacitor (IDC), whose value varies in the range 55-270 pF. The resulting signal ($V_{det}$, which presents a triangular waveform) is rectified by a diode ($D$). The cathode of the diode is connected to a capacitor (100 nF, $C_1$) and a shunt resistor

(1 MΩ, $R_2$). Hence at the output of the envelope detector $V_{OUT}$ is proportional to the value of the IDC.

The waveform at the output of the 555 timer ($V_{in}$) is a square wave with nearly ideal 50% duty cycle. This periodic signal can be expanded using Fourier series. The higher harmonics are filtered, therefore only the first harmonic is considered. Then the input signal at the filter can be expressed as:

$$V_{in}(t) = \frac{V_{DD}}{2} + \frac{V_{DD}}{\pi}\cos(\omega t) \tag{3.8}$$

Considering $H(j\omega)$ as the transfer function of the low-pass filter defined as:

$$H(j\omega) = \frac{V_{det}}{V_{in}} = \frac{1}{1 + j\omega RC} \tag{3.9}$$

The voltage at its output is given by:

$$V_{det}(t) = \frac{V_{DD}}{2} + \frac{V_{DD}}{\pi}\lfloor H(j\omega)\rfloor \cos(\omega t + \varphi) \tag{3.10}$$

Where $\varphi$ is the phase of the transfer function. Therefore, the output of the half-wave detector is proportional to the average amplitude:

$$V_{OUT} = \frac{V_{DD}}{2} - V_f + k\lfloor H(j\omega)\rfloor V_{DD} \approx \frac{V_{DD}}{2} - V_f + \frac{kV_{DD}}{\omega R}\frac{1}{C} \tag{3.11}$$

Where $k$ is a factor that depends on the waveform at the output of the filter ($V_{det}$, nearly triangular), and $V_f$ is an offset correction that considers the forward voltage of the diode. If the frequency of the oscillator is chosen higher than the cut-off frequency of the filter $f>>1/(2\pi RC)$, the signal at the output of the detector ($V_{out}$) is approximately proportional to the inverse of the capacitance. Figure 3.7 compares the model given by (3.5), the circuit simulations considering a conventional silicon diode (1N914), the measurements with a multimeter, and the measures read by the NFC reader. Assuming a nearly triangular waveform at the filter's output, the value of $k$ is 0.5. The forward correction is obtained empirically, and it is considered $V_f$=0.35 V. Good agreement has been obtained. Different values of 0603 Surface Mount (SMD) capacitors have been

mounted to emulate the IDC and the measurements have been performed both using a multimeter (Agilent 34450) and the analog readout of the microcontroller powered by energy harvesting coming from a smart phone working as reader.

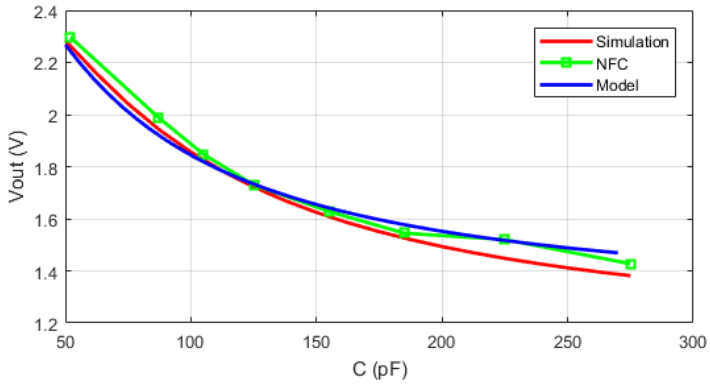


Figure 3.7. Output voltage of the measurement system as a function of the sensor capacitance $C$. Comparison between the model proposed (11), the simulation, and the NFC read using a smartphone.

Performing a sensitivity analysis from the slope of the voltage as a function of the capacitance, the average error obtained from the 10-bits ADC of the microcontroller shown in Figure 3.8 is under 2%, considering the capacitance range (55-270 pF) of the capacitor sensor proposed in this work.

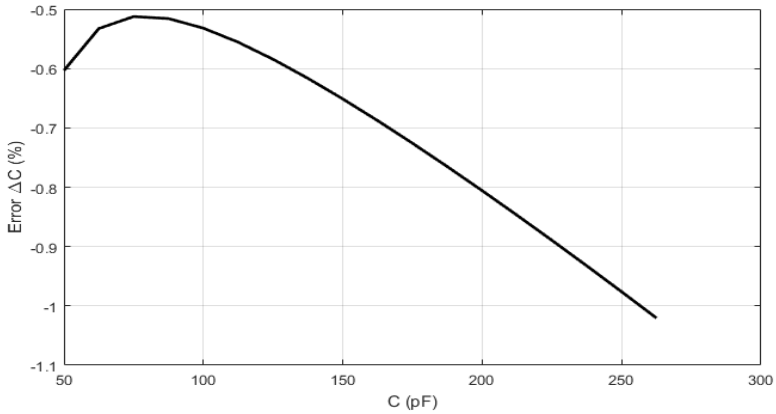


Figure 3.8. Estimated error in the measurement of the capacitance from the analysis of sensitivity.

Figure 3.9 shows the prototype manufactured on a FR4 PCB that consists of an NFC antenna, the chipset with a connector that gives access to the microcontroller in order to program it, and the interdigital capacitor which will be sunk into the soil.

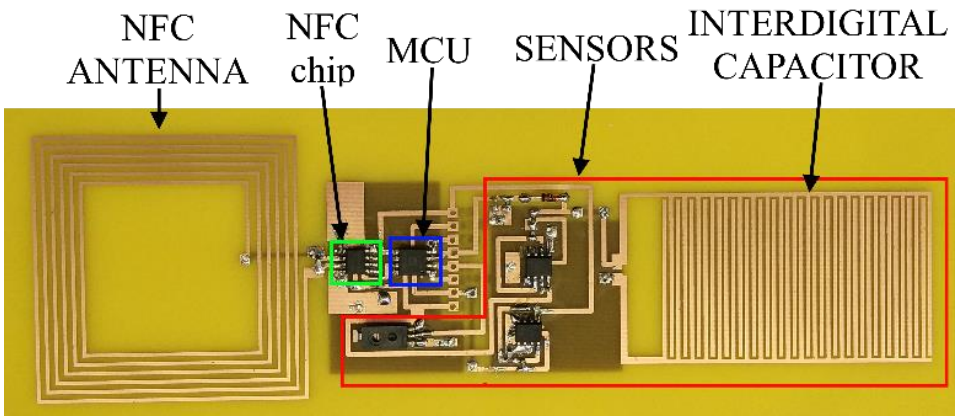


Figure 3.9. Designed PCB prototype with the antenna, the IDC and the chipset.

### 3.3.3 Software

In order to read, display and save the sensed data, it is needed to program both sides: the reader and the tag. Figure 3.10 shows the flow diagram of the system. Once the tags NFC IC receive a magnetic field higher than the $H_{min}$ it supplies the rectified voltage to the tag triggering the software programmed on the microcontroller, which gets the data from the sensors, compute it and writes it on the NFC IC memory in NDEF format. This NDEF message will be retrieved and processed by the reader software.

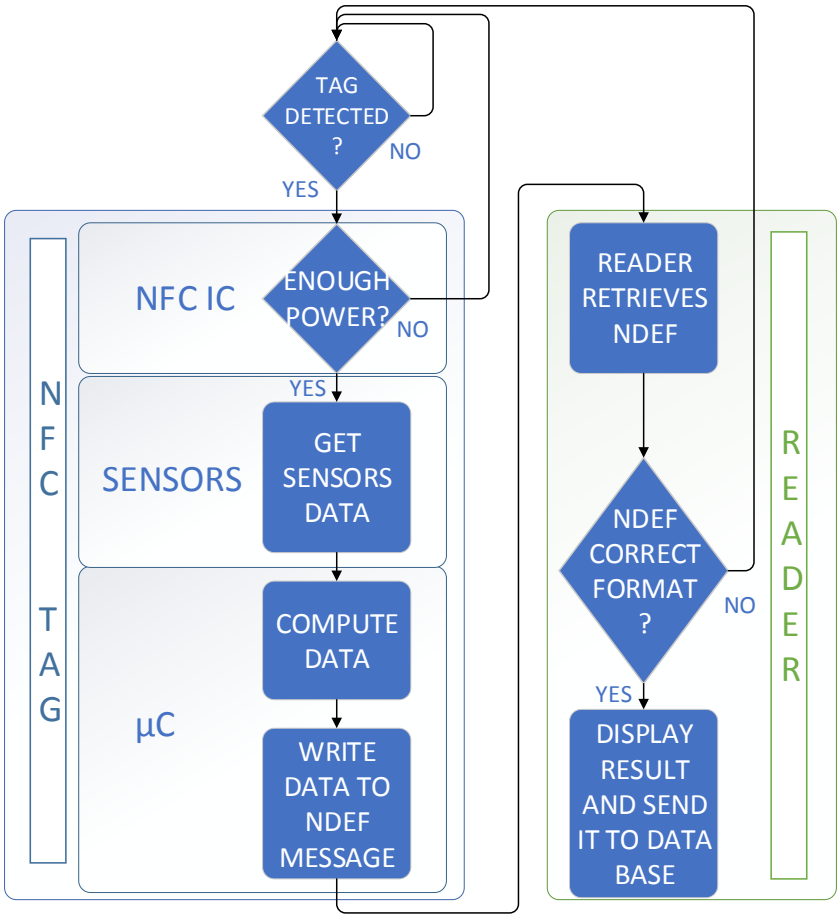


Figure 3.10. Flow diagram of the system, indicating the tag on the left and the reader on the right.

#### 3.3.3.1 Tag side

To compute and store the sensors data it is necessary to program the tag's microcontroller. The prototype presented has been designed including the pin accesses to program the microcontroller. These pins can be connected to a programmer such an Arduino UNO with an ISP (In-System Programmer) code, allowing to upload the code from the Arduino IDE in an easy way, to adjust the calibration curve or the sampling timing if necessary. Figure 3.11 shows the flow diagram of the tag. Once the tag is power up by the harvested energy from the RF, the sensors start to work. The first code to be executed is dedicated to configuring the NFC IC energy harvesting options, which implies 2 registers of the system area. The first one is located

at I²C location 2336, which contains the "*EH_ enable*" bit that must be set to 1 to activate the energy harvesting option. However, this register is volatile, and it will be updated each time that the IC is powered-up according to the other register that implies options regarding the energy harvesting, which can be acceded through the I²C address 2320. From this register it is necessary to configure the "*EH_ mode*" which is used to configure whether the energy harvesting mode is enabled or not by default. The same register contains 2 bits ("*EH_ cfg0*" and "*EH_ cfg1*") used to choose the sink current level. For this work the maximum sink current is selected, which requires a minimum magnetic field strength ($H_{min}$) of 3.5 A/m and provides up to 6 mA. The configuration of these registers can be done via I²C from the microcontroller or by RF messages from the reader. By default the energy harvesting option is disabled, in order to have the desired configuration the tag must be powered externally to power-up the microcontroller to write those registers. Alternatively these registers can be configured by RF commands from the smartphone using an app provided by the manufacturer. Once the configuration byte is written, it will last unless it is overwritten. Nonetheless the register is configured each time to ensure that the expected sink configuration is defined.

Timing is an important factor to take into account in NFC systems, and delays on the code must be considered. Thus, after writing the configuration registers, the microcontroller's firmware will wait 50 milliseconds to provide time to the sensors to avoid erroneous readings. After that, the microcontroller makes an average over 5 readings of the 10 bits ADC connected to the IDC ( $V_{OUT}$ in Figure 3.6) and calculates the VWC with the calibration curve explained in section 3.4.1. The relative humidity is gauged with the average of 5 readings of the output voltage of the sensor and applying the equation provided by the sensor's manufacturer on its datasheet. The last parameter to measure is the temperature, which is obtained from a digital sensor. To get the value the microcontroller has been programmed to begin a transmission via I²C bus to the address of the sensor (configured by hardware) asking for the register where the temperature is stored.

Once the data of the 3 sensors has been computed, the values are formatted to keep a fixed length and arranged in NDEF format to

be sent to the NFC IC through the I²C bus. The NDEF message is stored into the EEPROM of the NFC chip and it will be used to modulate the backscattered signal which will be received, demodulated and interpreted by the reader.

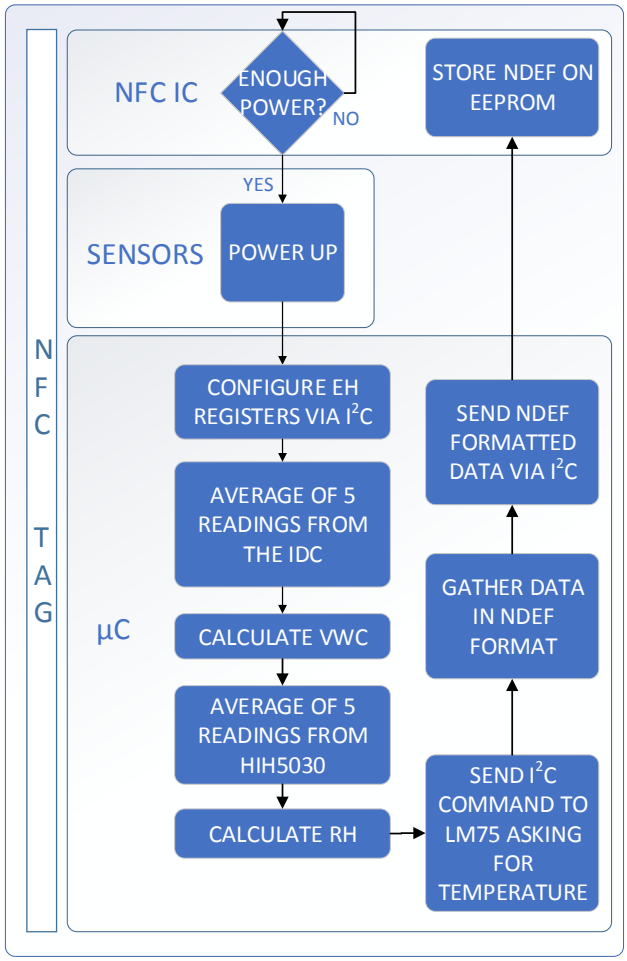


Figure 3.11. Flow diagram of the tag firmware

The main drawback of the system happens when the magnetic field received by the NFC IC from the reader is not enough to supply the rectified voltage to the tag's circuitry, but it is enough to read the tag. In that case the reader will retrieve the last stored message on the memory instead of a new reading. This drawback can be solved by applying some type of timestamp or control bit on the NDEF message.

#### 3.3.3.2 Reader side

An application that runs in Android smartphone (shown in Figure 3.12) has been developed as proof of concept. Beyond the sensed data, the system allows to send more information to the reader, such as a link to a website, or it can make use of the user identifier (UID) of each tag to give additional information of that specific product.

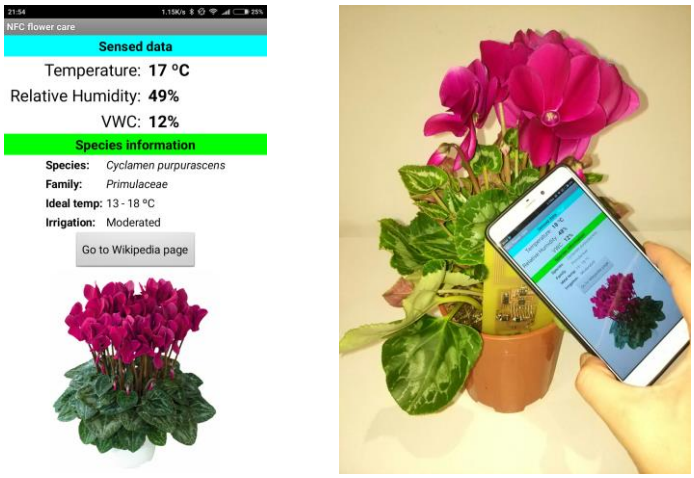


Figure 3.12. Image of the developed app graphic interface which uses the tag UID to retrieve the information of the plant (a) and the flower pot with the device on it being powered and read by the smartphone (b).

## 3.4 Experimental results

### 3.4.1 Calibration

To check the sensor operation an experimental setup and a calibration procedure is proposed. A typical soil used in greenhouses is chosen to perform the experiments. Different samples of soil are used with different volumetric water content, ranging from dry to water saturation. The interdigital capacitor is connected to a vector network analyser (VNA) that is used to measure the capacitance at 1 MHz. Figure 3.13 shows the measurements of the capacitance as a function of the volumetric water content (blue squares) altogether with the two-point $\alpha$-mixing model (3.12) (blue line). A capacitance of 65 pF is obtained when the soil is dried, which is considerably higher than when the sensor is on air (around 55 pF). It also shows

the soil permittivity obtained from the relationship between the capacitance and the permittivity given by (3.7).

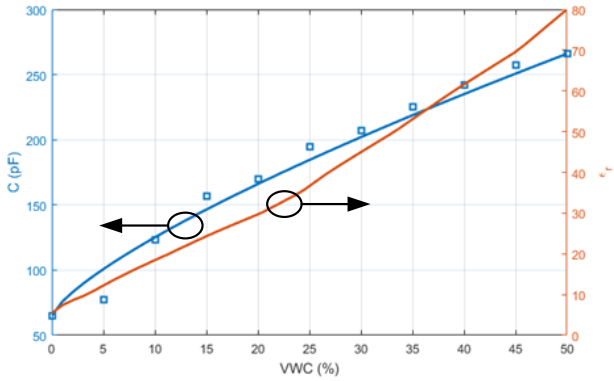


Figure 3.13. Measured capacitance (blue squares), model (3.12) (blue line) and relative permitivity (orange line) as a function of the volumetric water content.

In order to achieve high accuracy, the sensor must be calibrated because the relation between the capacitance and the volumetric water content depends on the soil composition [22]. In addition, the capacitance as it is shown in Figure 3.4 depends on the coating thickness and the coating material. Therefore, a calibration system is needed. In order to calibrate the sensor, the two-point α-mixing model is fitted [22]. The volumetric water content is modelled as:

$$VWC(\%) = \frac{X^{\alpha} - X_{sat}^{\alpha}}{X_{dry}^{\alpha} - X_{sat}^{\alpha}}\phi \tag{3.12}$$

Where $X$ is a variable that depends on the sensor measurement, $\alpha$ is a fitting parameter that depends on the sensor and $\phi$ is the porosity of the medium. The sub-indexes dry and sat correspond to the sensor output values when soil is dry and when it is water-saturated, respectively.

The fitting parameter $\alpha$ depends on the sensor and is obtained from the slope in logarithmic scale:

$$\alpha = \frac{ln\left(1 - \frac{VWC}{\phi}\right)}{\ln(X)} \tag{3.13}$$

Considering that the proposed circuit has an output voltage proportional to the VWC, it is possible to define $X$ as the normalized measured voltage (Figure 3.6):

$$X = \frac{V_{out} - V_{out,min}}{V_{out,max} - V_{out,min}} \tag{3.14}$$

Where $V_{out,min}$ and $V_{out,max}$ are the minimum (on water) and maximum (on air) measured output voltages, respectively. Therefore, using this normalized variable $X$, $X_{dry}$=1 and $X_{sat}$=0. It is straightforward to calculate $\alpha$ and $\phi$ from a linear fitting in logarithmic scale.

The values obtained for $\alpha$ and $\phi$ are 0.33 and 50%, respectively. Figure 3.14 shows the results of the volumetric water content as a function of the normalized voltage, comparing the model with the measured values.

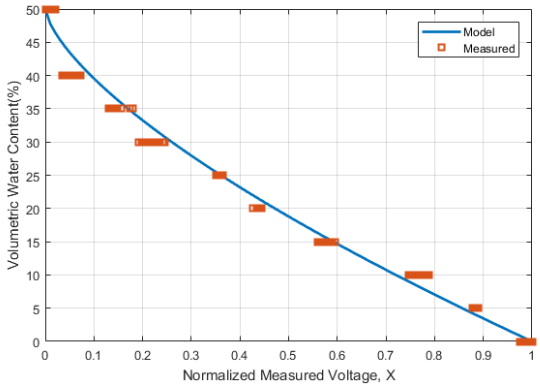


Figure 3.14. Comparison of measured (□) and modelled (3.13) volumetric water content as a function of the normalized voltage, X.

### 3.4.2 Irrigation

In order to analyse the behaviour of the sensor during the irrigation process a setup with 11 different pots, containing a blended mixture with different quantities of water, from dried soil to 50% of VWC in steps of 5% have been set. Thus, a heterogeneous distribution of the water along the soil is assured. The sensor has been on each pot enough time to take 50 samples. The result is shown in Figure 3.15, where it can be seen the stability of the measured VWC until it

reaches the 45%, where the sensor is saturated. In order to simulate the drying process, the same procedure has been done from 50% to 0%. VWC.

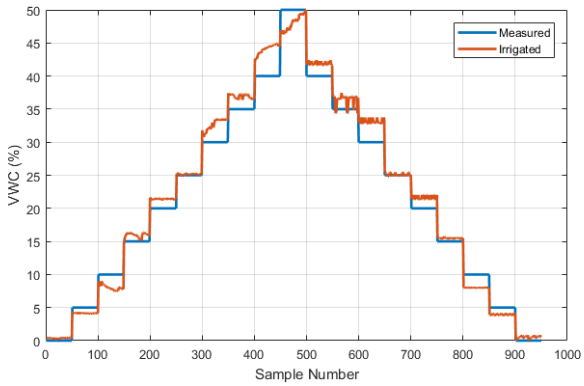


Figure 3.15. Computed VWC compared to the irrigated water.

### 3.4.3 Comparison against commercial sensor

Figure 3.16 shows the behaviour of the sensor after an irrigation of 150 ml of water on a 1-liter pot which initially had present about 13% of VWC. The figure compares the measurements of the presented sensor with a commercial sensor (Decagon EC-5). As it is shown, the commercial sensor has a smother response whereas the NFC sensor has a faster reaction. The fast-initial increase of VWC (at 5 min) is due to the presence of the water on the sensor surface. The two sensors give the same final steady state value after all the water has been diffused in the recipient.

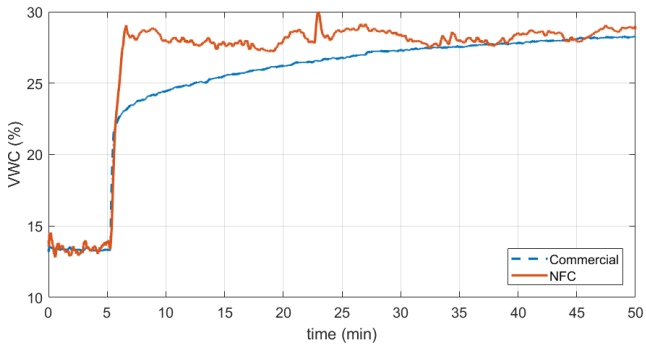


Figure 3.16. Measurement of VWC after irrigation of the proposed NFC sensor and a commercial soil moisture sensor.

## 3.5 Conclusion

This chapter has presented a low-cost, battery-less, NFC-powered device that is capable to measure volumetric water content (soil moisture), temperature and relative humidity and show it on a smartphone application or upload it to the cloud to be shared or stored. The proposed solution combines commercial sensors for temperature and relative humidity along with a specific method to measure the soil's volumetric water content, based on a capacitive measure which has been selected between the different possible methods found in the literature considering the NFC constraints. A printed interdigital capacitor using conventional PCB technology has been designed, fabricated, and measured for this purpose. The effect of an insulator layer for corrosion protection has been analysed. An accurate capacitance measurement method based on a low-power oscillator and a diode-based detector is employed. A procedure for the calibration of the sensor has been presented based on a simple expression whose coefficients can be experimentally obtained.

## 3.6 Bibliography

[1] S. G. Reynolds, "The gravimetric method of soil moisture determination Part I A study of equipment, and methodological problems," *J. Hydrol.*, vol. 11, no. 3, pp. 258–273, 1970.

[2] K. Yunseop and M. I. William, "Remote Sensing and Control of an Irrigation System Using a Distributed Wireless Sensor Network," *Ieee Trans. Instrum. Meas. Vol. 57, No. 7*, vol. 57, no. 7, pp. 1379–1387, 2015.

[3] and M. Á. P.-G. Joaquín Gutiérrez, Juan Francisco Villa-Medina, Alejandra Nieto-Garibay, "Automated Irrigation System Based on Wireless Sensor Network and GPRS Module," vol. 63, no. 1, pp. 166–176, 2014.

[4] D. A. Robinson, S. B. Jones, J. M. Wraith, D. Or, and S. P. Friedman, "A Review of Advances in Dielectric and Electrical Conductivity Measurement in Soils," *Water*, no. 1996, pp. 444–475, 2002.

[5] D. F. Sinclair and J. Williams, "Components of variance involved in estimating soil water content and water content change using a neutron moisture meter," *Aust. J. Soil Res.*, vol. 17, no. 2, pp. 237–247, 1979.

[6] S. R. Evett, J. A. Tolk, and T. A. Howell, "A depth control stand for improved accuracy with the neutron probe," *Vadose Zo. J.*, vol. 2, no. 4, pp. 642–649, 2003.

[7] J. M. Bremner, "Part 1 , Second Edition," *Total Nitrogen. Methods soil Anal. Part 2- Chem. Microbiol. Prop.*, pp. 1149–1178, 1986.

[8] S. B. Jones, J. M. Wraith, and D. Or, "Time domain reflectometry measurement principles and applications," *Hydrol. Process.*, vol. 16, no. 1, pp. 141–153, 2002.

[9] A. Cataldo, E. De Benedetto, G. Cannazza, E. Piuzzi, and E. Pittella, "TDR-based measurements of water content in construction materials for in-the-field use and calibration," *IEEE Trans. Instrum. Meas.*, vol. 67, no. 5, pp. 1230–1237, 2018.

[10] T. D. R. Reflectometer, S. C. Mulitplexer, and C. S. T. D. R. Probes, "Non-destructive measurements."

[11] K. Xu, Q. Sheng, X. Zhang, P. Li, and S. Chen, "Design and calibration of the unilateral sensitive soil moisture sensor," *IEEE Sens. J.*, vol. 15, no. 8, pp. 4587–4594, 2015.

[12] S. D. Soil, "Frequency Moisture," *Computer (Long. Beach. Calif).*, vol. 1, no. 2, 1978.

[13] Z. You, J. Mills-Beale, B. D. Pereles, and K. G. Ong, "A Wireless, Passive Embedded Sensor for Real-Time Monitoring of Water Content in Civil Engineering Materials," *IEEE Sens. J.*, vol. 8, no. 12, pp. 2053–2058, 2008.

[14] T. J. Dean, J. P. Bell, and A. J. B. Baty, "Soil moisture measurement by an improved capacitance technique, Part I. Sensor design and performance," *J. Hydrol.*, vol. 93, no. 1–2, pp. 67–78, 1987.

[15] I. S. O. Rf, "M24LR04E-R I 2 C interface Digital output pin," vol. 8, no. July, pp. 1–146, 2017.

[16] Atmel, "ATTiny - MCU ARM 8 bit AVR RISC ATTiny85 ATTiny45 ATTiny25," 2014.

[17] Texas Instruments, "LM75x Digital Temperature Sensor and Thermal Watchdog with Two-Wire Interface Datasheet," vol. SNIS153D, no. July, 2009.

[18] HONEIWELL, "HIH-5030/5031," p. 43, 2001.

[19] S. S. Gevorgian, T. Martinsson, P. L. J. Linnér, and E. L. Kollberg, "CAD models for multilayered substrate interdigital capacitors," *IEEE Trans. Microw. Theory Tech.*, vol. 44, no. 6, pp. 896–904, 1996.

[20] J. Svacina, "Analysis of multilayer microstrip lines by a conformal mapping method," vol. 40, no. 4, pp. 4–7, 1992.

[21] J. W. Kim, "Development of Interdigitated Capacitor Sensors for Direct and Wireless Measurements of the Dielectric Properties of Liquids," p. 115, 2008.

[22] T. Sakaki, A. Limsuwat, and T. H. Illangasekare, "A simple method for calibrating dielectric soil moisture sensors: Laboratory validation in sands," *Vadose Zo. J.*, vol. 10, no. 2, pp. 526–531, 2011.

# 4. Smart diaper

## 4.1 Motivation

This chapter presents a smart diaper that includes a wet detector based on a battery-less Near Field Communication tag. Diapers are used to absorb moisture not only in babies but also for individuals such as the elderly who cannot control their bladders or bowel movements or who are unwilling to use the toilet. This includes people with special medical conditions, such as the bedridden and those in a wheelchair. Since average life expectancy is increasing. The elderly population has therefore grown and the number of people who require special care is increasing [1], [2]. It is difficult to check the state of the diaper in babies and the elderly without removing their clothes. Nurses and other caregivers spend a lot of time performing this task. Optimizing this process can therefore help to reduce the cost of health services. Diapers must be changed to prevent skin rash caused by the skin being exposed for a long time to wetness and the high pH levels of urine and faeces [3]. It is therefore important to reduce the time that the moisture is in contact with the skin by periodically replacing the diaper [4]. Skin rash is often avoided by adding absorbent gels, but these may have drawbacks such as irritation and allergies.

Several sensors have been proposed in the literature to detect the degree of moisture in diapers [5]–[14]. Diapers that incorporate these devices are often called smart diapers. The most recent devices incorporate methods for wirelessly transmitting the state of the diaper to a mobile phone to set off an alarm [2], [15]–[17]. However, these communication functionalities increase the cost of the diaper. Moreover, they require batteries that need to be replaced or recharged. These batteries can also be a source of contamination if they are not recycled.

This chapter focuses on the feasibility of developing a smart diaper that uses a battery-less Near Field Communication (NFC) tag. The tag is designed to be reusable, in order to lower the cost of the system, and can be installed in conventional commercial diapers without modification. A smartphone with NFC capability can be used to read the tag. The moisture detector is based on a capacitive sensor. This sensor detects the change in capacitance between two

electrodes. The main novelties of this NFC-based smart diaper are: 1) can detect urine without having to insert the tag into the diaper (simply by adhering it to the output layer); and 2) uses a capacitive detection method (which enables the volume of urine to be detected) rather than a resistive switch [5], [6], [11], [12] (which enables the detection of only two states, i.e. wet or dry).

## 4.2 Capacitive moisture detection

Figure 4.1 shows a block diagram of the NFC tag embedded in the smart diaper. The capacitive moisture detector proposed in this study consists of two parallel electrodes that sense the variation in capacitance between them due to the presence of urine. The electrodes are connected to a low-power microcontroller (Atmel ATTINY 85) that is powered by the M24LR04E (M24) NFC IC from ST Microelectronics.

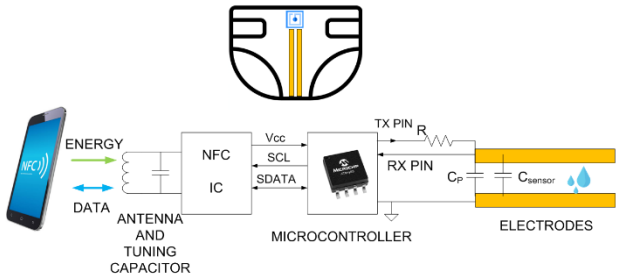


Figure 4.1. Block diagram of the smart diaper NFC tag.

A prototype of a flexible tag has been designed on flexible Rogers Ultralam 3000 substrate ($\varepsilon_r$=3.14, tan $\delta$=0.0025, thickness 100 µm) [18]. The antenna is a 6-turn loop with an area of 25 × 25 mm. The width of the strips ($W$) and the spacing ($S$) between them are 0.5 mm. A prototype of an antenna was measured with a vector network analyser, obtaining an inductance ($L_2$, see Figure 2.5) of 1.15 µH and a quality factor of 61 at 13.56 MHz in free-space ($Q_2$, equation (2.25). However, the presence of the smartphone's metallic case (when brought closer to the tag to read it) reduces the inductance to 0.9 µH and the quality factor to 48 and also detunes the antenna [19]. The influence of the body is low because the diaper acts as a spacer. The resonance frequency of the tag was adjusted by adding a 100 pF capacitor ($C_{tun}$, see Figure 2.5) in parallel to the input of the NFC

IC. The typical read range at which the sensor can be fed and read is up to 1 cm with a Xiaomi Mi Note 2 smartphone.

A key commercial aspect is the cost of the prototype. For large quantities (>1000), the cost of the M24 and the ATTiny85 is 0.3 € and 1 €, respectively. In commercial products, the Ultralam substrate can be replaced by another low-cost dielectric, such as polyamide. The cost can therefore be below 1.5 €. The typical price of an adult diaper package is roughly 15 € (with 10 units) and that of a baby's diaper package is roughly 20 € (100 units). Therefore, the commercial device, at least the electronic part, should be reusable. Another option is for the electrode to be printed using conductive ink on the diaper surface and for the tag and microcontroller to be purchased as stand-alone parts.

Figure 4.2 shows a cross-section of a typical diaper made up of several layers [20]. The top layer is the one in contact with the skin. Its aim is to transfer the fluids to the core while remaining soft and dry to the touch. Some diapers include a skin-care lotion that protects the skin from over-hydration and reduces irritation. The layer between the top sheet and the absorbent core is called the acquisition layer. This channels the fluid away from the skin and spreads it over the entire diaper core for better absorbency. The diaper's most internal layer is the absorbent core. This generally consists of a blend of cellulose fluff pulp and polyacrylate (polyacrylic acid sodium salt, $(C_2H_3NaO_2)_n$) granules. The cellulose material quickly absorbs and transfers the liquid to the polyacrylate superabsorbent material, where it becomes trapped. This material is used because it can absorb and retain large quantities of liquid relative to its own mass. After it absorbs the liquid it solidifies into a gel. The diaper's outer layer is the back sheet, which is designed to be water-resistant to prevent the liquids from leaking onto the clothes. This layer is made of polyethylene or a cloth-like film that allows water vapor and air (but not liquids) to pass through, thus reducing moisture and keeping the skin drier. To avoid any modification of commercial diapers, the NFC tag was designed on a flexible substrate to be attached to the back sheet on the outer surface.

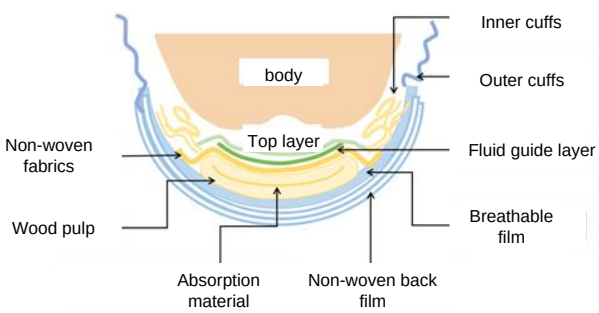


Figure 4.2. Cross-section of a diaper.

Since the aim of this chapter is to detect whether the capacitance between electrodes is higher than a threshold value that indicates the urine content in the diaper core, an absolute capacitance measurement is therefore not necessary and only a differential measurement is required. Although the NFC IC can provide up to 5 mA at the maximum magnetic field, it is better to reduce this value to enable small loop tag antennas to be used. To this end, we reduced the clock frequency to 1 MHz and achieved a maximum current consumption of 300 µA at 3 V. A capacitance measurement method that only requires the General Input/Output (GPIO) pins of the microcontroller and an external resistance $R$ is used. It therefore does not add any active components that could increase power consumption. The method uses the charge time of the capacitive electrode, which is driven by a large resistor $R$ (4 MΩ in the prototype) connected between a GPIO microcontroller digital output (TX PIN) and the electrode (see Figure 4.3). The microcontroller program toggles the TX PIN from a low to a high state, reads an input pin (RX PIN), and waits until its state is the same as that of the TX PIN. An integer variable is incremented inside a while loop until the RX pin state changes. The output of this counter is therefore proportional to the delay between the states. The delay $\Delta t$ between the TX PIN change and the RX PIN change is determined by the $RC$ time constant, where $C$ is the total capacitance at the RX pin, including the electrode and parasitic capacitances. The delay can be computed as:

$$\Delta t = -R \cdot C \cdot ln\left(1 - \frac{V_t}{V_{DD}}\right) \tag{4.1}$$

where $V_t$ is the threshold voltage level that toggles a digital pin in the microcontroller and $V_{DD}$ is the digital voltage power supply provided from the energy harvesting output of the NFC IC. If the RX PIN is configured as a digital input, this threshold corresponds to the logic threshold (usually $V_{DD}/2$ in CMOS). Another threshold voltage can be chosen if RX PIN is configured as an analog-to-digital converter input. The counter value (NFC reading) is proportional to the delay $\Delta t$ and therefore, to the capacitance (4.1). However, in this application, the absolute value of capacitance $C$ is not required because we are only interested in comparing the counter value between the dry and the wet states. The resolution is determined by the minimum time step the microcontroller can measure, which is limited by the clock frequency and delays in the internal microcontroller. Although the proposed method is simple, it provides enough precision for this application. The accuracy involved in measuring $C$ can therefore be increased by increasing the resistor value. This method is often used successfully in low-cost touch-button libraries in microcontrollers to avoid the need to add specialized integrated circuits based on measuring capacitance using the charge transfer method [21]–[23].

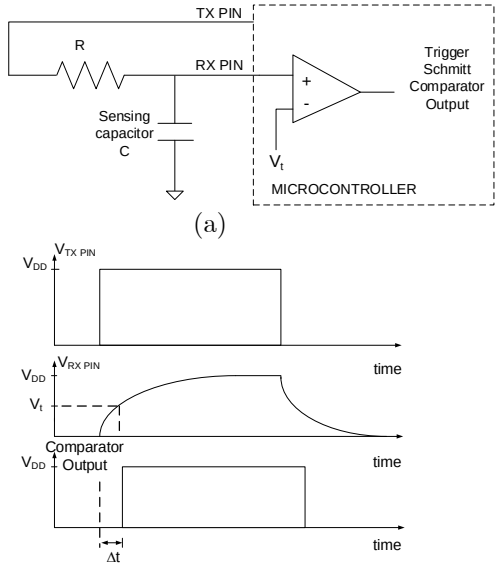


Figure 4.3. (a) Scheme of the circuit used for measuring the capacitance. (b) Waveforms at TX PIN, RX PIN and at the output of the internal microcontroller comparator.

## 4.3 Capacitance simulations

Several electromagnetic simulations were carried out to estimate the change in capacitance between the dry and the wet diapers. The S parameters of two coplanar electrodes were simulated with the Keysight Momentum simulator as a function of the frequency. The capacitance between the two electrodes was obtained from the imaginary part of the input admittance. Figure 4.4 shows a simplified structure of the diaper with the coplanar electrodes. The height of the back sheet including the flexible PCB substrate is $h_1$. The permittivity of this layer ($\varepsilon_{r1}$) is assumed to be 3, which is the typical permittivity of polyamide. The permittivity of the absorption layer ($\varepsilon_{r2}$) is considered to be 2 when dry, which is the permittivity of the cellulose layers. The permittivity of urine is roughly $\varepsilon_r$=50, and the conductivity is 1.75 at 1 MHz [24]. For the laboratory experiments, urine was simulated with a solution of water with salt (NaCl). The relative permittivity of the solution is close to that of water ($\varepsilon_{r2}$=78) and the conductivity can be adjusted with salt concentration. In accordance with Stogryn's model [25], a solution of normality 0.175 N (43 g/l) at 25ºC produces conductivities that are close to those of urine. When the core layer is saturated with liquid, it is assumed that the permittivity is close to that of the liquid. The dielectric properties of the body are frequency dependent. At low frequencies, the body has a high permittivity. Permittivity is difficult to estimate because there may be a gap of air between the body and the top layer of the diaper, which reduces the effective permittivity. The maximum bandwidth of a pulse depends on its rise-time. However, it is considered to be 10 MHz (10 times the microcontroller's clock frequency). The permittivity of the body ($\varepsilon_{r3}$) is considered equal to 170 in the simulations, which is the value of muscle permittivity at 10 MHz [26]. Note that this layer is included in the simulation in order to study the effect of the proximity of the body and to estimate the threshold capacitance between the dry and the wet states.

Table 4.I shows the main parameters used in the simulations.

Table 4.I. Parameters used in electromagnetic simulations

| Parameter | Symbol | Value |
|---|---|---|
| Permittivity of back sheet and flexible substrate | $\varepsilon_{r1}$ | 3 |
| Height of back sheet | $h_1$ | 200 µm |
| Permittivity of the core (dry) | $\varepsilon_{r2}$ | 2 |
| Permittivity of the core (wet with water) | $\varepsilon_{r2}$ | 78 |
| Height of the core | $h_2$ | 5 mm |
| Permittivity of the body | $\varepsilon_{r3}$ | 170 |

The sensor's electrodes were designed with geometrical parameters selected to ensure enough sensitivity. When the diaper is dry, the effective permittivity of the multilayer structure is expected to be low and so a low capacitance value between electrodes is obtained. The effect of the high permittivity of the body should be small if $h_2$ is higher than the penetration depth of the fields, $T$ (see Figure 4.4). However, when the diaper is wet, the urine is trapped in the absorbent core layer and the capacitance increases by several times. The field penetration depth of the sensor can be estimated using conformal mapping analysis [27]:

$$T = \frac{S}{2}\sqrt{\left(1+\frac{W}{S/2}\right)^2 - 1} \approx W + S/2 \tag{4.2}$$

The penetration depth of the fields is therefore a function of the width ($W$) and the spacing between electrodes ($S$). $T$ should be of the order of the height $h_2$ in order to maximize the ratio between the wet and the dry capacitances.

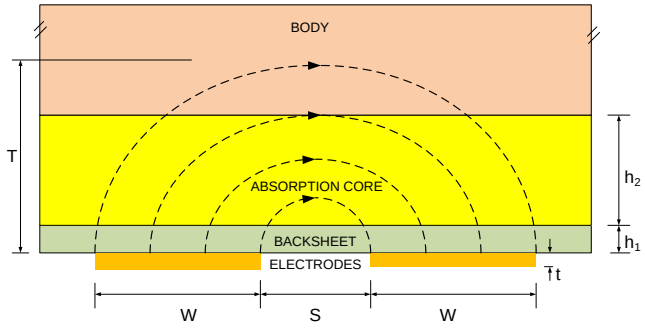


Figure 4.4. Cross-section used for capacitance simulation showing the electric field distribution inside the diaper at low permittivity.

Figure 4.5-8 show the simulated results as a function of the main parameters. To avoid excessive bending of the electrodes and improve contact with the diaper, the maximum width of the electrodes is considered to be roughly a quarter the width of the diaper (2–2.5 cm). Two cases are considered in all figures: (1) the diaper is in contact with the body, and (2) the diaper is in the air with no contact with the body. The variation in the capacitance per unit length of the electrode (in pF/mm) between the dry and the wet states is analysed according to one parameter, while the other parameters remain constant. Figure 4.5 shows that the change in capacitance increases when the width of the electrodes $W$ increases. As expected, $C$ increases because the area of the electrodes increases. The capacitance is not affected by the body for widths that are less than the height of the core layer ($h_2$=5mm). For greater widths, the field penetration depth is greater than $h_2$ and there is a dependence on the permittivity of the body. The increase in capacitance normalized with respect to the dry capacitance is shown in Figure 4.5(b). For an absorption core layer saturated with water ($\varepsilon_{r2}$=78), the ratio of capacitances $\Delta$C/C can reach values of 8. Figure 4.6 shows the capacitance as a function of the separation between electrodes $S$. As the separation is increased, the capacitance decreases steadily. $W$ is assumed to be 5mm in this figure ($T<h_2$ with a small effect of the body). However, an increase in the relative capacitance occurs when $S$ increases (Figure 4.6(b)). Figure 4.7 shows the relative capacitance as a function of the permittivity of the absorption layer. This permittivity is a function of the urine content, the pressure and the diffusion of the urine along the electrodes. Capacitance is expected to behave linearly with permittivity. However, this linear effect is observed only up to 10. This effect is due to the curvature of the field lines for high values of the dielectric constant in the interface between the back sheet and the core. This behaviour is not often taken into account in analytical formulae derived using conformal mapping in the literature [28] but it can be computed numerically with electromagnetic simulators. These formulae are often used and verified for a low permittivity range, in which they are accurate. However, this conformal mapping does not consider this strong field change. The same behaviour has been found in interdigital electrodes used in measurements of soil moisture (See chapter 3). It is important to note the strong

dependence of the normalized increment of capacitance on the effective dielectric permittivity of the absorption layer. Finally, the influence of the height of the absorption layer is shown in Figure 4.8. If the height $h_2$ is higher than the field penetration depth, the capacitance remains constant. For lower heights, $T$ increases. For thicker layers, the normalized increment is almost constant. The height of the absorption layer depends on the diaper manufacturer and plays an important role in the price of the diaper and the maximum volume of liquid the diaper can absorb. The absorption material increases in volume when the trapped urine content increases. Therefore, the diaper is thicker when it is wet than when it is dry and the cellulose layers are compressed.

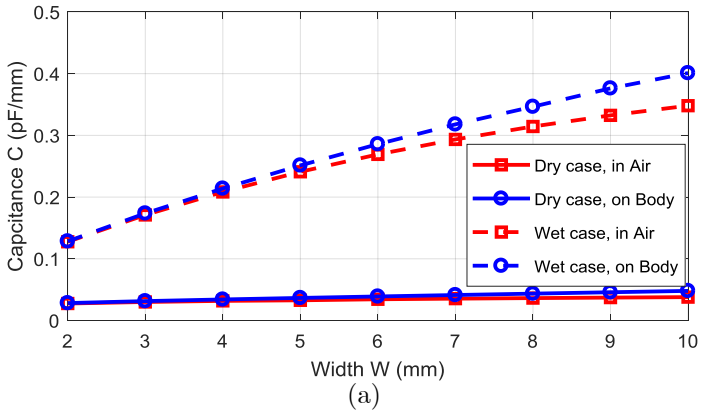


(a)

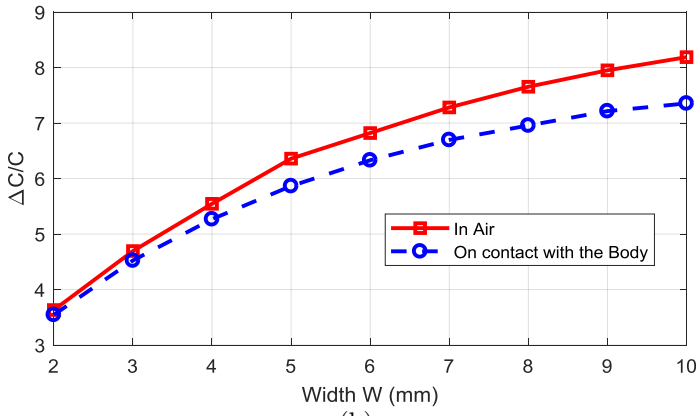


(b)

Figure 4.5. Simulated capacitance per unit length (a) and normalized increment in capacitance (b) between the wet and dry cases as a function of the electrode width $W$ with the diaper in contact with the body and the diaper in the air ($S$=1 mm, $h_2$=5 mm).

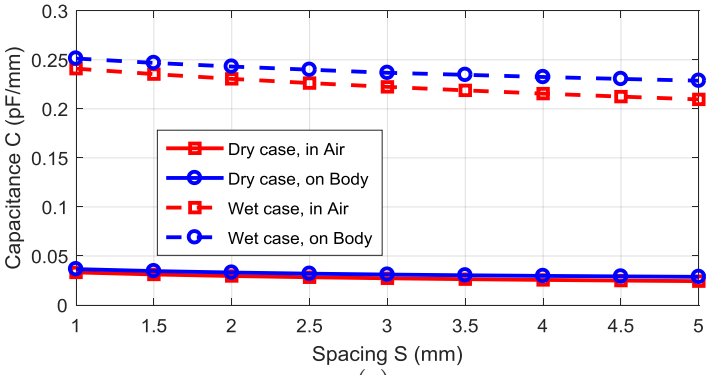


(a)

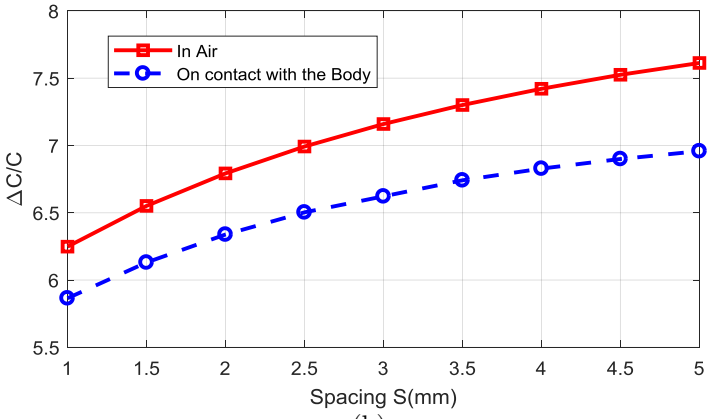


(b)

Figure 4.6. Simulated capacitance per unit length (a) and normalized increment in capacitance (b) between the wet and dry cases as a function of the electrode spacing $S$ with the diaper in contact with the body and with the diaper in the air ($W$=5 mm, $h_2$=5 mm).

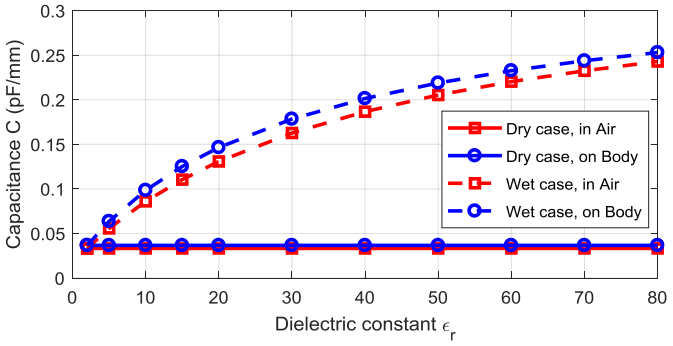


(a)

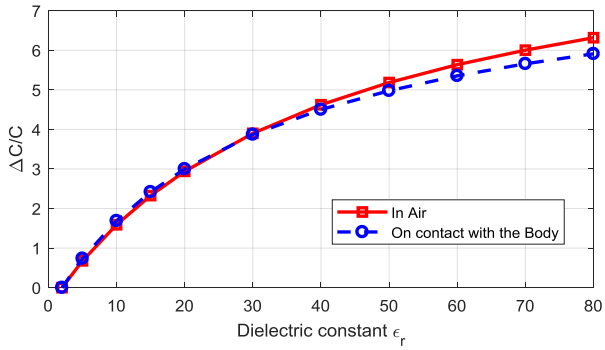


(b)

Figure 4.7. Simulated capacitance per unit length (a) and normalized increment in capacitance (b) between the wet and dry cases as a function of the effective permittivity of the absorption layer with the diaper in contact with the body and with the diaper in the air ($W$=5 mm, $S$=1 mm, $h_2$=5 mm).

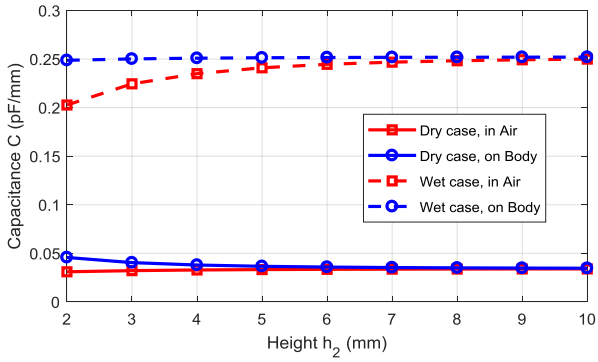


(a)

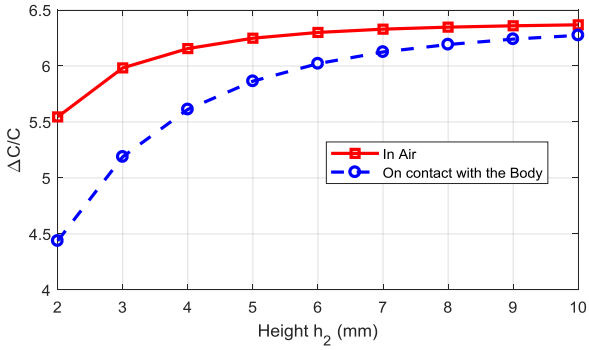


(b)

Figure 4.8. Simulated capacitance per unit length (a) and normalized increment in capacitance (b) between the wet and dry cases as a function of the height of the absorption layer with the diaper in contact with the body and with the diaper in the air ($W$=5 mm, $S$=1 mm).

## 4.4 Experimental results

To check the accuracy of the proposed capacitance measurement method, a set of measurements are conducted. Figure 4.9 shows the count value measured by the tag when discrete Surface Mount Device (SMD) capacitors are used instead of the electrodes. A resistor of 5 MΩ is used in these measurements. A linear regression was performed and a linear behaviour is obtained. The error between the model (line) and the measured values is less than the tolerance of the capacitors (5%). The repeatability of the measurement was below 1 count or 0.18 pF. The measurements were read by the NFC with two mobiles and the readout was identical. The offset error associated with parasitic capacitances and systematic errors was 24.2 pF. This accuracy is enough for the threshold detector.

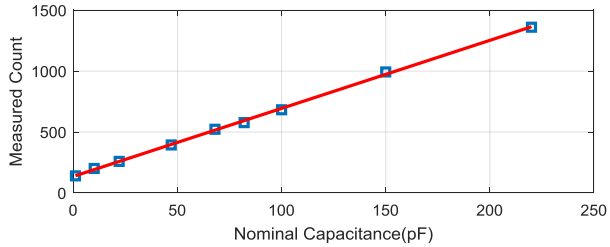


Figure 4.9. Measured count with the NFC as a function of discrete SMD capacitors ($C$).

Figure 4.10 shows a photograph of the tag, a photograph of the tag when adhered to a diaper, and several screens of the mobile APP designed to interface with the user. The experiments were performed with different diaper models and a saline solution (0.175M) was used to simulate urine. Figure 4.11 shows the sensor response as a function of time to a volume of 120 $cm^3$ injected uniformly with a pump to simulate urine discharge. An adult night diaper is chosen. It can been seen that the capacitance, and therefore the counter output (NFC reading), increases rapidly. However, there is a transitory period of roughly 100 s before the value stabilizes to the end value due to the diffusion of the liquid in the core. The rise time is of the order of 3.66 s, which demonstrates that the diaper can absorb urine flow rates of 33 ml/s. This is higher than the peak urine flow rate of roughly 27.3 ml/s for normal adults [29].


Figure 4.10. Layout of the tag and the screen of the mobile app.

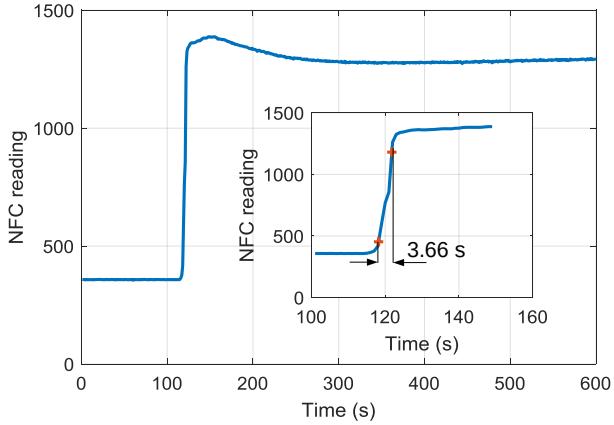


Figure 4.11. Time-dependent sensor response to a 120 $cm^3$ step injected into the diaper. The inset shows the rise time response between 10% and 90% of the end values.

Figure 4.12. shows the raw data output of the NFC sensor (output of the time counter) as a function of the volume of saline water. Two electrode widths are compared ($W$=5 mm and $W$=10 mm). The capacitance is proportional to the length of the electrodes. However, these electrodes must cover the active region where the absorption material is located. The loop antenna is located in the belt region to make reading easier. In the experiments, the spacing ($S$) and length ($L$) of both electrodes were 5 mm and 20 cm, respectively. The increase in capacitance between the dry and the wet diapers was roughly 1.5 times higher when $W$=10 mm than when $W$=5 mm,

which is in agreement with the simulations in Figure 4.5. Figure 4.13 compares the measurement of the NFC sensor and the capacitance of an LCR meter (Keysight U1733C) at 100 kHz. According to the manufacturer's datasheet, the accuracy of the LCR meter is 2%. The capacitance measurement error is therefore between 0.14 pF and 8 pF. A correlation coefficient of 99.5% was obtained between the two measurements. The small discrepancies along the line were mainly due to the diffusion of the water in the absorption layer. This effect is especially visible when the liquid concentration is low, and the liquid does not cover all the electrode area. To mitigate this effect, the measurements were taken 5 minutes after the liquid was poured onto the diaper in order to ensure the diffusion of the liquid into it. A range of measured capacitance variation between 7 pF and 395 pF was observed for water volumes between 0 and 400 $cm^3$ when $W$=10 mm. The simulated and experimental results show that wider electrodes are preferable because they provide higher capacitance values and a higher capacitance ratio between saturated and dry states. Also, it is easier to cover the surface covered by the absorption layers. Depending on the number of absorption layers in the core, the Super Absorbent Polymer (SAP) mass ratio and fluff pulp used [30], and the expansion of the diaper in the wet state, the capacitance (and therefore the NFC reading) varies as a function of the model. Diapers designed to contain high volumes (up to 1000 $cm^3$) can support several discharges during the night and contain several absorption layers. Diapers for babies can support up to 400 $cm^3$–500 $cm^3$ and the height is smaller than those designed for adults at night. However, when the volume reaches 200–250 $cm^3$, the urine covers all the area and the absorption layers start to expand, thus increasing the height of the diaper. The capacitance then tends to saturate, as we can see in Figure 4.8, where the capacitance remains almost constant when the height is greater than the penetration thickness. In the case of electrode 1, the resolution is roughly 0.16 $cm_3$ for the adult night diaper and 0.8 $cm^3$ for the baby's diaper. These resolutions are several times lower than for a normal urine discharge.

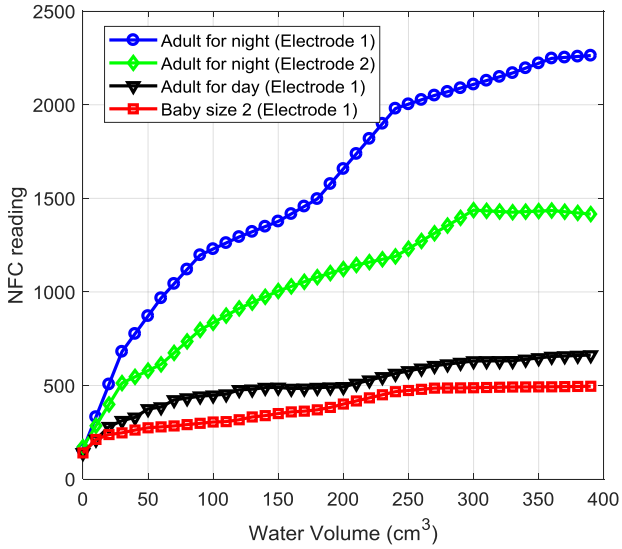


Figure 4.12. NFC reading as a function of the level of saline water for two electrode widths (Electrode 1: $W$=10 mm, S=5 mm, L=20 cm; and Electrode 2: $W$= 5mm, S=5 mm, L=20 cm) and different diapers (adult for night, adult for day, and baby size 2).

Figure 4.12 shows that the readings (and capacitance) increase steadily as the level of liquid increases until saturation is reached, and the diaper is considered full. However, the values tend to saturate when the core is saturated with liquid. The capacitance or NFC reading can therefore be used to estimate the volume of liquid in the diaper. We therefore propose the following model:

$$V(\%) = 100\frac{X^{\alpha} - X_{dry}^{\alpha}}{X_{sat}^{\alpha} - X_{dry}^{\alpha}} \tag{4.3}$$

where $V$ is the percentage of liquid volume in the diaper, $X$ is the normalized NFC reading, and $a$ is the slope in logarithmic scale. $X_{dry}$ and $X_{sat}$ are the normalized NFC readings for the dry and water-saturated cases, respectively. Note that parameters $X_{dry}$, $X_{sat}$ depend on the diaper model but they can be saved in the NFC message that is sent to the mobile.

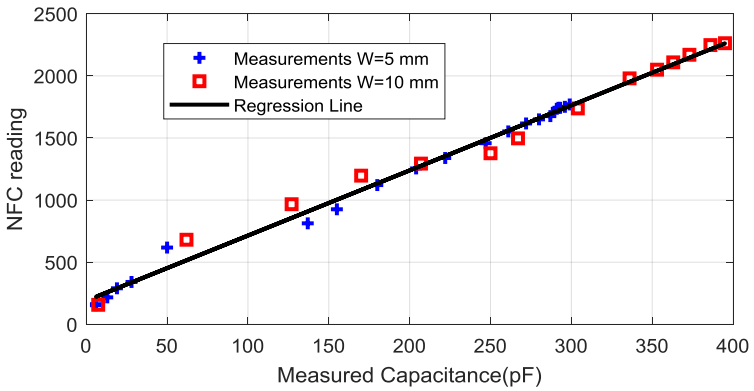


Figure 4.13. Comparison of the capacitance between the electrodes and the NFC reading for two electrode widths ($W$=5 mm and $W$=10 mm). The length of the electrodes is $L$=20 mm and the electrode spacing is $S$=5 mm. A regression line is included. The correlation coefficient is 99.5%.

Figure 4.14 compares the proposed model (4.3) and the measurements for the diapers in Figure 4.12. Agreement was good for $a$=2.5. The correlation coefficient between the model given by (4.3) and the measured normalized volume was between 96% (baby diaper size 2) and 99% (adult day diaper). The standard deviation of the error in the estimation of the volume was between 4.1% (adult day diaper) and 10.3% (baby diaper size 2). Although, as we can see from Figure 4.12, the dry and saturation values are a function of the diaper model, these values can be stored by the diaper manufacturer in the EEPROM of the NFC IC and saved in the NFC message read on the smartphone app.

Normal urinary frequency depends on how much fluid is taken in a day, the composition of the fluids taken, and whether the person is taking medication. For most people, the normal number of times to urinate per day is 6-7 over a 24-hour period [31]. Normal urine output depends on age [29],[31],[32]. The normal output is 2–3 $cm^3$/kg/hour for neonates, 1–2 $cm^3$/kg/hour for infants, and 0.5–1 $cm^3$/kg/hour for adolescents and adults [31]. Urine outputs below these limits are considered oliguria [31]. For an adult who weighs 70 kg, a normal urine output is therefore between 120 $cm^3$ and 280 $cm^3$. As adult night diapers are designed for a maximum capacity of 1000 $cm^3$, they can support more than two discharges. Figure 4.12 shows that for volumes above 250-300 $cm^3$, the reading is almost constant, thus indicating a risk of overfilling. For a neonate whose weight is 4 kg,

normal output is roughly 30–50 $cm^3$. Our experimental results in Figure 4.12 show that these threshold volume values may be detectable.

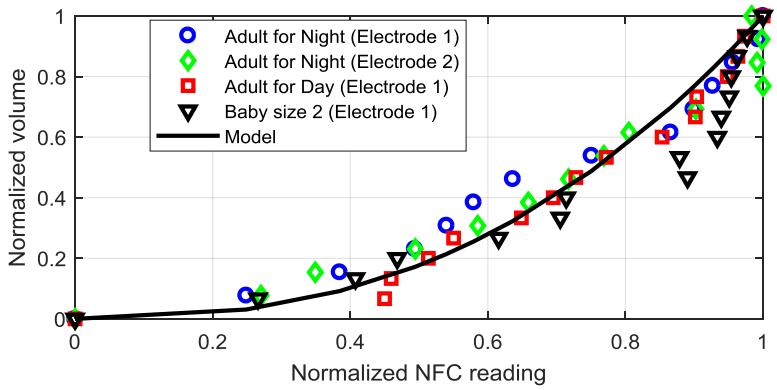


Figure 4.14. Comparison of the models proposed for the normalized volume (4.3) as a function of the normalized NFC reading with the measurements for the diapers in Figure 4.12.

To investigate the robustness of the readings when external materials are found below the diaper, several experiments are conducted. The worst case is the presence of metal under the diaper (e.g. a metal chair), which can increase the capacitance between the electrodes. Figure 4.15 compares the NFC readings as a function of the low permittivity spacer (cartoon, $\varepsilon_r \approx 1.8$), which simulates the thickness of clothes or chair cushion. An adult night diaper with electrode 1 was used in Figure 4.15, but similar conclusions have been found when other diaper models were used. As a reference we also include the measurement taken when the diaper was in contact with the body. In the measurements in Figure 4.15, a phantom consisting of a thick block of foam weighing 4 kg was used to simulate body pressure. In agreement with simulated results, differences of roughly 4.5% were observed between the low permittivity phantom and the body. From Figure 4.15 we can conclude that a spacer of roughly 5 mm is sufficient to offset the effect of the metal. However, even when the metal is very close to the electrode, it is possible to at least determine whether the diaper is dry or wet.

On the other hand, maximum differences of 1.1% were observed between the diaper when flat and when it had a curvature radius of

8 cm. Therefore, if the electrode is attached correctly to the diaper surface, the effect of bending is not very significant.

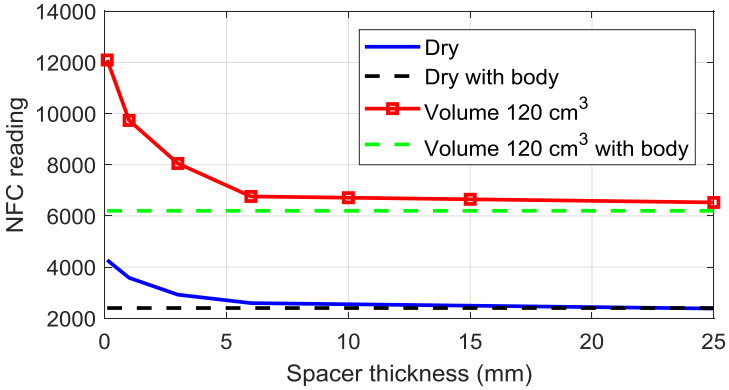


Figure 4.15. Comparison of the NFC readings as a function of the distance to metal. The dashed lines show the values measured in contact with the body.

The repeatability of the measurements is illustrated in Figure 4.16, which shows the histograms of 100 measurements for five diapers of the same model (adult night diaper) with the same volume of liquid (120 $cm^3$). The difference in the measurements for each diaper is less than 0.5% and the maximum difference with respect to the mean is ±2%. These differences can be attributed to small differences due to the location of the electrode, the distribution of the liquid in the absorption layers, and the surface roughness.

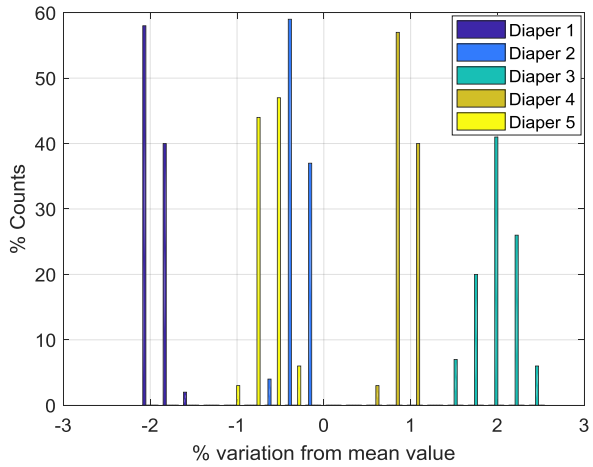


Figure 4.16. Histogram of variation in NFC reading from the mean for five adult night diapers with a volume of 120 $cm^3$.

### 4.5 Comparison with other technologies

Some techniques for sensing moisture in diapers are based on detecting changes in the colour of a reactive in contact with urine. Such techniques are low-cost, but they cannot detect the state of the diaper under clothes. However, because of their simplicity these technologies are commercially available in some diapers. Moreover, by using a nitride, a protein and leukocyte reactive, they can detect the presence of certain infections based on a change in colour [33], [34]. Other studies propose passive tags that are detuned in the presence of moisture. A UHF tag was used in [13], whereas an HF tag was used in [5] and [10]. The main drawback is that the read range is reduced in the wet state. This reduction may also be due to other reasons, such as misalignment between the reader and the tag antennas. Moreover, in [10], the tag must be inserted in the core layer. In [5], an NFC tag with energy harvesting based on the SL13A IC from AMS is used, which sense by means of a resistive switch, is used. The main drawback here is that the electrodes must either be inserted into the core layer (perforating the back sheet) or be in contact with the skin. In both [10] and [5], the commercial diapers must be modified and only a binary reading (wet or dry) can be made. In [7], the wet stage produces a shift in the resonance frequency of an LC resonator that is read with a non-standardized custom reader. Systems based on active devices have longer read ranges than passive alternatives. However, a battery is needed and so the cost is higher. The first devices reported in the literature, such as [6] and [12], use a custom TX transmitter. However, these communication systems usually consume more power and battery life is limited. With the appearance of smartphones with Bluetooth Low-Energy (BLE), several approaches based on this technology have recently been developed [17], [35], [36]. Most of these approaches are based on the resistive switch and so an electrode must be in contact with the core of the diaper. In [17], a method based on measuring the external temperature of the diaper was proposed. This non-invasive method can detect a rise in the temperature of the outer sheet layer as a result of urine accumulation at a temperature above ambient. Unfortunately, this detection method cannot be applied to battery-less devices such as the one proposed in this paper since it requires the temperature to be monitored periodically. However, it can be used if a battery is

included as in a data logger. Unlike the method proposed in this study, the smart diapers reported in the literature provide information only if the diaper is dry or wet and do not estimate the volume of liquid that can be used to determine certain pathologies associated with oliguria [37]. Unlike other HF RFID solutions for smart diapers (such as [7] and [10]), the proposed method is compatible with a commercial smartphone and does not require a specific reader. Table 4.II compares different smart diaper devices.

Table 4.II. Comparison of smart diaper devices

| Year/Ref. | Sensor technology | Communications technology and comments |
|---|---|---|
| This work | Capacitive | NFC based on M24, estimates the volume of liquid, do not require modify the diaper |
| Yambem et al. 2008 [7] | LC resonance shift | Inductive coupling, only dry or wet states detection, modification on the diaper is required, custom reader |
| Siden et al. 2011 [5] | Resistive switch | NFC based on SL13A, only dry or wet states detection, modification of the diaper is required |
| Sajal et al. 2014 [13] Nilsson et al. 2011 [9] | UHF antenna detuning | UHF RFID, measurement based on the horizontal and vertical polarization reading distances, only dry or wet states detection |
| Chen et al. 2014 [34] Karlsen et al. 2014 [14] | Colorimetric | Not available, it cannot be used with clothes |
| McKnight et al. 2015 [11] | Paper based biopotential | BLE, requires external amplifiers and impedance analyzer (AD5933) |
| Ziai et al. 2015 [10] | Resonance frequency detuning | Passive, HF at 13.56 MHz, only dry or wet states detection |
| Siden et al. 2004 [6] | Resistive switch | Tx at ISM 13.56 MHz activated by the sensor switch and custom reader |
| Simik et al. 2014 [12] | Resistive switch | GSM, only dry or wet states detection, modification of the diaper is required |
| Khan et al. 2018 [17] | Temperature | BLE, requires continuous monitoring of the temperature |
| Rahman et al. 2017 [35] | Resistive switch | BLE, only dry or wet states detection, modification on the diaper is required |
| Yu et al. 2016 [36] | Resistive switch and colorimetric nitride sensor | BLE, urine-activated urinary nitride sensor |

## 4.6 Conclusions

In this study a prototype for a smart diaper that measures moisture by measuring the change in capacitance between electrodes is designed. Capacitance is noninvasively determined by measuring its charge time when driven by a high-value resistor using a microcontroller. The tag is based on an NFC IC with energy harvesting and can be read with a mobile phone. As an alternative to urine detection based on a resistance switch, a tag based on capacity sensing that can be adhered to the outer layer of commercial diapers is proposed.

## 4.7 Bibliography

[1] 'WHO | 50 Facts: Global health situation and trends 1955-2025', *WHO*, 2013.

[2] A. A. P. Wai *et al.*, 'Towards developing effective Continence Management through wetness alert diaper: Experiences, lessons learned, challenges and future directions', no. March, 2012.

[3] R. W. Berg, M. C. Milligan, and F. C. Sarbaugh, 'Association of Skin Wetness and pH With Diaper Dermatitis', *Pediatr. Dermatol.*, vol. 11, no. 1, pp. 18–20, 1994.

[4] R. Adam, 'Skin care of the diaper area', *Pediatr. Dermatol.*, vol. 25, no. 4, pp. 427–433, 2008.

[5] J. Sidén *et al.*, 'Home care with NFC sensors and a smart phone', no. October, pp. 1–5, 2012.

[6] J. Siden, A. Koptioug, and M. Gulliksson, 'The smart diaper moisture detection system', in *2004 IEEE MTT-S International Microwave Symposium Digest (IEEE Cat. No.04CH37535)*, 2004, vol. 2, no. July, pp. 659–662.

[7] L. Yambem, M. K. Yapici, and J. Zou, 'A new wireless sensor system for smart diapers', *IEEE Sens. J.*, vol. 8, no. 3, pp. 238–239, 2008.

[8] L. Sheng, C. Dajing, G. Xishan, and C. Yuquan, 'Design of wireless SAW humidity sensor node based on radio wake-up technique', *Int. Conf. Commun. Technol. Proceedings, ICCT*, pp. 17–20, 2010.

[9] H.-E. E. Nilsson, J. Sidén, M. Gulliksson, J. Siden, and M.

Gulliksson, 'An incontinence alarm solution utilizing RFID based sensor technology', *2011 IEEE Int. Conf. RFID-Technologies Appl. RFID-TA 2011*, pp. 359–363, Sep. 2011.

[10] M. A. Ziai and J. C. Batchelor, 'Smart radio-frequency identification tag for diaper moisture detection', *Healthc. Technol. Lett.*, vol. 2, no. 1, pp. 18–21, 2015.

[11] M. McKnight, F. Lin, H. Kausche, T. Ghosh, and A. Bozkurt, 'Towards paper based diaper sensors', *IEEE Biomed. Circuits Syst. Conf. Eng. Heal. Minds Able Bodies, BioCAS 2015 - Proc.*, pp. 1–4, 2015.

[12] M. Y. E. Y. E. Simik, F. Chi, A. M. S. M. S. Abdelgader, and R. S. I. S. I. Saleh, 'Automated alarm system for diaper wet using GSM', *Proc. - 17th IEEE Int. Conf. Comput. Sci. Eng. CSE 2014, Jointly with 13th IEEE Int. Conf. Ubiquitous Comput. Commun. IUCC 2014, 13th Int. Symp. Pervasive Syst.*, pp. 1799–1803, Dec. 2014.

[13] S. Sajal, Y. Atanasov, B. D. Braaten, V. Marinov, and O. Swenson, 'A low cost flexible passive UHF RFID tag for sensing moisture based on antenna polarization', *IEEE Int. Conf. Electro Inf. Technol.*, pp. 542–545, 2014.

[14] H. Karlsen and T. Dong, 'A smart phone-based robust correction algorithm for the colorimetric detection of Urinary Tract Infection', *Proc. Annu. Int. Conf. IEEE Eng. Med. Biol. Soc. EMBS*, vol. 2015-Novem, pp. 1251–1254, 2015.

[15] A. A. P. A. P. Wai *et al.*, 'Smart Wireless Continence Management System for Persons with Dementia', *Telemed. e-Health*, vol. 14, no. 8, pp. 825–832, Oct. 2008.

[16] L. M. Ang *et al.*, 'Wireless intelligent incontinence management system using smart diapers', *5th Int. Conf. Electr. Eng. Comput. Telecommun. Inf. Technol. ECTI-CON 2008*, vol. 1, pp. 69–72, 2008.

[17] T. Khan, 'A Smart Wearable Gadget for Noninvasive Detection and Notification of Diaper Moister', *IEEE Int. Conf. Electro Inf. Technol.*, vol. 2018-May, pp. 240–244, 2018.

[18] R. C. ULTRALAM® 3000 Liquid Crystalline Polymer Circuit

Material Double-Clad Laminates, 'Ultralam datasheet.pdf'. .

[19] M. Boada, A. Lazaro, R. Villarino, E. Gil, and D. Girbau, 'Near-Field Soil Moisture Sensor with Energy Harvesting Capability', in *2018 48th European Microwave Conference, EuMC 2018*, 2018, pp. 235–238.

[20] K. Kosemund, H. Schlatter, J. L. Ochsenhirt, E. L. Krause, D. S. Marsman, and G. N. Erasala, 'Safety evaluation of superabsorbent baby diapers', *Regul. Toxicol. Pharmacol.*, vol. 53, no. 2, pp. 81–89, 2009.

[21] K. Blake and S. Bible, 'Measuring small changes in capacitive sensors', *Appl. Note*, pp. 1–20, 2005.

[22] J. E. Gaitan-Pitre, M. Gasulla, R. Pallas-Areny, J. E. Gaitán-Pitre, M. Gasulla, and R. Pallàs-Areny, 'Analysis of a direct interface circuit for capacitive sensors', *IEEE Trans. Instrum. Meas.*, vol. 58, no. 9, pp. 2931–2937, Sep. 2009.

[23] F. Akkoç, Ö. C. Şahin, Ö. Cihanbe, and ˘ Gendi¸sahingendi¸ Gendi¸sahin, 'Development and experimental comparison of low-cost, reliable capacitive touch sensing boards', *Sensors (Switzerland)*, vol. 16, no. 11, 2016.

[24] S. Gabriel, R. W. Lau, and C. Gabriel, 'The dielectric properties of biological tissues: II. Measurements in the frequency range 10 Hz to 20 GHz', *Phys. Med. Biol.*, vol. 41, no. 11, pp. 2251–2269, Nov. 1996.

[25] A. Stogryn, 'Equations for Calculating the Dielectric Constant of Saline Water', *IEEE Trans. Microw. Theory Tech.*, vol. 19, no. 8, pp. 733–736, 1971.

[26] S. Gabriel, R. W. Lau, and C. Gabriel, 'The dielectric properties of biological tissues: III. Parametric models for the dielectric spectrum of tissues', *Phys. Med. Biol. Phys. Med. Biol*, vol. 41, no. 41, pp. 2251–2269, 1996.

[27] J. Z. Chen, A. A. Darhuber, M. Troian, and S. Wagner, 'Capacitive sensing of droplets for microfluidic devices based on thermocapillary actuation', pp. 473–480, 2004.

[28] S. Gevorgian and H. Berg, 'Line capacitance and impedance of coplanar-strip waveguides on substrates with multiple dielectric layers', 2001.

[29] G. W. Drach, T. N. Layton, and W. J. Binard, 'Male peak urinary flow rate: relationships to volume voided and age.', *J. Urol.*, vol. 122, no. 2, pp. 210–4, Aug. 1979.

[30] G. B. Li, J. M. Ke, and H. J. Zhang, 'The Influence on the Absorption Properties of Paper Diapers by the SAP Mass Ratio and Fluff Pulp', *Adv. Mater. Res.*, vol. 1089, pp. 33–36, Jan. 2015.

[31] F. T. Fischbach and M. B. Dunning, *A manual of laboratory and diagnostic tests*. Wolters Kluwer Health/Lippincott Williams & Wilkins, 2009.

[32] K. Van Hoeck *et al.*, 'Urine Output Rate and Maximum Volume Voided in School-Age Children with and without Nocturnal Enuresis', *J. Pediatr.*, vol. 151, no. 6, pp. 575–580, Dec. 2007.

[33] C. Chen, Y. Wu, and T. Dong, 'Dipsticks integrated on smart diapers for colorimetric analysis of urinary tract infections in the field', *Proc. 16th Int. Conf. Mechatronics, Mechatronika 2014*, pp. 423–427, 2014.

[34] C. Chen and T. Dong, 'Microfluidic paper - based analytical devices for colorimetric detection of urinary tract infection biomarkers on adult diapers *', pp. 5892–5895, 2015.

[35] S. Rahman, C. Choi, Y. Kim, S. Kim, and J. Choi, 'A Low-Cost wet Diaper Detector Based on Smart Phone and BLE Sensor', vol. 12, no. 19, pp. 9074–9077, 2017.

[36] W. Yu *et al.*, 'A Diaper-Embedded Disposable Nitrite Sensor with Integrated On-board Urine-Activated Battery for UTI Screening *', *2016 38th Annu. Int. Conf. IEEE Eng. Med. Biol. Soc.*, pp. 303–306, Aug. 2016.

[37] J. R. Prowle *et al.*, 'Oliguria as predictive biomarker of acute kidney injury in critically ill patients.', *Crit. Care*, vol. 15, no. 4, p. R172, Jul. 2011.

# 5. NFC sensor for pH monitoring

## 5.1 Motivation

Microfluidic paper-based devices [1] for analyses based on colour determination are widespread in applications such as medical devices [2], [3] and pH measurements [4]–[6]. The main advantages of these devices are that they are inexpensive, do not require an energy source, allow for easy transportation of fluids, and are easy to use. However, since diagnosis depends on optical measurements, accuracy is poor especially when, as in pH measurements, classification between different levels is required. PH measurement has a wide range of applications. It is used, for example, to check the water condition of swimming pools, tap water and aquariums. It is also used in medical applications such as sweat or saliva analysis and skin control in wounds, where it can indicate an infection before the infection becomes visible. However, as pH electronic probes are expensive and require continuous calibration, the cost is prohibitive for home applications. In medical applications (e.g. urine tests [7]), the probes need to be sterilized each time they are used in order to avoid contamination between samples. For this reason, paper-based colour strips have been extended as the simplest and cheapest way to quickly indicate pH measurements. With the expansion of smartphones with high-quality integrated cameras, several methods for colorimeter measurement using smartphones have been proposed [3]–[6]. The main advantages of pH measurement using smartphone cameras are that these devices are easy available and portable. However, they have also important drawbacks. For example, the readout depends on ambient illumination and camera type and requires special image processing techniques, so there are variations between smartphone models and the programs used to process the images. To solve the problems related to ambient light condition variation, some studies propose the use of an enclosure to keep the sample in darkness just being illuminated by the smartphone cameras led [2], [5], [6]. This method permits the reading to be independent of the external light conditions. However, the absolute control of light conditioning is not possible since each camera uses a different led, so the colour temperature and intensity may change, as well as the led location on the camera's enclosure, which makes the sample enclosure device-dependent.

PH is defined as the decimal logarithm of the reciprocal of the hydrogen ion activity in a solution [8]. Paper-based colour strips change their colour depending on the substances used to create the reactive. Some of the most common compounds used to create pH indicators are: phenolphthalein ($C_{20}H_{14}O_4$), which turns colourless in acidic solutions but pink in basic solutions; methyl red ($C_{15}H_{15}N_3O_2$), which is red at a pH below 4.4 and yellow at a pH over 6.2; and thymol blue ($C_{27}H_{30}O_5S$), which turns red below pH 1.2, yellow for pH between 2.8 and 8, and blue above 9.6. These substances are combined to react to a specific range of pH. Universal paper strips are mixtures of several pH indicators that extend the pH range over which they operate. The molecular geometry of these chemical compounds changes depending on the pH. This is due to modifications in the number of protons, which alter wavelength absorption and translate into a change of colour.

Colour evaluation has a wide field of applications. It can be used in medicament doses control [9], glucose detection [10], water quality control [3], gas detection [11] or pH determination [5]. The most common way to digitalise the colour for its further evaluation consists of using a photographic camera [2], [5], [6]. An alternative method for electronic colour measurements is based on colorimeters. Colorimeters are tristimulus devices that use red, green, and blue filters to emulate the response of the human eye to light and colour. Recently, low-cost colorimeters integrated into circuit devices have become commercially available and performed well. Low-cost colorimeters can therefore be designed for several applications [9]–[11]. Unlike the problems associated with smartphone cameras, colour measurement by colorimeter has the advantage of repeatability due to a controlled light condition.

Some references regarding pH monitoring systems based on NFC technology can be found in the literature. A low-power tag based on the SL13A chip from AMS, with potentiometric input to be used with pH and ion-selective electrodes is presented in [12]. A computer-based reader controls the sampling acquisition. A recent study [13] shows a medical application for wound care by measuring the colour of a pH reactive compound located on a bandage. The colour is measured using a photodiode and stored on a MLX90129 NFC chip

with datalogger function from Melexis. These methods use a battery on the tag to sense the data and save it into the memory.

In this chapter a low-cost NFC-based system that combines an NFC IC for communications and a colorimeter IC with a microcontroller is presented. The tag is completely passive and obtains energy from the RF interrogating signal from the reader using the energy-harvesting capabilities of the NFC IC. A simple calibration method is used to convert the measured colour of the pH strips into pH levels. A custom readout application that uses a smartphone with NFC compatibilities as a reader has also been developed.

## 5.2 System description

An overview of the system is shown in Figure 5.1. It consists of an electronic circuit made up of a colour light-to-digital TCS3472 converter from TAOS [14], a white 4150$^{o}$K LED to illuminate the sample, a low-power Atmel Tiny 85 microcontroller, and an NFC chip from ST Microelectronics (M24LR04E).

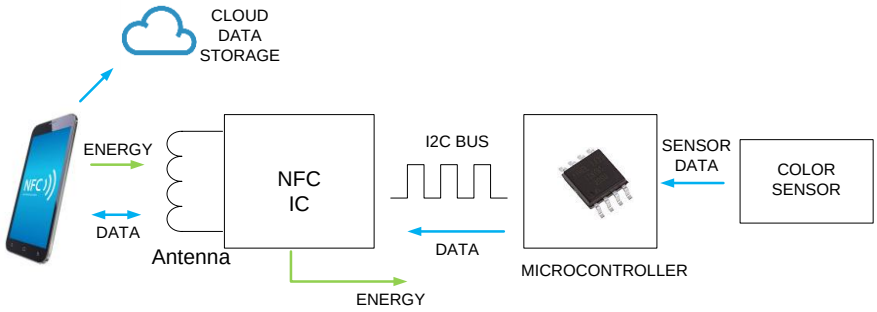


Figure 5.1. Block diagram of the proposed NFC-based pH sensor.

The TCS34725 has RGB and clear light sensing elements (Figure 5.2) and its light-to-digital converter contains a 3 × 4 photodiode array. This array comprises red-filtered, green-filtered, blue-filtered, and clear (unfiltered) photodiodes. These photodiodes are coated with an IR-blocking filter that minimizes the IR spectral component of the incoming light and enables colour measurements to be taken accurately. Spectral response curves of the four channels of the sensor is shown in Figure 5.2(b) [14]. The four integrating ADCs simultaneously convert the amplified photodiode currents to a 16-bit digital value. These three chips are connected to each other via an I$^2$C bus and the NFC IC is connected to a PCB loop antenna.

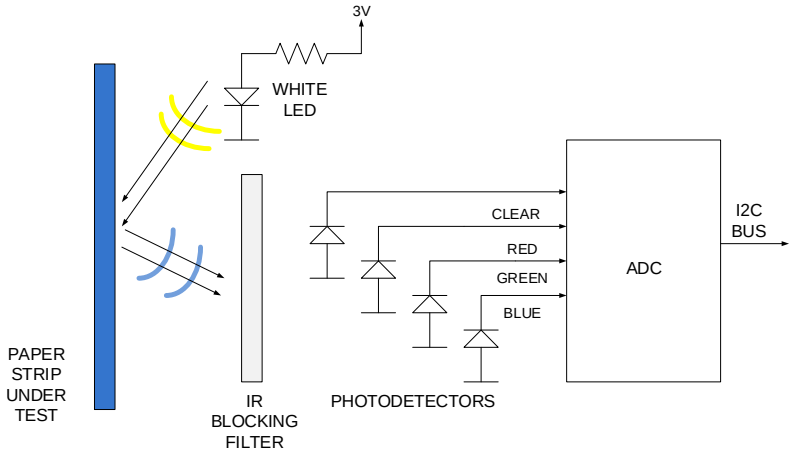


(a)

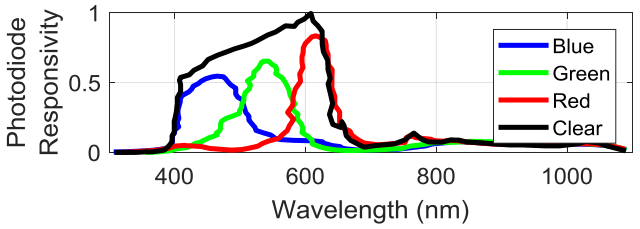


(b)

Figure 5.2. (a) Working principle of the colorimeter. (b) Spectral responsivity of the four channels.

The current consumption of each component is shown in Table 5.I. The NFC IC has four sink current configurable ranges. In this work, the mode with higher sink current (up to 5 mA) was selected to support the current need for the tag operation. The Atmel 8-bit AVR ATtiny85 microcontroller can be configured at different clock speeds and work down to 1.8V. Because of the power limitations presented by this system, it was configured to work at 1 MHz, where its consumption is around 300 µA at 3.3V. The total current consumption of the tag is about 3 mA, which is below the 5 mA that the NFC IC can harvest from the RF. A significant part of this consumption is due to the white LED used to illuminate the sample.

Table 5.I. Current consumption

| Component | Current consumption (µA) |
|---|---|
| M24 | 400 |
| TCS34725 | 235 |
| LED | 2000 |
| ATTiny85 | 300 |
| TOTAL | 2935 |

A photograph of the prototype is shown in Figure 5.3. The loop antenna, the NFC IC and the microcontroller are located on the top side, while the colour sensor and the LED are connected on the bottom side. The connector that links the two circuit boards is also used to download the firmware in the microcontroller. A plastic enclosure for the tag was designed using a 3D printer (see Figure 5.3(b)).

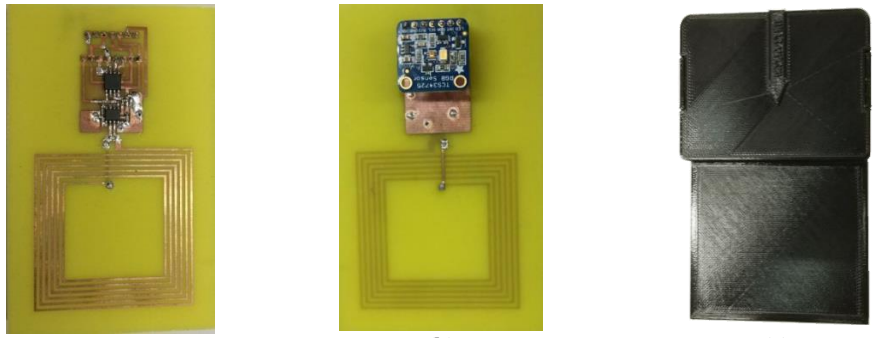

(a) (b) (c)

Figure 5.3. Photograph of the prototype from (a) the top and (b) the bottom and (c) the 3D printed enclosure.

## 5.3 Signal processing

A mathematical model is needed to transform the raw colour measurement in RGB provided by the colour sensor into pH. However, a colour model must be defined in order to digitalize a colour for its representation or analysis. Numerous colour models exist, the most common of which is the RGB. This additive colour model is widely used for displays, while the CMYK is another additive colour model that is widely used for colour printing. Since

colour models are abstract mathematical models, it is possible to convert from one model to another.

Figure 5.4(a) shows pH as a function of the colour of the paper strip. We can see that the concentration of pH produces a change in colour. One way to obtain the pH from the raw RGB measurement is to use a table-based method and an interpolation function. However, a simple model using HSV (Hue-Saturation-Value) colour space is also available and found on the literature [35], [36]. This model is useful not only because it is more intuitive than raw RGB values but also because the conversions to and from RGB are extremely quick to compute and can be run in real time on the microcontroller. When shifts in colours must be measured, the HSV model should be considered. HSV is an alternative representation of RGB based on how the human eye works. Instead of measuring the portion of each primary colour, the results are expressed in terms of Hue (representing pure colour and expressed in degrees from $0^{o}$ to $360^{o}$), Saturation (percentage of white colour), and Value (brightness, expressed in percentage), as can be observed in Figure 5.5.

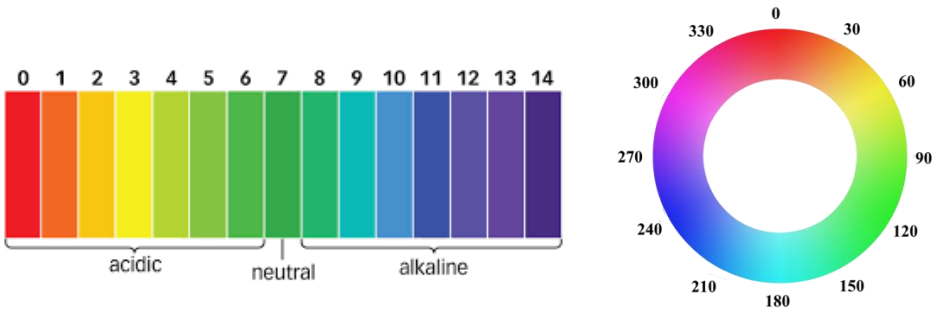


(a) (b)

Figure 5.4. (a) pH as a function of the colour of the paper strip. (b) Hue. Primary colours are at $0^{o}$ (red), $120^{o}$ (green), and $240^{o}$ (blue).

From Figure 5.4(b), a simple relationship between Hue (angle) and pH is expected. The transformation given in [34] to transform RGB into hue using the following equations (5.1)-(5.2) is used:

$$H = \begin{cases} \theta & \rightarrow if\ B \leq G \\ 360 - \theta & \rightarrow otherwise \end{cases} \tag{5.1}$$

where $\vartheta$ (in degrees) represents the Hue angle and R, G, and B are the values of red, green, and blue, respectively, in the 0 to 255 range.

$$\theta = arcos\left(\frac{\frac{1}{2}\left((R-G)+(R-B)\right)}{\sqrt{(R-G)^2+(R-B)(G-B)}}\right) \tag{5.2}$$

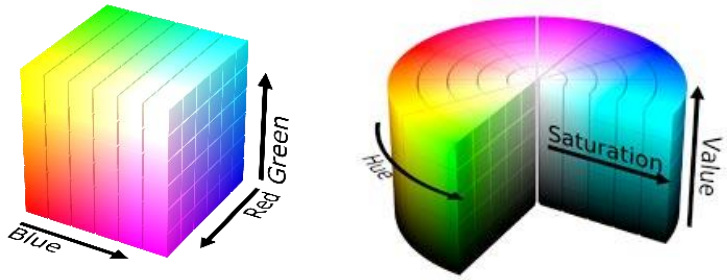


(a) (b)

Figure 5.5. (a) RGB colour space, (b) HSV colour space.

## 5.4 Experimental results

To test the system, the Hue obtained by measuring the colour of the pH reactive strips with the NFC colorimeter and the pH obtained by a calibrated pH probe (Hanna Checker HI 98103) are compared. The pH probe was previously calibrated using two reference solutions of pH 4 and 7. Three different paper strips with different pH ranges were tested. Figure 5.6 shows the colour charts of these pH paper strips. Figure 5.6(a) shows the colour palette of the full range strips from pH 1 to pH 14, while Figure 5.6(b) and Figure 5.6(c) correspond to the range's pH 3 to pH 6 and pH 5 to pH 9, respectively.

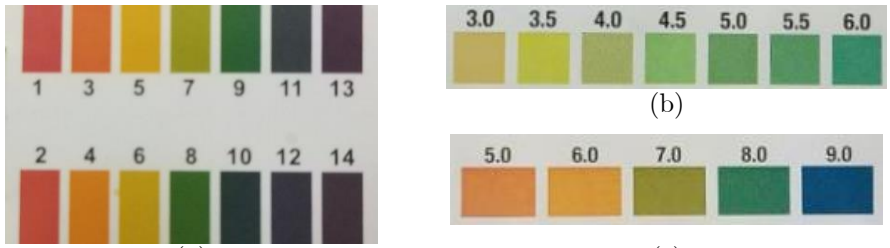


(a) (b) (c)

Figure 5.6. Colour charts for the three paper strips tested: (a) chart for scale pH 1 to pH 14, (b) chart for scale pH 3 to pH 6, and (c) chart for scale pH 5 to pH 9.

To verify the behaviour of the strips, several values of pH (see Figure 5.7) are measured. This figure shows a linear behaviour in the measured ranges. It shows that the Hue of the strips behaves in a linear fashion, thus enabling the creation of a linear regression model (the red line in Figure 5.7) to characterize each type of strip. Based on this linear model, the system can be calibrated by measuring two different pH values.

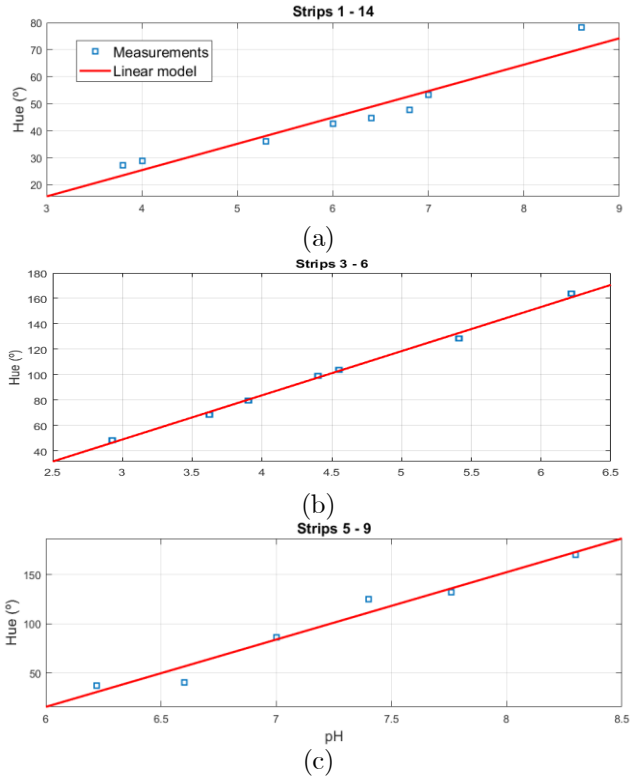


Figure 5.7. Hue measurements of several known pH values. (a) Strips 1 to 14, (b) strips 3 to 6: and (c) strips 5 to 9.

Since most current methods for determining the colour of reactive strips are based on the image processing of a photograph of the strips [4]–[6], The sensor colour reading and the image processed by two different cameras are compared. The main disadvantages of image processing systems are the variability in luminosity in the samples and the colour correction applied to the pictures by each vendor. To compare the two methods, we took 30 measurements of four different strips. Figure 5.8 shows the Hue calculated by placing and removing

30 times the strips from the 3D-printed enclosure (the black line with diamonds). The red and blue lines show the results of 30 pictures taken for each case at various distances (between 20 and 50 cm) and with smooth changes in angle. The images were taken by two different cameras in conditions of direct and indirect light for each (the continuous and dashed lines, respectively).

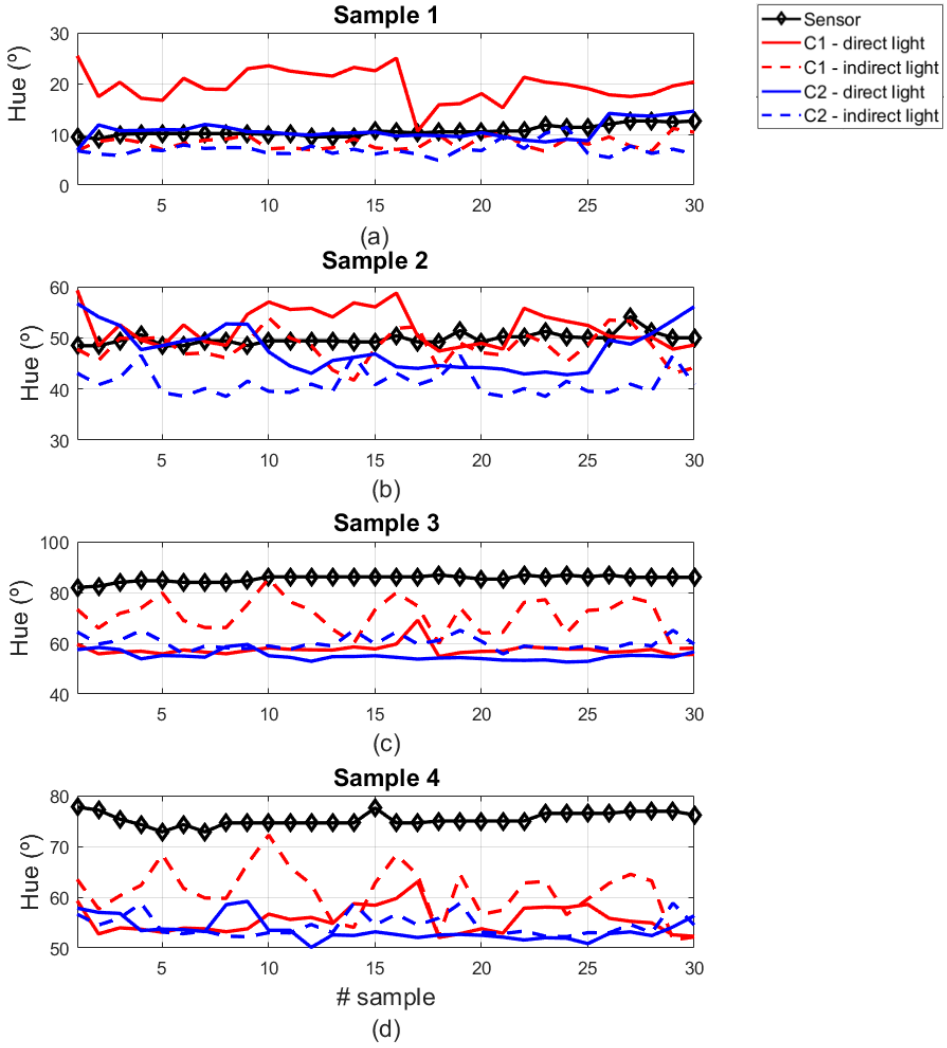


Figure 5.8. Comparison of Hue angle for 30 iterations of 4 different cases. (a) Strips from 1 to 14: pH 4, (b) strips from 1 to 14: pH 7, (c) strips from 3 to 6: pH 4 and (d) strips from 5 to 9: pH 7.

The pictures were taken at the maximum resolution for each camera (5488×4112 pixels for camera 1 and 5120×3840 pixels for camera 2). The images were analysed using Matlab. The exact reactive part of the strips was selected manually. The average RGB was measured and converted to HSV using (5.1) and (5.2). This was therefore the same process as that used by image-processing systems.

It can be seen how the iterations measured with this system behave linearly, since the lighting conditions and the distance between the sensor and the samples to be measured were always the same. For colour analysis based on photography, on the other hand, these parameters were much more unstable.

Table 5.II shows the standard deviation for each sample and each sensing method. The effects of different lighting conditions and the deviation from accurate focus are quantified. As the mean deviation values show, the results from camera 2 were better than those from camera 1. However, the best results were obtained with the proposed sensor.

Table 5.II. Hue standard deviation (degrees)

| | sample 1 | sample 2 | sample 3 | sample 4 | Mean deviation |
|---|---|---|---|---|---|
| Sensor | 1.01 | 1.16 | 1.25 | 1.27 | 1.17 |
| C1 direct light | 3.19 | 3.62 | 2.47 | 2.74 | 3.00 |
| C1 indirect light | 1.27 | 3.16 | 7.03 | 5.08 | 4.14 |
| C2 direct light | 1.82 | 4.23 | 1.76 | 2.24 | 2.51 |
| C2 indirect light | 1.34 | 2.49 | 2.73 | 2.14 | 2.18 |

To graphically represent the deviation observed when the same sample was measured several times, Figure 5.9 shows the histograms for the values obtained. In all cases the sensor obtained the best results.

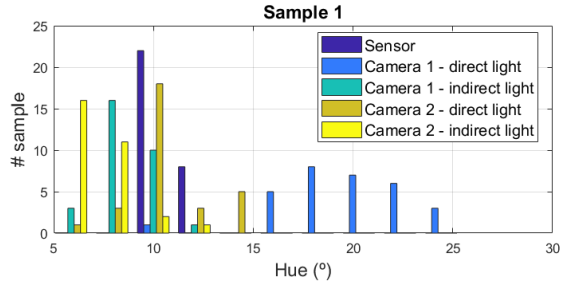


(a)

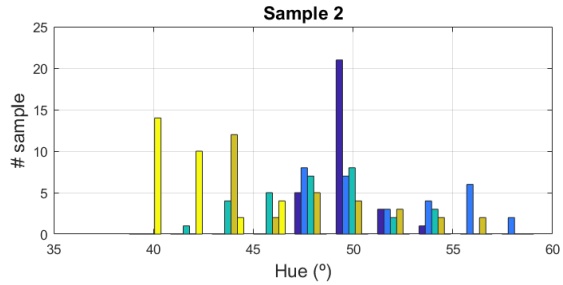


(b)

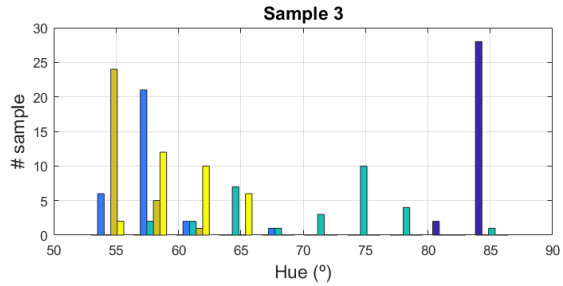


(c)

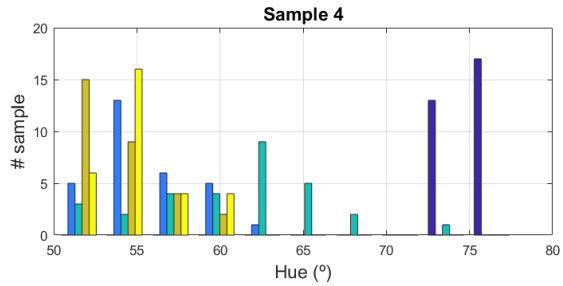


(d)

Figure 5.9. Histograms of measured values for 4 different cases. (a) Strips from 1 to 14: pH 4, (b) strips from 1 to 14: pH 7, (c) strips from 3 to 6: pH 4 and (d) strips from 5 to 9: pH 7.

Although light plays an important role when measuring colour, several other factors, including camera optics, image focusing, and processing software can also affect the reading. Moreover, systems based on image processing need complex software to detect which part of the image should be analysed. For this reason, the proposed system can achieve better results: the conditions are always the same and the smartphone used to obtain the pH has no effect on the colour reading. This system is therefore device-independent, does not depends on environment conditions, and is simpler than other methods for determining the colour of the reactive strips.

An Android application to display the results has been designed. This application reads the HSV values using the NFC protocol. Using the stored linear model, returns the pH. It also includes an option to calibrate strips from different manufacturers. For this purpose, two measurements for known pH values must be taken. The pH data are uploaded to a cloud database in order to store all historical measurements, and for further analysis. Figure 5.10(a) shows an image of the application's main screen, while Figure 5.10(b) shows the calibration screen indicating the two known pH values used to calculate the linear function that are used to estimate the pH of the measurements.

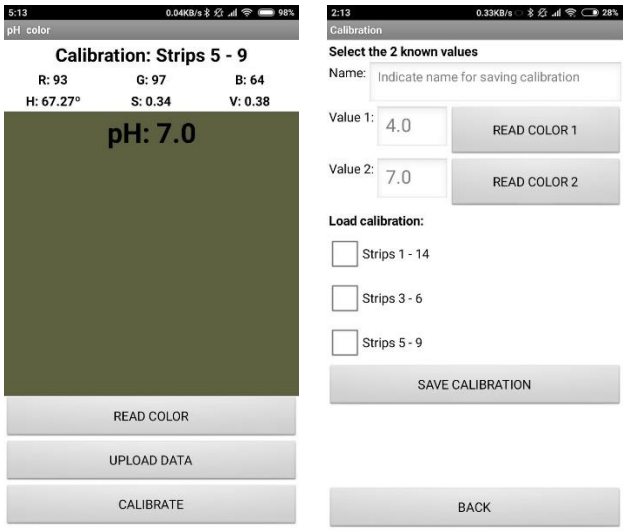


(a) (b)

Figure 5.10. Designed Android APP: (a) main screen, (b) calibration screen

Figure 5.11 shows the device with its 3D-printed enclosure and a strip. It also shows the smartphone used to power up the device and obtain the data and a display of the designed application. The theoretical and experimental read range obtained for the tag prototype is up to 18 mm depending on the smartphone used.

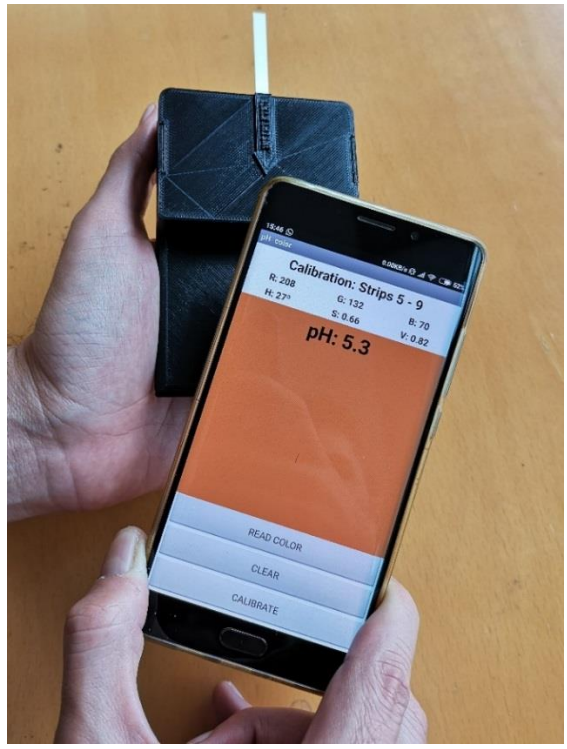


Figure 5.11. Reading the colour of a strip and calculating the pH with the Android application.

Figure 5.12 shows a graph on the ThingSpeak IoT database, which shows several measurements of the pH in a swimming pool. The measures have been done during the same day with Historical measurements can thus be accessed from any device connected to the internet. This is an example of a weekly water analysis performed by the pool's maintenance staff. In this way the maintenance routine can be monitored to ensure that the pH is kept within an acceptable range for the swimming pool. To simulate a real scenario, several pH

measurements have been done in the lab and updated to the database modifying the date, representing a larger period.

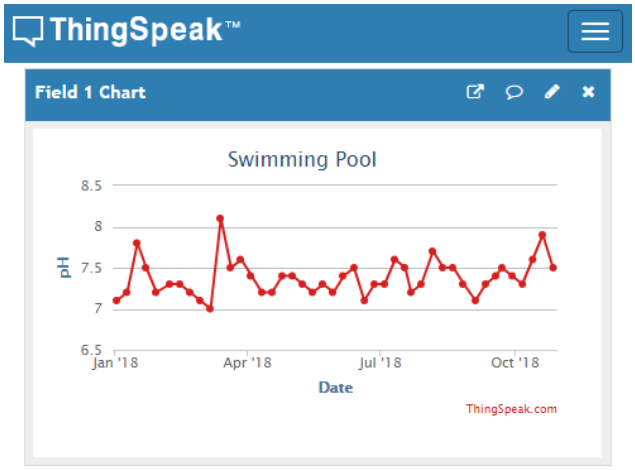


Figure 5.12. Cloud database showing the pH measurements of a swimming pool taken over several months.

## 5.5 Conclusions

A batteryless, low-cost colorimeter integrated into an NFC tag has been presented. While this device has several applications, in this chapter it has been applied to the measurement of pH using pH-sensitive paper strips. Raw RGB measurements of the colorimeter IC are transformed into HSV colour space. A simple linear relationship is found between pH and Hue for typical commercial strips. The pH is obtained from this model and can be easily calibrated using two known pH solutions. The repeatability and reliability of the measurement is higher than for methods based on smartphone cameras because the measurements are taken in controlled light conditions. A smartphone application to read the data from the NFC tag and send the pH to a cloud database has been designed.

## 5.6 Bibliography

[1] A. W. Martinez, S. T. Phillips, G. M. Whitesides, and E. Carrilho, "Diagnostics for the developing world: Microfluidic paper-based analytical devices," *Anal. Chem.*, vol. 82, no. 1, pp. 3–10, 2010.

[2] V. Oncescu, D. O'Dell, and D. Erickson, "Smartphone based health accessory for colorimetric detection of biomarkers in sweat and saliva," *Lab Chip*, vol. 13, no. 16, pp. 3232–3238, 2013.

[3] C. Sicard *et al.*, "Tools for water quality monitoring and mapping using paper-based sensors and cell phones," *Water Res.*, vol. 70, pp. 360–369, 2015.

[4] N. K. Vuong, S. Chan, and C. T. Lau, "PH levels classification by color quantization on a camera phone," *2010 WRI Int. Conf. Commun. Mob. Comput. C. 2010*, vol. 1, pp. 448–452, 2010.

[5] B. Y. Loh, N. K. Vuong, S. Chan, and C. T. Lau The, "Robust classification of pH levels on a camera phone," *IMECS 2011 - Int. MultiConference Eng. Comput. Sci. 2011*, vol. 1, pp. 600–604, 2011.

[6] S. D. Kim, Y. Koo, and Y. Yun, "A smartphone-based automatic measurement method for colorimetric pH detection using a color adaptation algorithm," *Sensors (Switzerland)*, vol. 17, no. 7, 2017.

[7] Y. Hashimoto, M. Hamaguchi, N. Nakanishi, A. Ohbora, T. Kojima, and M. Fukui, "Urinary pH is a predictor of diabetes in men; a population based large scale cohort study," *Diabetes Res. Clin. Pract.*, vol. 130, pp. 9–14, 2017.

[8] C. G. McCarty and E. Vitz, "pH paradoxes: Demonstrating that it is not true that pH = -log[H+]," *J. Chem. Educ.*, vol. 83, no. 5, pp. 752–757, 2006.

[9] "2018 - Handheld colorimeter as quality control tool for inkjet printed flexible levothyroxine doses for pediatric use.pdf." .

[10] R. B. Dominguez, M. A. Orozco, G. Chávez, and A. Márquez-Lucero, "The evaluation of a low-cost colorimeter for glucose detection in salivary samples," *Sensors (Switzerland)*, vol. 17, no. 11, pp. 19–21, 2017.

[11] P. Escobedo *et al.*, "Flexible Passive near Field Communication Tag for Multigas Sensing," *Anal. Chem.*, 2017.

[12] P. Kassal, I. M. Steinberg, and M. D. Steinberg, "Wireless smart tag with potentiometric input for ultra low-power chemical sensing," *Sensors Actuators, B Chem.*, vol. 184, pp. 254–259, 2013.

[13] R. Rahimi, U. Brener, M. Ochoa, and B. Ziaie, "Flexible and transparent pH monitoring system with NFC communication for wound monitoring applications," in *Proceedings of the IEEE*

*International Conference on Micro Electro Mechanical Systems (MEMS)*, 2017.

[14] TAOS, "TCS3472 COLOR LIGHT-TO-DIGITAL CONVERTER with IR FILTER," 2012.

[15] K. Finkenzeller, *Rfid handbook : fundamentals and applications in contactless smart cards, radio frequency identification and near-field communication*. Wiley, 2014.

[16] Dominique Paret., *Design Constraints for NFC Devices*. Wiley-ISTE, 2016.

[17] J. I. Agbinya, *Wireless power transfer*. .

[18] A. Costanzo, M. Dionigi, F. Mastri, M. Mongiardo, J. A. Russer, and P. Russer, "Rigorous network modeling of magnetic-resonant wireless power transfer," *Wirel. Power Transf.*, vol. 1, no. 1, pp. 27–34, 2014.

[19] M. Gebhart, "Analytical considerations for an ISO / IEC14443 compliant SmartCard transponder," *Proc. 11th Int. Conf. Telecommun.*, pp. 9–16.

[20] M. Ishii and K. Komiyama, "A Measurement Method for the Antenna Factor of Small Loop Antenna by Measuring the Input Impedance," pp. 80–81, 2007.

[21] A. Lazaro, R. Villarino, D. Girbau, A. Lazaro, R. Villarino, and D. Girbau, "A survey of NFC sensors based on energy harvesting for IoT applications," *Sensors (Switzerland)*, vol. 18, no. 11, p. 3746, Nov. 2018.

[22] X. Qing and Z. N. Chen, "Proximity effects of metallic environments on high frequency RFID reader antenna: Study and applications," *IEEE Trans. Antennas Propag.*, vol. 55, no. 11 I, pp. 3105–3111, 2007.

[23] H. Zhu, S. Lai, and H. Dai, "Solutions of metal surface effect for HF RFID systems," *2007 Int. Conf. Wirel. Commun. Netw. Mob. Comput. WiCOM 2007*, no. 1, pp. 2089–2092, 2007.

[24] M. Gebhart, R. Neubauer, M. Stark, and D. Warnez, "Design of 13.56 MHz Smartcard Stickers with Ferrite for Payment and Authentication," in *2011 Third International Workshop on Near Field Communication*, 2011, pp. 59–64.

[25] H. L. H.T. Jensen, "Chassis NFC antenna booster," U.S. Patent No.

9,729,210, 2017.

[26] B. Lee, B. Kim, and S. Yang, "Enhanced loop structure of NFC antenna for mobile handset applications," *Int. J. Antennas Propag.*, vol. 2014, 2014.

[27] J.-Q. Zhu, Y.-L. Ban, C.-Y.-D. Sim, and G. Wu, "NFC Antenna With Nonuniform Meandering Line and Partial Coverage Ferrite Sheet for Metal Cover Smartphone Applications," *IEEE Trans. Antennas Propag.*, vol. 65, no. 6, pp. 2827–2835, Jun. 2017.

[28] "NFC antenna assembly," May 2016.

[29] A. Zhao and H. Chen, "Small size NFC antenna with high performance," *2016 IEEE Antennas Propag. Soc. Int. Symp. APSURSI 2016 - Proc.*, vol. 3, pp. 1469–1470, 2016.

[30] H. Chen and A. Zhao, "NFC antenna for portable device with metal back cover," *2016 IEEE Antennas Propag. Soc. Int. Symp. APSURSI 2016 - Proc.*, pp. 1471–1472, 2016.

[31] M. A. Chung and C. F. Yang, "Miniaturized NFC Antenna Design for a Tablet PC With a Narrow Border and Metal Back-Cover," *IEEE Antennas Wirel. Propag. Lett.*, vol. 15, pp. 1470–1474, 2016.

[32] B. Lee and F. J. Harackiewicz, "Design of a simple structured NFC loop antenna for mobile phones applications," *Prog. Electromagn. Res. C*, vol. 76, no. June, pp. 149–157, 2017.

[33] M. Boada, A. Lazaro, R. Villarino, E. Gil, and D. Girbau, "Near-Field Soil Moisture Sensor with Energy Harvesting Capability," in *2018 48th European Microwave Conference, EuMC 2018*, 2018, pp. 235–238.

[34] F. Pierre, J. F. Aujol, A. Bugeau, and V. T. Ta, "Luminance-Hue specification in the RGB space," in *Lecture Notes in Computer Science (including subseries Lecture Notes in Artificial Intelligence and Lecture Notes in Bioinformatics)*, 2015, vol. 9087, pp. 413–424.

[35] N. Lopez-Ruiz *et al.*, "Smartphone-based simultaneous pH and nitrite colorimetric determination for paper microfluidic devices," *Anal. Chem.*, vol. 86, no. 19, pp. 9554–9562, 2014.

[36] S. Capel-Cuevas *et al.*, "A compact optical instrument with artificial neural network for pH determination," *Sensors (Switzerland)*, vol. 12, no. 5, pp. 6746–6763, 2012.

# 6. Fruit ripeness sensor

## 6.1 Motivation

Food appearance determined by surface colour is the first sensation that the consumer perceives and has a great influence on the consumer's choice. Food colour depends on various factors, including the chemical, biochemical, microbial and physical changes that occur during growth, maturation, postharvest handling and processing [1]. Therefore, food colour can be used as a quality indicator. Colour is one of the most widely measured product quality attributes in postharvest handling and in food processing research and industry.

In recent years, the consumers' interest in ecological food, the origin, and the traceability have grown. RFID technology could play an important role in the following years. With the long marketing chain for many fruits and vegetables that is currently operating, the used-by-date or recommended date of consumption is difficult to establish for these products. Surface colour can be a good parameter to give an indication of the freshness and flavour quality of fresh products. For example, the ripening process of tomatoes is clearly characterized by the colour evolution of the fruit surface. After harvesting, the fruit continues to ripen and its colour turns from green to red. Due to transportation delays, tomatoes that are already ripe (red) must be sold to local markets and green tomatoes can be shipped to customers at much greater distances [2]. Colour has been used to evaluate fruit maturity for tomatoes [3], bananas [4], apples [5], pears [6], oranges [7] and dates [8]. Some colours are associated with food products. For instance, yellow is associated with ripe bananas in a good state and good tomatoes are associated with red instead of orange.

Food colour measurements have been made using a large variety of instruments [1]: colorimeters [9], spectrophotometers [10], [11] and colour measurement by computer vision with digital cameras [3]–[8], [12]. However, sometimes these instruments are expensive, or the measurement setups are not suitable for performing real-time measurements by a consumer in a supermarket or at home.

Colorimeters and spectrophotometers are devices that can be used to measure the colour of a test sample. A spectrophotometer is an

instrument with high precision and is adequate for more complex colour analyses because it can measure the spectral reflectance at each wavelength. However, spectrophotometers are more expensive than colorimeters. Therefore, a colorimeter is the best choice for quality inspection. In this chapter, a low-cost battery-less NFC tag is presented for food colour measurement and classification based on the measured colour and using a smartphone. A simple tap is required for the colour measurement using the smartphone equipped with NFC to read the colour measured by a colorimeter integrated into the tag. This low-cost device can be used to classify different fresh products in the supermarket or at home.

## 6.2 System overview

A system overview is shown in Figure 6.1. The food being tested is placed over the aperture of the colorimeter integrated into the NFC tag. Its colour is a function of the temperature, humidity and days since it was harvested. When the user taps his smartphone equipped with an NFC reader, the NFC IC in the tag obtains energy from the RF interrogating signal that is used to feed the circuitry and returns the colour measurement as an NFC message. The application in the smartphone reads the message, classifies the quality of the food and gives additional information about the origin or some other useful information. This information, as well as the parameters needed for food classification, can be automatically downloaded from the cloud.

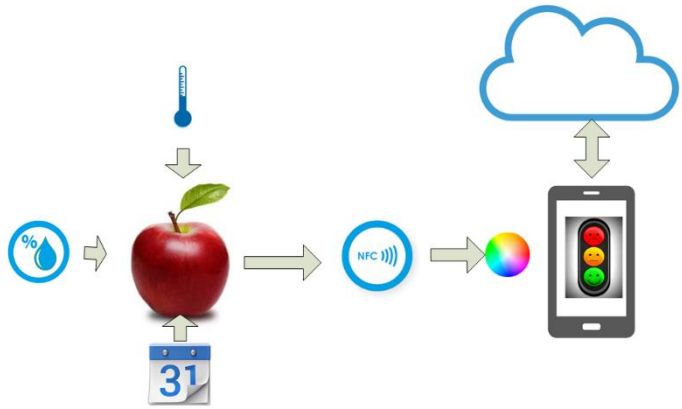


Figure 6.1. System overview.

The tag is identical to the one presented in the previous chapter, composed by an M24LR04E NFC IC, an ATtiny85 as a microcontroller, and the colour sensor TCS34725, with a total consumption of nearly 3 mA (see Table 5.I). For the purpose of this work a 3D printed enclosure for the tag with an opening on the colour sensor has been designed (Figure 6.2).

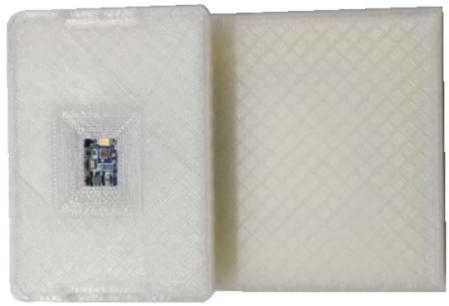

Figure 6.2 Tag within the 3D printed enclosure.

## 6.3 Experimental results

In order to test the system, different typical fruits (bananas, and red and golden apples) were measured with the NFC colorimeter. Several samples on different days at room temperature and within the fridge were tested. The objective was to classify the quality of the pieces of fruit depending on the number of days outside the fridge and using the colour information. A fruit is considered to belong to the good class if the days at room temperature outside the fridge are equal to or less than six. The aim is to find a simple but accurate method that, after a training process performed by the product manufacturer, the consumer can apply using a smartphone without sophisticated tools such as Matlab.

The colour of an object can be described by several colour coordinate systems (called colour spaces). Figure 6.3 shows the representation of the RGB, HSV and CIELab colour spaces. The first decision is to choose the colour space. The most popular is RGB (red, green and blue), which is used in video monitors. The raw RGB information given by the colorimeter is rarely used in the literature on food classification. HSV [15] and Lab [15] are alternative representations of the RGB colour model designed to be more closely aligned to the way human vision perceives colour-making attributes. HSV and Lab

colour spaces are the most used in the literature for this application [16]–[18]. The most frequently used is the CIELab colour space, due to its uniform colour distribution and because its colour perception is closest to that of the human eye. The colour in the CIELab colour space is determined by three values: L* is the lightness, and a* and b* are the green-red and blue-yellow colour components, respectively. Humans identify a coloured object through its chromaticity and brightness. The chromaticity can be further divided into two parts: hue and saturation.

The ratio a/b was used as a colour index in apples, tomatoes, citrus and carambola fruit [1]. A high correlation between peel colour related to maturity and Hunter's a/b ratio for mangos has been found in [19]. However, this ratio is a function of the hue, which is the angle that can be computed from ratio *atan*(a/b). Therefore, the HSV model is used in this work.

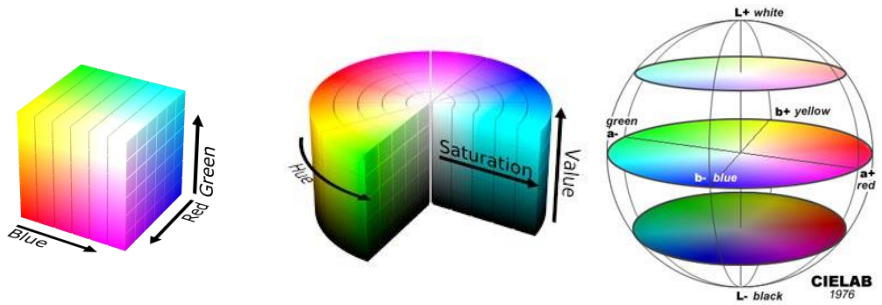


(a) (b) (c)

Figure 6.3. (a) RGB colour space, (b) HSV colour space, (c) CIELab colour space.

Three kinds of fruit are considered (bananas, red apples, and golden apples). Figure 6.4-6 shows the histograms of HSV measurements of a golden apple, banana and red apple, as a function of the days and the ripening conditions (in the fridge and at room temperature). The measurements were taken with the colorimeter of the NFC tag. For example, the Cumulative Distribution Function (CDF) of the hue for the golden apple in the fridge and at room temperature as a function of the number of days is shown in Figure 6.7. It can be observed that the colour variation is smooth in the case of the fruit conserved in the fridge, whereas the shift is faster at room temperature. Therefore, the ripeness grade is also a function of environment parameters. Figure 6.5-6.11 show the histograms of HSV measurements and CDF of the hue parameter for the banana

(Figure 6.5-6.9) and red apple (Figure 6.6-6.10). Similar behaviour is obtained for both the banana and red apple.

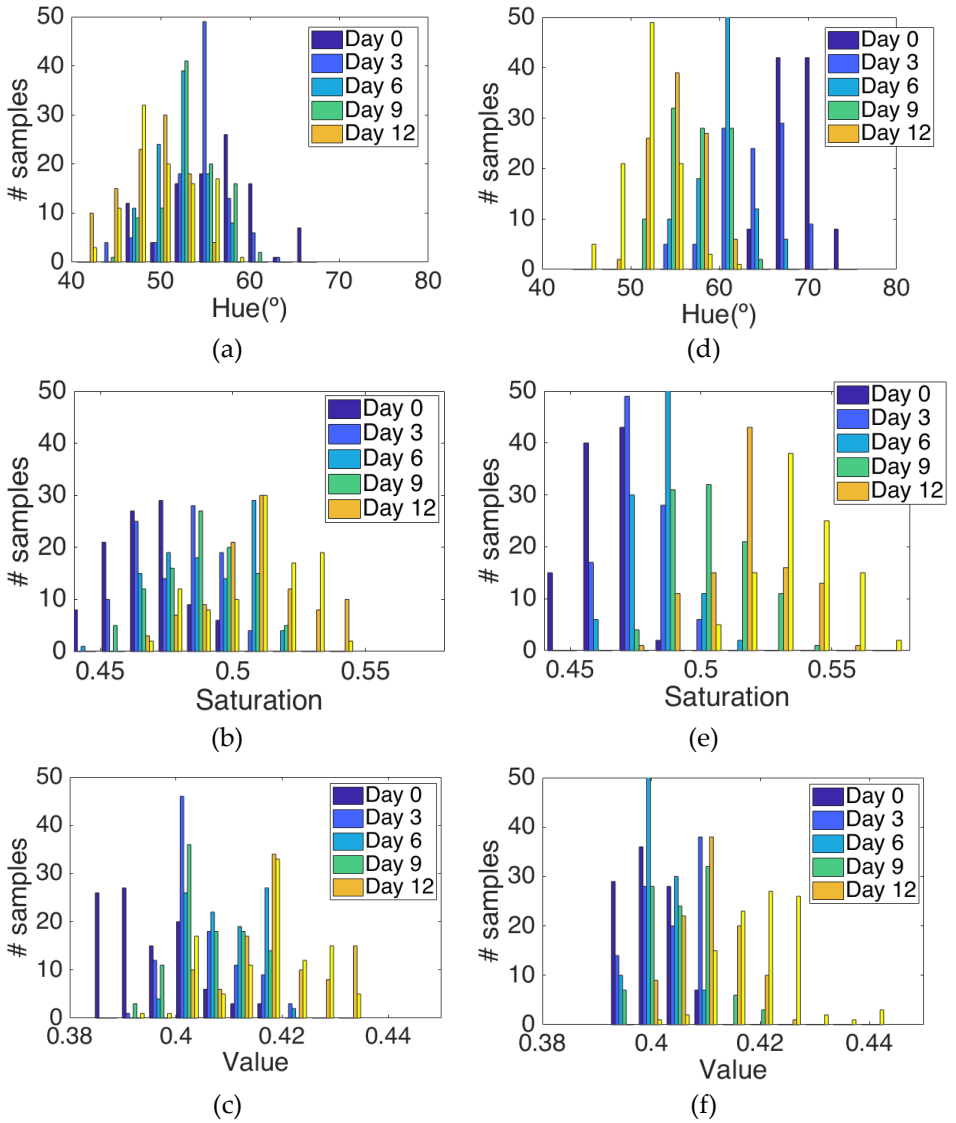


Figure 6.4. Histogram for the golden apple for different days: histogram of the Hue (a), Saturation (b) and Value (c) parameters in the fridge. Histogram of the Hue (d), Saturation (e) and Value (f) parameters at room temperature.

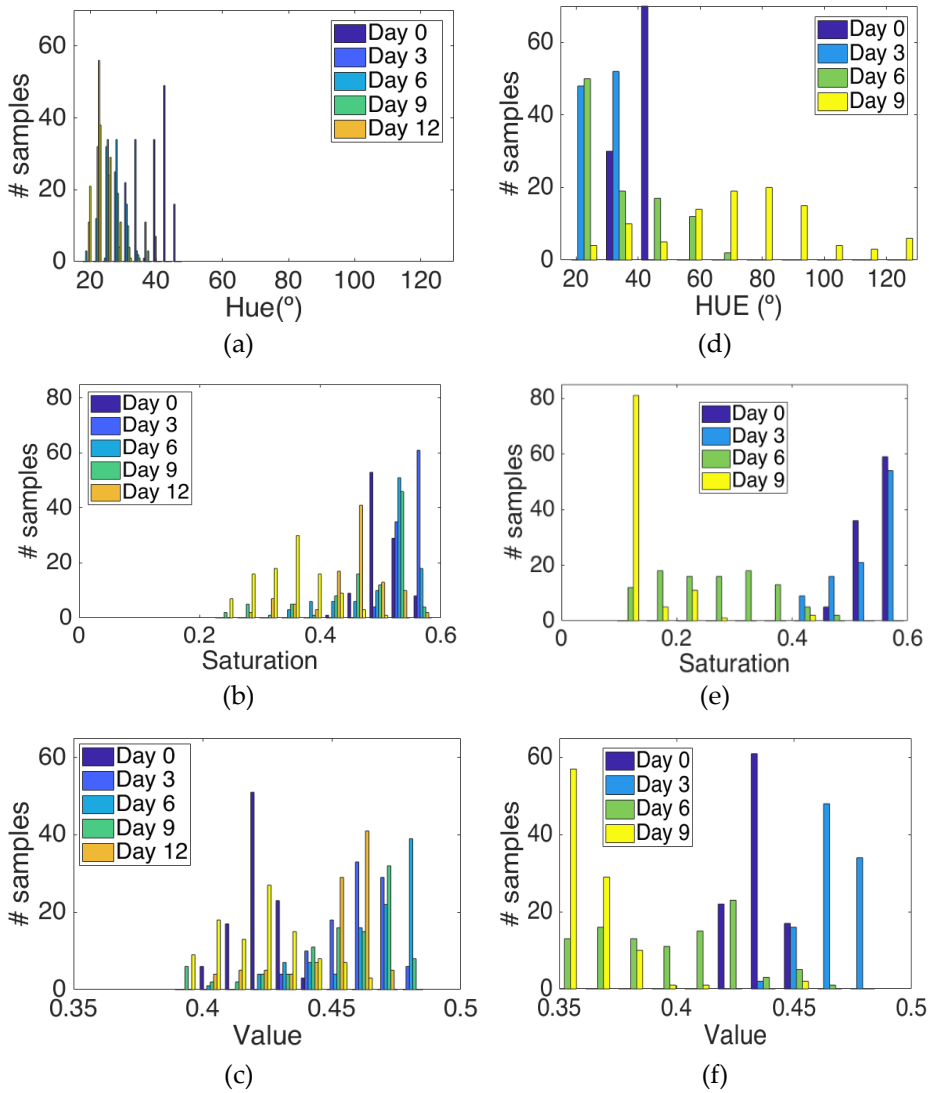


Figure 6.5. Histogram for a banana for different days: histogram of the Hue (a), Saturation (b) and Value (c) parameters in the fridge. Histogram of the Hue (d), Saturation (e) and Value (f) parameters at room temperature.

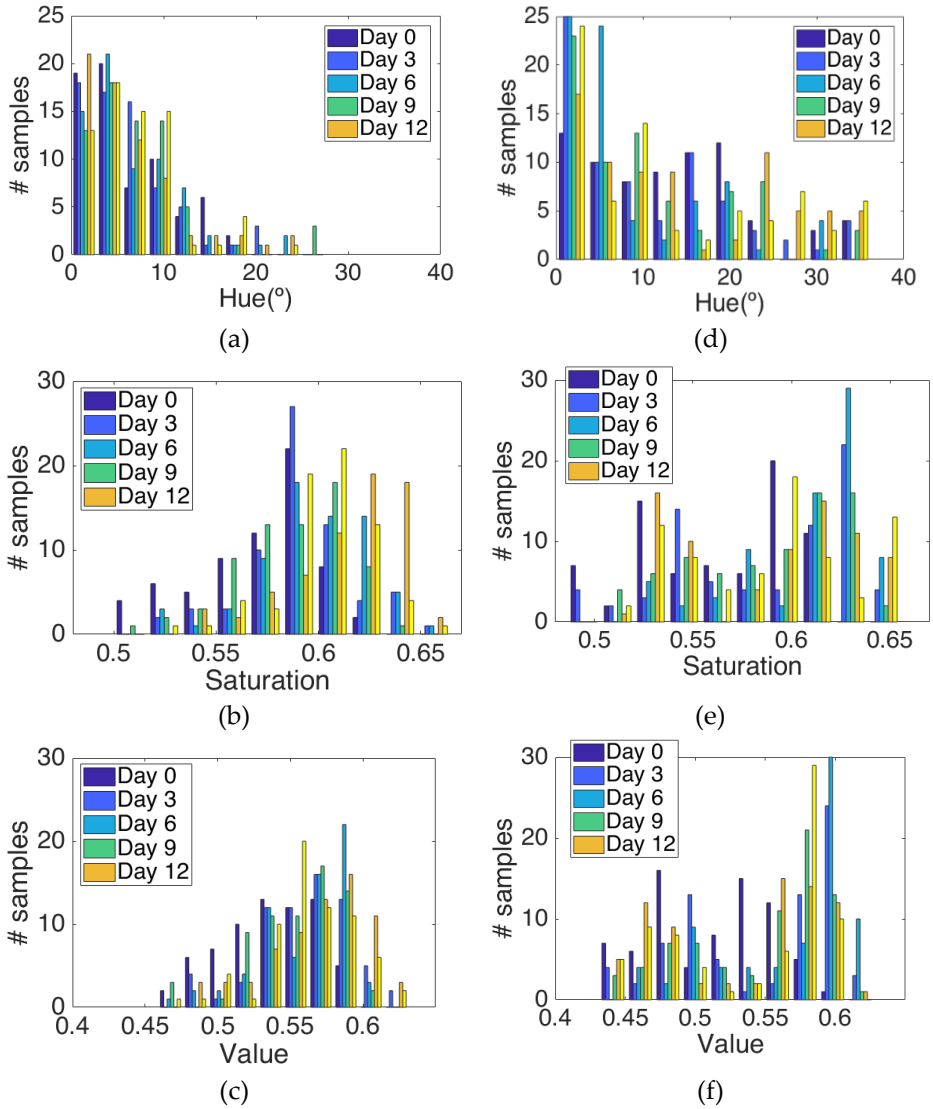


Figure 6.6. Histogram for a red apple for different days: histogram of the Hue (a), Saturation (b) and Value (c) parameters in the fridge. Histogram of the Hue (d), Saturation (e) and Value (f) parameters at room temperature.

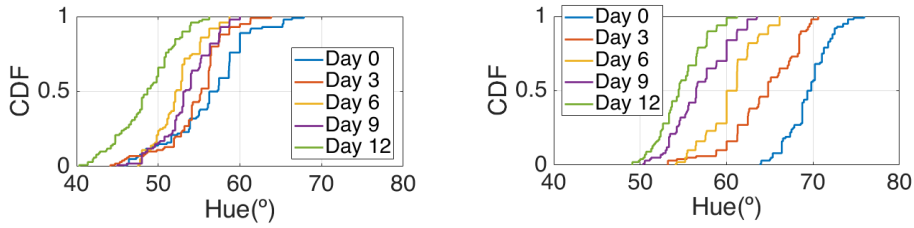


Figure 6.7. Cumulative Distribution Function (CDF) of the Hue parameter for the golden apple in the fridge (a) and at room temperature (b) as a function of the number of days out of the fridge.

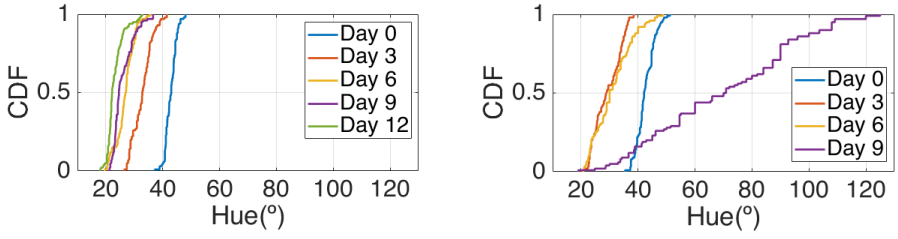


Figure 6.8. Cumulative Distribution Function (CDF) of the Hue parameter for the banana in the fridge (a) and at room temperature (b) as a function of the number of days.

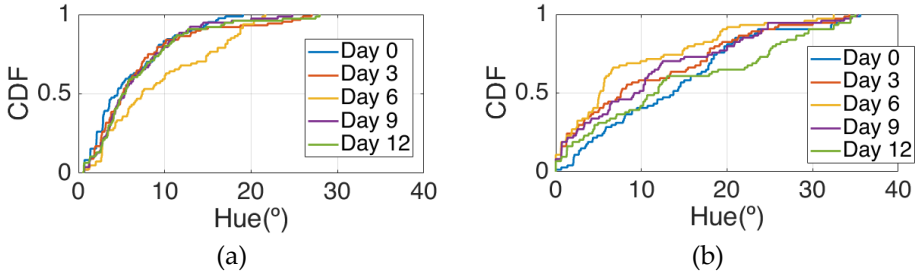


Figure 6.9. Cumulative Distribution Function (CDF) of the Hue parameter for the red apple in the fridge (a) and at room temperature (b) as a function of the number of days.

HSV and CIELab values were studied in order to select the most suitable values to analyse the ripeness state of the fruit. Table 6.I shows the average of 100 samples for each fruit stored at room temperature, comparing the measurements of the first day (day 0) against the measurements after a few days (day 15 for apples, and day 9 for bananas). The $\Delta\%$ row shows the percentage increment/ of each parameter, considering the range of each parameter. It can

be observed that the best combination is obtained using the H and S values. Hue changes 8.7% for red apples, 5.4% for golden apples and 1.6% for bananas; whereas saturation (S) changes 42% for red apples, 12% for golden apples and 2% for bananas. However, the variations are smaller using CIELab colour space, with differences between 0.1% and 2% for L, 1.2% and 4.3% for parameter a* and 1.4% and 8.2% for parameter b*.

Table 6.I. Average readings of HSV and L*a*b of 100 samples. Comparative change of each parameter over time.

| Fruit | Days | H | S | V | L* | a* | b* |
|---|---|---|---|---|---|---|---|
| Golden Apple | Day 0 | 59.4 | 0.48 | 0.40 | 41.1 | -7.3 | 26.6 |
| | Day 15 | 40.0 | 0.60 | 0.46 | 40.9 | 3.6 | 30.2 |
| | Δ % | 5.4 | 12.00 | 6.00 | 0.1 | -4.3 | 1.4 |
| Banana | Day 0 | 17.4 | 0.58 | 0.51 | 37.9 | 20.6 | 22.1 |
| | Day 15 | 23.2 | 0.60 | 0.51 | 39.4 | 17.6 | 25.8 |
| | Δ % | 1.6 | 2.00 | 0.00 | 1.5 | 1.2 | 1.4 |
| Red Apple | Day 0 | 41.2 | 0.55 | 0.44 | 40.0 | 2.0 | 27.1 |
| | Day 9 | 72.5 | 0.13 | 0.36 | 38.0 | -2.4 | 6.0 |
| | Δ % | 8.7 | 42.00 | 8.00 | 2.0 | -1.7 | 8.2 |

Extracting and selecting features helps to improve a machine learning algorithm by focusing on the data that are most likely to produce accurate results. The challenge is to find the minimum number of features that will capture the essential patterns in the data. From the histograms presented above, it can be concluded that the hue angle and saturation are good choices. The variation over time is higher compared to the Value parameter. Another possibility is to apply PCA (Principal component analysis) to find the principal components in order to reduce the number of features. However, PCA is not considered to simplify the implementation in a mobile environment because it can increase the computational complexity.

The next step is to select a machine learning algorithm. No single machine learning algorithm works for every problem; therefore, the best algorithm is found by exploring the datasets for different algorithms. The comparisons were performed using the statistics and machine learning toolbox in the Matlab R2017a software. The training is performed using a computer with Matlab and ideally should be performed by the manufacturer or a laboratory; however,

once the training is finished, the parameters are sent to the cloud server, from where the consumer can download the parameters that are necessary for predicting the class. Therefore, as the prediction step will be made on a mobile, the simplicity of the algorithm and minimal tuning play an important role. Another possibility is that a cloud server executes a program that returns the results as a function of the colour measurement. However, mobile computing is preferred. Two classes were considered: good state (days <6) and bad state (days>=6) assuming that the fruit is outside the refrigerator. Other intermediated classes can be defined if necessary. Half of the measurements in the dataset were used for training and the other half were used for testing the prediction. In this chapter the following algorithms are considered: linear SVM [20], linear discriminate analysis (LDA) [21], Naive Bayes [22], decision tree [23] and nearest neighbour [24]. Neural networks are not included because they often require a lot of tuning parameters.

Although SVM and LDA have the same boundary decision (a line), their assumptions are different. LDA assumes that data are distributed normally. SVM makes no assumptions about the data at all, which means that it is a very flexible method. LDA makes use of the entire data set to estimate covariance matrices, and therefore is somewhat prone to outliers. SVM is optimized over a data subset that includes those data points that lie on the separating margin. The data points used for optimization are called support vectors because they determine how the SVM discriminate between groups and thus support the classification.

The Naive Bayes classifier is designed to be used when predictors are independent of one another within each class; however, it appears to work well in practice even when the independence assumption is not valid. It is a classification technique based on Bayes' theorem with an assumption of independence among predictors. In simple terms, a Naive Bayes classifier assumes that the presence of a particular feature in a class is unrelated to the presence of any other feature.

The decision tree classifier is a simple and widely used classification technique. It repetitively divides the working area (plot) into subparts by identifying lines. In general, decision trees are constructed via an algorithmic approach that identifies ways to split a data set based on different conditions. It is one of the most widely

used and practical methods for supervised learning. Decision tree is a non-parametric supervised learning method used for both classification and regression tasks. The goal is to create a model that predicts the value of a target variable by learning simple decision rules inferred from the data features. Decision trees divide the feature space into axis-parallel rectangles or hyperplanes.

The nearest neighbour search locates the k-nearest neighbours or all neighbours within a specified distance from certain query data points, based on the specified distance metric. An object is classified by a majority vote of its neighbours, with the object being assigned to the most-common class among its k nearest neighbours (k is a positive integer, typically small). If k = 1, then the object is simply assigned to the class of that single nearest neighbour. One of the simplest decision procedures that can be used for classification is the nearest neighbor (NN) rule. This classifies a sample based on the category of its nearest neighbor.

In order not to introduce any bias in the classification results, the dataset is composed of the same number of measurements each day. Another fruit that is not included in the training dataset is used for testing. Figure 6.10-6.12 show the decision regions found for each algorithm superposed on the scatter plot of the training measurements of the dataset.

To explore the trade-off between different kinds of misclassification, a confusion matrix is used. Table 6.II summarizes the confusion matrix calculated with different methods: linear SVM, Naive-Bayes, decision tree, and Nearest Neighbor, showing the true positives ($TP$), false positive ($FP$), false negative ($FN$), and true negative ($TN$) percentages. In order to compare the methods, the accuracy is also included. The accuracy of the confusion matrix is computed using (6.1) and the results for each feature are illustrated in the last column in Table 6.II.

$$Accuracy(\%) = 100\frac{TP + TN}{TOTAL\ DATA} \tag{6.1}$$

The highest accuracy is obtained for the banana and the worst for the red apple. In the case of the golden apple, the two features (hue and saturation) are clearly correlated because all the training points

fall along a line. Therefore, a single feature (for example the Hue or using PCA decomposition) can be used for classification. A smooth variation of the colour is found as a function of the time. The decision boundary found for all classifiers is a perpendicular line to this line. Accuracies of about 82-84% are obtained depending on the classifier algorithm considered. In the case of the banana, as it can be observed from the histogram, the colour remains nearly constant for the first days, and then starts to degrade fast from the $6^{th}$ day. The change in the colour is in both hue and saturation features and the relation is not as linear as in the case of the golden apple. However, the two classes are clearly separable and high accuracy is obtained for all the classifiers. The last case is more complicated to classify because the colour is not homogeneous. This fruit has regions of red but other regions are close to yellow. To avoid this problem only the red region is considered, and the points are filtered before the training in the range of hue$<50^{o}$. If a point falls outside this range, the application asks the user to repeat the measurement in another point in the red region. After outliers have been filtered, the colour degradation is smooth as in the case of the golden apple. However, due to the heterogeneous distribution of the colour on the surface, the accuracy obtained for the different classifier algorithms is considerably lower than in the previous cases. Only LDA and Nearest Neighbour with k=5 obtained reasonable values of 73% and 71%, respectively. An improvement is found if a quadratic discriminant analysis (QDA) is used, achieving an accuracy of 80% because the boundary decision can be described better for a parabolic function.

Machine learning applications can be deployed in production systems on desktops, in enterprise IT systems (either onsite or in the cloud), and embedded systems. For prediction, the linear SVM, LDA or QDA give an analytic boundary decision function (a line or quadratic function) that only needs to know the polynomial coefficients to define the decision region. The evaluation of the algorithm in the other methods requires the training data from the server. In addition, it requires the implementation in JAVA, C, PHP or another language in the mobile environment or in the cloud. In order to avoid this problem, a table (or image) can be downloaded from the cloud service that is used to interpolate the results.

Table 6.II. Confusion matrix for ripeness grading identification for different classifiers.

| Fruit | Classifier | TP % | FP % | FN % | TN % | Accu. % |
|---|---|---|---|---|---|---|
| Golden Apple | Naive Bayes | 73.66 | 6.67 | 26.33 | 93.33 | 83.50 |
| | Linear Discriminant Analysis | 73.00 | 8.67 | 27.00 | 91.33 | 82.17 |
| | Decision Tree | 76.33 | 12.33 | 23.67 | 87.67 | 82.00 |
| | Nearest Neighbor | 81.33 | 13.33 | 18.67 | 86.67 | 84.00 |
| | Nearest Neighbor k=5 | 80.00 | 13.67 | 20.00 | 86.33 | 83.17 |
| | SVM | 68.00 | 2.00 | 32.00 | 98.00 | 83.00 |
| Banana | Naive Bayes | 90.00 | 4.00 | 10.00 | 96.00 | 93.00 |
| | Linear Discriminant Analysis | 90.50 | 5.00 | 9.50 | 95.00 | 92.75 |
| | Decision Tree | 84.50 | 3.50 | 15.50 | 96.50 | 90.50 |
| | Nearest Neighbor | 87.00 | 13.00 | 13.00 | 87.00 | 87.00 |
| | Nearest Neighbor k=5 | 87.00 | 3.00 | 13.00 | 97.00 | 92.00 |
| | SVM | 90.50 | 5.50 | 9.50 | 94.50 | 92.50 |
| Red apple | Naive Bayes | 73.33 | 46.67 | 26.67 | 53.33 | 63.33 |
| | Linear Discriminant Analysis | 86.67 | 40.00 | 13.33 | 60.00 | 73.33 |
| | Decision Tree | 63.33 | 40.00 | 36.37 | 60.00 | 61.67 |
| | Nearest Neighbor | 60.00 | 66.67 | 40.00 | 33.33 | 46.67 |
| | Nearest Neighbor k=5 | 80.00 | 36.67 | 20.00 | 63.33 | 71.67 |
| | SVM | 96.67 | 90.00 | 3.3 | 10.00 | 53.33 |
| | QDA | 86.67 | 26.67 | 13.33 | 73.33 | 80.00 |

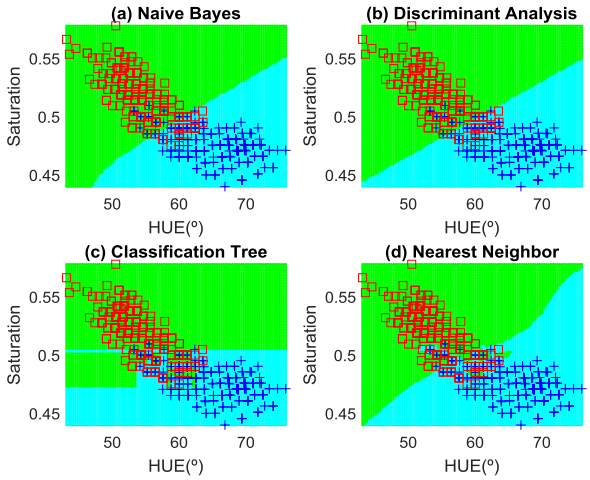


Figure 6.10. Decision boundaries and scatter plot (class 1 squares, class 2, crosses) for the golden apple. (a) Naive Bayes, (b) Linear discriminant analysis, (c) Classification tree and (d) Nearest Neighbour (k=5).

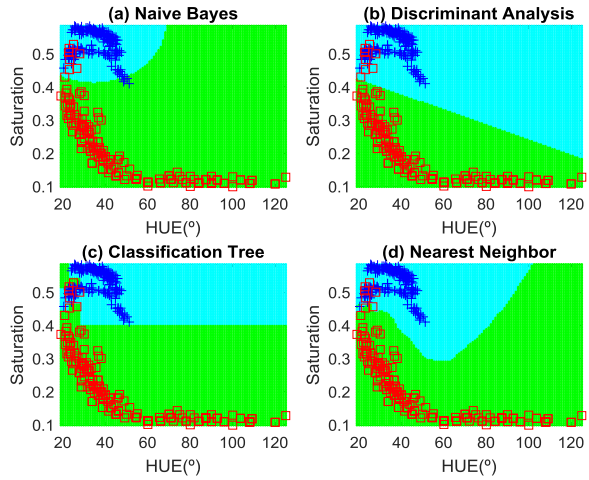


Figure 6.11. Decision boundaries and scatter plot (class 1 squares, class 2, crosses) for the banana. (a) Naive Bayes, (b) Linear discriminant analysis, (c) Classification tree and (d) Nearest Neighbour (k=5).

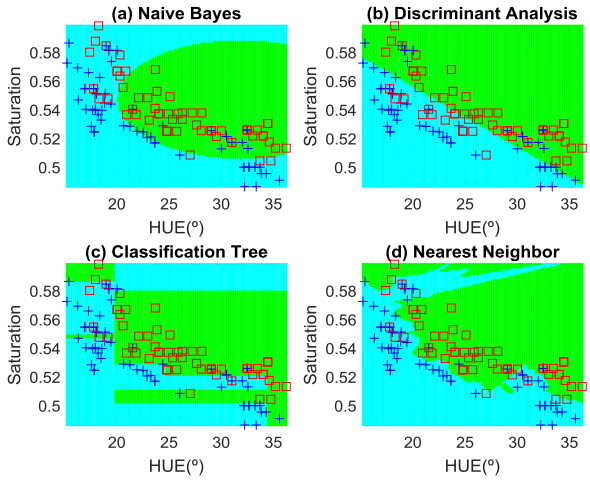


Figure 6.12. Decision boundaries and scatter plot (class 1 squares, class 2, crosses) for the red apple. (a) Naive Bayes, (b) Linear discriminant analysis, (c) Classification tree and (d) Nearest Neighbour (k=5).

An Android application has been developed to analyse the sample and show the result to the user. The operation flow is described in the flowchart of

Figure 6.13. When the application is launched it connects to a server to obtain a list of available fruits and downloads an image and some information about each of them. Then it shows the list of the possible fruits to analyse (Figure 6.14(a)), the user selects the fruit and a message appears to place the smartphone over the tag (Figure 6.14(b)). When the tag is triggered, it performs the colour reading, and sends the NDEF message with the HSV and RGB values to the smartphone, which processes the message and shows the result on the screen (Figure 6.14(c)). The hue and saturation values are calculated to extrapolate the point using the image previously downloaded, which represents the decision boundaries of the training (Figure 6.14(d)). The application obtains the resolution and the minimum and maximum values of hue and saturation for each image. This makes it possible to check the colour of a specific point of the classification matrix and determine the class the measured colour belongs to. This method is computationally cheap on the reader side. Furthermore, the fact that the axis boundaries and the image resolution are retrieved from the server makes it possible to adapt this system to any kind of image, no matter which classification

algorithm has been used or how many classes it contains, whereas the colours of each class are well differentiated.

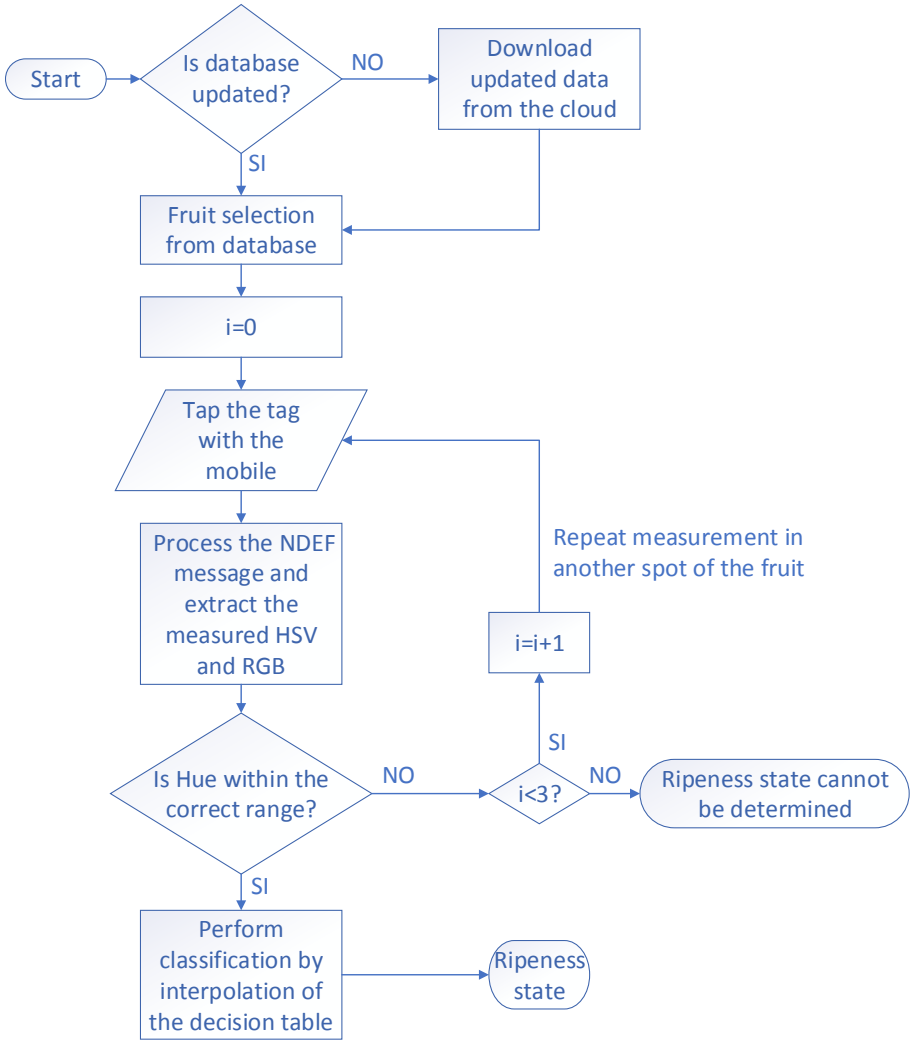


Figure 6.13. Flowchart of the mobile application.

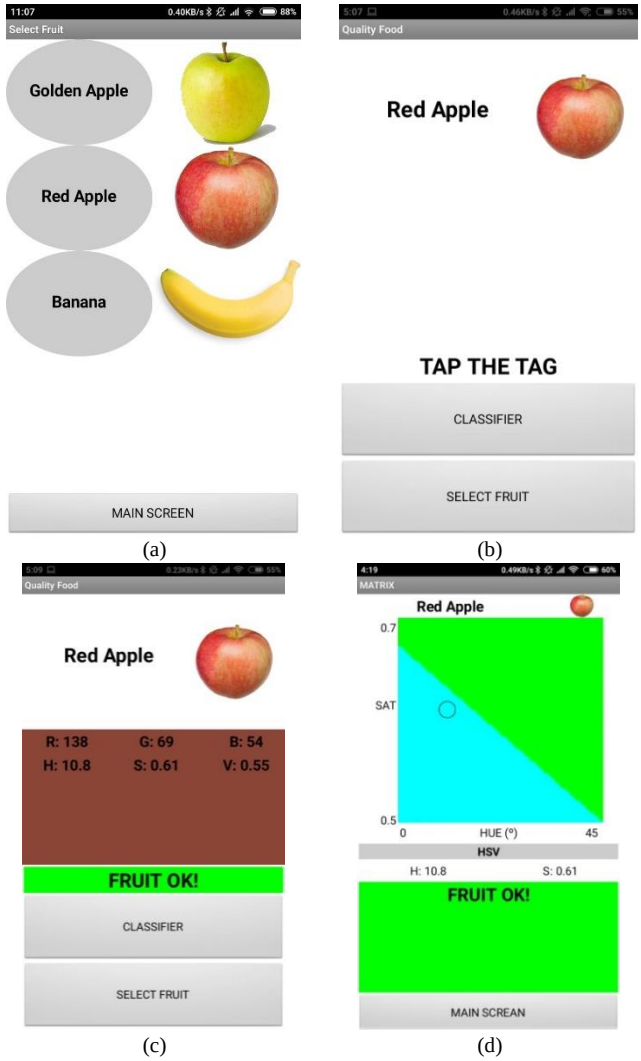


Figure 6.14. Phone screen of the developed application. (a) Fruit selection, (b) screen indicating to tap the tag, (c) representation of the detected colour, (d) decision boundaries of the training.

Figure 6.15 shows a smartphone with the main screen of the application after measuring the colour of a red apple that is on top of the 3D printed enclosure that contains the tag.

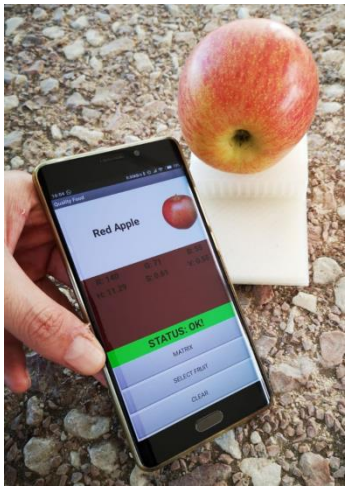


Figure 6.15. Measurement of a red apple using the designed application.

## 6.4 Conclusions

In this chapter a system for classifying the fruit ripeness grade based on its colour measured with a battery-less NFC tag and read from a mobile phone is presented. The tag integrates a microcontroller, a colorimeter, a led and an NFC IC. The tag is powered by the energy harvested from the mobile. Experimental results show that the ripeness grade is a function of time and environment conditions (especially the storage temperature). This chapter uses HSV colour space for classification. It is observed that the main parameters that change are the hue and saturation, which are used as features for the classification. Different classification algorithms have been compared in order to show the robustness of the system. Linear Discriminant Analysis and nearest neighbour work well in all cases. The proposed system is a low-cost solution compared with expensive spectrometers. In addition, the measurement is not influenced by external illumination, and therefore the measurements are repeatable in comparison with computer vision systems based on mobile cameras. A simple table-based method is proposed to avoid increasing the complexity of implementing the software in the mobile application when the boundary decision regions are not described by analytical functions, such as the case of the nearest neighbour classifier.

## 6.5 Bibliography

[1] P. B. Pathare, U. L. Opara, and F. A. J. Al-Said, "Colour Measurement and Analysis in Fresh and Processed Foods: A Review," *Food and Bioprocess Technology*, vol. 6, no. 1. pp. 36–60, 2013.

[2] D. J. Lee, J. K. Archibald, and G. Xiong, "Rapid color grading for fruit quality evaluation using direct color mapping," *IEEE Trans. Autom. Sci. Eng.*, vol. 8, no. 2, pp. 292–302, Apr. 2011.

[3] W. M. Syahrir, A. Suryanti, and C. Connsynn, "Color grading in tomato maturity estimator using image processing technique," in *Proceedings - 2009 2nd IEEE International Conference on Computer Science and Information Technology, ICCSIT 2009*, 2009, pp. 276–280.

[4] N. B. A. Mustafa *et al.*, "Image processing of an agriculture produce: Determination of size and ripeness of a banana," in *Proceedings - International Symposium on Information Technology 2008, ITSim*, 2008, vol. 1.

[5] G. Rennick, Y. Attikiouzel, and A. Zaknich, "Machine grading and blemish detection in apples," in *ISSPA 1999 - Proceedings of the 5th International Symposium on Signal Processing and Its Applications*, 1999, vol. 2, pp. 567–570.

[6] Y. Zhao, D. Wang, and D. Qian, "Machine vision based image analysis for the estimation of pear external quality," in *2009 2nd International Conference on Intelligent Computing Technology and Automation, ICICTA 2009*, 2009, vol. 1, pp. 629–632.

[7] M. Recce, J. Taylor, A. Piebe, and G. Tropiano, "High speed vision-based quality grading of oranges," in *Proceedings of International Workshop on Neural Networks for Identification, Control, Robotics and Signal/Image Processing*, pp. 136–144.

[8] D. J. Lee, J. K. Archibald, Y. C. Chang, and C. R. Greco, "Robust color space conversion and color distribution analysis techniques for date maturity evaluation," *J. Food Eng.*, vol. 88, no. 3, pp. 364–372, Oct. 2008.

[9] F. Mendoza, P. Dejmek, and J. M. Aguilera, "Calibrated color measurements of agricultural foods using image analysis," *Postharvest Biol. Technol.*, vol. 41, no. 3, pp. 285–295, Sep. 2006.

[10] "Colorimeters Versus Spectrophotometers," 2008.

[11] I. Vandekinderen *et al.*, "Effect of decontamination agents on the microbial population, sensorial quality, and nutrient content of grated carrots (Daucus carota L.).," *J. Agric. Food Chem.*, vol. 56, no. 14, pp. 5723–31, Jul. 2008.

[12] M. G. Scanlon, R. Roller, G. Mazza, and M. K. Pritchard, "Computerized video image analysis to quantify color of potato chips," *Am. Potato J.*, vol. 71, no. 11, pp. 717–733, Nov. 1994.

[13] TAOS, "TCS3472 COLOR LIGHT-TO-DIGITAL CONVERTER with IR FILTER," 2012.

[14] A. Lazaro, R. Villarino, D. Girbau, A. Lazaro, R. Villarino, and D. Girbau, "A survey of NFC sensors based on energy harvesting for IoT applications," *Sensors (Switzerland)*, vol. 18, no. 11, p. 3746, Nov. 2018.

[15] F. Pierre, J. F. Aujol, A. Bugeau, and V. T. Ta, "Luminance-Hue specification in the RGB space," in *Lecture Notes in Computer Science (including subseries Lecture Notes in Artificial Intelligence and Lecture Notes in Bioinformatics)*, 2015, vol. 9087, pp. 413–424.

[16] S. Trambadia and H. Mayatra, "Food detection on plate based on the HSV color model," in *Proceedings of 2016 Online International Conference on Green Engineering and Technologies, IC-GET 2016*, 2017.

[17] W. Chen, Y. Q. Shi, and G. Xuan, "Identifying Computer Graphics using HSV Color Model and Statistical Moments of Characteristic Functions Deep Learning for Steganalysis View project IDENTIFYING COMPUTER GRAPHICS USING HSV COLOR MODEL AND STATISTICAL MOMENTS OF CHARACTERISTIC FUNCTIONS," 2007.

[18] X. Ke, G. Guandong, and L. Jian, "An improved method of detecting pork freshness based on CRR features," in *Proceedings - 2013 9th International Conference on Intelligent Information Hiding and Multimedia Signal Processing, IIH-MSP 2013*, 2013, pp. 194–197.

[19] A. P. Medlicott, A. J. Semple, A. J. Thompson, H. R. Blackbourne, and A. K. Thompson, "Measurement of colour changes in ripening bananas and mangoes by instrumental, chemical and visual assessments." 1992.

[20] N. Cristianini and J. Shawe-Taylor, *An Introduction to Support Vector Machines and Other Kernel-based Learning Methods.*

Cambridge: Cambridge University Press, 2000.

[21] S. Mika, G. Ratsch, J. Weston, B. Scholkopf, and K. R. Muller, "Fisher discriminant analysis with kernels," in *Neural Networks for Signal Processing - Proceedings of the IEEE Workshop*, 1999, pp. 41–48.

[22] I. Rish and I. Rish, "An empirical study of the naive bayes classifier," 2001.

[23] L. Breiman, J. H. Friedman, R. A. Olshen, and C. J. Stone, *Classification and regression trees*. CRC Press, 2017.

[24] M. Muja and D. G. Lowe, "Fast approximate nearest neighbors with automatic algorithm configuration," in *VISAPP 2009 - Proceedings of the 4th International Conference on Computer Vision Theory and Applications*, 2009, vol. 1, pp. 331–340.

# 7. Implanted tag

## 7.1 Motivation

Implantable devices are increasing in widespread acceptance and becoming ever smaller and more powerful [1], [2]. Such devices include implantable glucose and oxygen sensors for diabetics [3]–[5], implantable chemical devices [6], [7], neural implants [8], [9], cochlear implants [10], ocular implants [11]–[13] and cardiovascular devices [14]. Advances in semiconductor technology, particularly in the area of micro-electro-mechanical systems (MEMS), have made it possible to reduce the dimension and increase the number of sensors that it is feasible to implant [10]. However, despite recent technological progress in implant technology, there are still challenges that must be solved [10]. One of the most critical of these challenges is the power source necessary by electronic devices. Rechargeable batteries can periodically be transcutaneous recharged by means of wireless telemetry, while single-use batteries require surgical removal to replace them. In order to increase the biocompatibility (associated with battery toxicity) and the lifetime of these devices, battery-less devices are preferred [15]. Although promising communication methods based on ultrasound [16], [17] have been proposed, radiofrequency (RF) is the most widely used communication method. However, the tissues that surround the implant present dielectric losses that heavily attenuate electromagnetic signals, thereby degrading the communications. Therefore, the read-range and size constraints imposed by the limited space available inside the body are fundamental challenges. As regards the powering of battery-less devices, although several methods of wireless power transfer (WPT) including inductive optical [18] and ultrasound [19] have been proposed in the literature, wireless powering through radiofrequency electromagnetic waves is the most established [1], [20]–[22].

Traditional WPT between the reader and implanted device is often performed with a specific design using discrete components or integrated circuits with embedded sensors. Due to size constraints, the dimensions of the implanted coil must be as small as possible. However, the maximum coupling is obtained for coils of similar size [23], [24] and the NFC readers in conventional smartphones are designed to read smart cards rather than miniature implanted coils.

Therefore, in medical applications the use of special readers is required for implanted sensors. The aim of this work is to study the viability of working with conventional NFC integrated circuits with energy harvesting in implanted devices using the smartphone as a reader. To this end a new method to increase the read range of implanted NFC sensors with energy harvesting capability using smartphones is presented, based on the use of a 3-coil system.

Wireless communication with implantable medical devices (IMDs) is fundamental for monitoring and reducing surgical operations [25]. However, the data transmitted wirelessly can be accessed by nearby third parties [25], [26]. Therefore, despite the advantage of this technology, privacy must be considered and safety issues must be addressed [27]. Nowadays, the main application of NFC tags is for payment [28]. Therefore, it can be considered a secure system. In addition to the short-read range that gives some degree of security, NFC messages can be protected with a password known only by authorized users and data can be encoded by the microcontroller included in the implant. Moreover, advanced security protocols can be implemented to improve the security [29]. This is a potential advantage of IMD based on NFC over custom wireless communication systems with less degree of security or wireless communication systems with higher read range than NFC.

## 7.2 System overview

Since there is not permeability difference between the body tissue and air, the magnetic field does not encounter any boundary conditions [21]. Hence, the most commonly used approach for transferring power through biological tissues is by magnetic induction. A typical wireless power transfer system consists of a power source, transmitter coil, receiver coil and load [21] (see Figure 7.1(a)). In addition to these elements, the proposed system in this chapter incorporates a relay coil between the transmitter and the receiver, as is shown in Figure 7.1(b). Notice that in this 3-coil topology the notation of the elements of the tag change from the notation explained in chapter 2 of this work, in order to keep the common nomenclature used in the literature when using 3-coil systems.

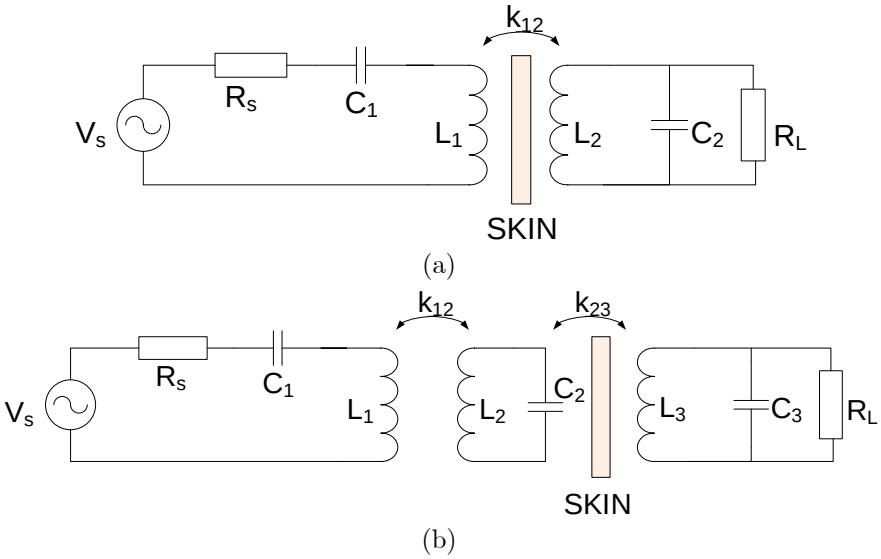


Figure 7.1. (a) Resonant coupling with 2 coils, and (b) resonant coupling with 3 coils.

The introduction of a relay coil between the source and the load introduces a degree of freedom to improve the system. Figure 7.2 shows the system using 3 resonant coils as proposed in this work. It is based on a smartphone with an integrated NFC reader, a relay coil located on the surface of the body, and the implanted NFC tag. The use of the relay coil inside the body would increase the size of the implant, and therefore it is placed on the skin outside the body. Another way of improving the WPT would be to use a system with 4 coils. However, with this topology both the second relay coil and the load coil should be implanted, thereby increasing the size of the implant and making the system impractical.

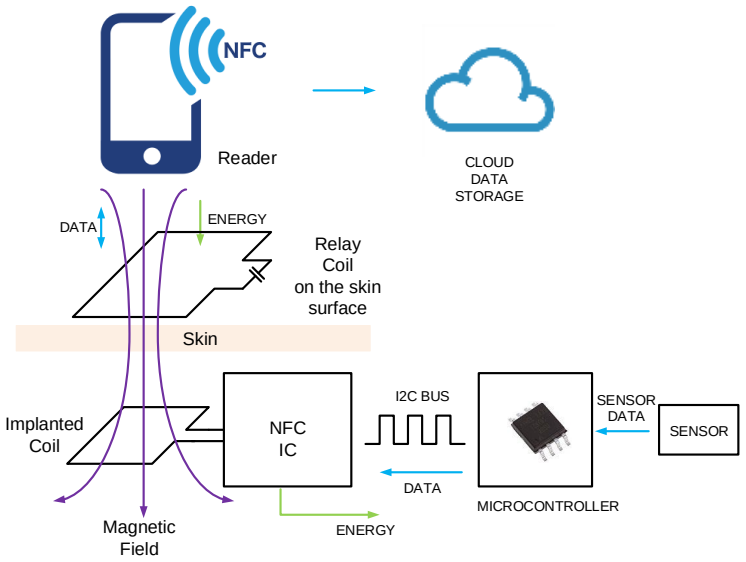


Figure 7.2. Schema of the proposed system with 3 coils.

The key requirement in the proposed biomedical link is the delivery of enough power to the load to activate the electronics with high power transfer efficiency (PTE). Achieving this is a challenge when the distance between transmitter and receiver is large or the coils are not aligned.

Efficiency ($\eta$), defined as the ratio between the power delivered at the load ($P_L$) and the input power ($P_{in}$), can be computed from the $S_{21}$ parameter using the source ($R_S$) and load resistance ($R_L$) as reference impedance in the S-parameter calculation. The efficiency and load power delivered for multiple resonant WPT have been studied in the literature [20]. Analytical expressions at the resonant frequency when all the LC resonators are tuned to the same frequency can be obtained for the cases of a 2-coil (7.1) and a 3-coil system (7.2) [20]:

$$\eta_{2coils} = \frac{P_L}{P_{in}} = \frac{k_{12}^2 Q_1 Q_{2L}}{1 + k_{12}^2 Q_1 Q_{2L}} \cdot \frac{Q_{2L}}{Q_L} \tag{7.1}$$

$$\eta_{3coils} = \frac{k_{12}^2 Q_1 Q_2}{1 + k_{12}^2 Q_1 Q_2 + k_{23}^2 Q_2 Q_{3L}} \cdot \frac{k_{23}^2 Q_2 Q_{3L}}{1 + k_{23}^2 Q_2 Q_{3L}} \cdot \frac{Q_{3L}}{Q_L} \tag{7.2}$$

In (7.2), the coupling between the first and the last coil is neglected as they are far away from each other. The power delivered at load $P_L$ for the two cases is given by:

$$P_{L,2coils} = \frac{V_S^2}{2R_1} \cdot \frac{1}{1 + k_{12}^2 Q_1 Q_{2L}} \cdot \eta_{2coils} \tag{7.3}$$

$$P_{L,3coils} = \frac{V_S^2}{2R_1} \cdot \frac{(k_{12}^2 Q_1 Q_2) \cdot (k_{23}^2 Q_2 Q_{3L})}{(1 + k_{12}^2 Q_1 Q_2 + k_{23}^2 Q_2 Q_{3L})^2} \cdot \frac{Q_{3L}}{Q_L} \tag{7.4}$$

where the unloaded quality factor of each coil is obtained from the coil inductance and resistance at angular resonance frequency $\omega_0$:

$$Q_i = \frac{\omega_0 L_i}{R_i} \quad , \quad i = 1,2,3 \tag{7.5}$$

The loaded quality factor is computed from:

$$Q_{iL} = \frac{Q_i Q_L}{Q_i + Q_L} \quad , \quad i = 1,2,3 \tag{7.6}$$

and the external quality factor is given by:

$$Q_L = \frac{R_L}{\omega_0 L_{end}} \tag{7.7}$$

where $L_{end}=L_2$ for the 2-coil system and $L_{end}=L_3$ for the 3-coil system.

The optimal coupling coefficient $k$ that maximizes the power delivered to the load (PDL) (7.3)-(7.4) and the efficiency (PTE) (7.1)-(7.2) are obtained from [20] by differentiation of the equations:

$$k_{12,PDL,2coils} = \frac{1}{(Q_1 Q_{2L})^{1/2}} \tag{7.8}$$

$$k_{12,PDL,3coils} = \left( \frac{1 + k_{23}^2 Q_2 Q_{3L}}{Q_1 Q_2} \right)^{1/2} \tag{7.9}$$

$$k_{23,PDL,3coils} = \left(\frac{1 + k_{12}^2 Q_1 Q_2}{Q_2 Q_{3L}}\right)^{1/2} \tag{7.10}$$

$$k_{23,PTE,3coils} = \left(\frac{1 + k_{12}^2 Q_1 Q_2}{Q_2^2 Q_{3L}^2}\right)^{1/4} \tag{7.11}$$

Maximum delivered power and maximum efficiency cannot be satisfied simultaneously [20]. Given that battery-less implants are considered in this work, the tag can only be powered in presence of the mobile. Therefore, the main goal is that the NFC IC receives enough power or AC voltage to ensure the correct rectification for feeding the sensors and the other electronics included in the implant, in contrast with other WPT systems used to charge batteries, in which the efficiency is fundamental. In addition, optimum couplings are often outside the typical values in an implanted system and depend on distance, coil alignment, the antennas used in the reader (that vary according to smartphone model) and the implanted antennas. Another important aspect not considered in the literature is that the load impedance and loaded quality factor depend on the IC impedance. It therefore depends on the power received and presents a nonlinear behaviour [32]–[34]. This nonlinearity must be considered in the simulations and in the system design. Simple linear network simulations are not enough, so more complex nonlinear simulation methods must be used. In order to perform an accurate simulation of the system, the different parts of the WPT system are analysed in the following sections. The overall system can be analysed using circuit simulators such as Keysight ADS. Harmonic balance nonlinear simulations have been carried out with this circuit simulator.

## 7.3 System analysis

This section presents the modelled implanted and relay antennas, and the models of reader and tag presented in chapter 2 are used for the simulations. In addition, the read range of the device powered by the reader in a smartphone is theoretically and experimentally analysed altogether with the effect of body materials on the implanted and relay antennas. The coupling between the smartphone reader and tag antennas is analysed in order to obtain the maximum

depth of the implant. Finally, simulations of the wireless power transfer performance are carried out.

### 7.3.1 Effect of the body on the implanted antennas and modelling

The effects of the body must be considered as regards both the antenna close to the skin surface (relay coil) and the antenna implanted inside the body. The epidermis, the outermost layer of skin, provides a waterproof barrier and has a thickness of around 100 µm. The dermis, beneath the epidermis, contains tough connective tissue, hair follicles and sweat glands. The dermis is around 1-2 mm thick and it has been shown that this thickness in the same body area can vary significantly with age [56], [57]. The deeper subcutaneous tissue (hypodermis) is made of fat and connective tissue. Its thickness varies from 1 to 15 mm. Under the fat there is a muscle layer. A schematic cross section is shown in Figure 7.3.

Table 7.I shows the dielectric permittivity and conductivity of tissue material at 13.56 MHz, taken from the literature [57]–[60] that are used in the EM simulator to simulate the body.

In order to study the effects of the body on the antennas, two cases are considered: the implanted antenna (section 7.3.1.1) and the relay antenna on the skin surface (section 7.3.1.2).

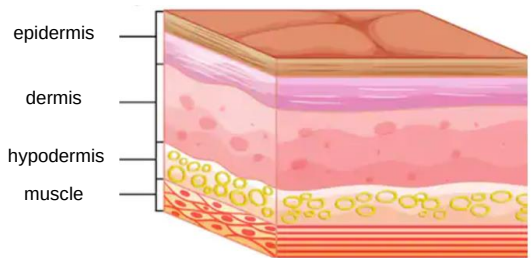


Figure 7.3. Skin cross section.

#### 7.3.1.1 Implanted antenna

Figure 2.18(a) shows the circuit model commonly used for a loop antenna in the air. At this point it is important to note that the inductance ($L_a$) is not affected by the dielectric substrate and is therefore unaltered when the antenna is implanted in the body. However, parasitic capacitance ($C_p$) increases due to the high permittivity of bodily matter, and the tag's resonance frequency therefore increases. The dielectric losses can be modelled by adding

a resistance in parallel to the antenna ($R_p$ in Figure 2.18). This resistance is in parallel with the load, reducing its value and degrading the quality factor.

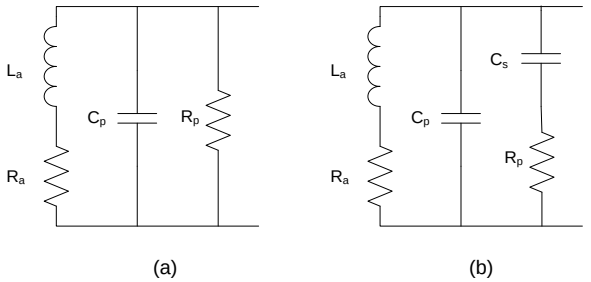


Figure 7.4. (a) Circuit antenna model for a loop antenna in the air, and (b) improved circuit model proposed for implanted loop antenna.

Implantable devices must be encapsulated to prevent contamination and to protect the electronics or mechanical systems. Implantable silicone materials can be used inside the body for long periods of time, depending on the needs of the medical device and the limitations of the material chosen [61]. Silicone rubber is the material normally chosen for implantable devices due its high chemical inertness and durability. Implantable grades of silicone are not rejected by the body and do not cause infection, since they are biocompatible for use in humans. The coating of the implanted antenna has a significant influence on its properties. The spacer ($h_c$) introduced by the coating isolates the antenna from the losses introduced by the body (muscle). In consequence, a reduction in the detuning and a noticeable increase in the quality factor is expected, compared to the use of the antenna without coating. An improved equivalent circuit for the implanted antenna is proposed to consider these effects (Figure 2.18(b)). The different contributions of the multilayer dielectric structure need to be analysed to obtain this lumped equivalent circuit. Figure 7.5(a) shows a simplified cross section of the implanted antenna surrounded by the coating material. This material is a low-loss dielectric (silicone) that introduces a series capacitance between the metal strips of the printed loop and the muscle material ($C_2$ in Figure 7.5). In the simulations it is considered that the dielectric properties of the silicone are $\varepsilon_r$=3, $\sigma$=2.26·10-6 S/m, and tan$\delta$=0.001. The material also introduces a resistance due

to its low conductivity. This distributed RC network can be modelled as an equivalent resistance ($R_1$) in series with a capacitance ($C_1$). Finally, a parasitic capacitance in parallel can be introduced to model the capacitance between the strips ($C_3$).

The components of the distributed circuit in Figure 7.5 are difficult to obtain. Therefore, a simplified lumped equivalent circuit (Figure 2.18(b)) is more useful, where the elements can be obtained from electromagnetic simulations or measurements. The resistor ($R_a$) in series with the inductor gives a quality factor that increases with frequency. The resistor ($R_p$) in parallel with the inductor gives a quality factor that decreases with frequency. The combination is therefore widely adjustable to give a peak in the quality factor at any arbitrary frequency. The equivalent capacitance $C_s$ considers the distributed capacitances of the coating layers.

The series antenna resistance ($R_a$) is frequency-dependent mainly due to the skin effect. The conductivities of biological tissues are much lower than those of the metal used for the coil strips, and thus the eddy-current generation in the tissue will be insignificant. The series antenna resistance can be computed using [62]:

$$R_a = R_{dc}\frac{t}{\delta(1-e^{-t/\delta})}\cdot\frac{1}{1+t/W} \tag{7.12}$$

where DC resistance $R_{dc}$ is given by;

$$R_{dc} = \frac{L}{\sigma W t} \tag{7.13}$$

and skin depth $\delta$is:

$$\delta = \frac{1}{\sqrt{\sigma\pi f\mu_0}} \tag{7.14}$$

In (7.12)-(7.15), $L$ is the length of the strip, $t$ the thickness of the strip, $W$ the width of the strip, $\mu_0$ the vacuum magnetic permeability constant ($4\pi\cdot10^{-7}$ H/m) and $\sigma$ the conductor conductivity.

Table 7.I. Dielectric layers used in the simulation of the body at 37$^{o}$C

| Layer | Relative permittivity | Conductivity (S/m) | Thickness (mm) |
|---|---|---|---|
| Skin (epidermis+dermis) | 120 | 0.25 | 1.5 |
| Fat (hypodermis) | 38 | 0.21 | 4 |
| Muscle | 138 | 0.62 | 25 |

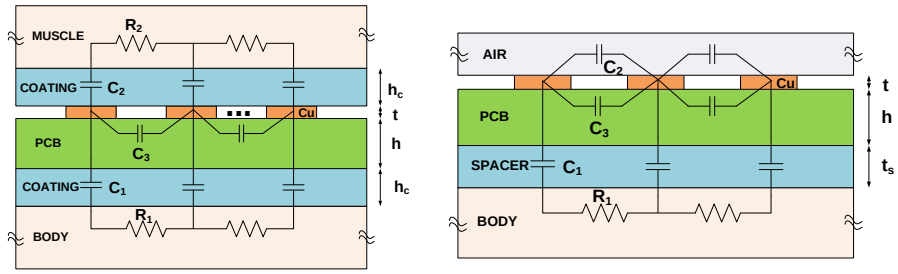


(a) (b)

Figure 7.5. (a) Cross section of a subcutaneously implanted antenna and (b) cross section of the relay antenna on the body.

Figure 7.6 compares the quality factors of a printed antenna coil in the air and one within the body surrounded by muscle tissue, assuming that it is covered by a coating of silicone of different thicknesses. The permittivity and conductivity are provided in

Table 7.I. The implanted antenna is designed using a 0.8 mm thick FR4 PCB substrate. The antenna is a double-sided loop with 3 turns on each side, with a strip width of 0.5 mm, strip spacing of 0.5 mm and external length of 15 mm. The antenna presents an inductance of 0.68 µH, which is higher than the value required to meet the bandwidth specification given by (2.29). Good agreement is found between the electromagnetic simulations and the circuit model in Figure 2.18(b) obtained from optimization using Keysight ADS. $R_{dc}$ is optimized to consider the exact length $L$ of the antenna. The antenna resistance is computed from (7.12) using $R_{dc}$, the width $W$ and thickness $t$. The initial values for $C_p$ and $C_s$ are set to the half of the value of $C_p$ obtained in the air (extracted from the resonance frequency). The initial value of the inductance is extracted at low

frequency from the imaginary part of the impedance. The main antenna parameters are listed in Table 7.II. The cases of the antenna in the air and the antenna implanted with different thicknesses of silicone cover are compared in the table. The tuning capacitances $C_{tun}$ that need to be added in parallel for the antenna to become resonant at 13.56 MHz (including the chip capacitance) are also listed.

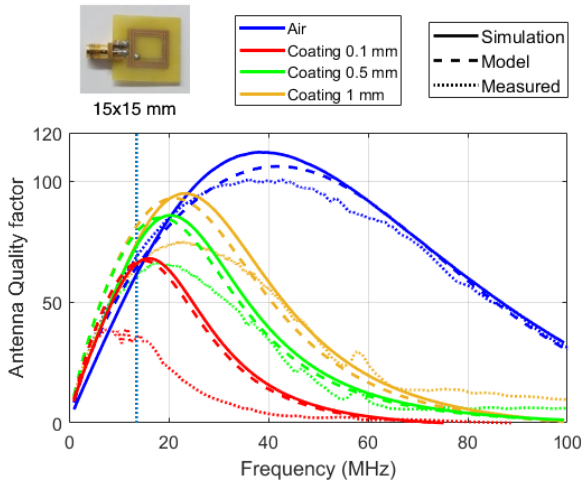


Figure 7.6. Antenna quality factor as a function of frequency, in air and implanted, with different coating thicknesses. Continuous line: electromagnetic simulation; dashed line: circuit model. Dotted line: measurements of the antenna.

The dotted line on Figure 7.6 shows the measurements of the quality factor of a prototype inserted in a phantom. The phantom consists of a piece of pork steak. In order to simulate a flat coating, the antenna is covered by 3D-printed polylactic acid (PLA) of different thickness and inserted within the meat. The permittivity of the PLA is close to the one of silicone ($\varepsilon_r \approx 3$) [63]. The quality factor ($Q_3$) obtained considering the case in air is slightly lower than the simulated. The improvement of the quality factor when the coating thickness increases is also observed in the measurements. The quality factor values are close to 40 for coating thickness of 0.1 mm, increasing to more than 63 for a coating thickness of 1 mm. However, the quality factor obtained with the phantom is smaller than that reached in the simulations. This fact can be explained by the higher conductivity of the meat compared to the one used in the simulations due to the high content of water.

It can be observed that, when implanted, and due to the dielectric permittivity of the tissue, the resonance frequency decreases in comparison to the air case. When increasing the thickness of the silicone coating, the effective permittivity decreases, and thus the resonance frequency increases, as does the peak frequency of the quality factor. The fields are therefore concentrated between the electrodes and the coating material, resulting in a reduction of the losses. There is an optimum thickness of the silicone cover, around 0.5 mm, that maximizes the quality factor. Although the maximum quality factor is smaller than that of the maximum in the air case, the peak frequency is closer to the operating frequency. Thus, slightly higher values of quality factor are obtained in the implanted antenna compared to those obtained in the air.

Table 7.II. Antenna parameters for the implanted antenna

| Parameter | In air | Implanted antenna with different thicknesses of silicone coating | | |
|---|---|---|---|---|
| Thickness of coating (mm) | 0 | 0.1 | 0.5 | 1.0 |
| $R_{dc}$ (Ω) | 0.38 | 0.38 | 0.38 | 0.38 |
| $R_a$(Ω) | 0.95 | 0.89 | 0.78 | 0.78 |
| $f_r$ (MHz) | 135.8 | 75.1 | 104.6 | 120.9 |
| $C_p$ (pF) | 2.02 | 0.93 | 0.94 | 0.90 |
| $Q_a$ | 61.4 | 65.9 | 74.2 | 73.2 |
| $L_a$ (µH) | 0.68 | 0.68 | 0.68 | 0.68 |
| $R_p$ (Ω) | | 78.5 | 72.56 | 192.01 |
| $C_s$(pF) | | 7.20 | 3.45 | 2.78 |
| $C_{tun}$ (pF) | 201.04 | 200.18 | 203.8 | 143.05 |

#### 7.3.1.2 Relay antenna on the skin surface

A similar analysis to that performed for the implanted antenna (section 7.3.1.1) is repeated for relay coil placed in contact with the skin (see schema of Figure 7.5(b)). The data on the stack materials described in

Table 7.I is also used to simulate the body in the electromagnetic simulations with Keysight Momentum. However, the dielectric properties of tissue and skin vary greatly between individuals, depending on the water content of their tissues. One strategy for

reducing this effect in the relay – and therefore also in the detuning associated with this variability, which has an impact on the electromagnetic properties of the tissues – consists of adding a buffer layer with low losses and low permittivity. This coating layer is also needed to protect the electronics, preventing short circuits and for biocompatibility. Silicone is again proposed in this case because it is a biocompatible material. However, other materials with low permittivity (around 2-3) can be used to integrate the coil into a flexible band-aid to be more breathable.

Figure 7.7 illustrates the effect of the silicone spacer layer (thickness $t_s$) in the antenna model. The prototype of relay antenna considered in this study consists of a square loop (25×25 mm) with 4 turns, a track width of 0.5 mm and spacing between tracks of 0.5 mm, printed on FR4 substrate with a thickness of 0.8 mm. When the thickness of the coating layer increases, the frequency response tends to reach the values obtained in the isolated loop antenna in the air. This antenna presents a higher quality factor in the air compared to that achieved in the implanted antenna, but, due to the substrate height plus the spacer thickness up to the skin, the quality factor remains approximately constant and close to the air value, at around 75. Good agreement is obtained between the simulated model and the improved model of Figure 2.18(b). The parameters of this model are fitted by optimization using Keysight ADS optimization tools in order to match the frequency impedance of the antenna and are listed in Table 7.III. The dotted line on Figure 7.7 shows measurements of the quality factor of a prototype of relay coil in the air and on a phantom. The phantom is a piece of pork steak with a spacer made of PLA. As in the case of the implanted coil, the values of the quality factor are smaller than those obtained from the literature, whose parameters are used in the simulations, mainly due to the higher water content of the meat. However, the improvement due to the increase of the spacer thickness is clearly perceptible, approaching to the value of air case. The measured quality factor increases from 40 for a spacer of 0.1 mm to 73 for a spacer of 2 mm.

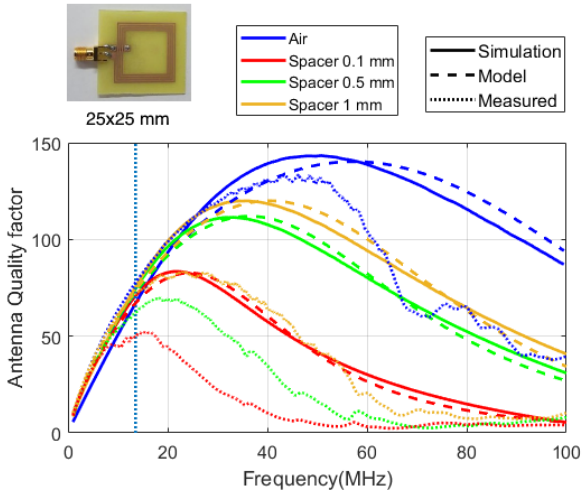


Figure 7.7. Antenna quality factor of the relay loop antenna as a function of the frequency in air and on the skin with different spacer thicknesses. Continuous line: electromagnetic simulation; dashed line: circuit model. Dotted line: measurement of the antenna.

Table 7.III. Parameters of the relay antenna

| Parameter | In air | Implanted antenna with different thicknesses of silicone coating | | |
|---|---|---|---|---|
| Thickness of coating (mm) | 0 | 0.1 | 0.5 | 1.0 |
| $R_{dc}$ (Ω) | 0.43 | 0.42 | 0.42 | 0.42 |
| $R_a$(Ω) | 0.98 | 0.98 | 0.98 | 0.98 |
| $f_r$ (MHz) | 173.3 | 113.5 | 140.3 | 150.0 |
| $C_p$ (pF) | 2.0 | 0.07 | 0.07 | 0.07 |
| $Q_a$ | 61.7 | 69.9 | 74.2 | 74.0 |
| $L_a$ (µH) | 0.70 | 0.70 | 0.70 | 0.70 |
| $R_p$ (Ω) | | 790.7 | 685.9 | 727.3 |
| $C_s$(pF) | | 1.0 | 0.5 | 0.4 |
| $C_{tun}$ (pF) | 194.8 | 196.7 | 196.7 | 196.7 |

### 7.3.2 Coupling between antennas

Since biological materials are non-magnetic, the coupling between antennas is mainly the same as in the air. The coupling coefficient is needed in order to estimate the maximum depth of the implant for a given distance between the body and the smartphone. The coupling

coefficient k between two coils can be calculated from the Z parameters obtained from the S parameters using equation (2.20).

Several loop antennas are manufactured on 0.8 mm thick FR4 substrate with a track width of 0.5 mm and the coupling between them is measured. The distance between the coils is changed using a linear actuator controlled by a stepper motor. The nomenclature and main parameters of the antennas (inductance and resistance at 13.56 MHz) are described in Table 7.IV . In addition, a comparison between the simulated and measured inductance and resistance at 13.56 MHz is also shown in Table 7.IV. Small differences are found due to the PCB tolerances. The implanted antenna consists of a double-sided 15×15 mm square loop with 6 turns. Two relay antennas (Relay 1 and Relay 2) measuring 25×25 mm with 4 and 6 turns respectively are considered. Three antenna sizes for the reader are studied. The reader 1 and 2 antennas have a similar size to the antennas integrated around the camera in smartphones, which is the typical position in mobiles with metallic cases [64]. The size of reader antenna 3, on the other hand, is similar to the antenna placed on the top of the battery integrated in smartphones with plastic cases. [65] demonstrate that the ferrite material used to isolate the coil from the battery or other metallic parts has a small influence in the coupling coefficient. Therefore, the following simulations and measurements were performed in the air.

Table 7.IV. Dimensions of antennas used in the coupling study

| Antenna name | Dimensions | Number of turns | $L_a$ (nH) | $R_a$ ($\Omega$) |
|---|---|---|---|---|
| Implanted | 15 mm × 15 mm | 6 | 666<br>684* | 0.83<br>0.91* |
| Relay 1 | 25 mm × 25 mm | 4 | 697<br>716* | 0.98<br>0.98* |
| Relay 2 | 25 mm × 25 mm | 6 | 1185<br>1172* | 1.12<br>0.99* |
| Reader 1 | 25 mm × 25 mm | 4 | 697<br>716* | 0.98<br>0.98* |
| Reader 2 | 25 mm × 25 mm | 6 | 1185<br>1172* | 1.12<br>0.99* |
| Reader 3 | 50 mm × 50 mm | 4 | 2965<br>2893* | 2.39<br>2.89* |

Simulated and measured (*) inductance ($L_a$) and resistance ($R_a$) at 13.56 MHz

Figure 7.8-7.10 compare the simulations and the measurements with Vector Network Analyzer (VNA) of the coefficients obtained using (2.20) from S parameters, as a function of the distance between coils. The coupling coefficient ($k_{12}$) between the reader and the implanted antenna in the 2-coil system (see Figure 7.1(b)) is shown in Figure 7.8. Figure 7.9 compares the coupling ($k_{12}$) between the relay and reader antennas in the 3-coil system. The coupling coefficient ($k_{23}$) between the relay and implanted antennas in the 3-coil system is shown in Figure 7.10. Good agreement has been obtained between the measured and simulated coupling coefficients. Some discrepancies are found when the coils are very close due to the high sensitivity to the small misalignment and the position errors for these distances. The conclusion is that close antennas with similar areas present strong coupling coefficients for small distances, while antennas with large areas present high coupling at large distances.

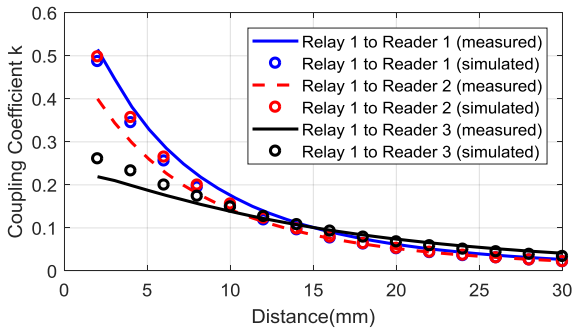


Figure 7.8. Simulated and measured coupling coefficient between the implanted antenna and different reader antennas described in Table 7.IVError! No s'ha trobat l'origen de la referència..

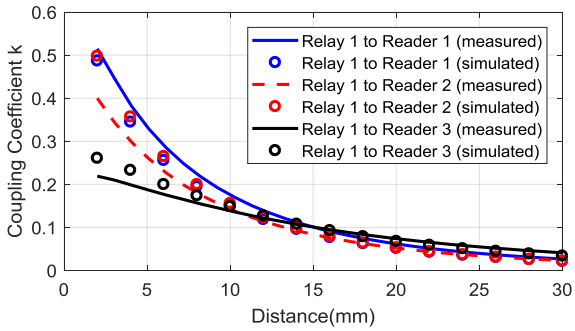


Figure 7.9. Simulated and measured coupling coefficient between the relay antenna (Relay 1) and different reader antennas described in Table 7.IV.

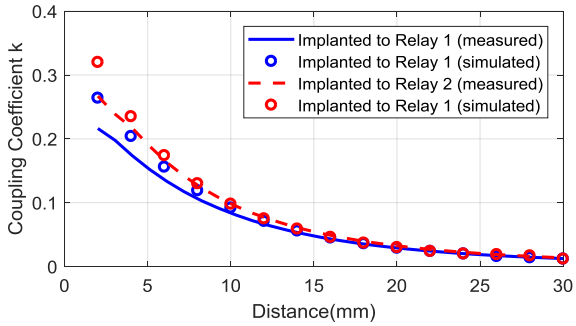


Figure 7.10. Simulated and measured coupling coefficient between the implanted antenna and different relay antennas described in Table 7.IV.

### 7.3.3 System simulations

In order to study the viability of using smartphones to power up implanted sensors, a number of simulations are carried out using the nonlinear model of the tag for both the 2-coil and the 3-coil links. Using the values for the inductance and quality factors obtained in the simulations of the implanted and relay antennas, Table 7.V shows the parameters considered for the simulations of efficiency and power transfer.

Table 7.V. Parameters used in the system simulations

| Parameter | Value |
|---|---|
| Source power (dBm) | 20 |
| Source resistance $R_2$ (Ω) | 4.86 |
| Reader antenna inductance (µH) | 2 |
| Reader quality factor $Q_1$ | 35 |
| Relay inductance $L_2$ (µH) | 0.7 |
| Relay quality factor $Q_2$ | 70 |
| Tag antenna inductance $L_3$ (µH) | 0.7 |
| Tag antenna quality factor $Q_3$ | 60 |

Figure 7.11 shows simulations of the IC equivalent resistance and capacitance as a function of the coupling coefficient for the 2-coil system. Due to the nonlinear behaviour of the NFC IC [32]–[34], the $R_{IC}$ resistance depends on the power received. The values of $R_{IC}$ obtained are under the limit imposed by the maximum quality factor to ensure the bandwidth required for the backscattering communication given by (2.29). When the reader starts the interrogation, the $R_{IC}$ resistance is very high (several kΩ), but this

value decreases when the NFC IC is woken up and moves into operating mode. After this, the $R_{IC}$ resistance value drops when the AC voltage or power received at the antenna coil increases. For typical values of $R_{IC}$ during the IC operating mode, the tag quality factor is limited by the load quality factor $Q_L$, which is considerably lower than the maximum value required. The measurement of the nonlinear IC impedance is difficult to be done in the laboratory. This impedance is very mismatched compared to the standard RF laboratory instruments (50 Ω). Therefore, it is not easy to excite the IC with enough power level to activate it because power is mostly reflected and then high-power levels to excite the IC are required. The excitation power level in a commercial VNA is often limited to 20 dBm (over 50 Ω). A modified VNA setup with an external amplifier and a reflectometer [32]–[34] to characterize the IC under similar power conditions to the actual operation with a reader is required. Experimental results obtained in these works for different IC show the power dependence of the impedance obtained here in the simulations.

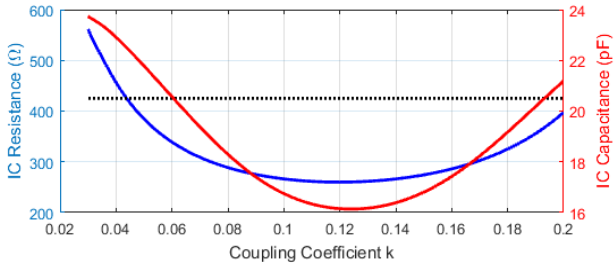


Figure 7.11. Simulated equivalent IC resistance (blue) and IC capacitance (red) as a function of the coupling coefficient in the 2-coil system. The threshold resistance at the threshold power is shown (dotted line).

Figure 7.12 shows the simulated AC voltage received at the (implanted) tag coil and the rectified voltage at the output of the shunt regulator, as a function of the coupling coefficient between the antennas and considering the 2-coil system. The threshold power is the minimum power needed to obtain a stable DC voltage in the energy harvesting output (e.g. 2.9V). In most commercial IC, the energy harvesting output is disabled below this threshold level. Therefore, under this level, the external microcontroller and sensors are not biased and a new sensor measurement cannot be done. In commercial IC, this power level is higher than the minimum power

required to read a previously stored data in the NFC EEPROM. The RF limiter protection is designed to start to actuate for AC levels in the antenna terminals higher than 4.8V. For higher levels, the AC voltage saturates preventing the damage of the transistors in the rectifier. Figure 7.13 shows the simulations of the Power Conversion Efficiency (PCE) of the rectifier as a function of the coupling coefficient and the received power. This efficiency is calculated loading the output of the energy harvesting with a sink current of 3 mA, which simulates the current consumption of the sensors. Efficiencies of about 44% are achieved for the threshold power (14 dBm).

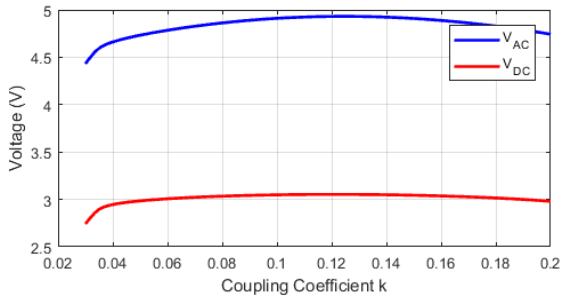


Figure 7.12. Simulated AC voltage at the receiver coil and DC voltage at the output of the shunt regulator as a function of the coupling coefficient in the 2-coil system.

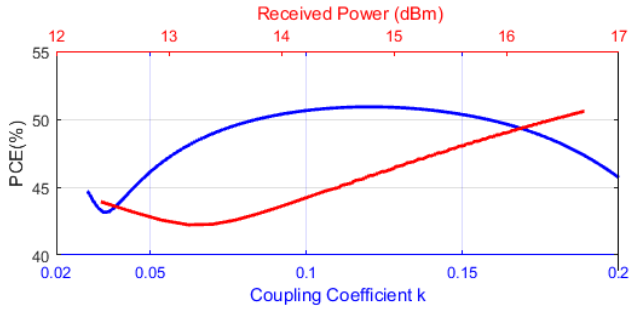


Figure 7.13. Simulated Power Conversion Efficiency as a function of the coupling coefficient in the 2-coil System (blue), and as a function of the received power (red).

Figure 7.14 shows the simulated received power and efficiency as a function of the coupling for the 2-coil system in the air. Using the data of Figure 7.8, the distance corresponding to the coupling between the reader antenna (reader 1) and the implanted antenna is added in the upper x-axis. For couplings higher than 0.04, the power received at the input of the tag is higher than the threshold power. The total distance between reader and implanted antenna is about 18 mm. Therefore, a smartphone located at 5-10 mm can provide energy to an implant at a depth about 8-13 mm. For power levels higher than the threshold, the harvesting output is stable and can support the external DC load (assumed 3 mA). When the coupling coefficient is very high (>0.12), the power received decreases due to activation of the shunt limiter protection, increasing the IC resistance. The mismatch at the input of the transmitter also increases for high coupling factors due to the load modulation phenomenon.

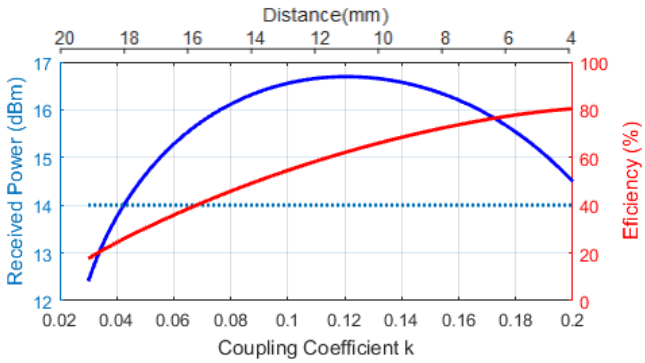


Figure 7.14. Simulated received power (blue) and efficiency (red) as a function of the coupling coefficient and the distance between reader and implanted antennas in the 2-coil system. The dotted line shows the power threshold.

Simulations are repeated for the 3-coil system. In this case, there are two degrees of freedom: the coupling between the reader and relay antennas ($k_{12}$), and that between the relay and implanted antennas ($k_{23}$). Figure 7.15. shows the received power and efficiency as a function of the coupling between the relay and implanted antenna ($k_{23}$) for different couplings between the reader and relay antennas (or equivalently, for different distances between the reader and the skin surface). The IC impedance (Figure 7.16) presents the same nonlinear behaviour as in the case of two coils.

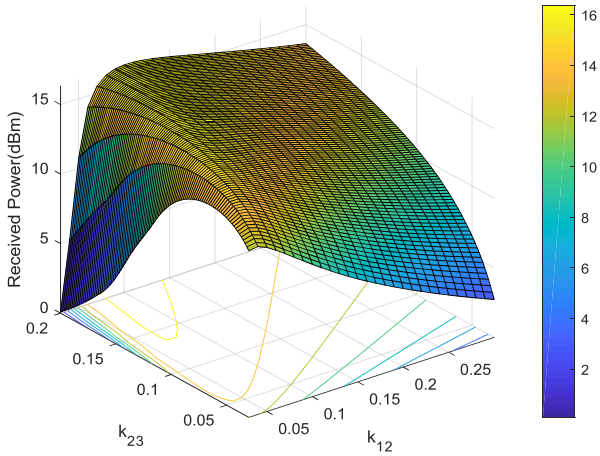


(a)

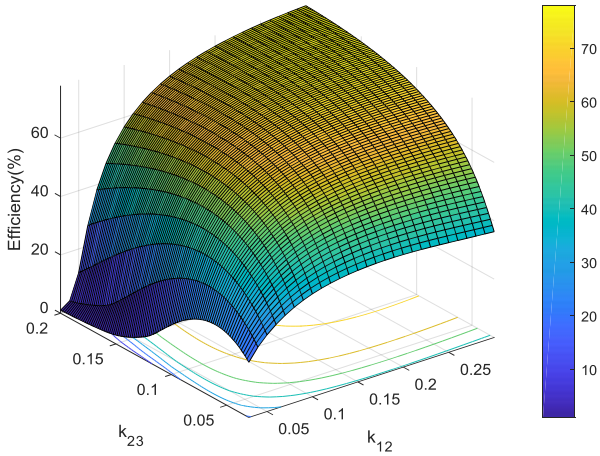


(b)

Figure 7.15. Simulated received power in dBm (a) and efficiency (b) as a function of the coupling coefficients in the 3-coil system.

Figure 7.17 shows the received AC and rectified DC voltages as a function of the coupling between the relay and the implanted antennas ($k_{23}$) for two values of coupling between the reader and relay antennas ($k_{12}$=0.05 and $k_{12}$=0.1). Coupling coefficients $k_{23}$ higher than 0.05 and 0.08 are required for correct DC conversion,

considering $k_{12}$=0.05 and 0.1 respectively. Figure 7.18 shows the received power and the efficiency as a function of the coupling coefficient $k_{23}$, or equivalently the depth of the implanted coil in the 3-coil system. In contrast with the 2-coil system in which efficiency is a monotonic function of the coupling, efficiency in the 3-coil system (Figure 7.18(b)) presents an optimum coupling $k_{23}$ value that depends on $k_{12}$ (7.11). In the upper x –axis is shown the distance corresponding to the reader 1 and relay 1 antennas obtained from the graphs of the coupling coefficient as a function of the distance (Figure 7.8-7.10).

In the case of the 3-coil system, for close coupling between the reader and relay (distance in the order of 1 cm in Figure 7.18), the maximum depth of the implant can increase up to 18-21 mm (Figure 7.18). Although the improvement seems not very big, the second system is more tolerant of misalignment between antennas. The relay and implanted antennas are assumed to be centre aligned. The relay antenna on the skin can easily be used to localize the tag, and small misalignments in the horizontal plane can be tolerated because the coupling between reader and relay is strong for typical distances (3-10 mm). In the 2-coil system it is more difficult to align the antennas due to the lack of reference indicating the exact position of the implant. Thus, horizontal misalignments for distances between the smartphone and the implant higher than 10 mm can bring about a rapid fall in the coupling coefficient [66], especially if the reader uses small area antennas (most common in modern mobiles with metallic cases). The last practical consideration makes the 3-coil system able to detect implanted NFC tags at up to a 16 mm depth inside the body with a distance between the mobile and the skin of 5-10 mm.

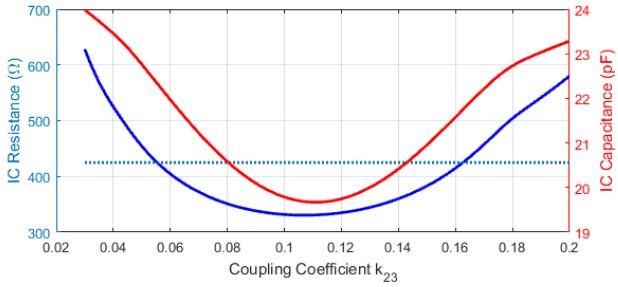


Figure 7.16. Simulated equivalent IC resistance (blue) and IC capacitance (red) as a function of the coupling coefficient in the 3-coil system ($k_{12}$=0.05). The threshold resistance at the threshold power is shown (dotted line).

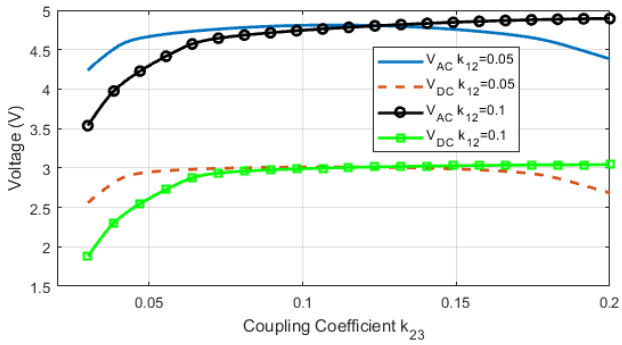


Figure 7.17. Simulated AC voltage at the receiver coil and DC voltage at the output of the shunt regulator as a function of the coupling coefficient between the implanted and relay antennas in the 3-coil system.

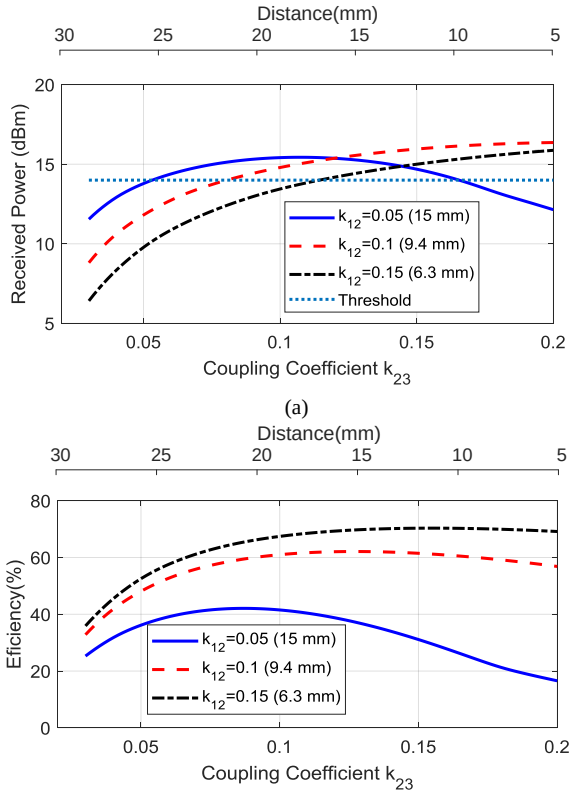


Figure 7.18. Simulated received power (a) and efficiency (b) as a function of the coupling coefficient and the distance between the relay and implanted antennas in the 3-coil system. Different coupling coefficients between reader and relay antennas are considered (the distance is indicated between parenthesis).

## 7.4 Experimental results

Several experiments have been conducted to check the two systems and compare them to the simulations. Some measurements with an implanted tag also have been performed. A phantom comprising slices of pork meat (tenderloin) is used. The tag is covered with a plastic bag (PTE) that emulates the protection layer in a real implant, assuming that the dielectric properties are similar to the silicone. The thickness of the bag (made of PET, $\varepsilon_r \approx 2.5$) is 0.1 mm. Therefore, it can be considered as a worst case. Relay antenna 1 as described in Table 7.V (4 turns, area 25 mm × 25 mm) is used in the experiments. However, in order to perform measurement closer to a real NFC patch attached to the skin, the relay antenna is designed and manufactured in flexible Ultralam 3000 substrate. This case can be considered as the worst case because the coil is very close to the skin. A parallel capacitor is used to adjust the resonance frequency to 13.56 MHz to avoid the detuning effect due to the high permittivity of the phantom. No significant changes in the read range compared to a rigid relay antenna manufactured on FR4 with thickness 0.8 mm tuned at 13.56 MHz are observed.

S parameters measurements have been performed using the vector network analyser for the 2-coil and 3-coil systems. From these measurements, the efficiency ($\eta$) and the received power at the input of the tag ($P_{in}$) are computed. The laboratory instruments present a reference impedance of 50 Ω, different from the IC input impedance and the source impedance of the reader. To refer to these impedances, the measurements are loaded in the Keysight ADS simulator using a two-port S parameter data item and it is loaded with the tuning capacitors ($C_{tun}$) and the desired loads according the schemes of Figure 7.1. According to the results presented before and the impedance simulations, a $R_{IC}$=525 Ω is considered. The source resistance ($R_s$) is set to achieve the maximum $Q_1$ factor of 35. A series capacitor ($C_1$, 220 pF) at the input and a parallel capacitor ($C_p$, 190 pF) at the output are included to tune the system at the operation frequency of 13.56 MHz. These values are not changed in all the measurements. The 15×15 mm implanted coil with 6 turns made with a 0.8 mm thick FR4 double-sided PCB is used. In order to simulate the reader, the coil reader 1 described in Table 7.V (25×25 mm with 4 turns on FR4 substrate) is used. The implanted coil is embedded within a piece of pork steak used as a phantom to

simulate the body. A linear actuator controls the distance with a stepper motor. Figure 7.19-7.22 show the measured efficiency and received power as a function of the distance between the surface of the meat and the reader coil for the 2-coil and 3-coil systems. In these graphs, different depths of the implant between 6 mm and 18 mm are considered. The backside is covered by 2 cm of meat. In order to investigate the effect of misalignment between coils, some measurements of efficiency and received power have been performed. The reader antenna (reader 1) is misaligned from the axis using the linear actuator. The distance between the reader antenna and the surface of the phantom is set to 1 cm. The depth of the implanted antenna is 6 mm. Figure 7.23 and Figure 7.24 compare the efficiency and the received power for the 2-coil and 3-coil systems. Whereas the efficiency and power level remain nearly constant for a range ±12.5 mm that corresponds to the overlap between the reader and the relay antennas, a fast fall is obtained for the 2-coil system. The higher robustness of the 3-coil system than the 2-coil system can be deduced from these results.

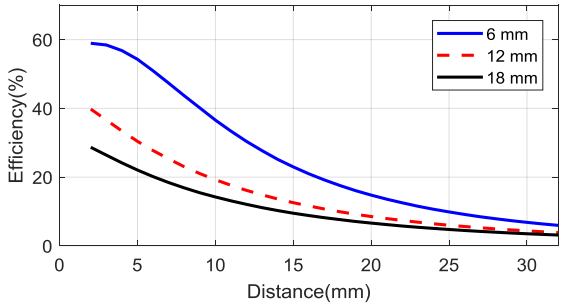


Figure 7.19. Measured efficiency as a function of the distance between antenna reader and skin surface for different depths of the implanted antenna for the 2-coil system.

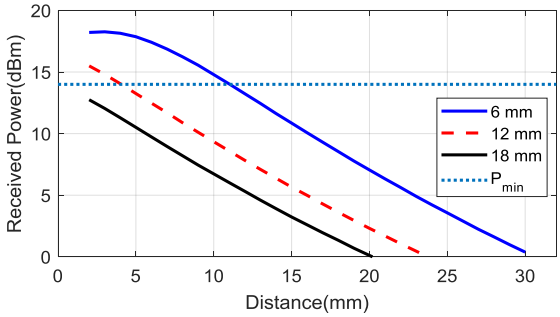


Figure 7.20. Measured received power as a function of the distance between antenna reader and skin surface for different depths of the implanted antenna for the 2-coil system.

In order to test the system with commercial smartphones as a NFC reader and commercial NFC IC, another experimental setup is designed. In this case, the main problem is that the antenna in the reader is not accessible. In addition, the last measurements do not consider the nonlinear behaviour of the tag or effects of the proximity of metal case of the mobile that can detune the coils [24]. To solve these problems, measurements of the average magnetic field ($H_{av}$) received by the tag as a function of the distance allows comparing the performance of readers and tags. $H_{av}$ measurements are often used in certification of devices in the NFC forum standards.

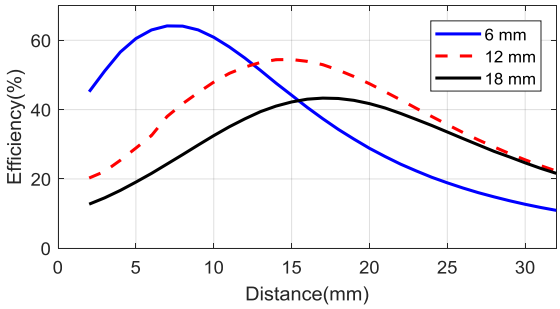


Figure 7.21. Measured efficiency as a function of the distance between antenna reader and skin surface for different depths of the implanted antenna for the 3-coils system.

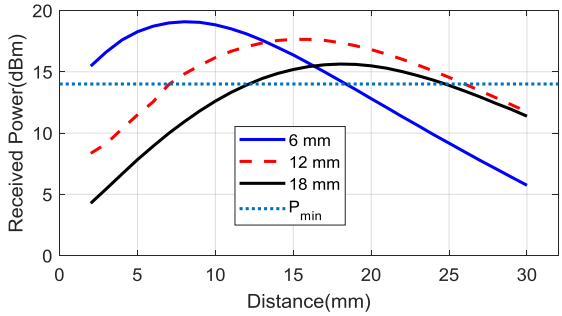


Figure 7.22. Measured received power as a function of the distance between antenna reader and skin surface for different depths of the implanted antenna for the 3-coil system.

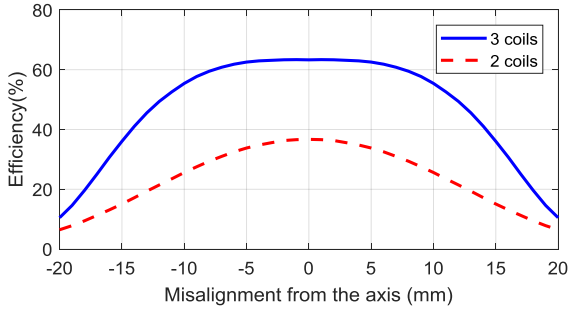


Figure 7.23. Measured efficiency as a function of the misalignment distance from the axis for the 2-coil and 3-coil systems. The depth of the implanted antenna is 6 mm and the distance between the reader antenna and the skin surface is 10 mm.

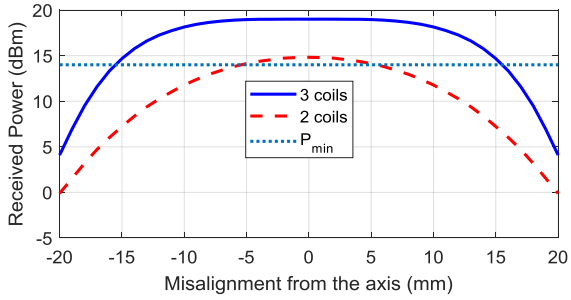


Figure 7.24. Measured received power as a function of the misalignment distance from the axis for the 2-coils and 3-coils systems. The depth of the implanted antenna is 6 mm and the distance between the reader antenna and the skin surface is 10 mm.

To this end, an experimental setup is designed to measure the average magnetic field and read range measurements. A schema of

the setup is shown in Figure 7.25(a). A photograph of the setup used for the read range measurement is shown in Figure 7.25(b). A mobile phone is used as a reader to interrogate the tag. An application has been designed for interrogating during the measurements and reading the sensor data stored in the NFC message using the NFC Data Exchange Format (NDEF) (Figure 7.25(b)). The same loop antenna as that used in the tag is connected to a microwave switch (Minicircuits model MSP2T-18) to select the spectrum analyser (SA, Rohde & Schwarz model FSP3) or vector network analyser (VNA, Agilent model E5062A) to perform measurements at each distance. The VNA is calibrated to the input of the antenna. When the switch is in the SA position, the power received at the carrier frequency is measured using the maximum hold trace. In the VNA position, the reflection coefficient of the antenna is measured to obtain its impedance from the $S_{11}$ parameter. Using these measurements, the average magnetic field can be obtained from the antenna factor ($AF$) obtained from the loop impedance using equations (2.31) and (2.19).

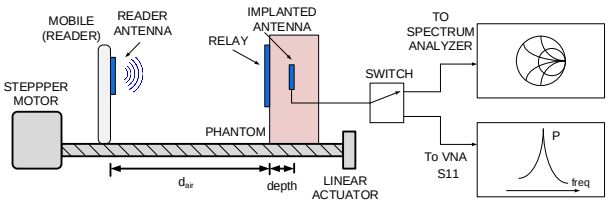


(a)

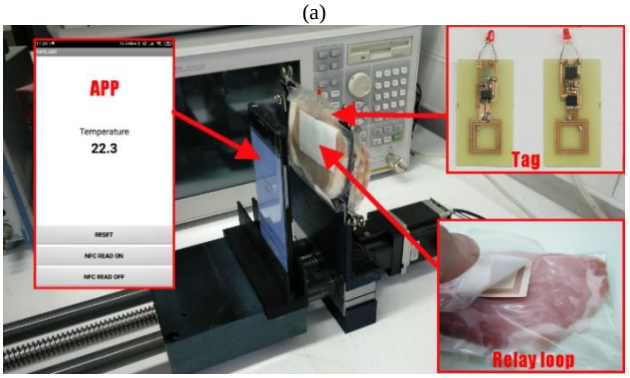


(b)

Figure 7.25. (a) Setup used for the measurement of the average magnetic field, (b) photograph of the setup for read range measurements including a screenshot of the mobile application.

The tag used in the experiments contains the 15x15 mm implanted coil with 6 turns made with a 0.8 mm thick FR4 double-sided PCB (see Figure 7.26). The tag uses the ST M24LR04E NFC IC with energy-harvesting capabilities and is connected to an Atmel ATtiny85 microcontroller with a clock frequency of 1 MHz that will be connected to the sensors. The microcontroller is responsible for reading the sensor data and saving them in the NDEF message in the internal EEPROM of the NFC IC by $I^2C$ bus. These data can be read by the mobile. It is important to note that the read range is limited by the energy harvesting required to power up the sensors and the microcontroller. The distance at which the data previously stored in the memory of the NFC IC can be downloaded by RF communication (downlink) is greater than in the downlink due to the high sensitivity of the NFC transceivers. As a proof of concept, a temperature sensor (Texas Instruments LM75A) is integrated. The temperature is read by the microcontroller using the $I^2C$ bus. The data is stored in the NDEF message that is read by the mobile. A red LED is connected to the energy harvesting voltage output for the fast monitoring of the energy harvesting. The current though the LED is limited with a resistor. The resistor was adjusted to simulate the case of maximum power consumption. The tag draws a total of 3 mA at 3V in its normal operating state. The two systems with 2 and 3 coils are measured. The NFC IC is configured to the highest energy-harvesting mode, which, in a worst-case scenario, would require a higher magnetic field. Since biological materials are not magnetic, their effect is expected to be small, except in the detuning of the antennas as explained earlier.

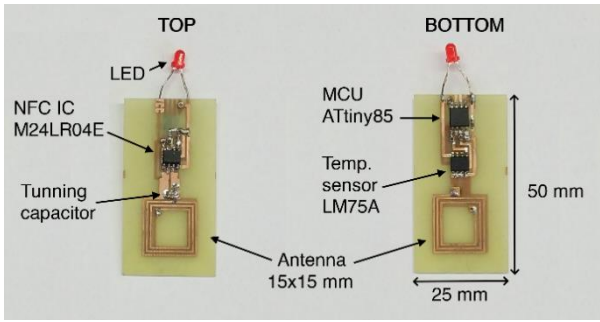


Figure 7.26. Photograph of the tag manufactured for measurements: top view (left) and bottom view (right).

Some tests are therefore first performed in the air. Figure 7.27 shows the measurement of the 2-coil system with no material between the tag and the reader (in air). In Figure 7.28, the measured average magnetic field is plotted as a function of the reader-to-tag distance for a different distance between the relay antenna and the coil tag antenna. The results show that the minimum threshold magnetic field ($H_{min}$) is around 2.8 $A_{RMS}$/m in both cases, which corresponds to a read range of around 12 mm in the case of the 2-coil system and read ranges of between 15-20 mm in the 3-coil system.

The value of the threshold average magnetic field $H_{min}$ is calculated using (2.32). Figure 7.29 shows the simulated $H_{min}$ obtained from (2.32) considering $R_{IC}$=525 Ω, tag inductance $L_2$=0.7 µH, $Q_{3L}$=70, $A$=15×15 mm$^2$ and $N$=6. An $U_{min}$=4.8V is obtained by measurement with a low capacitance probe with the oscilloscope at the read range distance. $H_{min}$ can be considered a figure of merit of the tag because it depends only on the tag parameters (IC and receiver antenna). Therefore, it can be employed to evaluate the tag performance independently of the reader used to generate the field. Good agreement has been achieved between the experimental characterization of the $H_{min}$ and the analytical model. From these results, the threshold or minimum power that activates the energy harvesting output is 13.2 dBm (very close to the 14 dBm considered in the simulation of section 7.3.3). The estimated power conversion considering a load of 3 mA and the static DC current consumption given in the datasheet (around 400 µA) gives a PCE of 42.82 %. This value is close to the one obtained with the rectifier simulated in section 7.3.3.

Figure 7.30 shows the measured average magnetic field as a function of the reader-to-skin distance ($d_{air}$) for different depths of the implanted tag in the case of the 2-coil system. Finally, Figure 7.31 shows the same measurement as Figure 7.30 but for the 3-coil system.

It is shown that implanted distances of up to 16 mm can be reached in the case of the 3-coil system. However, the detuning of the relay antenna can be observed due to the proximity of the metal of the mobile. Therefore, the peak of the magnetic field is obtained for distances between the reader and skin around 15 mm. The position of this peak can be tuned by changing the resonance frequency of

the relay antenna, adjusting the tuning capacitor. Figure 7.31 shows the higher robustness of the 3-coil system over the 2-coil system. In all the measurements a commercial mobile (Xiaomi Note 2) is used as the reader. The reader antenna in this mobile is around the camera and the size of the antenna is about 25 mm × 25 mm (as the reader antenna 1-2 in Table 7.IV).

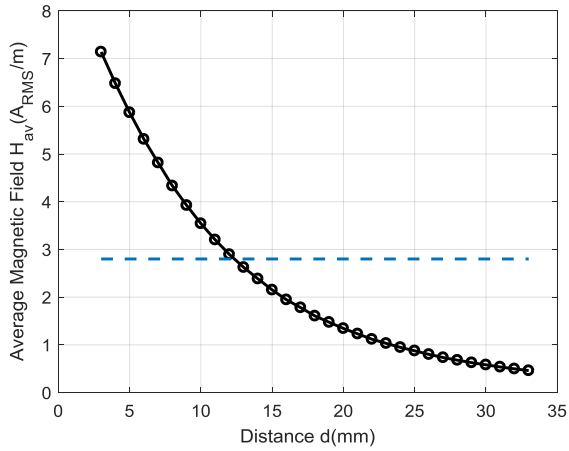


Figure 7.27. Average magnetic field ($H_{av}$), measured as a function of the tag-to-reader distance in the air for the 2-coil system. Threshold $H_{min}$ is shown as a dashed line.

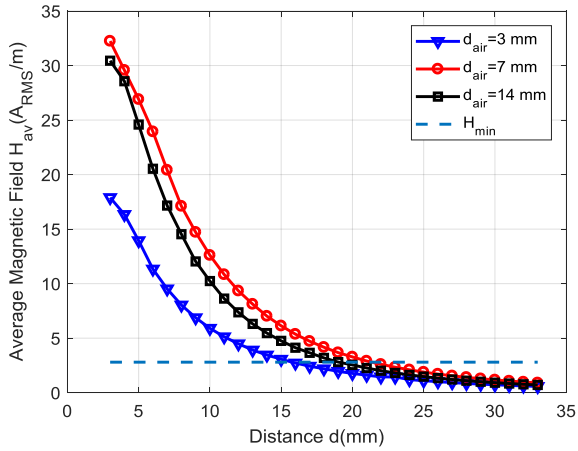


Figure 7.28. Average magnetic field ($H_{av}$) measured as a function of the distance between the tag and the relay antenna for different distances to the reader in the air ($d_{air}$) for the 3-coil system.

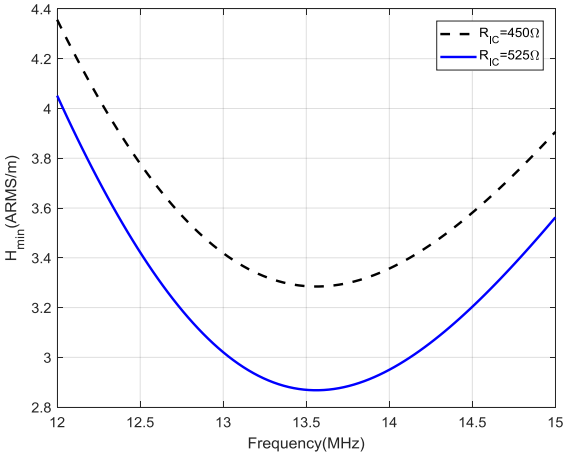


Figure 7.29. Simulated threshold magnetic field $H_{min}$ as a function of the frequency.

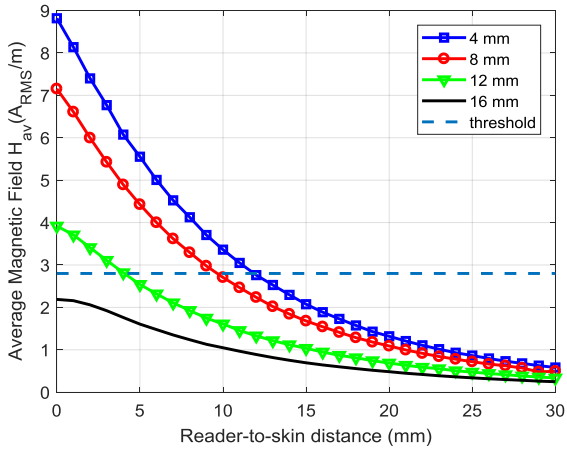


Figure 7.30. Measured average magnetic field ($H_{av}$) as a function of the reader-to-skin distance ($d_{air}$) for different depths of the implanted tag in the phantom for the 2-coil system. Threshold $H_{min}$ is shown as a dashed line.

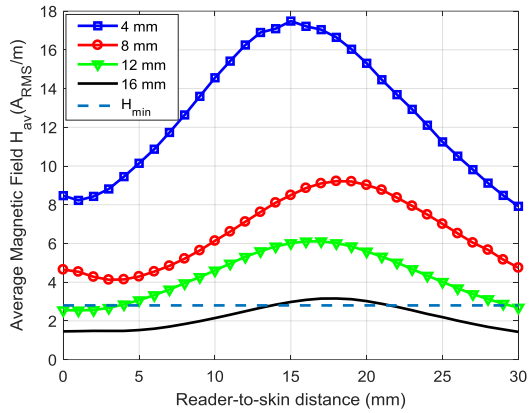


Figure 7.31. Measured average magnetic field ($H_{av}$) as a function of the reader-to-skin distance ($d_{air}$) for different depths of the implanted tag in the phantom for the 3-coil system. Threshold $H_{min}$ is shown as a dashed line.

## 7.5 Conclusions

This work has analysed the feasibility of using battery-less NFC tags for implants that can be read using commercial mobiles. The use of standardized NFC readers and devices presents several challenges compared to custom-designed WPT systems. Two of these are the size of the implanted antenna and the reader loop antenna. Others arise in connection with the limitations in power and the high bandwidth of the communication that limit the system's overall quality factor. The effects of the tag's nonlinearity must also be considered. The IC impedance decreases with the power received and, as a consequence, the loaded quality factor decreases, and efficiency cannot achieve high values compared with other WPT cases in which this limitation does not exist. Thus, the quality factor of the tag (implanted antenna) is not critical. Finally, other effects are the detuning due to the metallic cases of the mobile and the high permittivity of body materials. Two WPT systems have been theoretically and experimentally studied, these being the 2-coil and 3-coil systems. The latter is implemented using a relay antenna placed on top of the skin that makes it possible to reduce the effects of the low coupling coefficient between the reader and tag antennas, which can be of different sizes and enable the magnetic field received at the tag to increase. The result is an increase in the reliability of the link and a greater depth for the implant. The experimental results show that when using a standard 2-coil system, a maximum

depth of 12 mm can be achieved with the mobile close to the skin, whereas depths of up to 16 mm can be achieved with the proposed 3-coil system when placing the mobile phone at distances of 1-2 cm from the skin. The maximum distances obtained for activating the harvesting mode of the NFC IC and feeding the sensors are similar when considering the implant both inside the phantom and in the air, because the body is non-magnetic and thus barely attenuates the magnetic field at the operating frequency. However, both the implanted and the relay antennas need to be tuned for each case. The effect of detuning is studied by means of electromagnetic simulations, and an improved model has been proposed for modelling the quality factor of the antennas. The detuning effects due to high permittivity on the loop antennas are avoided by installing a low permittivity spacer in the order of 0.5 to 1 mm. The relay antenna can then be placed on top of the skin using adhesive patches. The use of low permittivity coating (e.g. a biocompatible material such as silicone) reduces degradation of the quality factor of the coils and sensitivity

## 7.6 Bibliography

[1] H. Dinis and P. M. Mendes, "Recent Advances on Implantable Wireless Sensor Networks," in *Intech*, vol. i, 2016, p. 13.

[2] M. Schormans, V. Valente, and A. Demosthenous, "Practical Inductive Link Design for Biomedical Wireless Power Transfer: A Tutorial," *IEEE Trans. Biomed. Circuits Syst.*, Jul. 2018.

[3] B. D. McKean and D. A. Gough, "A Telemetry-Instrumentation System for Chronically Implanted Glucose and Oxygen Sensors," *IEEE Trans. Biomed. Eng.*, vol. 35, no. 7, pp. 526–532, 1988.

[4] N. Anabtawi, S. Freeman, and R. Ferzli, "A fully implantable, NFC enabled, continuous interstitial glucose monitor," in *2016 IEEE-EMBS International Conference on Biomedical and Health Informatics (BHI)*, 2016, pp. 612–615.

[5] S. Tankiewicz, J. Schaefer, and A. Dehennis, "A co-planar, near field communication telemetry link for a fully-implantable glucose sensor using high permeability ferrites," *Proc. IEEE Sensors*, 2013.

[6] M. C. Frost and M. E. Meyerhoff, "Implantable chemical sensors for real-time clinical monitoring: Progress and challenges," *Curr. Opin. Chem. Biol.*, vol. 6, no. 5, pp. 633–641, 2002.

[7] R. Farra *et al.*, "First-in-human testing of a wirelessly controlled drug delivery microchip," *Sci. Transl. Med.*, vol. 4, no. 122, 2012.

[8] G. Yilmaz and C. Dehollain, "Single frequency wireless power transfer and full-duplex communication system for intracranial epilepsy monitoring," *Microelectronics J.*, vol. 45, no. 12, pp. 1595–1602, 2014.

[9] Z. Yang, Q. Zhao, E. Keefer, and W. Liu, "Noise characterization, modeling, and reduction for in vivo neural recording," *Adv. Neural Inf. Process. Syst. 22 - Proc. 2009 Conf.*, pp. 2160–2168, 2009.

[10] K. Bazaka and M. V. Jacob, *Implantable devices: Issues and challenges*, vol. 2, no. 1. 2012.

[11] J. C. Chiou *et al.*, "Toward a Wirelessly Powered On-Lens Intraocular Pressure Monitoring System," *IEEE J. Biomed. Heal. Informatics*, vol. 20, no. 5, pp. 1216–1224, 2016.

[12] M. H. Ghaed *et al.*, "Circuits for a cubic-millimeter energy-autonomous wireless intraocular pressure monitor," *IEEE Trans. Circuits Syst. I Regul. Pap.*, vol. 60, no. 12, pp. 3152–3162, 2013.

[13] G. Chitnis, T. Maleki, B. Samuels, L. B. Cantor, and B. Ziaie, "A minimally invasive implantable wireless pressure sensor for continuous IOP monitoring," *IEEE Trans. Biomed. Eng.*, vol. 60, no. 1, pp. 250–256, 2013.

[14] P. D. Costa, P. P. Rodrigues, A. H. Reis, and A. Costa-Pereira, "A review on remote monitoring technology applied to implantable electronic cardiovascular devices," *Telemed. e-Health*, vol. 16, no. 10, pp. 1042–1050, 2010.

[15] M. A. Hannan, S. Mutashar, S. A. Samad, and A. Hussain, "Energy harvesting for the implantable biomedical devices: Issues and challenges," *Biomed. Eng. Online*, vol. 13, no. 1, pp. 1–23, 2014.

[16] D. Seo *et al.*, "Wireless Recording in the Peripheral Nervous System with Ultrasonic Neural Dust," *Neuron*, vol. 91, no. 3, pp. 529–539, 2016.

[17] G. Enrico Santagati and T. Melodia, "Experimental Evaluation of Impulsive Ultrasonic Intra-Body Communications for Implantable Biomedical Devices," *IEEE Trans. Mob. Comput.*, vol. 16, no. 2, pp. 367–380, 2017.

[18] K. Goto, T. Nakagawa, O. Nakamura, and S. Kawata, "An

implantable power supply with an optically rechargeable lithium battery," *IEEE Trans. Biomed. Eng.*, vol. 48, no. 7, pp. 830–833, 2001.

[19] W. B. Phillips, B. C. Towe, and P. J. Larson, "An Ultrasonically-Driven Piezoelectric Neural Stimulator," *Annu. Int. Conf. IEEE Eng. Med. Biol. - Proc.*, vol. 2, pp. 1983–1986, 2003.

[20] M. Kiani, U. M. Jow, and M. Ghovanloo, "Design and optimization of a 3-coil inductive link for efficient wireless power transmission," *IEEE Trans. Biomed. Circuits Syst.*, vol. 5, no. 6, pp. 579–591, 2011.

[21] J. I. Agbinya, *Wireless Power Transfer, 2nd edition*, no. December. River Publishers Serires in Communications, 2015.

[22] G. Yilmaz, "Wireless Power Transfer and Data Communication for Intracranial Neural Implants Case Study," pp. 460–463, 2014.

[23] D. Paret, *Design contraints for NFC devices*. 2016.

[24] A. Lazaro, R. Villarino, D. Girbau, A. Lazaro, R. Villarino, and D. Girbau, "A survey of NFC sensors based on energy harvesting for IoT applications," *Sensors (Switzerland)*, vol. 18, no. 11, p. 3746, Nov. 2018.

[25] D. Halperin *et al.*, "Pacemakers and implantable cardiac defibrillators: Software radio attacks and zero-power defenses," in *Proceedings - IEEE Symposium on Security and Privacy*, 2008, pp. 129–142.

[26] S. Gollakota, H. Haitham, B. Ransford, D. Katabi, and K. Fu, "They can hear your heartbeats: non-invasive security for implantable medical devices," *Proc. ACM SIGCOMM Comput. Commun. Rev.*, vol. 203, no. 1, pp. 181–191, 2011.

[27] A. Jara and M. Zamora, "Secure use of NFC in medical environments," *2009 5th Eur. Work. RFID Syst. Technol. (RFID SysTech)*, pp. 1–8, 2009.

[28] S. Bojjagani and V. N. Sastry, "A secure end-to-end proximity NFC-based mobile payment protocol," *Comput. Stand. Interfaces*, vol. 66, no. 1, p. 103348, 2019.

[29] R. Altawy and A. M. Youssef, "Security Tradeoffs in Cyber Physical Systems: A Case Study Survey on Implantable Medical Devices," *IEEE Access*, vol. 4, pp. 959–979, 2016.

[30] A. Kurs, A. Karalis, R. Moffatt, J. D. Joannopoulos, P. Fisher, and

M. Soljacic, "Wireless power transfer via strongly coupled magnetic resonances.(RESEARCH ARTICLES)(Author abstract)," *Sicnece*, vol. 317, no. 5834, p. 83(4), 2007.

[31] B. L. Cannon, J. F. Hoburg, D. D. Stancil, and S. C. Goldstein, "Magnetic Resonant Coupling As a Potential Means for Wireless Power Transfer to Multiple Small Receivers," *IEEE Trans. Power Electron.*, vol. 24, no. 7, pp. 1819–1825, 2009.

[32] M. Gebhart, J. Bruckbauer, and M. Gossar, "Chip impedance characterization for contactless proximity personal cards," in *2010 7th International Symposium on Communication Systems, Networks and Digital Signal Processing, CSNDSP 2010*, 2010, pp. 826–830.

[33] N. Gvozdenovic, L. W. Mayer, and C. F. Mecklenbrauker, "Measurement of harmonic distortions and impedance of HF RFID chips," in *8th European Conference on Antennas and Propagation, EuCAP 2014*, 2014, pp. 2940–2944.

[34] B. Couraud, T. Deleruyelle, E. Kussener, and R. Vauché, "Real-Time Impedance Characterization Method for RFID-Type Backscatter Communication Devices," *IEEE Trans. Instrum. Meas.*, vol. 67, no. 2, pp. 288–295, 2018.

[35] X. Qing and Z. N. Chen, "Proximity effects of metallic environments on high frequency RFID reader antenna: Study and applications," *IEEE Trans. Antennas Propag.*, vol. 55, no. 11 I, pp. 3105–3111, 2007.

[36] H. Zhu, S. Lai, and H. Dai, "Solutions of metal surface effect for HF RFID systems," *2007 Int. Conf. Wirel. Commun. Netw. Mob. Comput. WiCOM 2007*, no. 1, pp. 2089–2092, 2007.

[37] H. L. H.T. Jensen, "Chassis NFC antenna booster," U.S. Patent No. 9,729,210, 2017.

[38] B. Lee, B. Kim, and S. Yang, "Enhanced loop structure of NFC antenna for mobile handset applications," *Int. J. Antennas Propag.*, vol. 2014, 2014.

[39] J. Q. Zhu, Y. L. Ban, C. Y. D. Sim, and G. Wu, "NFC antenna with nonuniform meandering line and partial coverage ferrite sheet for metal cover smartphone applications," *IEEE Trans. Antennas Propag.*, vol. 65, no. 6, pp. 2827–2835, Jun. 2017.

[40] D. C. Q. Liu, J. Zhou, "NFC antenna assembly," U.S. Patent No. 9,941,572, 2018.

[41] A. Zhao and H. Chen, "Small size NFC antenna with high performance," *2016 IEEE Antennas Propag. Soc. Int. Symp. APSURSI 2016 - Proc.*, vol. 3, pp. 1469–1470, 2016.

[42] H. Chen and A. Zhao, "NFC antenna for portable device with metal back cover," *2016 IEEE Antennas Propag. Soc. Int. Symp. APSURSI 2016 - Proc.*, pp. 1471–1472, 2016.

[43] M. A. Chung and C. F. Yang, "Miniaturized NFC Antenna Design for a Tablet PC With a Narrow Border and Metal Back-Cover," *IEEE Antennas Wirel. Propag. Lett.*, vol. 15, pp. 1470–1474, 2016.

[44] B. Lee and F. J. Harackiewicz, "Design of a simple structured NFC loop antenna for mobile phones applications," *Prog. Electromagn. Res. C*, vol. 76, no. June, pp. 149–157, 2017.

[45] Bing Jiang, J. R. Smith, M. Philipose, S. Roy, K. Sundara-Rajan, and A. V. Mamishev, "Energy Scavenging for Inductively Coupled Passive RFID Systems," *2005 IEEE Instrumentationand Meas. Technol. Conf. Proc.*, vol. 2, no. May, pp. 984–989, 2005.

[46] C. Marechal and D. Paret, "The loading effect of proximity contactless smart card. Incidences of impedance of the shunt regulator," *2008 Int. Conf. Wirel. Commun. Netw. Mob. Comput. WiCOM 2008*, pp. 8–11, 2008.

[47] M. Gebhart, "Analytical considerations for an ISO / IEC14443 compliant SmartCard transponder," *Proc. 11th Int. Conf. Telecommun.*, pp. 9–16.

[48] C. H. Lu, J. A. Li, and T. H. Lin, "A 13.56-MHz passive NFC tag IC in 0.18-μm CMOS process for biomedical applications," *2016 Int. Symp. VLSI Des. Autom. Test, VLSI-DAT 2016*, pp. 7–10, 2016.

[49] B. Jamali, D. C. Ranasinghe, and P. H. Cole, "Analysis of UHF RFID CMOS rectifier structures and input impedance characteristics," *Microelectron. Des. Technol. Packag. II*, vol. 6035, no. January 2006, p. 60350D, 2005.

[50] J. Teichmann, K. Burger, W. Hasche, J. Herrfurth, and G. Täschner, "One time programming (OTP) with Zener diodes in CMOS processes," in *European Solid-State Device Research Conference*, 2003, pp. 433–436.

[51] Z. Zhu, "RFID analog front end design tutorial," *Auto-ID lab Univ. Adelaide*, pp. 3–34, 2004.

[52] J. Hu, S. Wu, K. Lin, and H. Tan, "Low-power energy supply circuit for passive RFID transponder," *2009 IEEE Int. Conf. RFID, RFID 2009*, no. 2008, pp. 1–6, 2009.

[53] F. Alcalde, O. Alpago, and J. Lipovetsky, "CMOS design of an RFID interface compatible with ISO/IEC-14443 type a protocol," *Proc. 2014 Argentine Sch. Micro-Nanoelectronics, Technol. Appl. EAMTA 2014*, pp. 41–47, 2014.

[54] H. Jianguo, T. Hongzhou, and X. Yongjian, "A novel design of low power RFID tag interface circuit," *IET Conf. Publ.*, no. 533 CP, pp. 478–481, 2007.

[55] "Mosis integrated circuit fabrication service." [Online]. Available: https://www.mosis.com/vendors/view/tsmc/018. [Accessed: 22-Aug-2019].

[56] C. Y. TAN, B. STATHAM, R. MARKS, and P. A. PAYNE, "Skin thickness measurement by pulsed ultrasound; its reproducibility, validation and variability," *Br. J. Dermatol.*, vol. 106, no. 6, pp. 657–667, 1982.

[57] S. Huclova, D. Erni, and J. Fröhlich, "Modelling and validation of dielectric properties of human skin in the MHz region focusing on skin layer morphology and material composition," *J. Phys. D. Appl. Phys.*, vol. 45, no. 2, 2012.

[58] C. Gabriel, S. Gabriel, and E. Corthout, "The dielectric properties of biological tissues: I. Literature survey," *Phys. Med. Biol.*, vol. 41, no. 11, pp. 2231–2249, 1996.

[59] S. Gabriel, R. W. Lau, and C. Gabriel, "The dielectric properties of biological tissues: II. Measurements in the frequency range 10 Hz to 20 GHz," *Phys. Med. Biol.*, vol. 41, no. 11, pp. 2251–2269, Nov. 1996.

[60] S. Gabriel, R. W. Lau, and C. Gabriel, "The dielectric properties of biological tissues: III. Parametric models for the dielectric spectrum of tissues," *Phys. Med. Biol.*, vol. 41, no. 41, pp. 2251–2269, 1996.

[61] P. E. K. Donaldson and E. Sayer, "A technology for implantable hermetic packages. Part 2: An implementation," *Med. Biol. Eng. Comput.*, vol. 19, no. 4, pp. 403–405, Jul. 1981.

[62] H. A. Wheeler, "Formulas for the Skin Effect," *Proc. IRE*, vol. 30, no. 9, pp. 412–424, 2007.

[63] C. Dichtl, P. Sippel, and S. Krohns, "Dielectric Properties of 3D Printed Polylactic Acid," *Adv. Mater. Sci. Eng.*, vol. 2017, 2017.

[64] M. Boada, A. Lazaro, R. Villarino, and D. Girbau, "Battery-Less NFC Sensor for pH Monitoring," *IEEE Access*, vol. 7, pp. 33226–33239, 2019.

[65] A. Lazaro *et al.*, "Color Measurement and Analysis of Fruit with a Battery-Less NFC Sensor," *Sensors*, vol. 19, no. 7, p. 1741, Apr. 2019.

[66] K. Fotopoulou and B. W. Flynn, "Wireless power transfer in loosely coupled links: Coil misalignment model," *IEEE Trans. Magn.*, vol. 47, no. 2 PART 2, pp. 416–430, 2011.

[67] M. Ishii and K. Komiyama, "A Measurement Method for the Antenna Factor of Small Loop Antenna by Measuring the Input Impedance," in *2004 Conference on Precision Electromagnetic Measurements*, 2004, pp. 80–81.

# 8. Conclusions

This Doctoral Thesis has studied the application of sensors in battery-less NFC tags powered by the radiofrequency generated by smartphones. Circuit models for the reader and the tag have been proposed to be subsequently analysed in order to achieve an efficient wireless power transfer as well as taking into account the standards related to NFC to assure the data communication.

Several sensors have been successfully embedded in battery-less tags. A custom sensor for volumetric water content has been implemented along with commercial sensors, both analog and digital. It has been shown the viability of developing such low-cost sensors with an acceptable accuracy and time response. Another approach to measure moisture in diapers in a non-invasive way has been developed, by measuring the change in capacitance between 2 electrodes. Such method could be implemented with other technologies such as BLE to overcome the limitations of NFC, achieving longer read ranges and constant monitoring, however, the use of NFC reduces the price dramatically as well as expands its shelf life due the lack of batteries, and increases simplicity avoiding the need of pairing the devices.

A more demanding colour sensor, with current requirements of a few microamperes has been developed and studied. This sensor uses a led to light up the sample. The persistence has been proved with two different applications and compared with other techniques (i.e. image processing). Even though the presented work focus on the hardware, the possibilities brought from the software side are shown with an application of fruit classification, where, after analysing several items, a pattern has been determined to decide the ripeness state of the fruit by determining certain boundaries. The fact of using smartphones as a readers, ease the development of powerful and user-friendly applications, which must be considered for further study, along with the firmware on the tag's microcontroller and the exploit of NDEF record types.

There are two main advantages of using NFC battery-less tags: the use of an affordable, common and user-friendly readers, and the possibility of avoiding batteries. The first brings, to any end-user with a smartphone, the possibility to use the technology in a very

easy way keeping the *tap-and-go* concept. The second, beyond the fact of getting rid of the maintenance an spreading the useful life of the tags, allows to use tags in environments where the toxic components of batteries are inadvisable or entails an increase of the production cost, such as when the tag is placed near food or even inside the body. Hence the interest of study the feasibility of using this device for implantable tags. This leads to the development of small tags, and, consequently, small antennas. All this constrains have been addressed in this work, presenting a small tag, and showing the improvements of using a relay coil between reader and the tag, which extends the read range as well as the energy harvesting range. Furthermore, the use of an external relay may help for the alignment of the coils, whose effect is accentuated when using small coils, as has been proved. The viability of using implantable devices, surrounded by body matter, has been proved, after tuning the tag consequently.

The use of a microcontroller in passive-tags has been tested for very different applications, some more demanding than others, proving that can perfectly work with the energy constrains presented in the NFC scenario. The restrictions, then, comes from the consumption of the sensors or other circuitry used in the tag, and the acquisition time, since it is important to keep the *tap-and-go* idea, hence the sensing must be done in a few seconds. The development of low-power sensors has an increasing interest in the industry and is expected to keep growing. NFC tags will benefit for that, spreading its possibilities.

The future of NFC is promising, being its implementation assured due the growing use as payment system. There are several research interests for future work. On the one hand, hardware improvements on the design of NFC chips and systems as well as low-power sensors, will bring new possibilities to implement more variety of sensors. On the other hand, there is a promising future on the possible applications. As mentioned above, the main advantage of NFC technology is the use of conventional smartphones as a reader. The fact of having a reader in almost any pocket, altogether with the simplicity of its use, turns this technology into a very interesting player within the IoT scenario. The low price and long-life of the tags make possible the spread of those around. Thus, an interesting

future research work could be the implementation of a massive collaborative system, where the users would bring the phone close to a tag which, for instance, would measure the air or water quality, and at the same time that they get the information it will be sent to a database in the cloud. Other collaborative applications may use gamification to motivate the users to get some kind of points or something similar by tapping the tags, and the retrieved data could be stored for a further big data analysis.

Maybe the most promising use of NFC at short or mid-term, would be its use in implantable tags and other telemedicine applications, since it provides a standardized communication system which does not require a specific and expensive reader, neither an application specific IC, as most of the current works presented in the literature need. A further study on the long-term use and improvements on the sensing capabilities of miniaturised tags is needed for the commercial industrialisation.

# Annex 1

## Near Field Communication (NFC)

NFC is a subset of protocols within RFID technology, which operates at 13.56 MHz, mainly aimed for mobile or handheld devices. It started around the year 2000 when two of the main leaders in the industry, Sony and Philips, decided to cooperate to create a standard for multiple, generic and varied applications for digital data. Few years later, in 2004, and with the support of a bunch of companies, the NFC Forum was born. The goals of the NFC Forum are: develop specification and test mechanisms, take a leadership role in the industry to ensure NFC can deliver a positive user experience, educate enterprises, service providers and developers about the benefits of NFC, and establish the NFC Forum and NFC technology brand as well recognised and utilised marks (see Figure A.1) [1]. To accomplish these goals, it is mandatory to achieve an environment where the technology is used for any end-user just with a simple geasture over the tag, no matter the application, either to pay a coffee or getting an alarm because his/her glucose level is falling. But that is not an easy thing since there are several existing contactless communication protocols which use RFID at the UF band, a bunch of companies developing NFC devices, using different standards, hence the importance of a "big player" like the NFC Forum to unify the ecosystem to spread it successfully worldwide.


Figure A.1. NFC Forum N-Mark.

## Operating modes

There are three possible operating modes for an NFC tag based on the ISO/IEC 18092 [2], ISO/IEC 14443 [3] and ISO/IEC 15693 [4] standards:

- Card emulation: the device acts like a contactless card, the typical use case is for using the device for payments or ticketing. Can be based on ISO/IEC 14443 or 15693.
- Reade/write: the device can read a tag and overwrite the content if the tag allows it. Used for smart posters, get an URL or getting the sensed data from a tag. Can be based on ISO/IEC 14443 or 15693.
- Peer to Peer (P2P): allows to exchange data between 2 devices. Used to transfer data such as photos or any other data. Based on ISO/IEC 18092.

There is a fourth mode, whose technical specification is still a candidate, waiting for approval:

- Wireless charging (WLC): power transfer from a device to another device such as a smartwatch or fitness tracker. Four power transfer classes are specified: 250, 500, 750 and 1000 mW.

### NFC Forum specifications

To give a better view of the relationship between RFID and NFC, Figure A.2 depicts the set of standards and protocols related to NFC. As can be seen, NFC uses the physical characteristics, air interface and some protocols of the existing standards used by RFID. The contribution of the NFC Forum has been to add a number of technical specifications like a specific data exchange format with differentiated record types and tag types. An above application layer groups all the standards with a same data exchange format. The ambition of the NFC Forum is the pervasiveness of NFC technology among all the manufacturers, making devices compatibles with all the different existing standards.

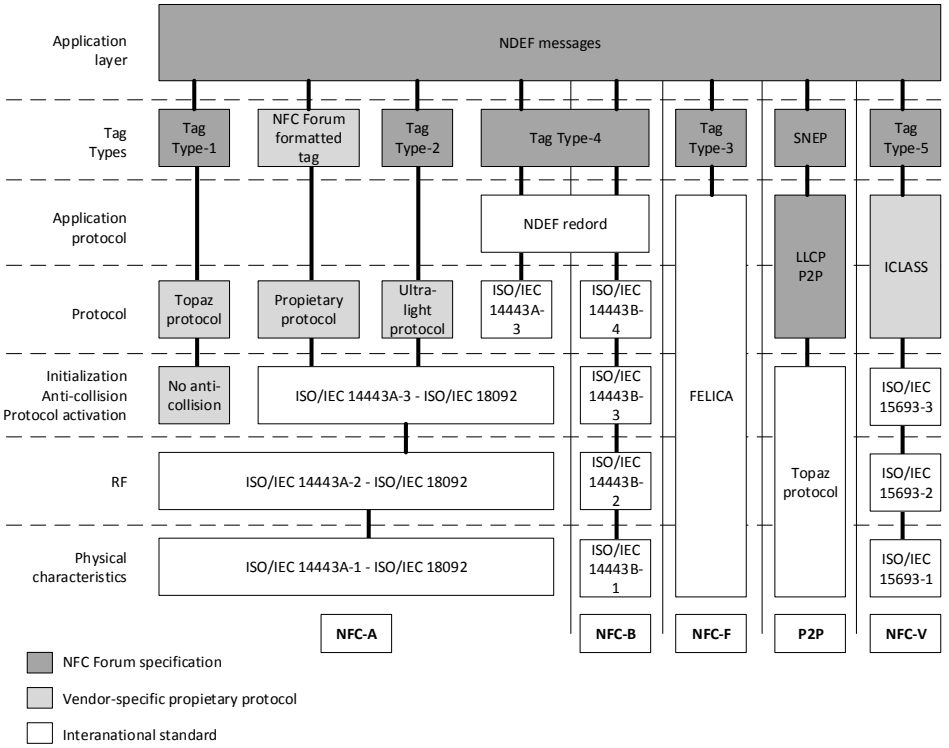


Figure A.2. RFID and NFC standards and specifications

The set of specifications created by the NFC Forum allow NFC Forum compliant devices to communicate with readers/cards compliant with ISO/IEC 14443 Type A and B standards, cards compliant with ISO/IEC 15693, devices compliant to ISO/IEC 18092, Readers/cards compliant to JIS-X 6319-4 [5], as well as with NFC Forum tags and NFC Forum devices. A structured logical stack of functional layers over which NFC is built is depicted in Figure A.3, from physical to software layers implementation.

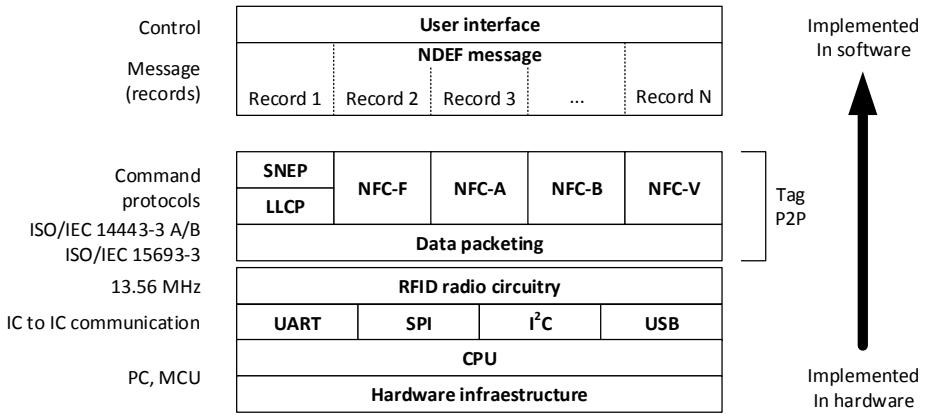


Figure A.3. NFC system functional architecture.

NFC Forum specifications [6] include:

- Protocol
  - Logical Link Control Protocol (LLCP)
  - Digital Protocol
  - Activity Technical
  - Simple NDEF Exchange Protocol (SNEP)
  - Analog
  - NFC Controller Interface (NCI)
- Data exchange
  - NFC Data Exchange Protocol (NDEF)
- Forum tag types
  - Type 1 to Type 5
- Record type definition
  - Record Type Definition (RTD): Text, URI, Verb, Smart poster, Generic control, Signature, NFC device information
- Reference application
  - Connection handover
  - Personal health device communication
- Wireless charging
  - Wireless Charging

Even though NFC has the shortest range among radiofrequency technologies, it has been widely extended due its security, compatibility, user friendly interface, large amount of applications, and low-cost components. The main reason of the current growing

implementation of NFC in almost any smartphone is due its use for contactless payments, making it increasingly indispensable for the end-user, like happens with other wireless technologies such as Wi-Fi or Bluetooth. As the IoT scenario grows, the number of devices and the ways people interact with devices grows with it. The present work is motivated by the possibilities that NFC brings us, to create applications without batteries, thus, avoiding toxic waste while extending life-time of devices.

## Forum tag types

Five type tags are defined by the NFC Forum, each of them with a certain characteristics (see Table 1.IV).

Table A.I. NFC Forum type tags.

| | Type 1 | Type 2 | Type 3 | Type 4 | Type 5 |
|---|---|---|---|---|---|
| Technology | NFC-A | NFC-A | NFC-F | NFC-A NFC-B | NFC-V |
| Standard | ISO14443A | ISO14443A | JIS 6319-4 | ISO14443 A/B | ISO15693 |
| Memory size | Up to 2 kBytes | Up to 2 kBytes | Up to 1 MBytes | Up to 32 Kbytes | Up to 64 kBytes |
| Transmission Speed (kbits/s) | 106 | 106 | 212 /424 | 106 | Up to 26.5 |
| Unit price | Low | Low | High | Medium / High | Low / Medium |
| Range | Proximity | Proximity | Proximity | Proximity | Proximity & vicinity |
| Chip examples | Innovision Topaz | Mifare ultralight | Felica | Mifare DESFire | ICODE SLI |
| Use case | Business cards, smart poster | Event tickets, transit tickets | e-money, membership cards | Transit tickets | Packaging, ticketing |

Each type of tag is based on a NFC technology. Table A.II summarises the modulations, coding, and sub-carrier frequencies used by these technologies.

Table A.II. NFC Technologies.

| | NFC-A | NFC-B | NFC-F | NFC-V |
|---|---|---|---|---|

| Standard | ISO14443A | ISO14443B | JIS 6319-4 | ISO15693 |
|---|---|---|---|---|
| Modulation (Reader to tag) | ASK 100% | ASK 10% | ASK 10% | ASK 10% or 100% |
| Data coding (Reader to tag) | Miller | Miller | Manchester MSB first | ¼ PPM or 1/256 PPM |
| Load modulation | ASK | ASK | ASK | ASK |
| Sub-carrier modulation | OOK | OOK | n/a | OOK/FSK |
| Data coding (Tag to reader) | Manchester | Manchester | Manchester | Manchester |
| Sub-carrier (kHz) | 848 | 848 | n/a | 424/848 |
| Anti-colision | No | No | Yes | Yes |

ASK: Amplitude Shift Keying
MSB: Most Significant Bit
PPM: Pulse Position Modulation
OOK: On-Off Keying
FSK: Frequency Shift Keying

## NDEF

One of the most significant features that NFC add upon the RFID standards is the data exchange format NDEF (NFC Data Exchange Format). NDEF is independent from the command protocols and NFC technologies, being on the top of the NFC architecture stack (as shown in Figure A.2), thus, NDEF can be used across all NFC devices, regardless of the underlying tag type.

NDEF is a light-weight binary message format used to encapsulate one or more application-defined payloads of arbitrary type and size into a single message construct. Each payload is described by a type, a length and an optional identifier [7].

The NFC Forum standardises the different types of NDEF records in order to ease the interpretation of the messages by the NFC devices. Some of NDEF records are: text, URI, smart poster, signature, vCard or pairing Bluetooth or Wi-Fi. The payload type is used to dispatch the message to the appropriate user application.

The structure of a NDEF message is depicted in Figure A.4 and consists of one or more records, each one with a header and payload. The header contains some flags indicating the beginning and end of the message, the message type, the payload length, and an ID.

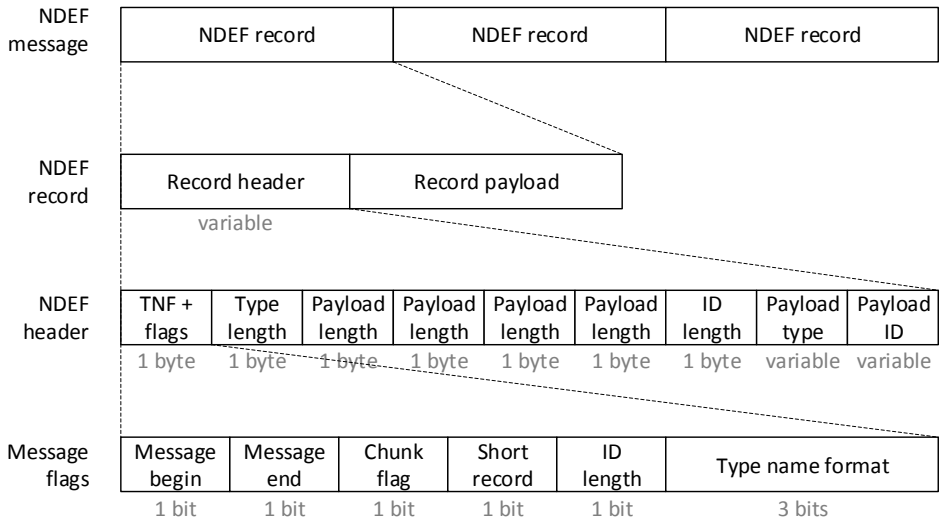


Figure A.4. NDEF message structure

## Security

NFC arose with the main purpose of replacing credit cards, event and transport tickets, personal ID cards, access keys, and other data-sensible applications, hence security has been intrinsically related to NFC since its birth. In fact, the short operational range, which would be an undesired factor for almost any wireless system, turns to be an important benefit regarding security. Existing literature demonstrates the importance of security with a large quantity of studies. Since the early development of NFC, the possible threats like eavesdropping, data corruption, insertion or modification, and relay attacks [8] have been addressed [9]–[12]. The security perception and concerns of end users for using mobile payment systems has been studied by the unified theory of acceptance and use of technology (UTAUT) model for some specific cases [13].

The growing interest on healthcare applications with sensible data is another scenario to consider [14]. Privacy, identity authentication, low power devices, limited storage capacity, accuracy, and integrity are the main points to take into account.

At the same time that it is a great chance for developing innovative applications, card emulation mode makes the system more likely to be attacked [15]. NFC devices with card emulation mode use a

secured piece of hardware called Secure Element (SE), connected to the NFC module. The SE can be embedded on the phone, or can be located on another elements such the user SIM card [16]. The SE only accepts new software from a Trusted Services Manager (TSM), who holds the private key to authenticate to the SE. Cryptography plays an important role and its effects over the operation speed must be considered [17] to keep a secure but still fast and easy-to-use user experience. Cryptographic protocols such as the Transport Layer Security (TLS) are used for P2P mode, applied, for instance, in IoT applications [18].

The current standards allow each application to adopt the required level of security and the possibility to incorporate security measures such as passwords, strong authentication, and access control, that further protect the integrity of the transactions as well as the stored information and the devices itself.

## Bibliography

[1] 'Our Mission & Goals - NFC Forum'. [Online]. Available: http://nfc-forum.org/about-us/the-nfc-forum/. [Accessed: 02-Nov-2019].

[2] 'ISO/IEC 18092: Information technology — Telecommunications and information exchange between systems — Near Field Communication — Interface and Protocol (NFCIP-1)'. International Organization for Standardization, 2013.

[3] 'ISO/IEC 14443: Identification cards – Contactless integrated circuit cards – Proximity cards'. International Organization for Standardization, 2018.

[4] 'ISO/IEC 15693: Identification cards — Contactless integrated circuit cards — Vicinity cards'. International Organization for Standardization, 2010.

[5] 'JSA - JIS X 6319-4: Specification of implementation for integrated circuit(s) cards'. Japanese Standards Association, 2016.

[6] NFC Forum, 'NFC Forum Technical Specifications', 2019. [Online]. Available: https://nfc-forum.org/our-work/specifications-and-application-documents/specifications/nfc-forum-technical-

specifications/. [Accessed: 03-Nov-2019].

[7] 'NFC Data Exchange Format (NDEF)'. NFC Forum Technical Specification, 2006.

[8] G. Hancke, 'A practical relay attack on ISO 14443 proximity cards', *Tech. report, Univ. Cambridge Comput. ...*, no. January 2005, pp. 1–13, 2005.

[9] E. Haselsteiner and K. Breitfuß, 'Security in Near Field Communication ( NFC ) Strengths and Weaknesses'. Philips Semiconductors, 2006.

[10] S. A. Weis, S. E. Sarma, R. L. Rivest, and D. W. Engels, 'Security and Privacy Aspects of Low-Cost Radio Frequency Identification Systems', in *International Journal of Security and Networks*, vol. 5, no. 2/3, 2004, pp. 201–212.

[11] K. Grassie, 'Easy handling and security make NFC a success', *Card Technol. Today*, vol. 19, no. 10, pp. 12–13, 2007.

[12] N. A. Chattha, 'NFC - Vulnerabilities and defense', *Conf. Proc. - 2014 Conf. Inf. Assur. Cyber Secur. CIACS 2014*, no. 1, pp. 35–38, 2014.

[13] J. Khalilzadeh, A. B. Ozturk, and A. Bilgihan, 'Security-related factors in extended UTAUT model for NFC based mobile payment in the restaurant industry', *Comput. Human Behav.*, vol. 70, no. 2017, pp. 460–474, 2017.

[14] A. Alzahrani, A. Alqhtani, H. Elmiligi, F. Gebali, and M. S. Yasein, 'NFC security analysis and vulnerabilities in healthcare applications', *IEEE Pacific RIM Conf. Commun. Comput. Signal Process. - Proc.*, pp. 302–305, 2013.

[15] M. Roland, 'Software Card Emulation in NFC-enabled Mobile Phones : Great Advantage or Security Nightmare', *Fourth Int. Work. Secur. Priv. Spontaneous Interact. Mob. Phone Use (IWSSI/SPMU 2012)*, p. 6, 2012.

[16] M. Reveilhac and M. Pasquet, 'Promising secure element alternatives for NFC technology', *Proc. - 2009 1st Int. Work. Near F. Commun. NFC 2009*, pp. 75–80, 2009.

[17] G. Van Damme and K. Wouters, 'Practical Experiences with NFC Security on mobile Phones', *Proc. RFIDSec*, p. 13, 2009.

[18] P. Urien, 'LLCPS: A new security framework based on TLS for NFC P2P applications in the Internet of Things', *2013 IEEE 10th Consum. Commun. Netw. Conf. CCNC 2013*, pp. 845–846, 2013.

# List of Acronyms

| | |
|---|---|
| AC | Alternating Current |
| ADC | Analog-to-Digital Converter |
| AIDC | Automatic Identification Data Capture |
| ASCII | American Standard Code for Information Interchange |
| ASIC | Application Specific Integrated Circuit |
| ASK | Amplitude Shift Keying |
| BLE | Bluetooth Low-Energy |
| BPF | Band-Pass Filter |
| CDF | Cumulative Distribution Function |
| CMOS | Complementary Metal Oxide Semiconductor |
| CMT | Coupled-Mode Theory |
| CTI | Critical Temperature Indicator |
| DBS | Deep Brain Stimulation |
| DC | Direct Current |
| ECL | Electrochemiluminescence |
| EEPROM | Electrically Erasable Programmable Read-Only Memory |
| EH | Energy Harvesting |
| EMI | Electromagnetic Interference |
| FDR | Frequency Domain Reflectometry |
| FR4 | Fiber-glass substrate |
| GPIO | General Purpose Input/Output |
| HSV | Hue Saturation Value |
| $I^2C$/I2C | Inter-Integrated Circuit |
| IC | Integrated Circuit |
| IDC | Inter-Digital Capacitor |
| IDE | Integrated Development Environment |
| IEC | International Electrotechnical Commission |
| IMD | Implantable Medical Device |

| | |
|---|---|
| IoT | Internet of Things |
| ISO | International Organization for Standardization |
| LDA | Linear Discrimination Analysis |
| MCU | Microcontroller |
| MEMS | Micro-Electro-Mechanical Systems |
| MOS | Metal Oxide Semiconductor |
| MUT | Material under test |
| MWCNT | Multi-Walled Carbon Nanotubes |
| NDEF | NFC Data Exchange Format |
| NFC | Near Field Communication |
| NMM | Neutron Moisture Meters |
| NMOS | N-type Metal Oxide Semiconductor |
| NN | Nearest Neighbour |
| P2P | Peer to Peer |
| PCA | Principal Component Analysis |
| PCB | Printed Circuit Board |
| PCE | Power Conversion Efficiency |
| PDL | Power Delivered to the Load |
| PLA | Polylactic Acid |
| PTE | Power Transfer Efficiency |
| QDA | Quadratic Discriminant Analysis |
| QR | Quick Response |
| RF | Radio Frequency |
| RFID | Radio Frequency Identification |
| RGB | Red Green Blue |
| RX | Reception |
| SA | Spectrum Analyser |
| SAP | Super Absorbent Polymer |
| SMD | Surface-Mount Device |
| TDR | Time Domain Reflectometry |

| | |
|---|---|
| TVBN | Total Volatile Basic Nitrogen |
| TX | Transmission |
| UL | Ultralam |
| USB | Universal Serial Bus |
| VNA | Vector Network Analyser |
| VWC | Volumetric Water Content |
| WISP | Wireless Identification and Sensing Platform |
| WLC | Wireless Charging |
| WPT | Wireless Power Transfer |